



PhD in Physics

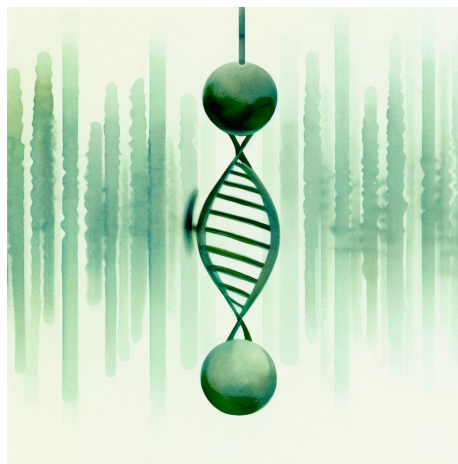
Exploring the complex dynamics of biological oscillators and their downstream effects

Neuronal synchronization, p53-mediated DNA repair and entrainment to external periodic signals

Alessandra Lucchetti

Supervisors: Mogens H. Jensen, Mathias S. Heltberg

September 2023



This thesis has been submitted to the PhD School of The Faculty of Science, University of Copenhagen

Alessandra Lucchetti

Exploring the complex dynamics of biological oscillators and their downstream effects

PhD in Physics, September 2023

Supervisors: Mogens H. Jensen and Mathias S. Heltberg

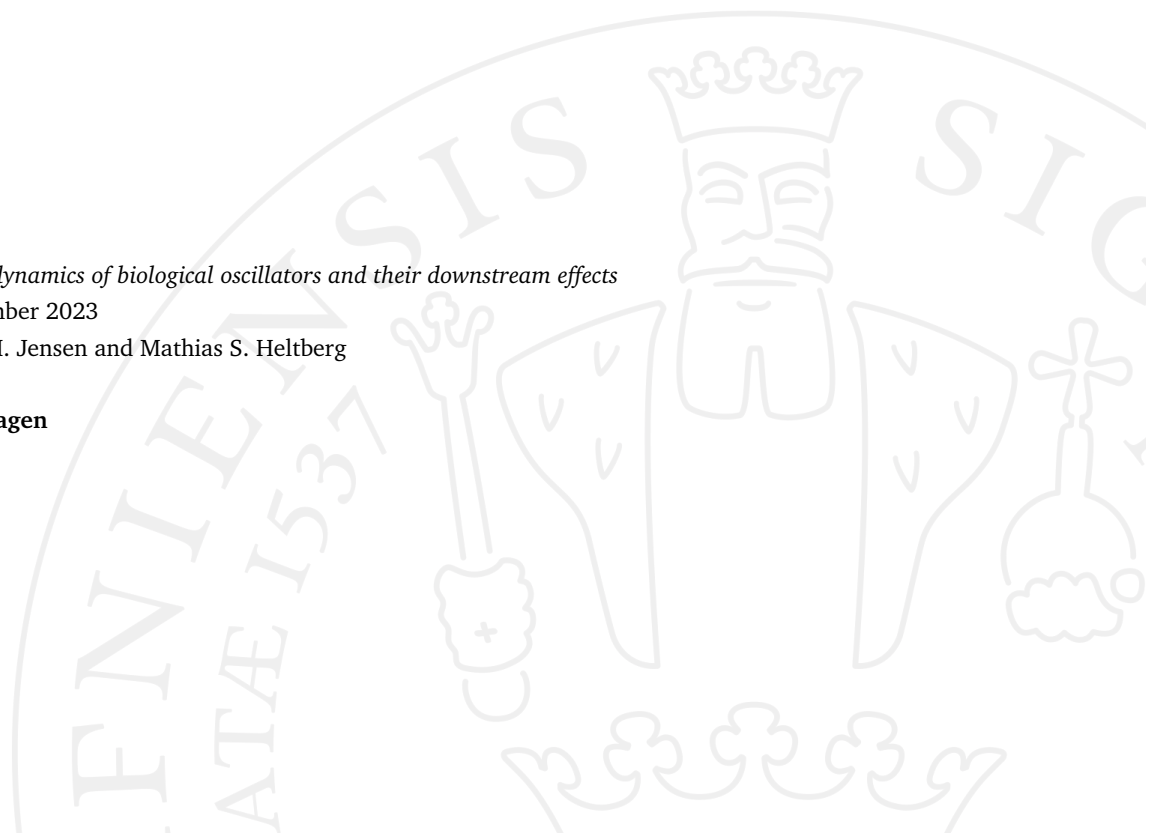
University of Copenhagen

Faculty of Science

Niels Bohr Institute

Blegdamsvej 17

2100 Copenhagen



"Nothing in life is to be feared, it is only to be understood. Now is the time to understand more, so that we may fear less."

Maria Skłodowska Curie, Nobel Prize in Physics 1903

"The way you do science should have an intrinsic beauty to it."

Elizabeth H. Blackburn, Nobel Prize in Physiology or Medicine 2009

Acknowledgements

First of all, I want to express my deep gratitude to my supervisors Mogens H. Jensen and Mathias S. Heltberg, for being an immense source of inspiration, both from a professional and a human point of view. Their exceptional knowledge, coupled with their infectious enthusiasm and optimistic outlook on research, have profoundly influenced my own approach to science. They unfailingly ensured that my projects were not just work, but something I found so fun, I would "be eager to delve into, even on a Saturday night". The trust in granting me absolute freedom to pursue any idea that crossed my mind is something I hold in the highest regard. They taught me the importance of celebrating every discovery, no matter how small, and embracing both achievements and setbacks. In moments of difficulty, they provided unwavering encouragement, shared laughs over problems, and engaged in insightful discussions at the blackboard, all in an effort to navigate through challenges together. This is something I am incredibly grateful for and that I will always treasure.

I would like to extend my heartfelt thanks to my colleagues at the institute, in particular my dear friends Anastasios and Fabio, for being such great companions along this journey. I am also extremely grateful to all the people of the Biocomplexity Group. Describing the vibrant atmosphere we experience daily at the institute to outsiders is no easy feat. It is a blend of enriching seminars, lively lunch discussions, "publication-cakes", game nights, summer schools, and the laughters of people teasing each other echoing in the corridors. I would also like to thank our experimental collaborators, in particular Galit Lahav's group at Harvard Medical school, for their kindness in hosting me in their lab for four months, offering me a unique and enriching experience. A special thanks to Alba Jiménez, I will never cease to be amazed by your contagious joy, you are truly a special person.

I would also like to express my gratitude to my dear friends from Italy, Alessio, Alessandro, Francesco, Alice, Maddalena, and Tommaso, that have kept my spirit up through the hard moments of the PhD, and have always been there for me, even from afar. A special thank you goes to my parents, Antonella and Enrico, and my dear sisters, Agnese and Francesca, for being the most caring and loving family I could ask for. I would like to thank my grandparents, too, for being my role models and examples of resilience, endurance and an immense joy and appreciation for life.

Lastly, I would like to thank my life partner, Andrea, from the bottom of my heart. I could list a million reasons, and they would not be enough: thank you for helping with optimizing my code, with making to-do lists and organizing my schedules, for actively listening to my brainstorms of ideas while strolling in the park, for engaging in discussions and getting excited with me about new projects. But mostly, for being my safe haven in the storms of life. Without you, none of this would have been possible.

Abstract

This work revolves around the mathematical modelling of biological oscillators and seeks to explore how their dynamics shapes the functionality of the associated systems; the thesis comprises three main parts.

In the first part, we investigated the ability of biological oscillators, in particular neurons, to synchronize their activities when coupled to each other. Understanding the spontaneous emergence of synchronization is of the utmost importance, as several neuronal diseases, such as Parkinson's disease or epileptic seizures, are believed to arise as a result of an abnormal synchronization in certain brain regions. We studied a network made of two subpopulations of neurons, an excitatory and an inhibitory one, interconnected through a negative feedback loop with time-delayed couplings. We observed that with strong inter-population couplings, neurons could not only internally synchronize within each population, but also portray a type of complex dynamics known as *chimera state*. In this state, one population is synchronized while the other remains unsynchronized, with the time delay ensuring the stability of this state. Indeed, with instantaneous connections, the chimera state became neutrally stable, with a family of so-called *breathing chimeras* around it, namely with one population synchronized and the other periodically switching between more coherent and incoherent states.

In the second part, we analysed the dynamics of oscillating transcription factors, in particular, p53, and its downstream effect in the process of DNA repair. p53 is also known as "guardian of the genome" for its role in cancer prevention and maintenance of genomic stability. As a result of severe DNA damage, p53 nuclear abundance starts to oscillate, with a periodicity of 5.5 h, whose role is still highly debated. At the same time, the formation of microenvironments rich of repair proteins has been observed around the sites of damage, which are believed to arise from liquid-liquid phase separation, effectively giving rise to biomolecular condensates. In this context, the question we sought to address was: how can the cell regulate the distribution of repair material in the presence of multiple DNA damages? Does p53 oscillatory dynamics, and its specific frequency, play a role in this process? We found that p53 oscillations ensure the optimal repair rate in the presence of multiple DNA breaks, by regulating the formation and coarsening of the condensates around the sites of damage, thus ensuring a spatio-temporal resource distribution within the cell.

In the third part, we explored the possibility of entraining p53 oscillations to an external pulsing signal, in order to regulate its frequency. Through a microfluidic device coupled with live-cell imaging, we were able to track the dynamics of p53 oscillations after administering single or repeated pulses of small molecule nutlin-3a. By examining the response of p53 to single perturbations, we successfully predicted the system's behaviour in response to a train of pulses, leading to the identification of Arnold tongues - an essential characteristic of entrainment. Our investigations revealed that the

system becomes entrained to the external signal, giving rise to not only higher order entrainment, but also multi-stability and period-doubling. Finally, we highlighted a potential relationship between p53 frequency and its downstream target, p21. Remarkably, we observed that the natural p53 frequency minimizes p21 accumulation, potentially serving as a mechanism to prevent rapid commitment of cells to specific fates. Collectively, our findings provide valuable insights into the dynamic interplay between p53 oscillations, external stimuli, and downstream cellular processes, contributing to our understanding of cellular regulation and decision-making.

Resume

Denne Ph.D. afhandling omhandler den matematisk-fysiske modellering af biologiske oscillatorer og søger at udforske, hvordan deres dynamik påvirker funktionen af de tilknyttede systemer. Afhandlingen består af tre hoveddele.

I den første del undersøgte vi biologiske oscillatorers, især neuroners, evne til at synkronisere deres aktivitet, når de er koblet til hinanden. At forstå en spontan synkronisering er af afgørende betydning, da flere neuronale sygdomme, såsom Parkinsons sygdom eller epileptiske anfald, menes at opstå som følge af en unormal synkronisering i visse hjerneområder. Vi studerede således et netværk bestående af to subpopulationer af neuroner, en excitorisk og en hæmmende, forbundet gennem en negativ feedback-loop med tidsforsinkede koblinger. Vi observerede, at med stærke inter-populationskoblinger kunne neuroner ikke blot synkronisere internt i de enkelte populationer, men også udvise en type kompleks dynamik kendt som *chimera state*. I denne tilstand, hvis stabilitet bestemmes af tidsforskellen mellem neuronerne, er én population synkroniseret, mens den anden forbliver usynkroniseret. Med instantane forbindelser blev chimera state faktisk neutralt stabil, med tilstande af såkaldte *breathing chimeras* omkring sig. Her var en population synkroniseret, mens den anden skiftede periodisk mellem mere kohærente og u-kohærente tilstande.

I den anden del analyserede vi dynamikken af oscillerende transkriptionsfaktorer, især p53, og dens effekt på andre gener i forbindelse med reparation af skader på DNA-strengen. p53 er også kendt som "guardian of the genome" for dens rolle i cancerforebyggelse og opretholdelse af genomisk stabilitet. Som et resultat af alvorlig DNA-skade begynder concentrationen af p53 i cellekernen at oscillere med en periode på 5,5 timer. Oscillationernes rolle stadig er meget diskuteret. Samtidig er dannelsen af mikromiljøer rige på reparationsproteiner blevet observeret omkring de skadede områder. Disse mikromiljøer menes at opstå som resultat af en væske-væske fase-separation, som så danner biomolekylære kondensater. I denne sammenhæng var spørgsmålet, vi ønskede at adressere: hvordan kan cellen regulere fordelingen af reparationsmateriale, hvis der er flere DNA-skader? Spiller p53 oscillerende dynamik og dens specifikke frekvens en rolle i denne proces? Vi fandt ud af, at p53-oscillationer sikrer optimal reparationshastighed, hvis der er flere DNA-brud ved at regulere dannelsen og ændringen i størrelserne af kondensaterne omkring de skadede områder, og dermed sikre en rumlig-temporal ressourcefordeling i cellen.

I den tredje del undersøgte vi muligheden for at koble p53-oscillationer til et eksternt pulserende signal for på den måde at regulere dets frekvens. Gennem en mikro-fluid enhed koblet med 'live-cells imaging' kunne vi følge dynamikken i p53-oscillationer efter vi påførte enkelte eller gentagne pulser af molekylet nutlin-3a. Ved at undersøge hvordan p53 reagerede på enkelte perturbationer, forudsagde vi succesfuldt systemets opførsel som reaktion på en serie af pulser, hvilket førte til

identifikation af Arnold-tunger - en væsentlig egenskab ved fase-låsning Vores undersøgelser viste, at systemet udviser fase-låsning til det eksterne signal, hvilket ikke kun giver anledning til højere ordens fase-låsning, men også til kompleks dynamisk som multistabilitet og periodefordobling. Endelig fremhævede vi et potentielt forhold mellem p53 frekvensen og dets underlæggende gen, p21. Bemærkelsesværdigt observerede vi, at den naturlige p53-frekvens minimerer p21-akkumulering, hvilket potentielt fungerer som en mekanisme til at forhindre, at celler hurtigt ender i en bestemt endelig tilstand. Samlet giver vores resultater værdifuld indsigt i det dynamiske samspil mellem p53-oscillationer, eksterne stimuli og cellulære processer og relaterede gener, hvilket bidrager til vores forståelse af cellulær regulering og genetisk kontrol.

List of Figures

1.1	Inferring function from dynamics of biological systems	2
1.2	Dynamical systems theory to describe biological oscillators	3
1.3	Limit cycles and biological oscillators	6
1.4	Noise in biology	8
1.5	Chapters overview and the corresponding graphical abstracts	10
2.1	Background theory on phase models	13
2.2	Kuramoto order parameter and chimera states	14
2.3	The continuum limit and Ott-Antonsen (OA) ansatz	17
2.4	Summary of results about neuronal synchronization	22
3.1	Description of the system including p53 oscillatory dynamics, liquid foci, DNA repair	40
3.2	Central dogma of biology and p53 role as transcription factor	42
3.3	Physics of phase separation for biomolecular condensates	46
3.4	DNA repair with liquid foci	47
3.5	Mathematical model description of p53 oscillations and foci formation	52
3.6	Main theoretical predictions and experimental results for p53 dynamics and DNA repair mechanism	54
3.7	Summary of the theoretical predictions of the paper	55
4.1	Entrainment of oscillators and Arnold tongues	87
4.2	Theory of Phase Transition Curves to predict Poincaré maps and Arnold Tongues	90
4.3	Theoretical and experimental setup and single pulse experiments	93
4.4	Prediction of Arnold tongues from single pulse experiments	96
4.5	Periodic pulses experiments show p53 entrainment	98
4.6	Multistability in entrainment modes	100
4.7	Mode-hopping, period-doubling, chaos and memory effects	102
4.8	p21 accumulation rate is minimized at the endogenous p53 frequency	104

List of abbreviations

Double-Strand Break (DSB) A type of DNA damage that occurs when both strands of the DNA molecule are severed. It is one of the most dangerous forms of DNA damage and can have significant consequences for cell function and genetic stability. DSBs can be caused by various factors, including exposure to ionizing radiation (such as X-rays or γ -rays), certain chemicals, and errors during DNA replication.

Nuclear Factor kappa B (Nf- κ B) A protein complex that plays a key role in regulating the immune response and controlling the expression of genes involved in inflammation, cell proliferation, and cell survival. It acts as a transcription factor, influencing the production of various proteins important for immune and inflammatory processes.

Ostwald Ripening (OR) A phenomenon observed in solid or liquid solutions above the supersaturation level, where it is energetically favourable for the dispersed phase to phase-separate into droplets. At this stage, the droplets start competing for material, with the larger droplets growing at the expense of smaller one, via a diffusive transfer of molecules. This stems from the fact that molecules on the surface of small droplets are more easily lost, due to the difference in surface curvature, therefore have fewer favourable interactions between themselves. The result is a gradual increase in the average size of the particles in the system, until only one dominant droplet remains, that absorbs all the available material in the solution.

Ott-Antonsen (OA) Introduced by Arne Ott and Thomas Antonsen, it is a mathematical framework used in the analysis of synchronization phenomena in coupled oscillator systems. It provides a powerful tool for reducing the dimensionality of large networks of coupled oscillators, by assuming rotational symmetry in the phase space of the oscillators and exploiting the fact that the coupling between oscillators depends solely on their relative phase differences.

Phase Response Curve (PRC) A function that measures the phase shift $\Delta\theta$ of an oscillatory system in response to stimuli delivered at different times in its cycle.

Phase Transition Curve (PTC) A function that describes the final phase θ_f of an oscillatory system when perturbed by an external signal, as a function of the phase θ_i at which the stimulus is received.

Radial Isochron Clock (RIC) Also known as Poincaré oscillator, it is a simple 2D model that has been used to describe the circadian clock, and neuronal and cardiac rhythms. It is the

topological normal form for any system near an Andronov-Hopf bifurcation. The name stems from the fact that the isochrons of the model (i.e. the loci of all points with the same phase) radially spread from the center of the limit cycle, which is a circle.

Saddle Node on Invariant Circle (SNIC) A type of dynamical system bifurcation where the creation or destruction of a stable closed trajectory (invariant circle) occurs as a control parameter varies, by coalescence of a stable and an unstable fixed point that lie on the circle.

Transcription Factor (TF) A protein that regulates gene expression by binding to specific DNA sequences called enhancers or promoters. TFs play a crucial role in controlling the activation or repression of genes, thereby influencing various biological processes, including development, growth, and response to stimuli. They act as molecular switches, initiating or blocking the transcription of genes into RNA molecules, which ultimately determines the synthesis of specific proteins in the cell. TFs are essential for the proper functioning and regulation of genetic information in living organisms.

Contents

1	Introduction	1
1.1	Dynamical systems theory	2
1.2	Biological oscillators	5
1.3	Noise in biology	6
1.4	Thesis overview	8
2	Emergence of chimera states in a neuronal model of delayed oscillators	11
2.1	Introduction and Objectives	11
2.2	Background theory	13
2.2.1	Neurons as oscillators	13
2.2.2	Phase models	13
2.2.3	The Kuramoto model and chimera states	16
2.2.4	The continuum limit	17
2.2.5	The Ott-Antonsen (OA) ansatz	18
2.3	Main results	19
2.4	Discussion and Perspectives	23
2.5	Manuscript: Emergence of chimera states in a neuronal model of delayed oscillators .	25
3	Enhanced DNA repair through droplet formation and p53 oscillations	39
3.1	Introduction and Objectives	39
3.2	Background theory	41
3.2.1	Transcription Factors (TFs) role in biology: p53 as "guardian of the genome" .	41
3.2.2	Foci formation and physics of phase separation	43
3.2.3	Diffusion-limited repair processes	47
3.2.4	How to simulate stochastic processes: the Gillespie algorithm	49
3.3	Main results	51
3.4	Discussion and Perspectives	53
3.5	Manuscript: Enhanced DNA repair through droplet formation and p53 oscillation . .	56
4	Entrainment as control mechanism for the p53 oscillator	83
4.1	Introduction and Objectives	83
4.2	Background theory	84
4.2.1	Arnold tongues theory	84
4.2.2	Poincaré maps to predict entrainment from single perturbations	86
4.3	Results	92
4.3.1	Derivation of the Phase Transition Curves (PTCs)	92
4.3.2	Prediction of the Arnold Tongues from the Poincaré maps	95

4.3.3	The pace of the p53 oscillator can be locked to a wide range of entrainment periods	97
4.3.4	Higher-order entrainment of the p53 oscillator	99
4.3.5	Complex dynamics: mode-hopping, period doubling and hunt for chaos . . .	101
4.3.6	P21 accumulation rate is lowest at the natural frequency of p53	103
4.4	Discussion and Perspectives	105
5	Conclusion	107
6	Bibliography	109

Introduction

In recent decades, the field of biology has witnessed a transformative shift, propelled by the growing recognition that mathematical and physical modelling are great tools for unraveling the intricate mechanisms governing the organization and function of natural phenomena (Murray, 2002). By providing simple quantitative and mechanistic descriptions of biological processes, theoretical models offer unique insights, enabling biologists not only to explain current experimental data, but also to have testable predictions which can guide future research (Bianchi *et al.*, 2019). The collaboration of experimentalists and physicists/mathematicians has already proven invaluable in a plethora of classical examples, from the Hodgkin-Huxley model to describe the electrical activity of neurons (Hodgkin and Huxley, 1952), to the Lotka-Volterra equations to describe predator-prey dynamics in ecology (Lotka, 1910; Volterra, 1927), from Turing patterns (Turing, 1952) which explain the formation of spatial patterns in developing biological systems, to the many mathematical models of carcinogenesis and tumour growth (Byrne, 2010).

Currently, one of the most promising collaborative areas between biologists and physicists lies in comprehending how functional information can be encoded not only in the structural components of a biological system, but also in the *dynamics* (i.e. the temporal behaviour) of its constituents (Purvis and Lahav, 2013). As an example, consider neurons, the cells of the nervous system (Figure 1.1A): their structure, which is elongated and branched, has been shaped by evolution to efficiently transmit electrical signals to many other neurons (if they were cube-shaped and arranged orderly within the brain, a single neuron could, at most, form connections with six others). This shows how information on neuronal function can be retrieved by looking at their structure. However, much more information can be retrieved by analysing the dynamics of neuronal signalling, in particular the frequency (which separates states of sleep and consciousness), but also the amplitude and the duration of electrical pulses. The ability of different neurons to portray different dynamics in response to external signals is at the core of the phenomenon of emergent collective synchronization in the brain (Izhikevich, 2018). This has tremendous clinical implications, given that several diseases, such as Parkinson's disease or epileptic seizures, are believed to arise as a result of an aberrant synchronization of neuronal activity in certain brain regions (Uhlhaas and Singer, 2006).

Another example in which function is reflected in structure is *gene expression* (Purvis and Lahav, 2013), the process by which information encoded in a gene's DNA sequence is used to create functional products, typically proteins (Figure 1.1B). It involves transcription, where a gene's DNA is copied into a molecule called messenger RNA (mRNA), and translation, where the mRNA is used as a template to assemble the corresponding protein. This process is tightly regulated by the so called Transcription Factors (TFs), which control the activation or repression of genes, thus acting as molecular switches. In this context, a growing number of studies are now revealing a striking feature, that is how the concentration of certain TFs in the nucleus of cells display time variation in the form of pulses and oscillations, prompting questions about their evolutionary significance (Purvis

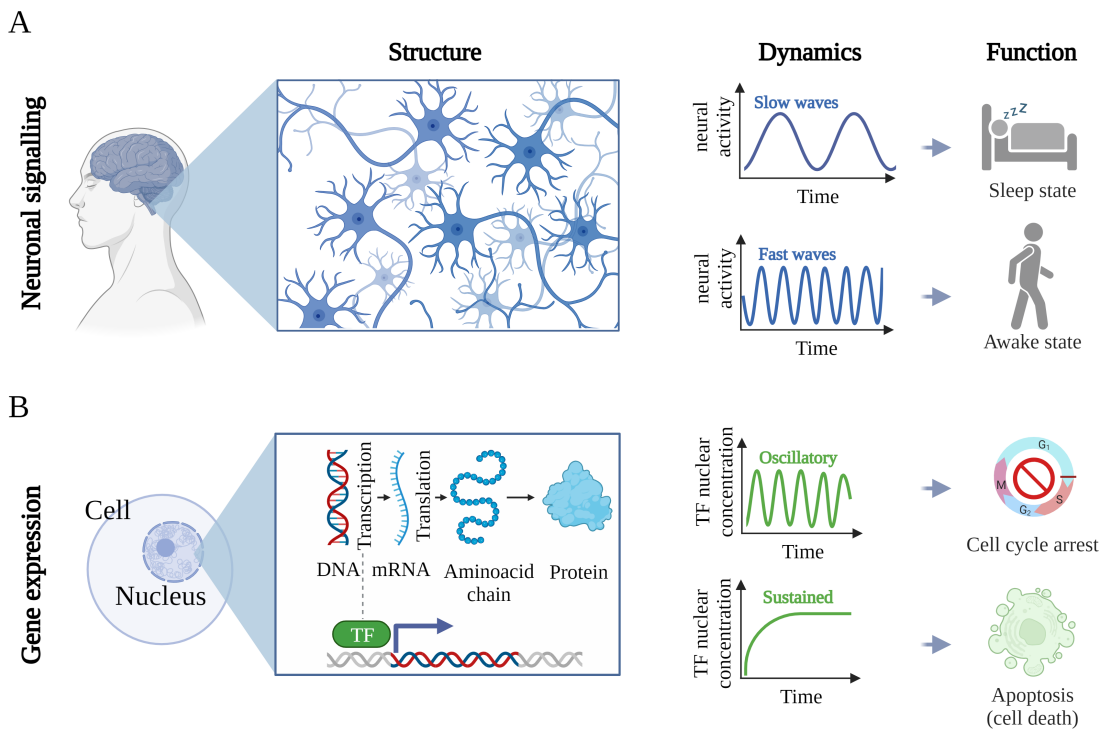


Figure 1.1: The relation between structure, dynamics and function of biological systems in the context of (A) Neuronal signalling (B) Gene expression.

and Lahav, 2013; Behar and Hoffmann, 2010; Venkatachalam *et al.*, 2022; Heltberg *et al.*, 2019; Heltberg *et al.*, 2022). For example, it has been shown how different dynamics in the TF p53, in response to DNA damage, lead to different cell fates: while pulses of p53 lead to cell-cycle arrest, a constant high level in p53 nuclear concentration leads to apoptosis (cell death) (Purvis *et al.*, 2012). Overall, understanding how these dynamics contribute to finely-tuned genetic pathway regulation is nowadays largely considered the Holy Grail of biology. In particular, the mechanisms underlying how cells regulate the expression of an astounding number of genes in a coordinated manner in response to environmental signals, external stresses and stimuli, is somehow still a mystery (Lambert *et al.*, 2018).

1.1 Dynamical systems theory

These seemingly different topics can be investigated within the same mathematical framework, which is used to describe phenomena that evolve in time and is called *dynamical systems theory*. The biological processes that we are interested in can be generally described as variables that follow ordinary differential equations (ODEs), which, for an n-dimensional system, take the form (Strogatz, 2018)

$$\begin{cases} \dot{x}_1 = f_1(x_1, \dots, x_n, t) \\ \vdots \\ \dot{x}_n = f_n(x_1, \dots, x_n, t) \end{cases} \quad (1.1)$$

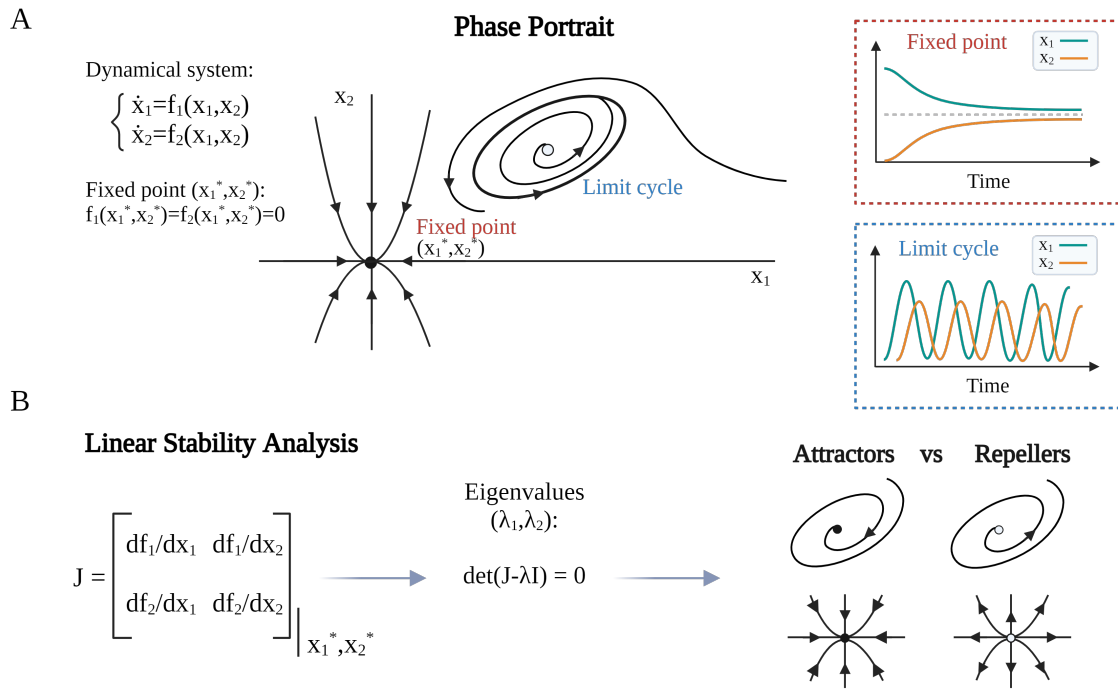


Figure 1.2: (A) Left: Example of a phase portrait for a 2D system (x_1, x_2) with a fixed point and a limit cycle. Right: $x_1(t)$ and $x_2(t)$ traces corresponding to the fixed point and the limit cycle. (B) Linear Stability Analysis: the eigenvalues of the Jacobian are computed in order to determine whether the fixed point is an attractor or a repeller.

where the overdot on the LHS represents differentiation over time. Solving such equations analytically is usually an impossible task even for trivial low-dimensional systems, and although nowadays it is often possible to get numerical solutions for specific initial conditions, more information can be obtained by getting a geometrical intuition of the whole phase portrait where the trajectories lie (Figure 1.2A). In particular, the goal is to determine the presence of:

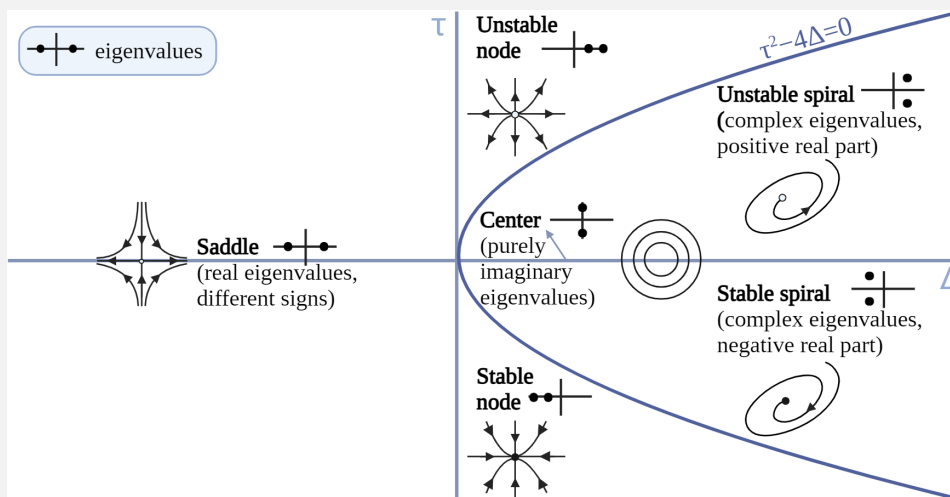
- the fixed points, \mathbf{x}^* , such that $\mathbf{f}(\mathbf{x}^*) = 0$, which correspond to equilibrium solutions, and their stability, i.e. if they are attractors or repellers;
- the closed orbits, such that $\mathbf{x}(t + T) = \mathbf{x}(t) \quad \forall t$, for some $T > 0$, which represent periodic solutions, and the flow close to them.

In order to determine the stability of the fixed points, the system is linearized around the equilibria (*Linear Stability Analysis*) and the Jacobian matrix \mathbf{J} is computed at the fixed point,

$$\mathbf{J} = \begin{bmatrix} \frac{\partial f_1}{\partial x_1} & \cdots & \frac{\partial f_1}{\partial x_n} \\ \vdots & \ddots & \vdots \\ \frac{\partial f_n}{\partial x_1} & \cdots & \frac{\partial f_n}{\partial x_n} \end{bmatrix} \quad (1.2)$$

The eigenvalues $(\lambda_1, \dots, \lambda_n)$ of \mathbf{J} can be found by solving $\det(\mathbf{J} - \lambda \mathbb{I}) = 0$, and define whether a small disturbance will grow (repeller) or decay (attractor) over time, as shown in Figure 1.2B (see Theory Box 1.1 for more details).

Theory Box 1.1.1: Stability of fixed points in 2D



We can easily illustrate how to determine the stability of fixed points via *Linear Stability Analysis* in 2D (Strogatz, 2018). Let's consider the system

$$\begin{cases} \dot{x}_1 = f_1(x_1, x_2) \\ \dot{x}_2 = f_2(x_1, x_2) \end{cases} \quad (1.3)$$

with a fixed point (x_1^*, x_2^*) . We linearize around the fixed point obtaining first order and higher order (h.o.) terms:

$$\begin{cases} \dot{x}_1 = f_1(x_1^*, x_2^*) + \frac{\partial f_1}{\partial x_1}|_{x_1^*, x_2^*}(x_1 - x_1^*) + \frac{\partial f_1}{\partial x_2}|_{x_1^*, x_2^*}(x_2 - x_2^*) + \text{h.o.} \\ \dot{x}_2 = f_2(x_1^*, x_2^*) + \frac{\partial f_2}{\partial x_1}|_{x_1^*, x_2^*}(x_1 - x_1^*) + \frac{\partial f_2}{\partial x_2}|_{x_1^*, x_2^*}(x_2 - x_2^*) + \text{h.o.} \end{cases} \quad (1.4)$$

Given that $f_1(x_1^*, x_2^*) = f_2(x_1^*, x_2^*) = 0$, if we define $u_1 = x_1 - x_1^*$ and $u_2 = x_2 - x_2^*$, we can rewrite the system in vector form as:

$$\begin{bmatrix} \dot{u}_1 \\ \dot{u}_2 \end{bmatrix} = \begin{bmatrix} \frac{\partial f_1}{\partial x_1} & \frac{\partial f_1}{\partial x_2} \\ \frac{\partial f_2}{\partial x_1} & \frac{\partial f_2}{\partial x_2} \end{bmatrix} \Big|_{x_1^*, x_2^*} \cdot \begin{bmatrix} u_1 \\ u_2 \end{bmatrix}. \quad (1.5)$$

The linearization matrix

$$J = \begin{bmatrix} \frac{\partial f_1}{\partial x_1} & \frac{\partial f_1}{\partial x_2} \\ \frac{\partial f_2}{\partial x_1} & \frac{\partial f_2}{\partial x_2} \end{bmatrix} \Big|_{x_1^*, x_2^*} \quad (1.6)$$

is the *Jacobian* of the system around the fixed point (x_1^*, x_2^*) . To determine the stability of the fixed point, we first look for "straight-line" solutions of the form $\mathbf{x}(t) = e^{\lambda t} \mathbf{v}$, where \mathbf{v} is a constant vector. These solutions simply exhibit exponential growth ($\lambda > 0$) or decay ($\lambda < 0$) along the direction of the vector. If we substitute such a solution in Equation (1.5) we get the condition $J\mathbf{v} = \lambda\mathbf{v}$, meaning that λ and \mathbf{v} are respectively the eigenvalues and eigenvectors of the Jacobian matrix J . To find them, we have to solve the characteristic

equation $\det(J - \lambda \mathbb{I}) = 0$ which can be written as $\lambda^2 - \tau\lambda + \Delta = 0$, where τ, Δ are the trace and the determinant of J respectively. Thus, the two eigenvalues, written in terms of τ, Δ are

$$\lambda_{1,2} = \frac{\tau \pm \sqrt{\tau^2 - 4\Delta}}{2}.$$

Depending on the sign of the eigenvalues, and whether they are real or complex values, different possible fixed points originate, such as spirals, nodes, saddles, which are summarized in the figure above.

It is generally safe to neglect second-order terms, as long as the fixed point for the linearized system is not a marginal case, such as a center, where both eigenvalues are purely imaginary. For centers, which are *neutrally stable* since the trajectories are neither attracted nor repelled from the fixed point, one can make use of the following theorem: if $\mathbf{x}^* = 0$ is a linear center for Equation (1.3), and the system is *reversible* (i.e. $f_1(x_1, -x_2) = -f_1(x_1, x_2)$ and $f_2(x_1, -x_2) = f_2(x_1, x_2)$), then sufficiently close to the origin, all trajectories are close, meaning that the fixed point is a non-linear center (Strogatz, 2018).

1.2 Biological oscillators

Limit cycles are special closed orbits which are isolated from the others, meaning that neighboring trajectories are not close, as they spiral either toward or away from the limit cycle (Strogatz, 2018). They are a non-linear phenomenon: the only type of closed orbits that can be found in linear systems are the *centers*, which are not isolated. Indeed, for a linear system $\dot{\mathbf{x}} = A\mathbf{x}$, if $\mathbf{x}(t)$ is a periodic trajectory, so is $c\mathbf{x}(t)$ for any constant c , as illustrated in Figure 1.3A.

In general, limit cycles can be created (or destroyed) through different types of *bifurcations*. A bifurcation is a change in parameter which gives rise to a qualitative change in the phase portrait of the system. Fixed points can be created or destroyed through bifurcations, or their stability can change. Bifurcations that create limit cycles are, among others, Hopf bifurcations or Saddle Node on Invariant Circle (SNIC) bifurcations. In the first case, a stable spiral loses stability, along with the emergence of a stable limit cycle (*super-critical*) or with the disappearance of an unstable limit cycle (*subcritical*) (Izhikevich, 2018). In the second case, a stable and an unstable fixed point that lie on a circle coalesce and disappear, giving rise to the limit cycle (Figure 1.3B).

Limit cycles are used to model a variety of real-world oscillatory systems, in a wide range of timescales, from hours to milliseconds, including slower processes like the circadian clock (Goldbeter, 1995; Kondo *et al.*, 1997) and the cell cycle (Ferrell *et al.*, 2011), as well as faster phenomena like oscillatory TF dynamics in cells (Lahav *et al.*, 2004; Zambrano *et al.*, 2016), cardiac rhythm (Glass *et al.*, 1987), and neuronal activity (Gerstner *et al.*, 2014) (Figure 1.3C).

In many cases, oscillations arise as a result of some negative feedback loop with time delay that is intrinsic in the system under consideration (Hastings *et al.*, 1977; Novák and Tyson, 2008). To understand why, let's imagine this very simple scenario: consider a thermostat that maintains a room temperature at 20 °C. If the temperature goes above or below this value, the thermostat takes action to bring it back to 20 °C. However, the thermostat cannot instantly respond to the temperature change, but instead reacts to a past temperature reading (time delay in the feedback). Due to this

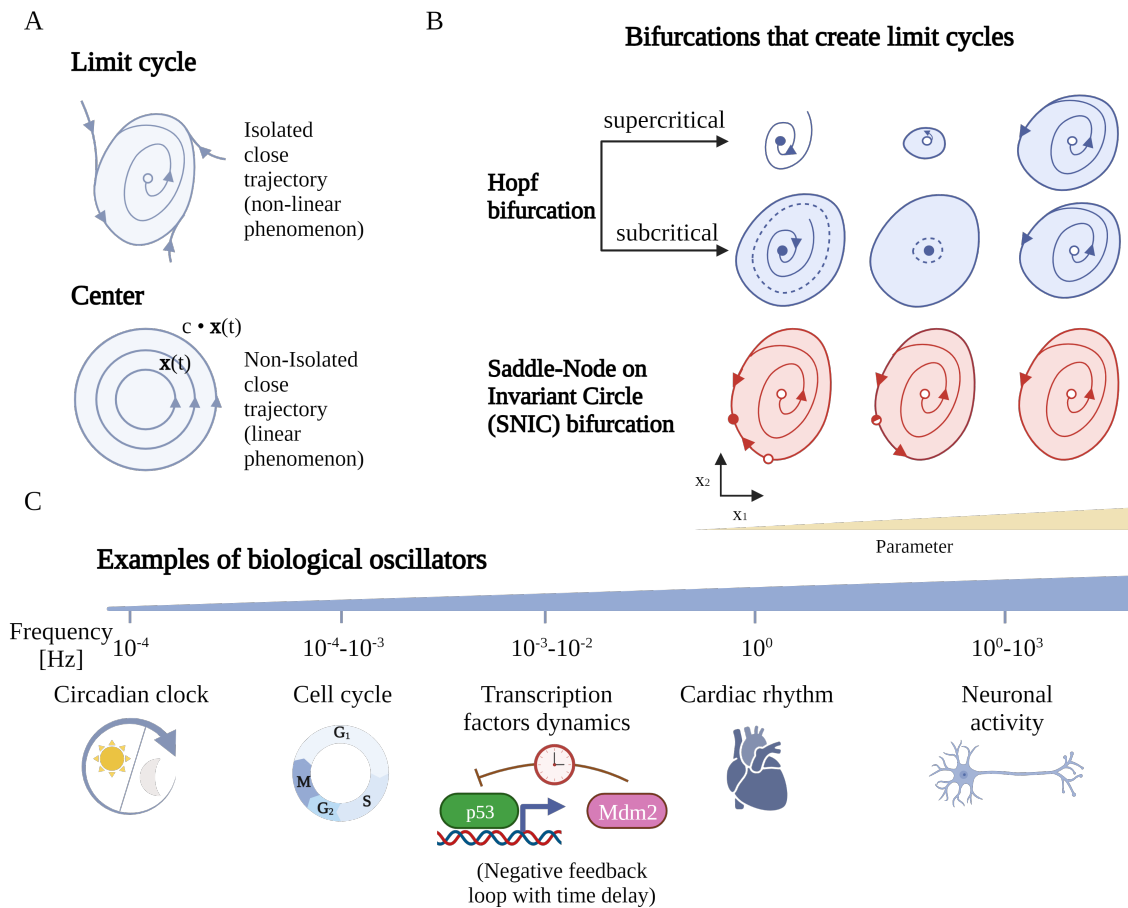


Figure 1.3: (A) Difference between limit cycles and centers. (B) Bifurcations that lead to the formation of limit cycles. (C) Examples of biological oscillators which span a wide range of timescales, from hours to milliseconds. The relation between transcription factor p53 and its own inhibitor Mdm2 is an example of a delayed negative feedback loop which gives rise to p53 oscillatory dynamics in cells.

delay, the thermostat may overcompensate for the temperature change, causing the temperature to overshoot the desired value. In response to this overshoot, the thermostat adjusts the system in the opposite direction, again based on a delayed temperature reading. This cycle of delayed response and overcorrection can lead to sustained oscillations in the system, in this case, causing the temperature to continuously fluctuate above and below the desired value. In biology, one of the most trivial examples is that of a protein that suppresses the transcription of its own gene (Holehouse *et al.*, 2020). In this case, the time delay corresponds to the actual time of transcription and translation of the protein. Another example is a TF that stimulates the production of a protein, which then binds to the TF and degrades it, such as in the case of p53 and Mdm2 (Lahav *et al.*, 2004) (Figure 1.3C).

1.3 Noise in biology

In the above description, we have essentially considered deterministic systems, where it is possible to predict the behaviour of the system uniquely from the governing equations and the initial conditions, without any uncertainty. However, noise is an essential factor that must be considered when

describing many biological processes at different spatial and temporal scales, such as neuronal activity or gene expression, which we are interested in.

Indeed, while noise is often negligible in the macroscopic world due to the Central Limit Theorem, which states that for a system at equilibrium the relative magnitude of fluctuations scales as $1/\sqrt{N}$ (N being the degrees of freedom), in many cases this does not apply in biological systems, which are driven out of equilibrium (Tsimring, 2014). At the cellular level, noise in gene expression manifests as thermal fluctuations of biochemical reactions, which occur through random collisions and transient binding of molecules such as genes, RNAs and proteins, that are present at low number of copies, thus prone to high stochasticity (Tsimring, 2014).

Noise origin can be traced back to *intrinsic* and *extrinsic* factors (Figure 1.4, left panel). While the first originates from the probabilistic nature of biochemical reactions within the system itself, the latter refers to environmental fluctuations outside the system under consideration that are global to a single cell. Experimentally, intrinsic noise for a given gene corresponds to the extent to which the activities of two identical copies of that gene fail to correlate in the same environment (Elowitz *et al.*, 2002). The two sources of noise can therefore be separated with a dual-reporter method (Elowitz *et al.*, 2002): by fluorescent-tagging of two genes (shown in green and red in Figure 1.4) whose transcription is driven by the same TFs, one can show that, in the absence of intrinsic noise, the fluorescence of both proteins would be correlated, thus resulting in the cells appearing all yellow. In the presence of intrinsic noise, cells would express more of one protein than the other, resulting in cells appearing more green or more red (Figure 1.4, right panel).

Discerning whether observed patterns arise from intrinsic biological oscillations or are the result of stochastic noise, is crucial to provide critical insights into the underlying dynamics and control mechanisms within the cell. Oscillations generally have a specific intrinsic frequency and follow precise, predictable patterns, resulting from underlying feedback loops and interactions within the system architecture. Random fluctuations, conversely, lack consistent frequencies and exhibit irregular behaviours over time, and also lack a discernible pattern, arising from probabilistic events and chance interactions.

For decades noise has been considered not only a nuisance for experimentalists, as it makes experiments difficult to interpret, but also for nature itself, that has evolved techniques to deal with its negative entropy-increasing effects of limiting the robustness, the fidelity and the channel capacity of information transmission (Tsimring, 2014). However, it is becoming apparent that evolution might have fine-tuned biological systems to being able to also take advantage of natural stochastic fluctuations, which might have a more constructive role than previously thought. In particular, in the context of oscillatory environments, researchers have found that there may be a positive interplay between random fluctuations and environmental oscillations, which take advantage of each other: the transmission of noisy signals may be advantageous in oscillatory environments (a phenomenon known as *stochastic resonance* (Douglass *et al.*, 1993)) and viceversa, that oscillations may take advantage of fluctuations in the environment: for instance, Kellogg and Tay (2015) have recently shown how intrinsic noise within individual cells improve oscillations in Nuclear Factor kappa B (Nf- κ B), a TF central in the organism immune response, whereas extrinsic noise (i.e. heterogeneity among different cells) improves the robustness of the population.

Noise in biology

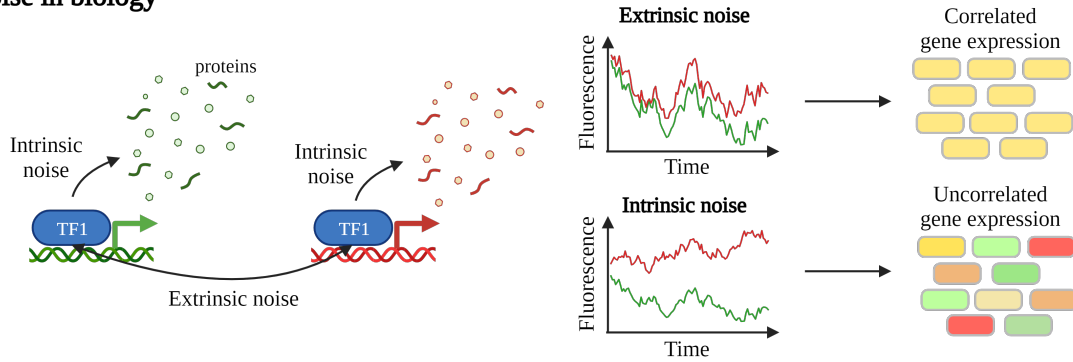


Figure 1.4: Noise permeates biology on all levels. In gene expression, noise can be intrinsic, from stochasticity of biochemical reactions, which result in uncorrelated gene expression, or extrinsic (e.g. from fluctuations in activity and concentration of Transcription Factors (TFs)) which results in correlated gene expression. The right panel is adapted from Elowitz *et al.* (2002)

In order to model stochastic processes, one can make use of the *Langevin equation*, which describes the dynamics of particles in fluctuating environments, considering both deterministic and random forces:

$$m \frac{dv}{dt} = -\lambda v + \eta(t)$$

where v is the particle velocity, m is the particle mass, λ is the friction coefficient, representing the damping effect of the surrounding medium on the particle's motion, and $\eta(t)$ represents the random force or noise acting on the particle at time t . One generally assumes that the average random force is zero, $\langle \eta(t) \rangle = 0$, and that the correlation function is $\langle \eta(t)\eta(t') \rangle = 2\lambda k_B T \delta(t - t')$, where k_B is Boltzmann's constant, and T is the temperature.

In order to numerically simulate systems with noise, it is possible to either simulate the Langevin equation directly, by using the Euler-Maruyama method: the equation is discretized (integrating it from t to $t + \Delta t$) and a random number, drawn from a Gaussian distribution, is added at each timestep Δt . Alternatively, it is common to use *event-driven methods* such as the Gillespie algorithm (Gillespie, 1976): in this case, the algorithm generates a trajectory of events by iteratively selecting the next event based on its associated rate, which reflects the likelihood of occurrence (this will be described in details in Chapter 3).

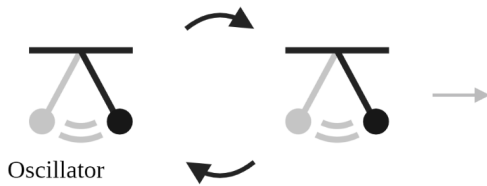
1.4 Thesis overview

The following thesis comprises three chapters that correspond to the three major projects I worked on during my PhD, which all revolve around the concept of biological oscillators, their properties and functionality. When oscillators are coupled to each other, they constitute a complex system, where emergent behaviour, such as synchronization, may take place. This will be the focus of Chapter 2 (Figure 1.5, top), in which we analyse a network of coupled neurons, finding interesting phenomena called *chimera states*, where only part of the population synchronizes to a common rhythm while the rest keep firing at seemingly random times, despite being all-to-all-coupled. Oscillators in biology may also regulate certain phenomena downstream: this will be the focus of Chapter 3 (Figure 1.5, center). We will see how the oscillations in the TF p53 and in particular its specific periodicity of 5 h may be optimal for the process of DNA repair after being damaged by radiation. Finally, oscillators

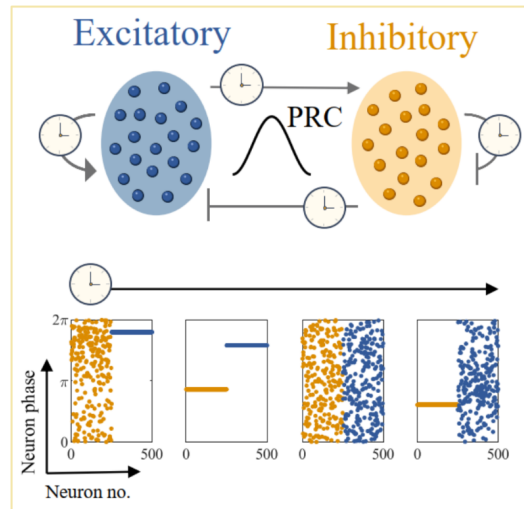
may also be coupled to an external forcing. Chapter 4 will be devoted to this aspect (Figure 1.5, bottom). In particular, again in the context of p53, we will see how it is possible to modulate the frequency of its oscillations by entraining its signal to an external pulsing signal. Every chapter comprises an Introduction and a Theoretical Background section, which give the tools to understand the following parts. The first two chapters then portray a sum-up of the main results, which can be found in greater details in the corresponding published papers reported at the end of each chapter. The third chapter, for which a manuscript is not available yet, reports the full results.

Chapter 2

Internal coupling: neuronal synchronization (bi-directional)

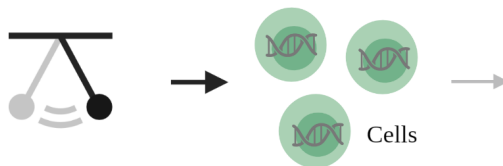


This work shows the emergence of chimera states in a neural network with delayed couplings.

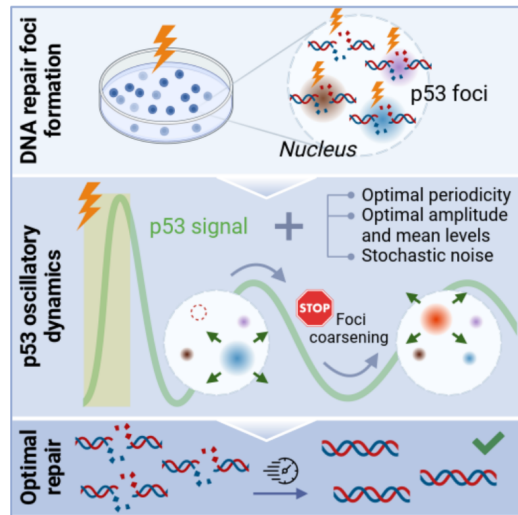


Chapter 3

Down-stream effects: cellular regulation (uni-directional)



Our theory explains how oscillations in p53 nuclear abundance optimize DNA damage repair.



Chapter 4

External input: entrainment (uni-directional)



Our study explores entrainment of p53 to an external pulsing signal, and uncovers potential senescence-regulation mechanism.

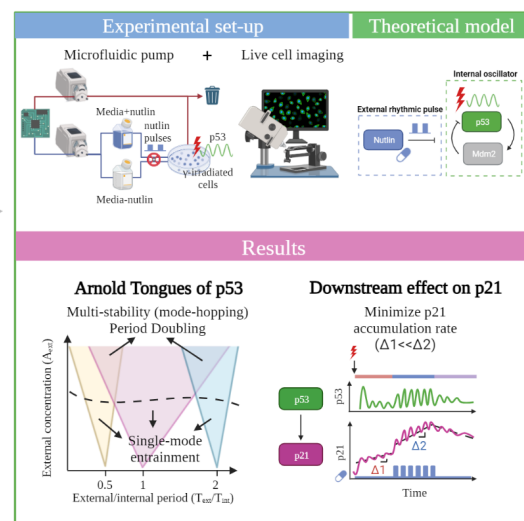


Figure 1.5: Chapters overview with the main result of each project and the corresponding graphical abstract.

Emergence of chimera states in a neuronal model of delayed oscillators

2.1 Introduction and Objectives

Imagine this experiment: a group of people is instructed to clap their hands in unison, without any underlying rhythm to follow. After an initial random noise, one can expect that the crowd would spontaneously set to a certain rhythm. Who decided? No one. What happened is that at every clap, people spontaneously adjusted their frequency, increasing or decreasing it, based on the feedback they received from the people around (in the form of their clapping sound). This is an example of *spontaneous synchrony*, that emerges naturally from the interplay between the components, without any leader to direct the process. What is extraordinary is that a spontaneous emergence of order pervades nature at every scale. From the initial discovery of the Dutch physicist C. Huygens (1665) that pendulum clocks placed side by side on a wall would eventually synchronize, researchers have later discovered many other examples: from the interplay of heart cells which gives rise to the heartbeat, to the coherent activity of millions of neurons that enable breathing, to the synchronization of certain species of fireflies which flash in unison (Strogatz and Stewart, 1993).

Now consider again the previous thought experiment: what if only a subgroup of people were instructed to clap in unison, while the rest kept clapping at random times? How hard could it be for the subgroup to find a uniform rhythm, surrounded by the random clapping noise? One could argue that this would indeed be impossible. If the discovery that natural systems can spontaneously fall into a steady, uniform rhythm is already mesmerizing, the idea of a spontaneous *symmetry break* for a population of identical oscillators, which split into two distinct groups (a synchronized and an asynchronized one), had never been thought of until only 20 years ago. Kuramoto and Battogtokh (2002) were the first to mathematically predict the possibility of this state, which was later defined as a *chimera* by Abrams and Strogatz (2004), from the name of the mythological creature made of incongruous parts. Since their discovery, chimera states have been reproduced not only in numerical simulations but also in several experimental settings, which include, among others, populations of coupled chemical oscillators (Tinsley *et al.*, 2012), identical metronomes (Martens *et al.*, 2013), as well as optical (Hagerstrom *et al.*, 2012) and electronic systems (Larger *et al.*, 2013).

Much of the current research effort in the field is concentrated on revealing if and under which conditions these patterns of synchronization could occur in real-world scenarios (see Panaggio and Abrams (2015), Omel'chenko (2018), and Haugland (2021) for extensive reviews). In the context of neuroscience, understanding how to predict and control the emergence of neuronal synchronization would have tremendous implications: indeed, not only cognitive processes, such as visual information processing and memory formation, rely on the ability of different brain regions to coordinate their activity (Rodriguez *et al.*, 1999; Fell and Axmacher, 2011). Several pathological

states, such as Parkinson's disease or epileptic seizures, stem from an aberrant, excessive neural synchronization localized within certain brain regions only (Uhlhaas and Singer, 2006), which drives many researchers to believe it might be some sort of chimera state (Majhi *et al.*, 2019).

One natural question to ask, in this context, is whether all neurons in the brain have the same ability to coordinate their activities, and portray these exotic patterns of synchronization. When neurons process and transmit information, they may essentially behave in two modes: either as *resonators* or *integrators* (Izhikevich, 2018). In the first case, neurons exhibit selective responses to specific input frequencies, amplifying and resonating with inputs at their preferred frequency. In the second case, they instead accumulate inputs over time, summing and integrating signals to produce an output that represents the temporal history of the inputs. In other words, while integrators are basically low-pass filters of the electric inputs, resonators are band-pass filters (Galán *et al.*, 2007). Cortical pyramidal neurons, as well as thalamocortical neurons and neostriatal spiny projection neurons, are integrators; on the other hand, most cortical inhibitory interneurons are resonators (Izhikevich, 2018). The majority of studies in the field has up to now focused on the emergent properties of populations of resonators (Yeung and Strogatz, 1999; Wu and Dhamala, 2018), since integrators are considered to have limited propensity to synchronize, especially when bound by excitatory connections (Hansel *et al.*, 1995; Ermentrout, 1996; Galán *et al.*, 2007; Mofakham *et al.*, 2016; Ziaemehr *et al.*, 2020).

The primary objective of this study is to determine if and under which conditions, a population of neurons, of the type *integrators*, can synchronize, and if chimera states can be observed.

Specifically, we investigate a neuronal network made of two coupled subpopulations, an excitatory and an inhibitory one, with time-delayed connections. The interplay between excitation and inhibition is a known mechanism linked to rhythmogenesis in the brain, i.e. the emergence of large-scale neuronal oscillations which stem from the synchronized rhythmic activity of large populations of neurons. Moreover, including time-delay is essential to model the properties of spatially distributed systems, where the connection between neurons is not instantaneous. Therefore, the following objectives will be pursued:

- Analyse the conditions under which all the neurons in the system synchronize and the stability of this state;
- Explore the conditions necessary for the occurrence of chimera states in the coupled populations of neurons and their stability;
- Analyse the competition between excitation and inhibition and the role of the time-delay in the couplings.

Defining the rules for when and why various synchronization patterns emerge depending on the type of neurons, the type of connection and the time delay in the couplings, will provide invaluable insights in order to predict and control the possible intricate collective dynamics that can arise in networks of coupled neurons.

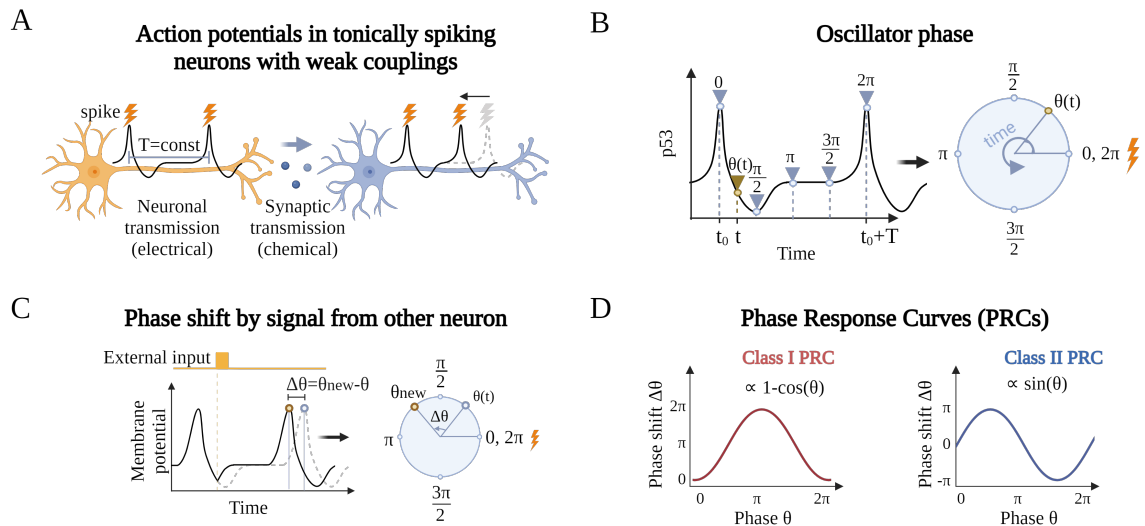


Figure 2.1: (A) Schematic of neuronal electrochemical signalling in tonically spiking neurons (i.e. with constant frequency of firing $T = \text{const}$) and weak couplings which only cause a delay/advance of subsequent spikes. (B) The oscillator phase of a neuron progresses along the unit circle and is reset to 0 every 2π , when the neuron fires. (C) An external input from another neuron causes a shift $\Delta\theta$ in the neuron phase $\theta(t)$. (D) The two classes of Phase Response Curves (PRCs).

2.2 Background theory

2.2.1 Neurons as oscillators

Neurons constitute the building blocks of the nervous system, whose main role is to process and transmit information throughout the brain and body, in the form of electrochemical signals, called *action potentials*. The electric signal travels along the neuron as a wave of depolarization of its membrane potential, that displays the characteristic "spikes", and is transmitted to another neuron via neurotransmitters (which are chemical messengers) (Figure 2.1A). In the following, we consider populations of *tonically-spiking* neurons (Izhikevich, 2004), namely with an intrinsic constant frequency of spiking, in which the inputs they receive from each other is weak so that it does not elicit an immediate spike, but has the effect to either delay or advance the timing of the next spike in neighbouring neurons. Therefore, we disregard the specific waveform of action potentials, and instead only focus on the timing of neuronal spikes. In this context, neurons are treated as oscillators, whose periodic activity is well described by a stable limit cycle that is temporarily perturbed by the mutual coupling. Despite the simplicity of this description, networks of weakly-coupled oscillators still carry enough complexity to display interesting emergent behaviours, such as the onset of collective synchronization (Hoppensteadt and Izhikevich, 1997).

2.2.2 Phase models

The simplest framework to describe populations of interacting neurons is that of *phase models* (Ermentrout, 1986; Izhikevich, 2000). Here, the complex neuronal activity is reduced to one variable, the phase of the neuron, which varies in the range $[0, 2\pi]$, and is reset to 0 every 2π (Figure 2.1B). The phase thus measures the "readiness of firing" for each neuron: it defines the position along the

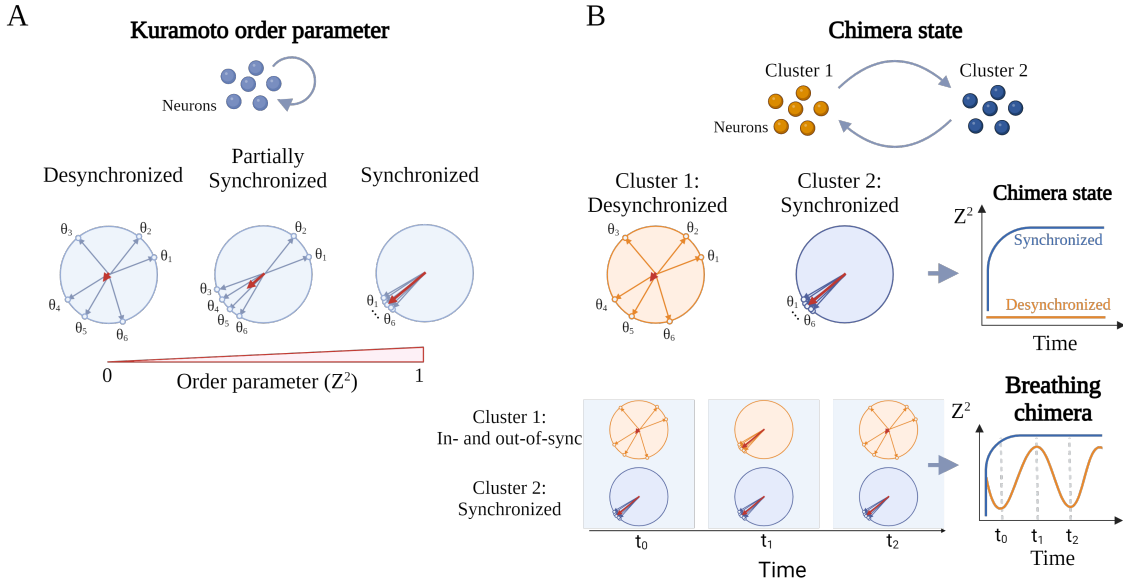


Figure 2.2: (A) The Kuramoto order parameter describes the level of synchronization of the neuronal population. (B) Schematic of a chimera state (top) and a breathing chimera (bottom) in a neuronal network made of two subpopulations.

limit cycle and can be thought of as a clock hand, which rotates at a certain intrinsic frequency. Every time the hand makes one full rotation, the neuron spikes an action potential. The effect of the other neurons is to slightly delay or advance the phase θ , bringing it to a new phase θ_{new} (i.e. causing a small rotation in the clockwise or counterclockwise direction of the hand) (Figure 2.1C). Such shift ($\Delta\theta$) may depend on the time at which the perturbation is received, which is expressed in the Phase Response Curve (PRC) (Hastings and Sweeney, 1958; Izhikevich, 2018) (Figure 2.1D).

$$PRC(\theta) = \Delta\theta = \{\theta_{new} - \theta\}. \quad (2.1)$$

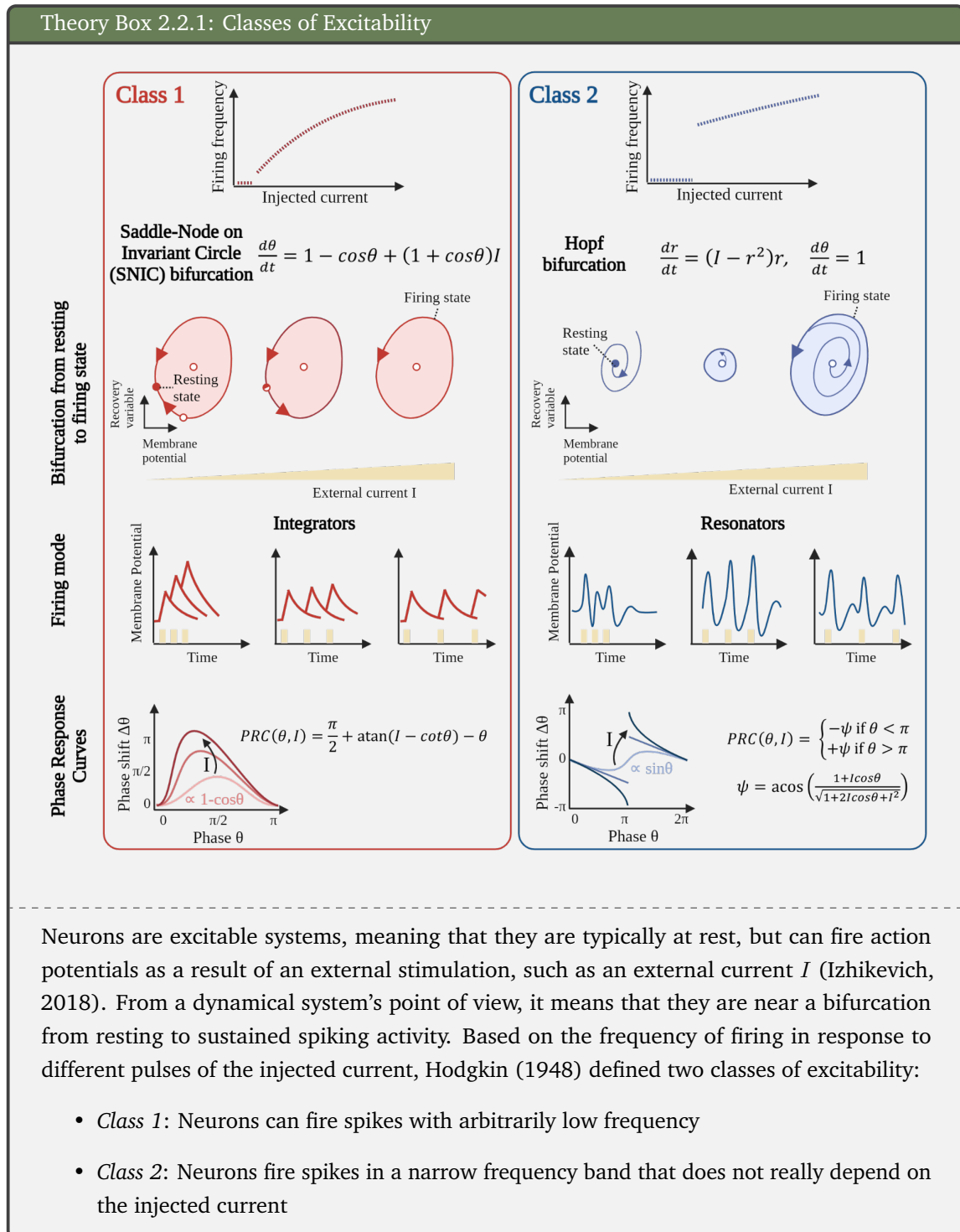
PRCs can be essentially classified in two types (Ermentrout and Kopell, 1986; Smeal *et al.*, 2010):

- *Class 1:* The curve is always positive, hence a small perturbation always results in an advance of the phase; the normal form in case of weak couplings has shape $\propto 1 - \cos \theta$ (Figure 2.1D, left).
- *Class 2:* The curve has both positive and negative values, hence a depolarizing perturbation may result in an advance or delay of the phase depending on the time of the signal. The normal form in case of weak couplings has shape $\propto \sin \theta$ (Figure 2.1D, right).

Neurons can be excitatory or inhibitory, meaning that in response to their signals, the neighbouring neurons will be more or less likely to fire. When it comes to inhibitory neurons, they follow the same PRCs as excitatory neurons, except with a negative sign. For example, in the case of Class 1 inhibitory neurons, a small perturbation would always result in a delay of the phase.

Given that the PRC of Class 1 excitatory neurons is always positive, these neurons have the ability to synchronize effectively with rapid inputs, yet struggle to synchronize with slower ones. Essentially, the oscillators can adjust their phases to align with faster pulse trains, but they lack the capacity to postpone their phases to match slower inputs (Izhikevich, 2018). On the other hand, Class 2 neurons

can synchronize with both faster and slower inputs, given that their PRC has well-defined positive and negative regions (Izhikevich, 2018). The shape of the two PRCs directly stems from the way neurons transition from silent (the resting state) to firing mode, which corresponds to a Saddle Node on Invariant Circle (SNIC) and a Hopf bifurcation for Class 1 and Class 2 respectively (Izhikevich, 2018). The two bifurcations also result in neurons having different behaviours in response to incoming pulses of currents: while Class 1 neurons act as *integrators*, Class 2 neurons act as *resonators* (see Theory Box 2.2.1 for more details).



Rinzel and Ermentrout (1989) later discovered that these two classes arise as a result of two different bifurcations: in Class 1 neurons, the bifurcation is a SNIC bifurcation, whose normal form corresponds to the theta model $d\theta/dt = 1 - \cos\theta + (1 + \cos\theta)I$ (Ermentrout and Kopell, 1986). Two fixed points, an unstable and a stable one, coexist on the invariant circle, coalesce and disappear as I increases past zero. This leaves the limit cycle as the only stable state (firing mode). It can be shown that this model is closely related to the quadratic integrate-and-fire model of neurons (Hoppensteadt and Izhikevich, 1997). Class 2 neurons, instead, go through a Hopf bifurcation. The normal form is the Poincaré oscillator or Radial Isochron Clock (RIC): $dr/dt = (I - r^2)r$, $d\theta/dt = 1$. Here, for $I < 0$, the resting state ($r = 0$) is a stable spiral. When $I > 0$, the stable state loses stability and a stable limit cycle emerges around it ($r = \sqrt{I}$). The two bifurcations also lead to different behaviours for the two neuron classes: in the first case, neurons behave as *integrators*, so that subsequent pulses of currents are integrated and lead to stronger responses. Class 2 neurons, instead, act as *resonators*. Indeed, the presence of a stable spiral leads to sub-threshold oscillations for small external pulses. Thus, there is a preferred frequency with which the neurons resonate. It can also be shown that the two excitability classes correspond to two different PRCs, which can be found explicitly for the normal forms: in the first case, $PRC = \pi/2 + \arctan(I - \cot\theta) - \theta$, which, for small I , has shape proportional to $1 - \cos\theta$, thus always positive. In the second case, $PRC = \mp\psi$ if $\theta \leq \pi$ with $\psi = \arccos\left(\frac{1+I\cos\theta}{\sqrt{1+2I\cos\theta+I^2}}\right)$, which has shape proportional to $\sin\theta$ for small I , thus admitting both advances and delays of the phase.

2.2.3 The Kuramoto model and chimera states

The Kuramoto model (Kuramoto, 1975) has been massively used in the literature to describe the emergent synchronization of a population of N weakly coupled tonically spiking neurons. The equation that governs the behaviour of the i -th oscillator phase θ_i is (see Theory Box 2.2.2 for the derivation)

$$\dot{\theta}_i = \omega_i + \frac{K}{N} \sum_{j=1}^N \sin(\theta_j - \theta_i), \quad i = 1, \dots, N \quad (2.2)$$

where ω_i is the intrinsic frequency, K is the coupling strength between neurons and the coupling is sinusoidal, therefore representing Class 2 neurons. In order to quantify the degree of synchronization of the population, the complex sum of all the neuron phases is calculated as

$$Z e^{i\psi} = \frac{1}{N} \sum_{j=1}^N e^{i\theta_j}, \quad (2.3)$$

with $\psi(t)$ being the average phase of all the neurons at time t and $Z(t)$ the degree of phase coherence. The long-term behaviour can thus be estimated by taking the time average of the absolute value, which corresponds to the Kuramoto order parameter Z^2 (Figure 2.2A)

$$Z^2 = \left\langle \left| Z(t) e^{i\psi(t)} \right|^2 \right\rangle_t = \left\langle \frac{1}{N^2} \sum_{i,j=1}^N \cos(\theta_i - \theta_j) \right\rangle_t. \quad (2.4)$$

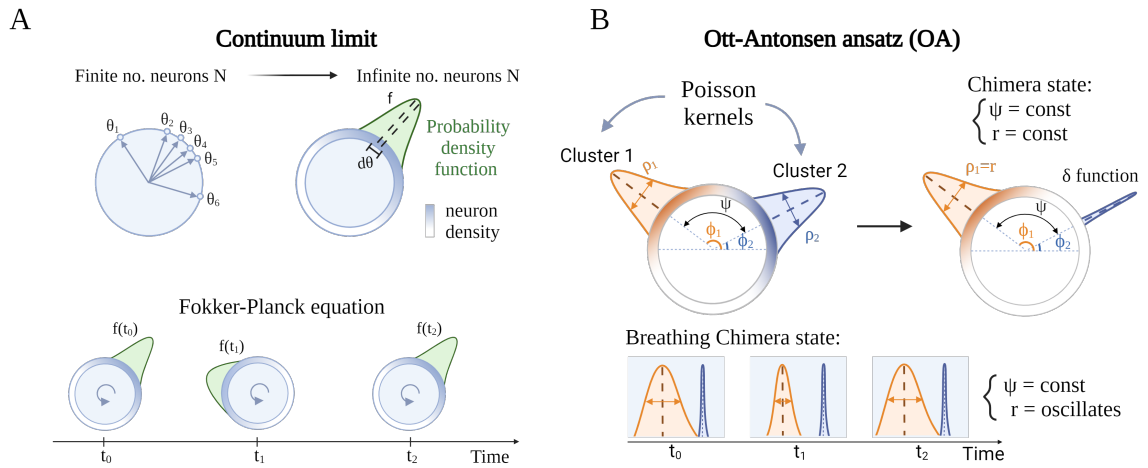


Figure 2.3: (A) In the continuum limit, the single phases are replaced by a probability density function f , whose time evolution is described by the Fokker-Planck equation. (B) The Ott-Antonsen (OA) ansatz considers Poisson kernels as probability density functions, which can be described in polar coordinates ρ, ψ ; the chimera state in this representation corresponds to the fixed point of the 2D system in the coordinates (ψ, r) , while a breathing chimera corresponds to a state with constant ψ and oscillatory r .

Z^2 thus varies in the range $[0-1]$, with 0 corresponding to no synchronization and 1 being the perfectly synchronized case. Intermediate values represent partially synchronized states, with only clusters of synchronized neurons.

Until around 20 years ago, it was believed that only heterogeneous oscillators (i.e. having different intrinsic frequencies) would show partial synchronization under certain conditions (Panaggio and Abrams, 2015), whereas identical oscillators could only either fully synchronize to the same rhythm or remain incoherent. As mentioned in the previous section, it was Kuramoto and Battogtokh (2002) who first discovered the coexistence of regions of coherence and incoherence within a population of identical neurons, which was later defined as a *chimera* by Abrams and Strogatz (2004) (Figure 2.2B). Other even more complicated states have also been observed in the literature, such as *breathing chimeras* (Abrams *et al.*, 2008), where one population is perfectly synchronized, while the other oscillates periodically between phases of higher and lower coherence.

2.2.4 The continuum limit

In order to describe the evolution of a population of neurons, it is common to consider the limit case of an infinite number of neurons ($N \rightarrow \infty$) (Figure 2.3A, top), such that the discrete set of phases and frequencies $[\theta_i, \omega_i]$ turns into a continuum of oscillators distributed in the unit circle, with probability density function f , where $f(\theta, \omega)d\theta$ describes the probability of finding neurons with frequency ω having phase within θ and $\theta + d\theta$. In this limit, the order parameter becomes,

$$Z(t) = \int_0^{2\pi} \int_{-\infty}^{+\infty} e^{i\theta} f(\theta|t, \omega) g(\omega) d\omega d\theta,$$

where $g(\omega)$ is the frequency distribution. The time evolution of f is described by the Fokker-Planck equation as schematized in the bottom panel of Figure 2.3A, which is defined as

$$\partial_t f = -\partial_\theta(fv) + D\partial_\theta^2 f, \quad (2.5)$$

with v corresponding to the drift velocity of the oscillators. Moreover, in order to study the stability of the solutions, it is convenient to make a Fourier transform of f , which yields

$$f(\theta|\omega, t) = \frac{1}{2\pi} \sum_l f_l(\omega, t) e^{il\theta}, \quad (2.6)$$

and to add a small perturbation to it

$$f \rightarrow f + \eta \delta f = \frac{1}{2\pi} \sum_l (f_l + \eta \delta f_l) e^{il\theta}, \quad (2.7)$$

with $\epsilon \ll 1$, and see whether the perturbation grows or decays in time for the different modes.

2.2.5 The Ott-Antonsen (OA) ansatz

A useful tool to study the synchronization of a neuronal network, is the so-called Ott-Antonsen (OA) ansatz (Ott and Antonsen, 2008), which considers a particular type of density functions f , that corresponds to a Poisson kernel:

$$f(\theta|\omega, t) = \frac{1}{2\pi} \left\{ 1 + \sum_{l=1}^{\infty} [f_1 e^{i\theta}]^l \right\} + \text{c.c.}, \quad (2.8)$$

where c.c. is the complex conjugate. These functions have the same coefficients in all the Fourier harmonics, except that they are raised to the l -th power for the l -th harmonic, $f_{l>1}(\omega, t) = [f_1(\omega, t)]^l$. In polar coordinates (ρ, ϕ) , the l -th harmonic becomes $f_1 = \rho e^{-i\phi}$, where ϕ can be thought of as the "center" of the density f , while ρ quantifies the width of the peak (Abrams *et al.*, 2008). Indeed, when $\rho \rightarrow 1$, $f(\theta|\omega, t) \rightarrow \delta(\theta - \phi(t))$, i.e. a delta function which is centered in $\phi(t)$. This is schematically represented in the left panel of Figure 2.3B. With this formalism, in the case of a population of neurons made of two coupled subpopulations, the chimera state corresponds to the state of constant phase shift between the center of the distributions f_1 and f_2 , ($\psi = \text{const}$), f_1 (the asynchronous population) having a constant spread $\rho_1 = r = \text{const}$ while f_2 (the synchronous one) being a delta function ($\rho_2 = 1$) (Figure 2.3B, right panel). In this way, the complexity of the system reduces immensely, to a 2D system in coordinates (ψ, r) in which the chimera state corresponds to the fixed point. The "breathing chimera" would instead correspond to the state in which $\psi = \text{const}$ and r oscillates, as shown in the lower panel of Figure 2.3B.

Theory Box 2.2.2: Derivation of phase models in case of weak couplings

Given a dynamical system that follows

$$\dot{x} = f(x) + \epsilon p(t), \quad (2.9)$$

which defines a periodic oscillator, $\dot{x} = f(x)$, forced by an external input $\epsilon p(t)$, that depends on time, with $\epsilon \ll 1$, we want to show how to derive the phase equation for weakly-coupled oscillators. The following derivation can be found in Izhikevich (2018). First, it can be shown that the system transforms into the phase model

$$\dot{\theta} = 1 + \epsilon PRC(\theta)p(t) + o(\epsilon), \quad (2.10)$$

where $p(t)$ represents the input of current from other oscillators in the network, such as

$$p(t) = \sum_s g_s(x(t), x_s(t)).$$

Here $x_s(t)$ represents the oscillators connected to x and g_s defines the type of interaction. We then make a separation of timescales by defining each $\theta_i(t)$ as $\theta_i(t) = t + \phi_i$: the first component represents the inherent oscillation that occurs naturally, while the second component pertains to the gradual build-up of phase deviation caused by the network. Substituting the previous relation in Equation (2.10), yields

$$\dot{\phi}_i = \epsilon PRC(t + \phi_i) \cdot \sum_{j=1}^n g_{ij}(x_i(t + \phi_i), x_j(t + \phi_j)).$$

Being the RHS of order ϵ , it reflects the slow dynamics of ϕ_i . Therefore, the two time scales, given by the fast oscillations and the slow phase modulations, can be split by the classical averaging method (Hoppensteadt and Izhikevich, 1997). The system thus becomes

$$\dot{\phi}_i = \epsilon \omega_i + \epsilon \sum_{j \neq i}^n H_{ij}(\phi_j - \phi_i), \quad (2.11)$$

with

$$H_{ij}(\phi_j - \phi_i) = \frac{1}{T} \int_0^T PRC(t) \cdot g_{ij}(x_i(t), x_j(t + \phi_j - \phi_i)) dt.$$

In the case of pulse-coupling, the function H is just a re-scaled PRC.

The Kuramoto model thus follows directly from Equation (2.11), when considering the slow time ($\tau = \epsilon t$) and H being replaced by its first Fourier term. In this case, the frequency deviations ω_i are interpreted as intrinsic frequencies of oscillators.

2.3 Main results

Our work aimed to explore the characteristics of Class I neurons, which are traditionally considered to have a limited tendency to synchronize. Therefore, we developed a model incorporating a feedback loop between an excitatory (E) and an inhibitory (I) population, a known neural mechanism for

generating oscillations, and time-delayed couplings, with positive PRC (thus proportional to $1 - \cos \theta$) (Figure 2.4A). The equations for the evolution of the phases of the two populations (E-I) are

$$\left\{ \begin{array}{l} \dot{\theta}_i^E = \omega_i^E + \frac{k_{EI}}{N_I} \sum_{j=1}^{N_I} \frac{1 - \cos(\theta_i^E - \theta_j^I(t - \tau_{EI}))}{2} + \\ \quad + \frac{k_{EE}}{N_E} \sum_{j=1}^{N_E} \frac{1 - \cos(\theta_i^E - \theta_j^E(t - \tau_{EE}))}{2} + \xi_i^E \\ \dot{\theta}_i^I = \omega_i^I + \frac{k_{IE}}{N_E} \sum_{j=1}^{N_E} \frac{1 - \cos(\theta_i^I - \theta_j^E(t - \tau_{IE}))}{2} + \\ \quad + \frac{k_{II}}{N_I} \sum_{j=1}^{N_I} \frac{1 - \cos(\theta_i^I - \theta_j^I(t - \tau_{II}))}{2} + \xi_i^I, \end{array} \right. \quad (2.12)$$

where $\omega_i^{E,I}$ are the intrinsic frequencies of each neuron, $N_{E,I}$ are the number of neurons in each population, $k_{EI} < 0$ and $k_{IE} > 0$ are the inter-population coupling strengths, $k_{EE} > 0$ and $k_{II} < 0$ are the intra-population coupling strengths and $\tau_{EI,IE,EE,II}$ are constant time delays in the connections. Gaussian noise is introduced in the system through ξ , where $\langle \xi(t) \rangle = 0$ and $\langle \xi(t)\xi(t') \rangle = 2D\delta(t - t')$, with $D = \text{const}$.

In the following, we will only report the main steps of the derivations regarding the main results of the paper, which can be read in full at the end of the chapter. First, we analysed the system in the continuum limit, namely with an infinite number of neurons in each population, thus we defined the probability density function f , which satisfies the Fokker-Planck equation

$$\partial_t f^{E,I} = -\partial_{\theta^{E,I}}(f^{E,I}v) + D\partial_{\theta^{E,I}}^2 f^{E,I}, \quad (2.13)$$

with v being the drift velocity, which can be obtained from Equation (2.12). We then made a Fourier expansion of f , and performed a Linear Stability Analysis around the fully asynchronous state (where the order parameter $Z^2 = 0$ for both sub-populations), which is a trivial solution of the system. The goal is to find the Boundaries of Stable Incoherence (BSI), i.e. to determine the region in parameter space - and its borders - where the system behaves in an asynchronous manner, in order to subsequently simulate the system around this region and see what other (more interesting) behaviours are possible.

Our analysis revealed that, for a system without external noise ($D = 0$), only inter-population couplings ($k_{EE,II} = 0$) and identical intrinsic frequencies and coupling strengths for the two sub-populations ($\omega_E = \omega_I = \omega_0$, $|k_{EI,IE}| = K$), the BSI are described by the following equation

$$\frac{K}{\omega_0} = \begin{cases} \pm \frac{2}{\sqrt{3}} \frac{m+2\tau/T}{\tau/T} & \text{if } m \text{ is even} \\ \pm \frac{2}{\sqrt{5}} \frac{m+2\tau/T}{\tau/T} & \text{if } m \text{ is odd,} \end{cases} \quad (2.14)$$

where τ is the sum of the delays of the two pathways ($\tau = \tau_{EI} + \tau_{IE}$) and $T = 2\pi/\omega_0$ is the intrinsic period of the oscillators. This shows that these BSI are periodic in the delay, and also that the dependence is only on the sum of the delays between excitatory and the inhibitory population (Figure 2.4B, red lines). We then simulated the system over a range of coupling strengths and time delays, and computed the order parameters $Z_{E,I}^2$ for each population, which is shown in Figure 2.4B as a 2D-gradient. This not only confirmed the presence of regions in parameter space in which the

two populations do not synchronize (Figure 2.4B, region III, black areas), but also revealed the emergence of regions in which either both populations are synchronized (Figure 2.4B, region II, white areas) or only one population synchronized to a common rhythm while the other kept firing out of sync (Figure 2.4B, region I-IV, blue and orange areas). The four possible regions are shown in the bottom of the panel, which portrays a snapshot of the phase of each neuron at a certain time t . Therefore, a line of dots (where each dot is a neuron) represents synchronization, whereas dots scattered around the plane corresponds to no synchronization. In this case, the chimera state was also found to be robust to noise.

Subsequently, we aimed to further investigate the role of time delay for this system and determine whether it was a prerequisite to observe synchronization and chimera states: what we found is that the presence of time delay significantly enhanced the dynamics of the network and contributed to the stability of the synchronized and chimera states. First of all, to gain analytical understanding of the system without time delay, we first examined a specific category of density functions. These functions adopt the structure of a Poisson kernel, where the coefficients remain consistent across all Fourier harmonics, except they are elevated to the power of l for the l -th harmonic (making use of the OA ansatz)

$$f^{E,I}(\theta|\omega, t) = \frac{1}{2\pi} \left\{ 1 + \sum_{l=1}^{+\infty} [f_1^{E,I} e^{i\theta}]^l \right\} + \text{c.c.}, \quad (2.15)$$

where c.c. stands for the complex conjugate. As explained in Section 2.2.5, we can use polar coordinates (ρ, ψ) to express the l -th harmonic as $f_1 = \rho_{E,I} e^{-i\phi_{E,I}}$. Here, ϕ indicates the position of the density f 's center, while ρ quantifies the sharpness of the curve's peak (Abrams *et al.*, 2008). With this formalism, the chimera state corresponds to the state in which there is a constant phase shift between the two distributions ($\psi = \phi_E - \phi_I = \text{const}$), with one distribution (the synchronized one) being a delta function ($\rho_E \rightarrow 1$), and the other having a certain constant spread ($\rho_I = r = \text{const}$). We thus reduced the complexity of the system to a 2D system in coordinates (ψ, r)

$$\begin{cases} \dot{r} = \frac{K}{4}(1 - r^2) \sin \psi \\ \dot{\psi} = \Delta\omega - K + \frac{K}{4}(2r + \frac{r^2+1}{r}) \cos \psi, \end{cases} \quad (2.16)$$

where $\Delta\omega = \omega_E - \omega_I$. The fixed point for this system (which corresponds to the chimera state), can be found very easily by taking $\dot{r} = \dot{\psi} = 0$, which yields

$$\begin{cases} \psi^* = m\pi, & m \in \mathbb{Z} \\ r_{1,2}^* = \frac{-2(\Delta\omega - K) \pm \sqrt{4(\Delta\omega - K)^2 - 3K^2}}{3(-1)^m K}. \end{cases}$$

In order to compute the stability of the fixed point we performed a Linear Stability Analysis. Given the system of differential equations of the form $\begin{cases} \dot{r} = f(r, \psi) \\ \dot{\psi} = g(r, \psi), \end{cases}$ the Jacobian J is

$$J = \begin{bmatrix} \frac{df}{dr} & \frac{df}{d\psi} \\ \frac{dg}{dr} & \frac{dg}{d\psi} \end{bmatrix} \Big|_{r^*, \psi^*} = \begin{bmatrix} 0 & 2/9K \\ -3/2K & 0 \end{bmatrix}.$$

Since the trace is zero and the determinant is $\Delta = K^2/3 > 0$, the linearization predicts that the fixed point should be a linear center. As we have seen in Chapter 1, this is a marginal case for which linearization does not always work. However, since the system is invariant under the

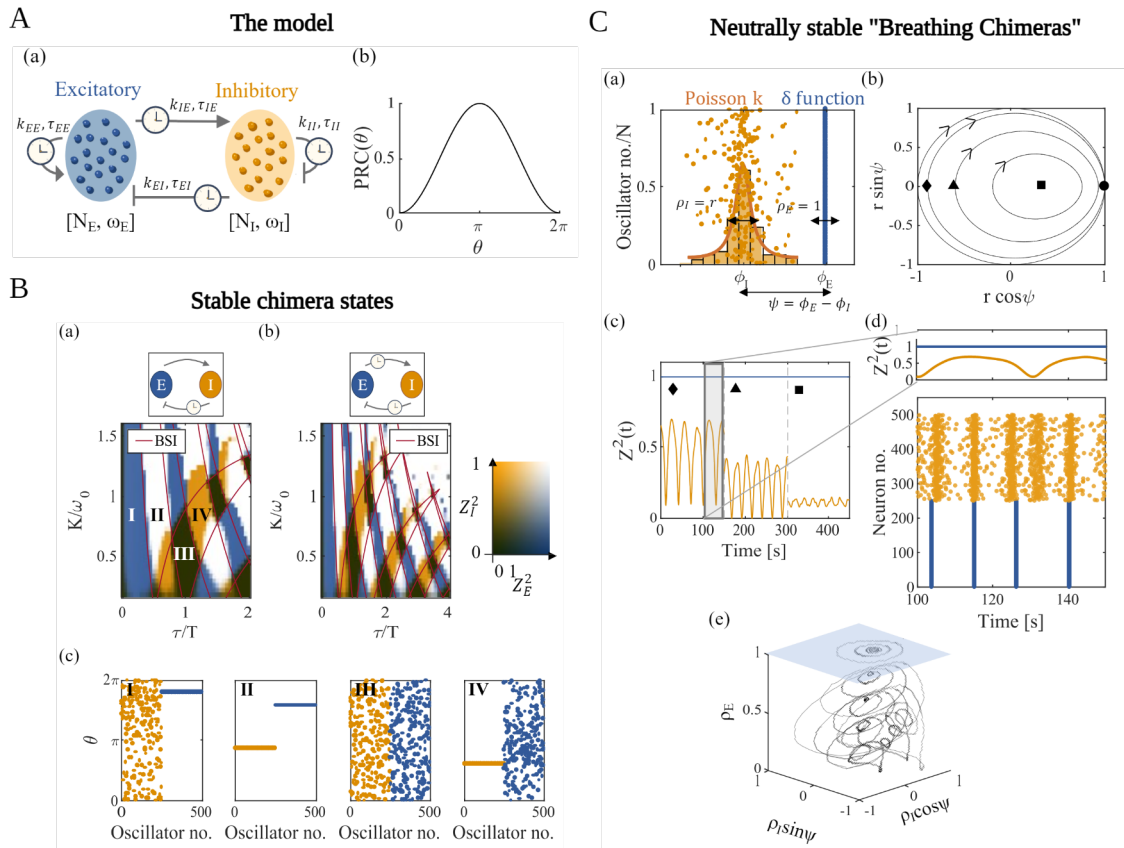


Figure 2.4: (A) The model: a negative feedback loop between an excitatory and an inhibitory population, with type 1 Phase Response Curve (PRC). (B) The emergence of stable chimera states (blue and orange areas), such as region I and region IV in the parameter space given by time delay (x-axis) and coupling strength (y-axis). (C) The emergence of "breathing chimeras" as shown by the oscillatory trace of the order parameter Z^2 , that are neutrally stable. (A-B-C) are adapted from Lucchetti *et al.* (2021)

change of variables $t \rightarrow -t, \psi \rightarrow -\psi$, it can be proven that the fixed point is also a nonlinear center (Figure 2.4C, top). Overall, these findings show that the chimera state should exist also without time delay, but that it is neutrally stable and that it has a family of periodic orbits around it. To see if this is the case also with a finite number of neurons, we simulated the system initializing one of the two subpopulation with phases drawn from a Poisson kernel, such as

$$f^I(\theta) = \sum_{n=-\infty}^{\infty} \rho_I^{|n|} e^{in\theta} = \frac{1 - \rho_I^2}{1 - 2\rho_I \cos(\theta - \phi_I) + \rho_I^2},$$

while the phases of the other were all initially synchronized. The simulations confirmed the presence of the chimera state and also of the "breathing chimeras", where one population is always synchronized while the other oscillates between periods of higher and lower synchrony (Figure 2.4C, middle). Finally, we tried to simulate the system in the three coordinates (ρ_E, ρ_I, ψ) . This showed that the plane in which we had restricted the system before ($\rho_E = 1$) is not attracting, therefore the system should be initialized in this state in order to observe it (Figure 2.4C, bottom). Overall, our results show that Class 1 neurons can display a more rich variety of collective behaviours than previously thought, including total synchronization and chimera states and that time delays help to stabilize these states which become neutrally stable with instantaneous connections.

2.4 Discussion and Perspectives

Since their discovery in 2004, chimera states have been studied extensively and found to occur in a plethora of examples, both theoretical and experimental, as summed-up in several review papers (Omel'chenko, 2018; Schöll, 2016; Panaggio and Abrams, 2015; Haugland, 2021). In the beginning, they were believed to be a peculiar characteristic of networks with non-locally coupled oscillators, namely networks whose coupling was neither local (nearest neighbour), nor global (all-to-all coupling) (Kuramoto and Battogtokh, 2002; Abrams and Strogatz, 2006). The original coupling explored by Kuramoto and Battogtokh (2002) was an exponentially decaying coupling kernel. Subsequently, it was observed that one of the simplest configurations supporting chimera states was a population made of two subpopulations with all-to-all coupling within each group and weaker couplings between the groups (Abrams *et al.*, 2008). More recently, chimera states have been shown to exist also in systems with global coupling (Schmidt *et al.*, 2014) and only local couplings (Laing, 2015).

However, as of today, the direct applicability of this theory in the context of neuroscience remains rather vague and superficial (Haugland, 2021), and there is still a lot of ongoing research on determining how and when chimera states can be observed in real-world scenarios. One of the most cited phenomena which may constitute a chimera state is that of *uni-hemispheric sleep* (Rattenborg *et al.*, 2000): this is observed in certain species of animals, such as dolphins or birds, where only one hemisphere of the brain enters into a sleep state while the other hemisphere remains awake. The sleeping hemisphere typically exhibits a synchronized activity which gives rise to slow brainwaves, while the awake hemisphere displays wakefulness characterized by an asynchronous rhythm. This allows animals to maintain some level of vigilance and perform critical functions while still getting the benefits of sleep. In this case, though, modelling the whole brain as a system of phase oscillators seems an immense simplification, given the implicit assumption of constant intrinsic frequency and weak couplings, so that amplitude changes of the limit cycle can be neglected.

In the context of pathological synchronization of neurons, such as in Parkinson's disease, it has been shown that some therapeutic strategies may highly benefit from administering an external stimulation at a specific patient-dependent phase of the ongoing rhythm, highlighting the importance of phase models (Holt *et al.*, 2019). In this case, the neuronal synchronization does occur in certain regions only, so that the chimera state theory could potentially be applied. However, it is important to note that the strict definition of chimera states applies to "identical oscillators," namely oscillators with the same inherent firing frequency. This assumption may be overly simplistic in real-world scenarios. Therefore, it is somewhat speculative to effectively classify this local clustered synchronization as a true chimera state.

To make the model less abstract, it would be interesting to include spatial coordinates and see if the chimera states are preserved and to what extent. Additionally, one could consider populations of neurons of different sizes, which could better represent the ratio of excitatory-inhibitory neurons in the brain (estimated to be approximately 4:1 in typical mammalian brains).

On the other hand, the abstract nature of this model could be exploited for its potential application in various contexts, as it lacks specificity to neurons. In fact, it could be extended to any other system of oscillators that exhibits similar phase responses to external perturbations.

2.5 Manuscript: Emergence of chimera states in a neuronal model of delayed oscillators

Authors: Alessandra Lucchetti, Mogens H. Jensen, and Mathias L. Heltberg

Affiliations: Niels Bohr Institute, University of Copenhagen, Copenhagen 2100, Denmark;

Journal: Physical Review Research




Vol./page: 3, 033041

DOI: 10.1103/PhysRevResearch.3.033041

My contributions: I designed the study in collaboration with M.L. Heltberg and M.H. Jensen., I performed the analytical study and made the numerical simulations. I wrote the article and made all the figures.

Notes in relation to Master's Thesis: Some of the results present in paragraph (A), (C) and (D) were part of the previous Master's Degree Thesis. The manuscript has been fully written during the PhD and includes new results in paragraph (B) (D) and (E).

Emergence of chimera states in a neuronal model of delayed oscillators

Alessandra Lucchetti ¹, Mogens H. Jensen ^{1,*} and Mathias L. Heltberg ^{1,2,†}

¹Niels Bohr Institute, University of Copenhagen, Blegdamsvej 17, 2100 Copenhagen Ø, Denmark

²Laboratoire de Physique, Ecole Normale Supérieure, Rue Lhomond 15, 07505, Paris



(Received 18 January 2021; accepted 15 June 2021; published 9 July 2021)

Neurons are traditionally grouped in two excitability classes, which correspond to two different responses to external inputs, called phase response curves (PRCs). In this paper we have considered a network of two neural populations with delayed couplings, bound in a negative feedback loop by a positive PRC (type I). Making use of both analytical and numerical techniques, we derived the boundaries of stable incoherence in the continuum limit, studying their dependence on the time delay and the strengths of both interpopulation and intrapopulation couplings. This led us to discover, in a system with stronger delayed external compared to internal couplings, the coexistence of areas of coherence and incoherence, called chimera states, that were robust to noise. On the other hand, in the absence of time delays and with negligible internal couplings, the system portrays a family of neutrally stable periodic orbits, known as “breathing chimeras.”

DOI: [10.1103/PhysRevResearch.3.033041](https://doi.org/10.1103/PhysRevResearch.3.033041)

I. INTRODUCTION

For the past few decades, models of coupled phase oscillators have proved to be particularly successful to describe the emergence of macroscopic rhythmic patterns in a huge variety of natural and artificial contexts [1]. In this framework, it is useful to consider the interplay between excitatory and inhibitory (E-I) time-delayed connections, in order to model spatially distributed self-organized systems, such as neuronal networks, that are known to exhibit synchronous behavior. This is associated with many cognitive processes such as memory formation [2], directed attention [3], and the processing of sensory stimuli [4], but it can also be the hallmark of certain disease states such as Parkinson’s disease or epileptic seizures [5–7]. In these cases, synchronization is generally localized to certain cerebral regions only, and coherence and incoherence coexist within the brain.

In the context of phase models, states in which synchronous and asynchronous clusters of identical oscillators coexist were discovered by Kuramoto and Battogtokh [8], and they were later defined “chimera states” by Abrams and Strogatz [9]. Since then, they were observed in a huge variety of settings, for instance in more realistic neuronal models [10–14], in time-discrete systems (maps) [15,16], in

social agent-based models [17], or even in certain experimental setups [18–20] (see [21–23] for extensive reviews).

Synchronization patterns largely depend on the individual oscillators properties. It is known that neurons can be grouped into two excitability classes, that differ in the bifurcation observed while transitioning from the silent mode to the firing mode, in particular, a saddle node on an invariant circle bifurcation or a Hopf bifurcation. Moreover, they are directly linked to two types of phase response curves (PRCs): either always positive (type I) or both positive and negative (type II) [24]. The dynamics of networks of type II neurons has been widely explored in the past, e.g., making use of the Kuramoto model and its many generalizations [25–30]. In this context, chimera states appear commonly in networks of two subpopulations with nonlocal couplings [31], typically with a large ensemble of oscillators (although they have also been observed with as few as two oscillators per group [32]). It has also been shown, in an adaptive Kuramoto model, that asymmetric inter- or intrapopulation couplings enhance the transition from the chimera state to the synchronized state [33]. Moreover, the presence of delayed couplings, which enriches the dynamics of the system by making it infinite dimensional, has been also observed to lead to the emergence of chimera states, for instance in Kuramoto-like oscillators [34,35] or in multilayer networks of Fitz-Hugh Nagumo oscillators [36].

On the other hand, there have been fewer investigations on the properties of type I neurons, which are generally considered to have low propensity for synchronization when coupled by excitation [37,38]. Most of the studies [39] only focused on either purely excitatory or inhibitory couplings, whereas Keane *et al.* [40] studied a small-world network with a ring of excitatory type I oscillators, with some random inhibitory delayed long interactions. It was shown that, as opposed to the

*mhjensen@nbi.ku.dk

†Mathias.heltberg@nbi.ku.dk

Published by the American Physical Society under the terms of the [Creative Commons Attribution 4.0 International](https://creativecommons.org/licenses/by/4.0/) license. Further distribution of this work must maintain attribution to the author(s) and the published article’s title, journal citation, and DOI.

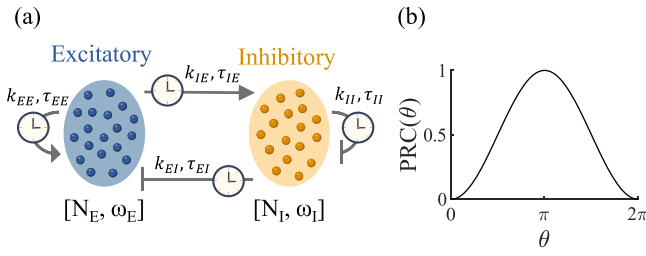


FIG. 1. (a) Schematic representation of the system with two subpopulations [blue, excitatory (E); orange, inhibitory (I)] having $N_{E,I}$ number of oscillators with intrinsic frequency $\omega_{E,I}$. They are bound in a negative feedback loop with delayed connections (with time delay $\tau_{EI,IE,EE,II}$, interpopulation coupling strengths $k_{EI,IE}$, and intrapopulation coupling strengths $k_{EE,II}$). (b) Type I PRC, with the form $(1 - \cos \theta)/2$.

same network of type II neurons, where adding the inhibitory couplings results in a sharp transition to incoherence [41], in this case there were multiple transitions between synchronization and desynchronization. The interplay between E and I was also studied by Ladenbauer *et al.* [42] in a two-population model of delayed integrate-and-fire neurons, where they observed how adaptation controls synchronization and the formation of cluster states. Moreover, Montbrío and Pazó [43] recently analyzed a network of instantaneously coupled E-I oscillators, showing that synchronization can emerge only if the E population is intrinsically faster than the I one. Finally, clustered chimera states have been observed by Vüllings *et al.* [44] in a ring of type I neurons, which depended on the distance from the excitability threshold, the range of nonlocal couplings, and the coupling strength.

We build on the basis of these results and apply this to a network of two populations of E-I identical type I oscillators with time delayed couplings [Figs. 1(a) and 1(b)]. The purpose of this paper is to analyze the dynamics of the system, with a particular focus on determining whether chimera states may arise in this framework and how they depend on the delay and the coupling strengths, both within and between the two populations.

The paper is organized as follows: the stability of the fully incoherent state is analyzed in Sec. II A with identical oscillators, no noise, and time delayed interpopulation connections; in Sec. II B with the addition of delayed or instantaneous internal couplings; and in Sec. II C with heterogeneous natural frequencies, noise, and instantaneous interpopulation couplings. Since it was observed that, starting from random initial conditions, the system approaches a chimera state for periodic values of the external time delay greater than zero, in Sec. II D the basin of attraction of the chimera is discussed making use of the Ott-Antonsen (OA) ansatz [45], in the absence of time delay. Finally, in Sec. II E the optimal parameters to display chimera states and the robustness of the system towards noise are evaluated.

II. METHODS AND RESULTS

The governing equations for the phases θ of the i th oscillator in the E and the I populations, with positive PRC,

are [24,37,38]

$$\begin{cases} \dot{\theta}_i^E = \omega_i^E + \frac{k_{EI}}{N_I} \sum_{j=1}^{N_I} \frac{1 - \cos(\theta_i^E - \theta_j^I(t - \tau_{EI}))}{2} \\ \quad + \frac{k_{EE}}{N_E} \sum_{j=1}^{N_E} \frac{1 - \cos(\theta_i^E - \theta_j^E(t - \tau_{EE}))}{2} + \xi_i^E, \\ \dot{\theta}_i^I = \omega_i^I + \frac{k_{IE}}{N_E} \sum_{j=1}^{N_E} \frac{1 - \cos(\theta_i^I - \theta_j^E(t - \tau_{IE}))}{2} \\ \quad + \frac{k_{II}}{N_I} \sum_{j=1}^{N_I} \frac{1 - \cos(\theta_i^I - \theta_j^I(t - \tau_{II}))}{2} + \xi_i^I, \end{cases} \quad (1)$$

where $\omega^{E,I}$ is the natural frequency, $N_{E,I}$ is the number of oscillators in each population, $k_{EI} < 0$ and $k_{IE} > 0$ are the interpopulation coupling strengths, $k_{EE} > 0$ and $k_{II} < 0$ are the intrapopulation coupling strengths, and $\tau_{EI,IE,EE,II}$ indicates constant time delays in the couplings. Moreover, ξ represents Gaussian noise, such that $\langle \xi(t) \rangle = 0$ and $\langle \xi(t)\xi(t') \rangle = 2D\delta(t - t')$, D being a constant value.

Moreover, Eq. (1) can be expressed in a more compact form as

$$\begin{aligned} \dot{\theta}_i^\sigma = & \tilde{\omega}_i^\sigma - \frac{k_{\sigma\sigma'}}{2N_{\sigma'}} \sum_{j=1}^{N_{\sigma'}} \cos(\theta_i^\sigma - \theta_j^{\sigma'}(t - \tau_{\sigma\sigma'})) \\ & - \frac{k_{\sigma\sigma}}{2N_\sigma} \sum_{j=1}^{N_\sigma} \cos(\theta_i^\sigma - \theta_j^\sigma(t - \tau_{\sigma\sigma})) + \xi_i^\sigma, \end{aligned} \quad (2)$$

where $\sigma = \{E, I\}$ and $\tilde{\omega}_i^\sigma = \omega_i^\sigma + \frac{1}{2}(k_{\sigma\sigma'} + k_{\sigma\sigma})$, showing that the excitatory and the inhibitory couplings have the effect to slightly shift the natural frequency of the oscillators.

The order parameter that quantifies the level of synchronization within each population is defined as

$$Z_\sigma(t) = R_\sigma(t) e^{i\psi_\sigma(t)} = \frac{1}{N_\sigma} \sum_{j=1}^{N_\sigma} e^{i\theta_j^\sigma(t)}.$$

For later use, taking the long time average $\langle \cdot \rangle_t$ of the absolute value of the order parameter, it is possible to obtain a single measure for the phase ordering, Z_σ^2 , given by

$$Z_\sigma^2 = \langle |R_\sigma(t) e^{i\psi_\sigma(t)}|^2 \rangle_t = \left\langle \frac{1}{N_\sigma^2} \sum_{i,j=1}^{N_\sigma} \cos(\theta_i^\sigma - \theta_j^\sigma) \right\rangle_t. \quad (3)$$

Finally, the average order parameter between the two populations is defined as

$$\langle Z^2 \rangle = (Z_E^2 + Z_I^2)/2.$$

Equation (2) can be expressed in terms of the order parameter, such that

$$\begin{aligned} \dot{\theta}_i^\sigma = & \tilde{\omega}_i^\sigma - \frac{k_{\sigma\sigma'}}{4} (e^{i\theta_i^\sigma} Z_{\sigma'}^*(t - \tau_{\sigma\sigma'}) + e^{-i\theta_i^\sigma} Z_{\sigma'}(t - \tau_{\sigma\sigma'})) \\ & - \frac{k_{\sigma\sigma}}{4} (e^{i\theta_i^\sigma} Z_\sigma^*(t - \tau_{\sigma\sigma}) + e^{-i\theta_i^\sigma} Z_\sigma(t - \tau_{\sigma\sigma})) + \xi_i^\sigma, \end{aligned} \quad (4)$$

where * indicates the complex conjugate.

The analysis of this system can be efficiently carried on in the case $N_\sigma \rightarrow \infty$, so that the discrete sets of phases and frequencies turns into the continuum limit $\{\theta_i^\sigma, \omega_i^\sigma\} \rightarrow \{\theta^\sigma, \omega^\sigma\}$.

In other words, for each ω there is a continuum of oscillators distributed along the unit circle; the probability density function is characterized by $f^\sigma(\theta|t, \omega)$ such that $f^\sigma(\theta|t, \omega)d\theta$ gives the fraction of oscillators with frequency ω which lie between θ and $\theta + d\theta$ at time t [29].

In general, in this limit the order parameter can be expressed as

$$Z_\sigma(t) = \int_0^{2\pi} \int_{-\infty}^{+\infty} e^{i\theta} f^\sigma(\theta, \omega|t) g_\sigma(\omega) d\omega d\theta,$$

where $g_\sigma(\omega)$ is the frequency distribution. Hence, $f^\sigma(\theta, \omega, t)$ satisfies the Fokker-Planck equation

$$\partial_t f^\sigma = -\partial_{\theta^\sigma} (f^\sigma v) + D \partial_{\theta^\sigma}^2 f^\sigma, \quad (5)$$

with

$$v = \tilde{\omega}_\sigma - \frac{k_{\sigma\sigma'}}{4} (e^{i\theta^\sigma} Z_{\sigma'}^*(t - \tau_{\sigma\sigma'}) + e^{-i\theta^\sigma} Z_{\sigma'}(t - \tau_{\sigma\sigma'})) \\ - \frac{k_{\sigma\sigma}}{4} (e^{i\theta^\sigma} Z_\sigma^*(t - \tau_{\sigma\sigma}) + e^{-i\theta^\sigma} Z_\sigma(t - \tau_{\sigma\sigma})).$$

It is convenient, for the following analysis, to introduce the Fourier expansion of f^σ :

$$f^\sigma(\theta|\omega, t) = \frac{1}{2\pi} \sum_l f_l^\sigma(\omega, t) e^{il\theta}. \quad (6)$$

Substituting Eq. (6) into Eq. (5) and setting the correspondent modes equal yields

$$\dot{f}_l^\sigma = -(il\tilde{\omega}_\sigma + l^2 D) f_l^\sigma \\ + il \frac{k_{\sigma\sigma'}}{4} (f_{l-1}^\sigma Z_{\sigma'}^*(t - \tau_{\sigma\sigma'}) + f_{l+1}^\sigma Z_{\sigma'}(t - \tau_{\sigma\sigma'})) \\ + il \frac{k_{\sigma\sigma}}{4} (f_{l-1}^\sigma Z_\sigma^*(t - \tau_{\sigma\sigma}) + f_{l+1}^\sigma Z_\sigma(t - \tau_{\sigma\sigma})). \quad (7)$$

To simplify the future notation, we define

$$\langle f(\omega) \rangle_\sigma = \int_{-\infty}^{+\infty} f(\omega) g_\sigma(\omega) d\omega,$$

so that the order parameter becomes $Z_\sigma(t) = \langle f_{-1}^\sigma(\omega, t) \rangle_\sigma$.

A linear stability analysis was performed around the fully incoherent state ($Z_\sigma = 0$), where all the oscillators are randomly distributed along the unit circle ($f^\sigma = 1/2\pi$). This is always a trivial solution. To do so, a small perturbation was added to the probability density function:

$$f^\sigma \rightarrow f^\sigma + \eta \delta f^\sigma = \frac{1}{2\pi} \sum_l (f_l^\sigma + \eta \delta f_l^\sigma) e^{il\theta}, \quad (8)$$

with $\eta \ll 1$. The analysis, reported in the Supplemental Material [46], reveals that the only possible unstable modes are $l = \pm 1$ and considering the case $l = 1$ results in

$$\delta \dot{f}_1^\sigma = -(i\tilde{\omega}_\sigma + D) \delta f_1^\sigma \\ + i \left[\frac{k_{\sigma\sigma'}}{4} \langle \delta f_1^{\sigma'} \rangle_{t-\tau_{\sigma\sigma'}} + \frac{k_{\sigma\sigma}}{4} \langle \delta f_1^\sigma \rangle_{t-\tau_{\sigma\sigma}} \right], \quad (9)$$

where $\langle \cdot \rangle_{t-\tau_{\sigma\sigma'}}$ means that the quantity within the brackets is evaluated at time $t - \tau_{\sigma\sigma'}$.

A. Identical oscillators with no internal couplings and positive external delay

First we considered the simplest case with identical oscillators ($\omega_E = \omega_I \equiv \omega_0$), no noise ($D = 0$), no internal couplings ($k_{EE} = k_{II} = 0$), and the same external coupling strength ($|k_{EI}| = |k_{IE}| \equiv K$). After substituting the ansatz $\delta f_1^\sigma(\omega, t) = b_\sigma(\omega) e^{\lambda t}$, and considering that the frequency distribution is a delta function for both populations ($g(\omega) = \delta(\omega - \omega_0)$), a brief analysis, reported in the Supplemental Material [46], leads to the characteristic equation for λ :

$$16((\lambda + i\omega_0)^2 + K^2/4) e^{(\tau_{EI} + \tau_{IE})\lambda} = K^2. \quad (10)$$

Since the dependence is only on the sum of the two delays, we define $\tau_{EI} + \tau_{IE} \equiv \tau$ for simplicity of notation.

At the bifurcation point between stable and unstable incoherence λ crosses the imaginary axis, $\lambda = iR$ with $R \in \mathbb{R}$, therefore

$$16(-(R + \omega_0)^2 + K^2/4) [\cos(R\tau) + i \sin(R\tau)] = K^2. \quad (11)$$

Given that the right-hand side is real, the left-hand side must also be real, so $\sin(R\tau) = 0$, which leads to the condition

$$R\tau = m\pi \quad \text{with } m \in \mathbb{Z}. \quad (12)$$

Finally, substituting Eq. (12) into Eq. (11) and considering that the natural period is $T = 2\pi/\omega_0$, Eq. (11) can be solved for K/ω_0 , which yields

$$\frac{K}{\omega_0} = \begin{cases} \pm \frac{2}{\sqrt{3}} \frac{m+2\tau/T}{\tau/T} & \text{if } m \text{ is even} \\ \pm \frac{2}{\sqrt{3}} \frac{m+2\tau/T}{\tau/T} & \text{if } m \text{ is odd.} \end{cases} \quad (13)$$

Therefore, the boundaries of stable incoherence (BSI) are periodic in the delay and only depend on the sum of the delays in the two pathways.

This aspect was fully confirmed by the numerical analysis, with the correspondent parameters used listed in the Supplemental Material [46]. The simulations were performed in MATLAB2020B, making use of the built-in function `dde23` (Fig. 2) and also confirmed via the Euler method (not shown). They were performed first with time delay in the inhibitory connection only [Fig. 2(a)], excitatory connection only (shown in the Supplemental Material [46]), and then in both [Fig. 2(b)]. Moreover, they were repeated over a range of values for K and τ . As initial condition, the phases of both populations followed a normal distribution centered at zero and with standard deviation 2π . Once the system had equilibrated, Z^2 was computed for each population. From the simulations, four possible scenarios emerged, that repeat periodically (denoted I–IV). In particular, the black areas (for instance, area III) were confirmed to be the areas in which both populations are internally not synchronized ($Z_E^2 \approx Z_I^2 \approx 0$), at the intersection between the curves. In white areas, for instance in area II, both populations were internally synchronized ($Z_E^2 \approx Z_I^2 \approx 1$). However, the remarkable phenomenon is the emergence of the blue and orange areas such as I and IV, where only one population is coherent while the other is incoherent. These corresponded to chimera states. In Fig. 2(c), a snapshot of the oscillator phases is reported at a fixed time, which confirms the four scenarios depicted above.

Considering only intercouplings between the two populations is a very particular case, that enabled us to highly

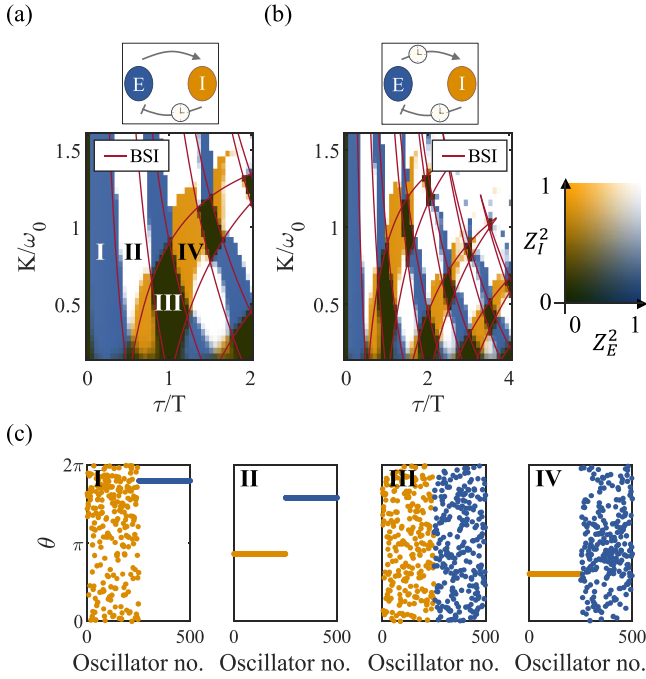


FIG. 2. Phase diagram obtained by simulating Eq. (1) with only external couplings and computing Z_E^2, Z_I^2 with (a) $\tau_{EI} > 0, \tau_{IE} = 0$ and (b) $\tau_{EI} = \tau_{IE} > 0$. The x axis represents the sum of the delays τ in units of the natural period T , while the y axis corresponds to the coupling strength K in terms of the natural frequency ω_0 . The value of the order parameters is indicated by the two-dimensional color gradient on the right. The parameters used are reported in the Supplemental Material [46]. The BSI are obtained from Eq. (13). (c) Snapshots of the oscillator phases with parameters in regions I–IV which confirm the presence of chimera states in region I and IV. Color scheme as in Fig. 1.

simplify the analytical calculations; however, it is not very realistic, therefore we analyzed whether the system phase diagram depicted in Fig. 2 would be robust to the inclusion of small intracouplings.

B. Identical oscillators with both internal and external couplings

First, we considered the case of equal external coupling strengths $k_{EI} = k_{IE} \equiv k_{\text{ext}}$, as well as equal internal ones $k_{EE} = k_{II} \equiv k_{\text{int}}$. Then we analyzed the robustness of the phase diagram depicted in Fig. 2, computing the number of overall synchronous, asynchronous, and chimera states while increasing the values of the internal couplings. As shown in Fig. 3(a), the number of asynchronous and chimera states are robust to the inclusion of internal couplings until $k_{\text{int}} \approx 10^{-1} k_{\text{ext}}$, when the system starts to transition to an overall synchronous state.

Secondly, we considered the case of internal and external couplings of equal strength ($|k_{EI,IE,EE,II}| \equiv K$) while assuming instantaneous intracouplings ($\tau_{EE,II} = 0$) and the same delayed cross-couplings ($\tau_{EI,IE} > 0$), which could represent the case of two neuronal populations that are spatially separated by some distance. In this case, Eq. (10) becomes (shown

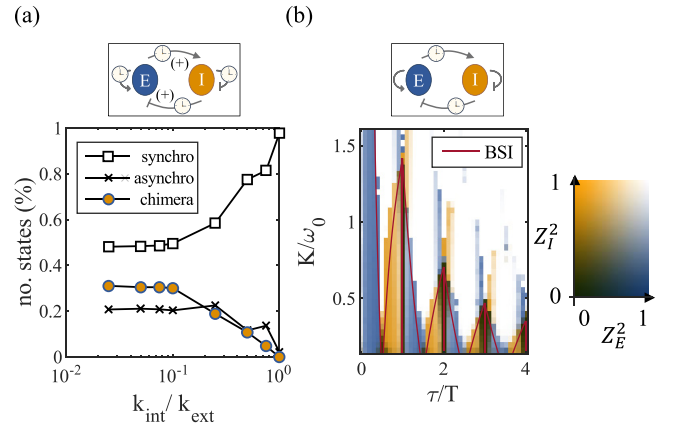


FIG. 3. (a) Percentage of “synchronized” (squares), “asynchronous” (crosses), and “chimera” states (circles) among all the measured states at increasing values of the internal couplings (k_{int}) compared to the external ones (k_{ext}). (b) Phase diagram obtained by simulating Eq. (1) with external delayed and internal instantaneous couplings and computing Z_E^2, Z_I^2 . The x axis represents the sum of the delays τ in units of the natural period T , while the y axis corresponds to the coupling strength K in terms of the natural frequency ω_0 . The value of the order parameters is indicated by the two-dimensional color gradient on the right. The parameters used are reported in the Supplemental Material [46]. The BSI are obtained from Eq. (15). Color scheme as in Fig. 1.

in the Supplemental Material [46])

$$(16(\lambda + i\omega_0)^2 + K^2)e^{\lambda\tau} = K^2, \quad (14)$$

where again $\tau = \tau_{EI} + \tau_{IE}$. Following the same reasoning as before, we found the BSI as

$$\begin{cases} \tau/T = -m/2 & \text{if } m \text{ is even} \\ \frac{K}{\omega_0} = \pm\sqrt{2}\frac{m+2\tau/T}{\tau/T} & \text{if } m \text{ is odd.} \end{cases} \quad (15)$$

Therefore, the equations representing the BSI are hyperbolas and vertical lines in the $(\tau/T, K/\omega_0)$ space. This is in accordance with the simulations, as depicted in Fig. 3(b). In this case, compared to Fig. 2, the regions of incoherence shrink around integer values of τ/T , while the area corresponding to the chimera states decreases for increasing values of the external delay. Because the inclusion of small delayed internal couplings did not alter significantly the plot depicted in Fig. 2, while it highly complicated the analytical calculations, we decided, for the rest of the paper, to consider negligible internal couplings.

From the simulations it seemed that the system would never display chimeras without external time delay, hence we analyzed whether the delay was the only necessary condition or whether other parameters could play a role in it as well. In order to do so, we relaxed some of the constraints, in particular that of identical oscillators and identical couplings, and included also some external noise in the system.

C. Heterogeneous oscillators without time delay

We considered the case with no time delay in the connections ($\tau_{EI,IE} = 0$), some external Gaussian noise ($D > 0$), and heterogeneity in the frequencies of the oscillators.

The calculations are particularly accessible when considering Lorentzian distributions for the frequencies, $g_\sigma(\omega) = \mathcal{L}(\tilde{\omega}_\sigma, \gamma_\sigma) \equiv \frac{\gamma_\sigma/\pi}{(\omega - \tilde{\omega}_\sigma)^2 + \gamma_\sigma^2}$. For simplicity we set $\gamma_E = \gamma_I = \gamma$ and $\tilde{\omega}_E = -\tilde{\omega}_I = \tilde{\omega}$, so that $\Delta\omega \equiv \omega_E - \omega_I = 2\tilde{\omega}$.

Considering symmetric frequencies over the origin is equivalent to considering a system of reference that is rotating with frequency $\Omega = (\omega_E + \omega_I)/2$ and does not modify the analysis of the stability. Moreover, we define $|k_{EI}| = \epsilon|k_{IE}| = \epsilon k$ both for simplicity of notation and because we will be interested in observing the ratio of the two coupling strengths, ϵ .

The following analysis builds on the work done by Montbrío and Pazó [43]. A brief linear stability analysis (see the Supplemental Material [46] for more details), again close to the incoherent state, leads to the condition

$$16\Lambda^2 - 8i(\epsilon - 1)k\Lambda + 4\Delta\omega^2 - 4k(\epsilon + 1)\Delta\omega + 3\epsilon k^2 = 0, \quad (16)$$

where $\Lambda \equiv \lambda + D + \gamma$ for simplicity of notation. Solving for λ results in

$$\lambda_{+,-} = -\gamma - D \pm \frac{1}{4}[4k(\epsilon + 1)\Delta\omega - 4\Delta\omega^2 - (3\epsilon + (\epsilon - 1)^2)k^2]^{1/2} + i\left(\frac{(\epsilon - 1)k}{4} - \Omega\right). \quad (17)$$

Finally, imposing the condition that $\text{Re}(\lambda_+) = 0$ gives the BSI:

$$\frac{\Delta\omega}{\gamma + D} = \frac{1}{2}(\epsilon + 1)\frac{k}{\gamma + D} \pm \frac{1}{2}\sqrt{\epsilon\left(\frac{k}{\gamma + D}\right)^2 - 16}. \quad (18)$$

This result confirms, as already shown by Montbrío and Pazó [43], that without time delay, coherence is only possible for positive values of $\Delta\omega$, namely, when the E population is faster than the I population. Moreover, increasing the disparity between the E-I couplings causes the area of coherence to shrink.

The simulations were performed with $D = 0$, spanning the parameter space given by $(k/\gamma, \Delta\omega/\gamma)$, and they were repeated first with $\epsilon = 1$ [Fig. 4(a)], namely, with the same coupling strength in the two pathways, and then with $\epsilon = 10$ [Fig. 4(b)]; again, the precise parameters used are reported in the Supplemental Material [46]. In both cases the simulations were in good agreement with the analytical curves, reported as continuous lines. In this case, though, no chimera states were observed. Indeed, the two populations either both synchronized (in the dark green areas where $\langle Z^2 \rangle \approx 1$) or both did not (in light areas where $\langle Z^2 \rangle \approx 0$).

D. Existence of chimera states without time delay

In the end, we investigated the possibility that chimera states theoretically exist without time delay in the couplings, even if they have not been observed in the previous simulations. In this context, inspired by Abrams *et al.* [47], we considered a special class of density functions f^σ , that have the form of a Poisson kernel, such that they satisfy the so-

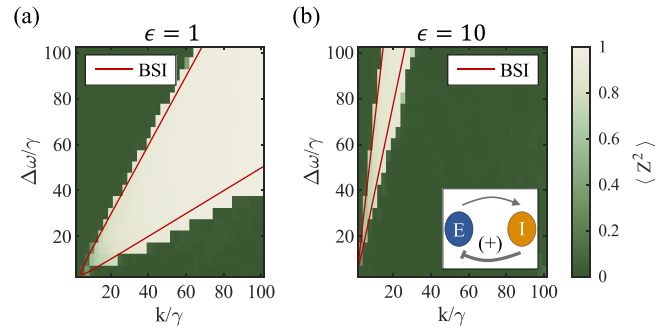


FIG. 4. Phase diagram obtained by simulating Eq. (1) and computing $\langle Z^2 \rangle$ with $\tau_{EI} = \tau_{IE} = 0$, Lorentzian distributed frequencies $D = 0$, and (a) same coupling strengths ($\epsilon = 1$) and (b) inhibitory coupling strengths greater than the excitatory one ($\epsilon = 10$). On the x and y axis there are the coupling strength k and the difference in the natural frequencies $\Delta\omega$, respectively, both in units of γ , the spread of the frequency distribution. The value of the order parameter is indicated by the color gradient. The parameters used are reported in the Supplemental Material [46]. The BSI are obtained from Eq. (18).

called OA ansatz [45]:

$$f^\sigma(\theta|\omega, t) = \frac{1}{2\pi} \left\{ 1 + \sum_{l=1}^{+\infty} [f_l^\sigma e^{i\theta}]^l \right\} + \text{c.c.} \quad (19)$$

These functions are characterized by having the same coefficients in all the Fourier harmonics, except that they are raised to the l th power for the l th harmonic, $f_{l>1}^\sigma(\omega, t) = [f_1^\sigma(\omega, t)]^l$. Substituting Eq. (19) in Eq. (7) with $D = 0$, and given that $Z_\sigma = f_1^{\sigma*}$, yields

$$f_1^{\dot{\sigma}} + i\left(\tilde{\omega}_\sigma f_1^\sigma - \frac{k_{\sigma\sigma'}}{4}(Z_{\sigma'}^* + f_1^{\sigma 2} Z_{\sigma'})\right) = 0. \quad (20)$$

Therefore, if this condition is fulfilled, such kernels satisfy the governing equations exactly. The OA ansatz is useful because it reduces the dynamics from infinite to finite dimensional.

It is convenient to introduce polar coordinates such as (ρ, ϕ) , defined by $f_1^\sigma = \rho_\sigma e^{-i\phi_\sigma}$. When $\rho_\sigma \rightarrow 1$, $f^\sigma(\theta|\omega, t) \rightarrow \delta(\theta - \phi_\sigma(t))$ centered at the phase $\phi_\sigma(t)$. Therefore, ϕ_σ can be considered the “center” of the density f_σ and ρ_σ measures how sharply peaked it is [47]. Hence, in terms of its real and imaginary part, Eq. (20) can be written as

$$\begin{cases} \dot{\rho}_\sigma - \frac{k_{\sigma\sigma'}}{4}(\rho_\sigma^2 - 1)\rho_{\sigma'} \sin(\phi_\sigma - \phi_{\sigma'}) = 0 \\ \dot{\phi}_\sigma - \tilde{\omega}_\sigma + \frac{k_{\sigma\sigma'}}{4}\frac{\rho_{\sigma'}}{\rho_\sigma}(\rho_\sigma^2 + 1)\cos(\phi_\sigma - \phi_{\sigma'}) = 0. \end{cases} \quad (21)$$

For simplicity, we considered the case with $|k_{EI}| = |k_{IE}| \equiv K$ and we defined $\psi \equiv \phi_E - \phi_I$. Therefore, Eq. (21), written explicitly in terms of E and I, reduces to

$$\begin{cases} \dot{\rho}_E + \frac{K}{4}(\rho_E^2 - 1)\rho_I \sin \psi = 0 \\ \dot{\rho}_I + \frac{K}{4}(\rho_I^2 - 1)\rho_E \sin \psi = 0 \\ \dot{\psi} + \Delta\omega - K - \frac{K}{4}\left(\frac{\rho_I}{\rho_E}(\rho_E^2 + 1) + \frac{\rho_E}{\rho_I}(\rho_I^2 + 1)\right)\cos \psi = 0, \end{cases} \quad (22)$$

where $\Delta\omega \equiv \omega_E - \omega_I$. We then considered the case in which the E population is perfectly synchronized ($\rho_E = 1$) and the other is not ($\rho_I \equiv r$), as shown in Fig. 5(a). This further

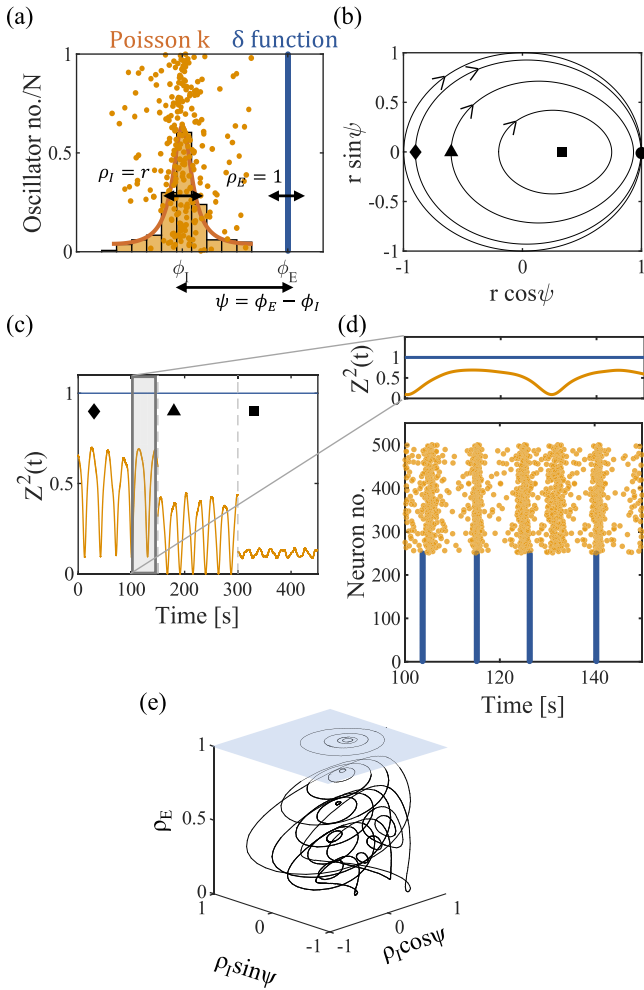


FIG. 5. (a) Distributions of E-I: I follows a Poisson kernel [Eq. (24)] centered at ϕ_I , with the spread dependent on $\rho_I = r$; E is a δ function centered at ϕ_E , with $\rho_E = 1$, as E is perfectly synchronized. The distance between the centers of the two distributions is $\psi = \phi_E - \phi_I$. (b) Trajectories in the (r, ψ) plane, in polar coordinates, obtained by simulating Eq. (23) with \blacksquare = chimera state and \bullet = perfectly synchronized case. (\blacklozenge , \blacktriangle , \blacksquare) correspond to the parameters used in (c). (c) Order parameter plotted as a function of time for the E, I populations with $N_{E,I} = 250$. (d) Raster plot of the E-I neurons at the breathing chimera state for $t \in [100-150]$ s]. (e) Simulation of the system in the space (ρ_E, ρ_I, ψ) following Eq. (22) represented here in cylindrical coordinates. Color scheme as in Fig. 1.

reduces the dynamics to a two-dimensional system:

$$\begin{cases} \dot{r} = \frac{K}{4}(1 - r^2) \sin \psi \\ \dot{\psi} = \Delta\omega - K + \frac{K}{4}(2r + \frac{r^2+1}{r}) \cos \psi. \end{cases} \quad (23)$$

In this way, the chimera states correspond to the fixed points, namely, $r(t) = \text{const}$ and $r \neq 1$ (since $r = 1$ corresponds to the perfectly synchronized case, that is always a trivial solution) and $\psi(t) = \text{const}$. Calculating the values of the fixed points yields

$$\begin{cases} \psi^* = m\pi, & m \in \mathbb{Z} \\ r_{1,2}^* = \frac{-2(\Delta\omega - K) \pm \sqrt{4(\Delta\omega - K)^2 - 3K^2}}{3(-1)^m K}. \end{cases}$$

As expected, considering the opposite case with $\rho_I = 1$ led to the same results [46], given that the system is symmetric.

When $\Delta\omega = 0$, that is, with identical oscillators, $(r^*, \psi^*) = (1/3, 2m\pi)$, independently of K , which means that chimera states could in principle exist even without time delay, because fixed points different from the perfectly synchronized case exist. To find out the stability of these fixed points, we linearized around them, by computing the Jacobian J . Given the system of differential equations of the form $\begin{cases} \dot{r} = f(r, \psi) \\ \dot{\psi} = g(r, \psi) \end{cases}$, the Jacobian J is defined as

$$J = \begin{bmatrix} \frac{df}{dr} & \frac{df}{d\psi} \\ \frac{dg}{dr} & \frac{dg}{d\psi} \end{bmatrix}_{|r^*, \psi^*} = \begin{bmatrix} 0 & 2/9K \\ -3/2K & 0 \end{bmatrix}.$$

As the trace is null and the determinant is $\Delta = K^2/3 > 0$, the linearization predicts a linear center. Moreover, since the system is invariant under the change of variables $t \rightarrow -t$, $\psi \rightarrow -\psi$, the fixed point is also a nonlinear center [48]. Hence, a family of periodic orbits surrounds the chimera, which can be defined as neutrally stable “breathing chimeras” [47].

Both the presence and the nature of the chimeras were fully confirmed by the numerical simulation, which was performed in the case of $\Delta\omega = 0$, $K = 0.5$ [Fig. 5(b)]. At the same time, the numerical analysis also showed the presence of the perfectly synchronized state, in which both populations synchronize to the same phase, that corresponds to $r = 1$, $\psi = 0$, which is a saddle on an invariant circle.

Consequently, we aimed to test whether this description—in the continuum limit—would agree with the simulations performed with finite N . For this purpose, it could be exploited that the distribution function f , in the OA ansatz, has the shape of a Poisson kernel, such as

$$P_r(\theta) = \sum_{n=-\infty}^{\infty} r^{|n|} e^{in\theta} = \frac{1 - r^2}{1 - 2r \cos \theta + r^2},$$

which, in this case, becomes

$$f^\sigma(\theta) = \frac{1 - \rho_\sigma^2}{1 - 2\rho_\sigma \cos(\theta - \phi_\sigma) + \rho_\sigma^2}. \quad (24)$$

Hence, the simulations were performed with the I population initially distributed according to f^I for some chosen (ρ_I, ϕ_I) , whereas the E population was perfectly synchronized ($\rho_E = 1$), as shown in Fig. 5(a). We obtained, as expected, that while $Z_E(t) = \text{const} = 1$, $Z_I(t)$ oscillates over time, corresponding to the periodic orbit in the (r, ψ) plane [Fig. 5(c)]. To explain this concept further, in Fig. 5(d) we report the raster plot of the two populations, with the corresponding order parameter $Z^2(t)$ superimposed. Every dot represents the moment each neuron is firing, i.e., when the phase of each neuron completes one full rotation: therefore, the blue dots are perfectly aligned, since the E neurons fire in synchrony, whereas the I neurons oscillate between moments of higher and lower synchrony, corresponding to peaks and troughs of $Z_I^2(t)$. As expected, the situation was totally symmetric when starting from $\rho_I = 1$ [46].

Moreover, the whole system was simulated in the coordinates (ρ_E, ρ_I, ψ) following Eq. (22), shown in the figure as cylindrical coordinates [Fig. 5(e)]. This revealed that the

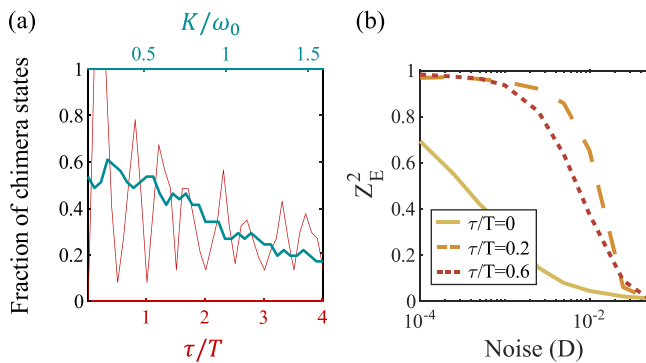


FIG. 6. (a) Fraction of chimera states registered in Fig. 2(b) calculated per coupling strength, which corresponds to the light-blue curve, and per time delay, shown by the red curve. (b) Noise robustness comparison of the chimera states between delayed (dashed and dotted lines) and instantaneous couplings (solid line), obtained computing the order parameter of the synchronized population (Z_E^2) for increasing values of D .

manifold $\rho_E = 1$, in which the system was restricted in Fig. 5(b), is not attracting. In other words, the system should be “prepared” in this initial condition in order to observe it, which is coherent with our previous simulations.

E. Robustness of chimera states

First, we considered what are the most likely configurations in the parameter space to display the coexistence of coherence and incoherence, by calculating the fraction of chimera states per time delay and per coupling strength observed in Fig. 2(b). This showed that a small (nonzero) time delay, for any value of K , would result in a chimera state;

moreover, increasing either τ or K progressively leads to the loss of these states [Fig. 6(a)].

Secondly, the robustness of the chimeras towards external perturbations was also evaluated, simulating the system with and without time delay in the cross-couplings with increasing values of D , which quantifies the level of stochastic noise [Fig. 6(b)]. As expected, it appears that the system without time delay is not very robust, as the manifold that corresponds to the chimera is not attracting, whereas time delays help to stabilize the system until higher values of noise.

III. CONCLUSIONS

In this paper we have sought to shed light on the properties of type I oscillators, that are traditionally believed to have low propensity to synchronize. To do so, we modeled a feedback loop between an excitatory and an inhibitory population, which is a known neural mechanism that produces oscillations. The analysis revealed that including time delayed couplings highly enriches the dynamics of the network. In case of stronger external than internal couplings, we observed the emergence of stable periodic chimera states, that are robust to noise. On the other hand, with negligible internal connections and instantaneous external ones, a family of “breathing chimeras” was observed, that is neutrally stable and less robust to external perturbations.

Future work may investigate whether the chimera states are preserved also in more realistic scenarios, such as when considering local couplings in a spatially distributed system. Moreover, this paper offers a theoretical framework to investigate more biologically inspired neuronal models and testable predictions that can be potentially verified experimentally.

ACKNOWLEDGMENT

The work is supported by the Independent Research Fund Denmark under grant 9040-00116B.

- [1] A. T. Winfree, *The Geometry of Biological Time*, 2nd ed., Interdisciplinary Applied Mathematics Vol. 12 (Springer, New York, 2001), p. 779.
- [2] N. Axmacher, F. Mormann, G. Fernández, C. E. Elger, and J. Fell, Memory formation by neuronal synchronization, *Brain Res. Rev.* **52**, 170 (2006).
- [3] C. Gaillard and S. Ben Hamed, The neural bases of spatial attention and perceptual rhythms, *Eur. J. Neurosci.*, **1** (2020).
- [4] C. M. Sameiro-Barbosa and E. Geiser, Sensory entrainment mechanisms in auditory perception: Neural synchronization cortico-striatal activation, *Front. Neurosci.* **10**, 361 (2016).
- [5] K. Lehnertz, S. Bialonski, M.-T. Horstmann, D. Krug, A. Rothkegel, M. Staniek, and T. Wagner, Synchronization phenomena in human epileptic brain networks, *J. Neurosci. Methods* **183**, 42 (2009).
- [6] E. Stein and I. Bar-Gad, Beta oscillations in the cortico-basal ganglia loop during parkinsonism, *Exp. Neurol.* **245**, 52 (2013).
- [7] P. J. Uhlhaas and W. Singer, Neural synchrony in brain disorders: Relevance for cognitive dysfunctions and pathophysiology, *Neuron* **52**, 155 (2006).
- [8] Y. Kuramoto and D. Battogtokh, Coexistence of coherence and incoherence in nonlocally coupled phase oscillators, *Nonlinear Phenom. Complex Syst.* **5**, 380 (2002).
- [9] D. M. Abrams and S. H. Strogatz, Chimera States for Coupled Oscillators, *Phys. Rev. Lett.* **93**, 174102 (2004).
- [10] J. Hizanidis, V. G. Kanas, A. Bezerianos, and T. Bountis, Chimera states in networks of nonlocally coupled Hindmarsh-Rose neuron models, *Int. J. Bifurcation Chaos* **24**, 1450030 (2014).
- [11] A. Calim, P. Hövel, M. Ozer, and M. Uzuntarla, Chimera states in networks of type-I Morris-Lecar neurons, *Phys. Rev. E* **98**, 062217 (2018).
- [12] S. Olmi, A. Politi, and A. Torcini, Collective chaos in pulse-coupled neural networks, *Europhys. Lett.* **92**, 60007 (2011).
- [13] I. Omelchenko, A. Provata, J. Hizanidis, E. Schöll, and P. Hövel, Robustness of chimera states for coupled Fitzhugh-Nagumo oscillators, *Phys. Rev. E* **91**, 022917 (2015).
- [14] T. A. Glaze, S. Lewis, and S. Bahar, Chimera states in a Hodgkin-Huxley model of thermally sensitive neurons, *Chaos* **26**, 083119 (2016).

- [15] I. Omelchenko, Y. Maistrenko, P. Hövel, and E. Schöll, Loss of Coherence in Dynamical Networks: Spatial Chaos and Chimera States, *Phys. Rev. Lett.* **106**, 234102 (2011).
- [16] A. Bukh, E. Rybalova, N. Semenova, G. Strelkova, and V. Anishchenko, New type of chimera and mutual synchronization of spatiotemporal structures in two coupled ensembles of nonlocally interacting chaotic maps, *Chaos* **27**, 111102 (2017).
- [17] J. González-Avella, M. Cosenza, and M. San Miguel, Localized coherence in two interacting populations of social agents, *Physica A* **399**, 24 (2014).
- [18] J. D. Hart, K. Bansal, T. E. Murphy, and R. Roy, Experimental observation of chimera and cluster states in a minimal globally coupled network, *Chaos* **26**, 094801 (2016).
- [19] E. A. Martens, S. Thutupalli, A. Fourrière, and O. Hallatschek, Chimera states in mechanical oscillator networks, *Proc. Natl. Acad. Sci. USA* **110**, 10563 (2013).
- [20] L. Larger, B. Penkovsky, and Y. Maistrenko, Laser chimeras as a paradigm for multistable patterns in complex systems, *Nat. Commun.* **6**, 7752 (2015).
- [21] M. J. Panaggio and D. M. Abrams, Chimera states: Coexistence of coherence and incoherence in networks of coupled oscillators, *Nonlinearity* **28**, R67 (2015).
- [22] O. E. Omel'chenko, The mathematics behind chimera states, *Nonlinearity* **31**, R121 (2018).
- [23] S. Majhi, B. K. Bera, D. Ghosh, and M. Perc, Chimera states in neuronal networks: A review, *Phys. Life Rev.* **28**, 100 (2019).
- [24] E. M. Izhikevich, *Dynamical Systems in Neuroscience: The Geometry of Excitability and Bursting* (MIT, Cambridge, MA, 2006).
- [25] G. H. Paissan and D. H. Zanette, Synchronization of phase oscillators with heterogeneous coupling: A solvable case, *Physica D* **237**, 818 (2008).
- [26] C. Xu, S. Boccaletti, Z. Zheng, and S. Guan, Universal phase transitions to synchronization in Kuramoto-like models with heterogeneous coupling, *New J. Phys.* **21**, 113018 (2019).
- [27] H. Wu and M. Dhamala, Dynamics of Kuramoto oscillators with time-delayed positive and negative couplings, *Phys. Rev. E* **98**, 032221 (2018).
- [28] P. F. C. Tilles, F. F. Ferreira, and H. A. Cerdeira, Multistable behavior above synchronization in a locally coupled Kuramoto model, *Phys. Rev. E* **83**, 066206 (2011).
- [29] M. K. Stephen Yeung and S. H. Strogatz, Time Delay in the Kuramoto Model of Coupled Oscillators, *Phys. Rev. Lett.* **82**, 648 (1999).
- [30] E. A. Martens, E. Barreto, S. H. Strogatz, E. Ott, P. So, and T. M. Antonsen, Exact results for the Kuramoto model with a bimodal frequency distribution, *Phys. Rev. E* **79**, 026204 (2009).
- [31] Y. Terada and T. Aoyagi, Dynamics of two populations of phase oscillators with different frequency distributions, *Phys. Rev. E* **94**, 012213 (2016).
- [32] M. J. Panaggio, D. M. Abrams, P. Ashwin, and C. R. Laing, Chimera states in networks of phase oscillators: The case of two small populations, *Phys. Rev. E* **93**, 012218 (2016).
- [33] C. Tian, H. Bi, X. Zhang, S. Guan, and Z. Liu, Asymmetric couplings enhance the transition from chimera state to synchronization, *Phys. Rev. E* **96**, 052209 (2017).
- [34] J. H. Sheeba, V. K. Chandrasekar, and M. Lakshmanan, Globally clustered chimera states in delay-coupled populations, *Phys. Rev. E* **79**, 055203(R) (2009).
- [35] J. H. Sheeba, V. K. Chandrasekar, and M. Lakshmanan, Chimera and globally clustered chimera: Impact of time delay, *Phys. Rev. E* **81**, 046203 (2010).
- [36] J. Sawicki, I. Omelchenko, A. Zakharova, and E. Schöll, Delay controls chimera relay synchronization in multiplex networks, *Phys. Rev. E* **98**, 062224 (2018).
- [37] S. Mofakham, C. G. Fink, V. Booth, and M. R. Zochowski, Interplay between excitability type and distributions of neuronal connectivity determines neuronal network synchronization, *Phys. Rev. E* **94**, 042427 (2016).
- [38] A. Ziaemehr, M. Zarei, and A. Sheshbolouki, Emergence of global synchronization in directed excitatory networks of type I neurons, *Sci. Rep.* **10**, 3306 (2020).
- [39] C. R. Laing, The dynamics of networks of identical theta neurons, *J. Math. Neurosci.* **8**, 4 (2018).
- [40] A. Keane, T. Dahms, J. Lehnert, S. A. Suryanarayana, P. Hövel, and E. Schöll, Synchronisation in networks of delay-coupled type-I excitable systems, *Eur. Phys. J. B* **85**, 407 (2012).
- [41] J. Lehnert, T. Dahms, P. Hövel, and E. Schöll, Loss of synchronization in complex neuronal networks with delay, *EPL (Europhysics Letters)* **96**, 60013 (2011).
- [42] J. Ladenbauer, J. Lehnert, H. Rankoohi, T. Dahms, E. Schöll, and K. Obermayer, Adaptation controls synchrony and cluster states of coupled threshold-model neurons, *Phys. Rev. E* **88**, 042713 (2013).
- [43] E. Montbrió and D. Pazó, Kuramoto Model for Excitation-Inhibition-Based Oscillations, *Phys. Rev. Lett.* **120**, 244101 (2018).
- [44] A. Vüllings, J. Hizanidis, I. Omelchenko, and P. Hövel, Clustered chimera states in systems of type-I excitability, *New J. Phys.* **16**, 123039 (2014).
- [45] E. Ott and T. M. Antonsen, Low dimensional behavior of large systems of globally coupled oscillators, *Chaos* **18**, 037113 (2008).
- [46] See Supplemental Material at <http://link.aps.org/supplemental/10.1103/PhysRevResearch.3.033041> for additional steps in the linear stability analysis, additional plots, and a table with the parameters used in the simulations.
- [47] D. M. Abrams, R. Mirollo, S. H. Strogatz, and D. A. Wiley, Solvable Model for Chimera States of Coupled Oscillators, *Phys. Rev. Lett.* **101**, 084103 (2008).
- [48] S. Strogatz, *Nonlinear Dynamics and Chaos: With Applications to Physics, Biology, Chemistry, and Engineering* (Westview, Boulder, CO, 2015).

Supplementary Material for “Emergence of Chimera States in a Neuronal Model of Delayed Oscillators”

Alessandra Lucchetti, Mogens H. Jensen, Mathias L. Heltberg

June 8, 2021

Derivation of Eq. (9)

Inserting Eq. (8) into Eq. (5) in the main text, while leaving only terms up to order η and setting the correspondent modes equal, yields

$$\begin{aligned} \delta \dot{f}_l^\sigma = & -(i\tilde{\omega}_\sigma + l^2 D)\delta f_l^\sigma + \\ & + il \left[\frac{k_{\sigma\sigma'}}{4} \left(\delta f_{l-1}^\sigma Z_{\sigma'}^*(t - \tau_{\sigma\sigma'}) + f_{l-1}^\sigma \langle \delta f_1^{\sigma'} \rangle_{t-\tau_{\sigma\sigma'}} + \delta f_{l+1}^\sigma Z_{\sigma'}(t - \tau_{\sigma\sigma'}) + f_{l+1}^\sigma \langle \delta f_{-1}^{\sigma'} \rangle_{t-\tau_{\sigma\sigma'}} \right) + \right. \\ & \left. + \frac{k_{\sigma\sigma}}{4} \left(\delta f_{l-1}^\sigma Z_\sigma^*(t - \tau_{\sigma\sigma}) + f_{l-1}^\sigma \langle \delta f_1^\sigma \rangle_{t-\tau_{\sigma\sigma}} + \delta f_{l+1}^\sigma Z_\sigma(t - \tau_{\sigma\sigma}) + f_{l+1}^\sigma \langle \delta f_{-1}^\sigma \rangle_{t-\tau_{\sigma\sigma}} \right) \right]. \end{aligned}$$

In the incoherent state $Z = 0$, all the modes save the 0-th disappear ($f_{l \neq 0}^\sigma = 0$) and $f_0^\sigma = 1$. Therefore, the equations reduce to

$$\begin{cases} \delta \dot{f}_{\pm 1}^\sigma = -(\pm i\tilde{\omega}_\sigma + D)\delta f_{\pm 1}^\sigma \pm i \left[\frac{k_{\sigma\sigma'}}{4} \langle \delta f_{\pm 1}^{\sigma'} \rangle_{t-\tau_{\sigma\sigma'}} + \frac{k_{\sigma\sigma}}{4} \langle \delta f_{\pm 1}^\sigma \rangle_{t-\tau_{\sigma\sigma}} \right] & \text{when } l = \pm 1 \\ \delta \dot{f}_l^\sigma = -(i\tilde{\omega}_\sigma + l^2 D)\delta f_l^\sigma & \text{when } |l| \geq 2. \end{cases} \quad (\text{S.1})$$

The only potential unstable modes are $l = \pm 1$, but we restrict our analysis to $l = +1$ only, since $l = -1$ is just the complex conjugate. Therefore, considering the case $l = 1$ directly leads to Eq. (9) in the main text.

Derivation of Eq. (10) and Eq. (14)

First, we substituted the ansatz $\delta f_1^\sigma(\omega, t) = b_\sigma(\omega)e^{\lambda t}$ into Eq. (9). Then, we multiplied by $g(\omega)$ and finally integrated in $d\omega$, which yields

$$\frac{4\langle b_\sigma(\omega) \rangle_\sigma}{k_{\sigma\sigma'} \langle b_{\sigma'}(\omega) \rangle e^{-\lambda\tau_{\sigma\sigma'}} + k_{\sigma\sigma} \langle b_\sigma(\omega) \rangle e^{-\lambda\tau_{\sigma\sigma}}} = i \int_{-\infty}^{+\infty} \frac{g_\sigma(\omega)}{\lambda + i\tilde{\omega}_\sigma} d\omega,$$

If we consider that the frequency distribution is a delta function for both populations, $g(\omega) = \delta(\omega - \omega_0)$ centered around the same frequency ($\omega_E = \omega_I = \omega_0$), the integral can be trivially solved to obtain an homogeneous system of two equations

$$\begin{bmatrix} 4(\lambda + i\tilde{\omega}_E) - ik_{EE}e^{-\lambda\tau_{EE}} & -ik_{EI}e^{-\lambda\tau_{EI}} \\ -ik_{IE}e^{-\lambda\tau_{IE}} & 4(\lambda + i\tilde{\omega}_I) - ik_{II}e^{-\lambda\tau_{II}} \end{bmatrix} \times \begin{bmatrix} \langle b_E \rangle \\ \langle b_I \rangle \end{bmatrix} = \begin{bmatrix} 0 \\ 0 \end{bmatrix}.$$

The only non trivial solution corresponds to having a null determinant, which, given the conditions of section A, leads directly to Eq. (10) and given the conditions of section B, to Eq. (14).

Time delay in the excitatory connection

Simulating the system with time delay in the external excitatory connection confirms that the dependence is only on the sum of the delays in the external excitatory and inhibitory pathways (Fig. S1).

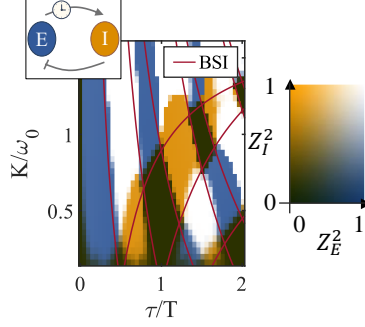


Figure S1: Phase diagram obtained by simulating Eq. (1) in the main text and computing $Z_{E,I}^2$ with $\tau_{EI} = 0$, $\tau_{IE} > 0$.

Parameters

	Fig. (2)			Fig. (3)		Fig. (4)	
	(a)	(b)	(c)	(a)	(b)	(a)	(b)
$N_{E,I}$	100	100	100	100	100	100	100
ω_0 [rad/s]	$2\pi \cdot 0.1$	$2\pi \cdot 0.1$	$2\pi \cdot 0.1$	$2\pi \cdot 0.1$	$2\pi \cdot 0.1$	$2\pi \cdot 0.1$	/
τ_{EI} [s]	[0-20]	[0-20]	[I: 1, II: 3, III: 5, IV: 6]	[0-20]	[0-20]	0	0
τ_{IE} [s]	0	[0-20]	[I: 1, II: 3, III: 5, IV: 6]	[0-20]	[0-20]	0	0
τ_{EE} [s]	/	/	/	[0-20]	0	/	/
τ_{II} [s]	/	/	/	[0-20]	0	/	/
$ k_{EI} $ [rad/s]	[0.1-1]	[0.1-1]	0.5	[0.1-1]	[0.1-1]	[0.1-1]	[0.25-10]
$ k_{IE} $ [rad/s]	[0.1-1]	[0.1-1]	0.5	[0.1-1]	[0.1-1]	[0.1-1]	[0.025-1]
$ k_{EE} $ [rad/s]	0	0	0	$[10^{-2}-1] \cdot k_{EI} $	[0.1-1]	0	0
$ k_{II} $ [rad/s]	0	0	0	$[10^{-2}-1] \cdot k_{EI} $	[0.1-1]	0	0
γ [rad/s]	/	/	/	/	/	0.01	0.01
$\Delta\omega$ [rad/s]	/	/	/	/	/	[0.05-1]	[0.05-1]
Tot time [s]	600	600	600	600	600	600	600

Table 1: Parameters used in the simulations of Fig. (2,3,4)

Derivation of Eq. (16)

Inserting the ansatz $\delta f_1^\sigma(\omega, t) = b_\sigma(\omega)e^{\lambda t}$ into (S.1), with $l = 1$, yields

$$\frac{4b_\sigma(\omega)}{k_{\sigma\sigma'}\langle b_{\sigma'}(\omega) \rangle_{\sigma'}} = i \frac{1}{\lambda + D + i\bar{\omega}_\sigma}.$$

Multiplying both sides by $g_\sigma(\omega)$ and integrating results in

$$\frac{4\langle b_\sigma(\omega) \rangle_\sigma}{k_{\sigma\sigma'}\langle b_{\sigma'}(\omega) \rangle_{\sigma'}} = i \int_{-\infty}^{+\infty} \frac{1}{\lambda + D + i\bar{\omega}_\sigma} g_\sigma(\omega) d\omega. \quad (\text{S.2})$$

The integral on the RHS can be calculated exactly if we consider Lorentzian distributions for the frequencies, $g_\sigma(\omega) = \frac{\gamma_\sigma/\pi}{(\omega - \bar{\omega}_\sigma)^2 + \gamma_\sigma^2}$. Thus the integral we aim to calculate is

$$\int_{-\infty}^{+\infty} \frac{1}{\lambda + D + i(\omega_\sigma + \frac{k_{\sigma\sigma'}}{2})} \frac{\gamma_\sigma/\pi}{(\omega - \bar{\omega}_\sigma)^2 + \gamma_\sigma^2} d\omega.$$

Substituting $\omega \in \mathbb{R}$ with $z \in \mathbb{C}$, the integral path can be closed with a semicircle with radius $R \rightarrow \infty$, in the half-plane with negative imaginary part. The only singularity that lies within the path is $z_1 = \bar{\omega}_\sigma - i\gamma$, so that, for the Residue Theorem, (S.2) becomes

$$\frac{4\langle b_\sigma(\omega) \rangle_\sigma}{k_{\sigma\sigma'}\langle b_{\sigma'}(\omega) \rangle_{\sigma'}} = \frac{1}{\bar{\omega}_\sigma + \frac{k_{\sigma\sigma'}}{2} - i(\lambda + D + \gamma_\sigma)}. \quad (\text{S.3})$$

Inserting (S.3) in (S.2) yields a system of two homogeneous equations in $\langle b_E \rangle_E$ and $\langle b_I \rangle_I$ as unknowns, that can be written explicitly for the two populations as

$$\begin{cases} \frac{4\langle b_E \rangle_E}{k_{EI}\langle b_I \rangle_I} = \frac{1}{\bar{\omega}_E + \frac{k_{EI}}{2} - i(\lambda + D + \gamma_E)} \\ \frac{4\langle b_I \rangle_I}{k_{IE}\langle b_E \rangle_E} = \frac{1}{\bar{\omega}_I + \frac{k_{IE}}{2} - i(\lambda + D + \gamma_I)} \end{cases} \quad (\text{S.4})$$

and in matrix form

$$\begin{bmatrix} 4\bar{\omega}_E + 2k_{EI} - 4i\Lambda_E & -k_{EI} \\ -k_{IE} & 4\bar{\omega}_I + 2k_{IE} - 4i\Lambda_I \end{bmatrix} \times \begin{bmatrix} \langle b_E \rangle_E \\ \langle b_I \rangle_I \end{bmatrix} = \begin{bmatrix} 0 \\ 0 \end{bmatrix}$$

where we have defined $\Lambda_E = \lambda + D + \gamma_E$ and $\Lambda_I = \lambda + D + \gamma_I$ to simplify the notation. We set $\gamma_E = \gamma_I = \gamma$ and $\bar{\omega}_E = -\bar{\omega}_I = \bar{\omega}$, so that $\Delta\omega = 2\bar{\omega}$. Moreover, we defined $|k_{EI}| = \epsilon|k_{IE}| = \epsilon k$. The only possibility to have a solution different from the trivial one is that the determinant of the matrix of the coefficients is zero, that leads directly to Eq. (16) in the main text.

Chimera state with no time delay: Symmetric case when $\rho_I = 1$

A simulation was performed with the E population (blue) initially distributed according to f^E for some chosen (ρ_E, ϕ_E) , whereas the I population (orange) was perfectly synchronized ($\rho_I = 1$), as shown in Fig. S2. We obtained, as expected, that while $Z_I(t) = \text{const} = 1$, $Z_E(t)$ oscillates over time, corresponding to the periodic orbit in the (ρ, ψ) plane.

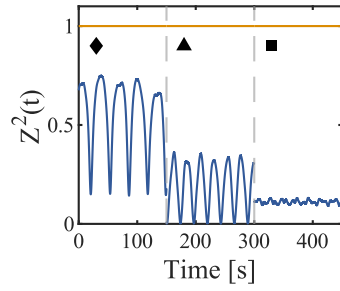


Figure S2: Order parameter plotted as a function of time for the E (blue), I (orange) populations with $N_{E,I} = 250$, with I initially synchronized and E distributed as a Poisson kernel. The symbols (\blacklozenge , \blacktriangle , \blacksquare) correspond to the three orbits shown in Fig 5b in the main text.

Enhanced DNA repair through droplet formation and p53 oscillations

3.1 Introduction and Objectives

Genes are DNA segments that contain the instructions for the production of a functional product, usually a protein. However, not all genes are active simultaneously. The DNA can be pictured as a complex symphony, with each gene holding a musical note waiting to be played. In this analogy, the molecular maestros, who dictate when and how each note is played, are the Transcription Factors (TFs), which ultimately ensure the harmonious melody of life itself. This process is called *gene regulation*. Indeed, the TFs (which are proteins themselves), by binding to specific DNA sequences, define which of the "instructions" present in the DNA will be translated into the corresponding products, thus acting as switches that turn the expression of specific genes on or off. This allows, among others, cells to differentiate into specific cell types (so that blood cells are substantially different from neurons, despite carrying the same DNA), and to respond to environmental signals (for example, activating genes related to melanin production after exposure to sunlight, resulting in a darker skin tone, which protects from UV radiation) (Alberts, 2017).

A myriad of different TFs coexist in the cell, therefore their concentration needs to be tightly regulated as well, switching from low to high levels to ensure that genes are activated or deactivated as needed for the cell's proper functioning. However, TF concentration has been shown to portray a wide range of dynamical patterns which goes beyond being either constant low or high, such as single-pulsed or oscillatory (Purvis and Lahav, 2013). This has been observed, among others, for the nuclear concentration of TFs such as Nuclear Factor kappa B (Nf- κ B), involved in the immune response (Hoffmann *et al.*, 2002; Nelson *et al.*, 2004; Zambrano *et al.*, 2016), Hes1, involved in cell fate determination and differentiation during development (Kay *et al.*, 2017; Kobayashi *et al.*, 2009; Jensen *et al.*, 2003), or p53 (Lahav *et al.*, 2004; Purvis *et al.*, 2012), that is crucial in DNA repair. As of today, the role of these different dynamics remains largely elusive (Kruse and Jülicher, 2005; Levine *et al.*, 2013).

Among these TFs, p53, also called *guardian of the genome* (Lane, 1992), famously serves as a master tumour suppressor, by ensuring that cells with damaged DNA are either repaired or eliminated (Riley *et al.*, 2008; Murray-Zmijewski *et al.*, 2008; Aylon and Oren, 2007), thereby maintaining the integrity of the genome and preventing the spread of mutations which would eventually give rise to malignant tumours. For decades, researchers have worked to understand its biological functions, in order to identify new cancer treatment strategies. Usually held at low concentration, in the presence of multiple DNA breaks, it shows sustained oscillations with a precise periodicity of 5.5 h (Lahav *et al.*, 2004), whose role is still highly debated.

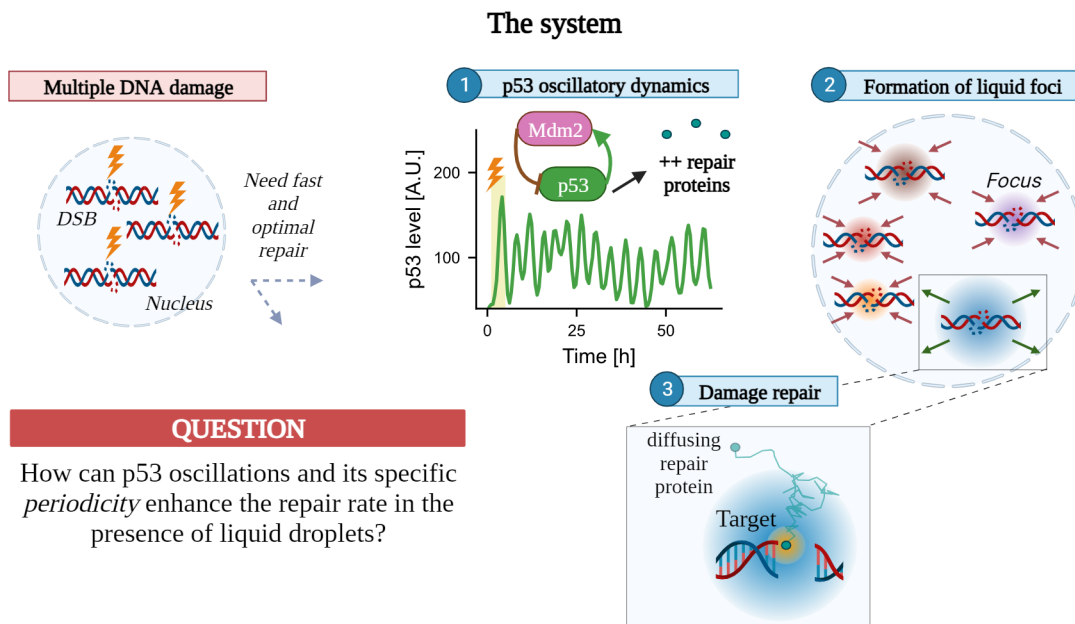


Figure 3.1: The system which consists of three main building blocks: p53 oscillatory dynamics, foci dynamics and the process of DNA repair. Adapted from Heltberg *et al.* (2022).

While the concentration of p53 portrays time-variation, the concentration of proteins that are responsible for DNA repair (recruited, among others, by p53), portrays substantial spatial-variations in the nucleus. Indeed, these proteins have been shown to segregate, around the sites of DNA ruptures, into membraneless compartments (known as foci) (Lisby *et al.*, 2004), which resemble liquid droplets, as they seem to arise as a result of phase-separation (the same mechanism that leads to the formation of droplets of oil in water). These micro-environments have been observed experimentally to form and dissolve at a timescale of hours (Pessina *et al.*, 2019), which is approximately the same as p53 periodicity. Despite that, a precise link between p53 and foci is still unknown.

The creation of these compartments results in an inhomogeneous environment within the nucleus, in which proteins must navigate in order to locate their target for repair. If we assume that the repair processes are diffusion-limited, meaning that the repair speed is primarily determined by how fast the proteins can move within the nucleus, and consequently, how long it takes to find their target, we can envision that the presence of foci will have a significant impact on how fast and efficiently DNA damage can be fixed.

The aim of this work, which is summarized in Figure 3.1, is to answer the questions:

"What is the evolutionary advantage of having oscillations in p53 dynamics, in particular on a timescale of hours? Is there a link between p53 oscillatory dynamics and the formation of repair foci? Could the combined action of p53 oscillations (in time) and the distribution of repair material through the foci (in space) enhance the repair rate?"

To answer these questions, we build a theoretical model in which we describe the foci as arising from liquid-liquid phase separation (Heltberg, Miné-Hattab, *et al.*, 2021), whose formation and dissolution is dictated by the p53 oscillatory concentration. In particular, our main goals are to:

- Investigate how the repair rates of multiple damaged sites are affected by the presence of foci in the environment;
- Establish a connection between the p53 protein dynamics and the observed phase separation that occurs in the nucleus;
- Analyse the role of p53 amplitude and frequency in this process;

Overall, we aim to unravel a natural reason for p53 oscillatory dynamics and understand the interplay between the temporal regulation of p53 and the spatial organization of repair foci.

3.2 Background theory

3.2.1 Transcription Factors (TFs) role in biology: p53 as "guardian of the genome"

The way genetic information flows within living organisms follows the so-called *central dogma of biology* (Crick, 1958), which consists of three essential steps: DNA replication, transcription, and translation (Figure 3.2A). During DNA replication, the DNA molecule is copied to ensure each new cell receives a complete set of genetic information. Transcription is the process in which genetic information encoded in DNA is transcribed into a complementary RNA molecule called mRNA. This mRNA carries the genetic code to the site of protein synthesis. Translation is the final step, where the mRNA code is read by ribosomes, and proteins are synthesized using transfer RNA (tRNA). This genetic information transfer is influenced by a wide array of regulatory factors. As introduced in the previous section, one crucial group of regulatory proteins is TFs, which bind to specific DNA sequences near genes and modulate their expression. By acting as switches, TFs can activate or repress gene transcription, enabling precise control over gene expression and contribute to the diversity and functionality of cells and organisms (Latchman, 1997). In particular, they play a pivotal role in determining which genes are turned on or off in response to various signals and environmental cues or stresses, such as chemical agents or radiation which cause severe DNA damage (Figure 3.2B).

Among all the TFs, p53 is perhaps one of the most widely studied: during the first thirty years after its discovery, almost 50 thousands articles have been published on p53 (Lane and Levine, 2010). Its encoding gene, TP53, is indeed found to be mutated in around 50% of human cancers (Vogelstein *et al.*, 2000). Under normal conditions, p53 is kept at low concentrations within cells, as it is negatively regulated by interaction with the oncoprotein MDM2 (Haupt *et al.*, 1997; Honda *et al.*, 1997; Kubbutat *et al.*, 1997). MDM2 and p53 engage in a negative-feedback loop, where p53 triggers the production of MDM2, which subsequently facilitates the breakdown of p53 (Ma *et al.*, 2005; Nag *et al.*, 2013). However, when multiple DNA damages (defined as Double-Strand Breaks (DSBs)) occur, as a result of radiation or other external stresses, MDM2 is suppressed, releasing the "break" on p53, whose concentration rises (Meek, 2004)(Figure 3.2C). Depending on the severity of the DNA damage, p53 portrays different dynamics. In case of severe damage, p53 transitions into a constant high level, which promotes senescence (growth arrest and cessation of cell division) or apoptosis (programmed cell-death)(YeARGIN and Haas, 1995). In this way, the organism prevents the spread of cells with potentially harmful genetic alterations. On the other hand, if the damage is moderate, p53

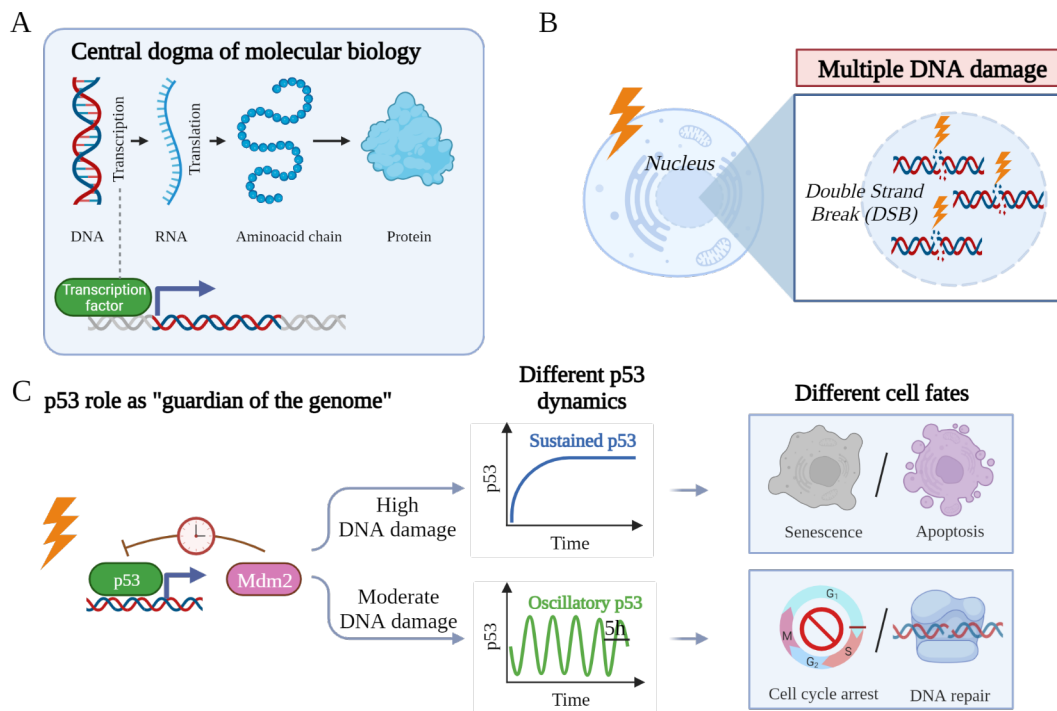


Figure 3.2: (A) Central dogma of biology. (B) Radiation may cause DNA Double-Strand Breaks (DSBs). (C) p53 as "guardian of the genome": it activates in response to DNA damage and portrays different dynamics (sustained vs oscillatory) which result in different cell fates (senescence/apoptosis vs cell cycle arrest/DNA repair) depending on the amount of DNA damage.

levels oscillate with a specific periodicity of 5.5 h, and the number of pulses is positively correlated to the amount of DNA damage (Lahav *et al.*, 2004). This dynamics is linked to cell cycle arrest and transcription of genes related to DNA repair: by halting the cell cycle, p53 provides an opportunity for DNA repair mechanisms to fix damaged DNA before replication occurs. Despite the molecular mechanism which gives rise to the oscillations being well-known (the negative feedback loop with MDM2), the evolutionary advantage of this type of dynamics is still highly debated.

In order to model the p53-Mdm2 network in the simplest way possible, while still capturing its essential dynamics, one can define a set of Ordinary Differential Equations (ODEs), such as (Mengel *et al.*, 2010):

$$\begin{cases} \frac{dp}{dt} = k_1 - k_2 M \frac{p}{k_3 + p} \\ \frac{dm}{dt} = k_4 p^2 - k_5 m, \\ \frac{dM}{dt} = k_6 m - k_7 M, \end{cases} \quad (3.1)$$

where p, m and M are the concentration of p53, of Mdm2-mRNA and Mdm2, respectively. The model assumes that p53 is produced at a constant rate k_1 and is degraded by binding to Mdm2 (with constants k_2, k_3). The Mdm2-mRNA is produced proportionally to a constant k_4 times the p53 level squared, given that p53 acts as a dimer, and is subjected to exponential decay (k_5). Mdm2 follows linearly the concentration of Mdm2-mRNA with constant k_6 and is also subjected to exponential decay (k_7). Depending on the parameters, this model shows all the possible dynamics portrayed by p53 (constant low levels, oscillations, and high levels).

3.2.2 Foci formation and physics of phase separation

Another central aspect that has been observed in DNA damage repair is the formation of so-called ionizing radiation-induced foci (IRIF) (Lisby *et al.*, 2001), which will be referred to simply as foci in the following. As mentioned in the introduction, these membraneless structures consist of micro-environments rich of repair proteins which arise around the site of damage, and are essentially biomolecular condensates (Figure 3.3A), as they are believed to stem from liquid-liquid phase separation (Heltberg, Miné-Hattab, *et al.*, 2021). Their role is to concentrate repair factors and DNA repair machinery at the site of damage, providing a confined and concentrated environment that facilitates efficient and coordinated repair processes. The formation of foci not only promotes the recruitment and assembly of repair factors, but also enables the spatial organization and segregation of repair activities within the nucleus, preventing the spread of DNA damage to other genomic regions.

The mathematical framework which describes the process of phase separation was developed by Lifshitz and Slyozov (1961). Intuitively, when there is a solute (proteins) that is dissolved in a solvent (water) such that the two species have more favourable interactions with the same than with the other species, there is a critical concentration of proteins above which it is more energetically favourable for them to segregate in a condensed state (the droplets) instead of being dissolved in water. Increasing the concentration even more would lead to a dense phase (Figure 3.3B).

In the presence of multiple droplets, competition for material arises. Proteins on the surface of small droplets will be more easily lost, given that they have fewer interactions than proteins on the surface of larger droplets. This leads to a concentration gradient which results in a flux of proteins from small to large droplets (Figure 3.3C). All the droplets smaller than a critical radius shrink, while the others grow. Since the critical radius also grows in time (Figure 3.3D), only one droplet dominates in the end, taking up all the material. This phenomenon is called Ostwald Ripening (OR) and can be visualized in the schematics of Figure 3.3E. The equation that regulates the time evolution of the radius of the i -th droplet is

$$\frac{dR_i}{dt} = \frac{Dc_{out}}{c_{in}} \frac{1}{R_i} \left(\frac{c_{\infty}(t)}{c_{out}} - 1 - \frac{l_{\gamma}}{R_i} \right), \quad (3.2)$$

where D is the diffusion constant, $c_{in,out}$ are the concentration inside/outside of a droplet in the thermodynamic limit ($R \rightarrow \infty$), c_{∞} is the concentration far away from the droplets and l_{γ} is the capillary length. Moreover, material conservation dictates that the medium concentration \bar{c} in the entire volume V_n must follow:

$$\bar{c}V_n = c_{in} \sum_i^N V_i + c_{\infty}(t) \left(V_n - \sum_i^N V_i \right). \quad (3.3)$$

where V_i is the volume of each droplet. The full mathematical derivation is reported in the Theory Box 3.2.1.

Theory Box 3.2.1: Derivation of droplets coarsening

Let's consider a system of infinite size with two inhomogeneous phases, with free energy $F = V_1 f(c_1) + V_2 f(c_2)$. Here f is the free energy density, $V_{1,2}$ are the volumes and $c_{1,2}$ are

the equilibrium concentrations of the two phases. The total volume V_T is assumed to be constant, as well as the number of molecules, so that $V_T = V_1 + V_2$ and $c_T V_T = V_1 c_1 + V_2 c_2$, with c_T being the average concentration. Expressed in terms of c_1, V_1, c_T, V_T , the expression for F yields

$$F = V_1 f(c_1) + (V_T - V_1) f\left(\frac{c_T V_T - V_1 c_1}{V_T - V_1}\right).$$

To determine the stability condition of the system, we aim to minimize the free energy with respect to the concentration and volume of one of the two phases. This involves computing the derivatives of F with respect to c_1 and V_1 and setting them to zero. This results in:

$$\partial_{c_1} F = 0 \quad \Rightarrow \quad f'(c_1) - f'(c_2) = 0, \quad (3.4)$$

$$\partial_{V_1} F = 0 \quad \Rightarrow \quad f(c_1) - f(c_2) + f'(c_2) \cdot [c_2 - c_1] = 0. \quad (3.5)$$

While surface effects may be negligible in the thermodynamic limit, they become pivotal in the context of droplets. Here, the free energy includes an additional term $+A\gamma$, where A represents the interface area and γ signifies the surface tension. Therefore, for a spherical droplet, the free energy is expressed as:

$$F = V_d f(c_{in}) + (V - V_d) f(c_{out}) + 4\pi R^2 \gamma,$$

where $V_d = \frac{4\pi}{3} R^3$ is the volume of a spherical droplet of radius R , $c_{in/out}$ are the internal/external concentrations and V is the volume of the whole system. Differentiating with respect to c_{in} and V_d leads to two equilibrium conditions

$$0 = f'(c_{in}^{eq}) - f'(c_{out}^{eq}), \quad 0 = f(c_{in}^{eq}) - f(c_{out}^{eq}) + (c_{out}^{eq} - c_{in}^{eq}) f'(c_{out}^{eq}) + \frac{2\gamma}{R},$$

where $c_{in/out}^{eq}$ are the internal/external equilibrium concentrations. The only difference with the infinite size system (Equations (3.4) and (3.5)) is the last term, the Laplace pressure, which is negligible in the thermodynamic limit.

To approximate the equilibrium concentrations, we consider them as being a linear correction of the corresponding concentrations in the thermodynamic limit ($c_{in/out}^{(0)}$), such that $c_{in/out}^{eq} = c_{in/out}^{(0)} + \delta c_{in/out}$.

In this way we find the *Gibbs-Thomson* relations

$$\delta c_{out} \approx \frac{2\gamma}{(c_{in}^{(0)} - c_{out}^{(0)}) f''(c_{out}^{(0)}) R}, \quad \delta c_{in} \approx \frac{f''(c_{out}^{(0)})}{f''(c_{in}^{(0)})} \delta c_{out},$$

which allow us to express the equilibrium concentrations as

$$c_{out}^{eq} = c_{out}^{(0)} \cdot \left(1 + \frac{l_{\gamma, out}}{R}\right), \quad c_{in}^{eq} = c_{in}^{(0)} \cdot \left(1 + \frac{l_{\gamma, in}}{R}\right),$$

with $l_{\gamma, in/out}$ defined as the capillary lengths

$$l_{\gamma, out} = \frac{2\gamma}{(c_{in}^{(0)} - c_{out}^{(0)}) f''(c_{out}^{(0)}) c_{out}^{(0)}}, \quad l_{\gamma, in} = \frac{f''(c_{out}^{(0)}) c_{out}^{(0)}}{f''(c_{in}^{(0)}) c_{in}^{(0)}} l_{\gamma, out}.$$

In the limit of $c_{in}^{(0)} \gg c_{out}^{(0)}$, thus $l_{\gamma,in} \ll l_{\gamma,out} = l_{\gamma}$ and $c_{in}^{eq} \approx c_{in}^{(0)}$, we get

$$c_{out}^{eq} = c_{out}^{(0)} \cdot \left(1 + \frac{l_{\gamma}}{R}\right), \quad c_{in}^{eq} = c_{in}^{(0)}.$$

Our objective is to establish an equation describing the concentration c of molecules at a distance r from a solitary droplet with radius R , situated within an unbounded medium. The concentration at a significant distance from the droplet remains fixed to a constant c_{∞} . Due to the system's symmetry, the concentration c solely depends on the distance r . Additionally, we make the assumption that the droplet's radius changes slowly enough, allowing us to treat it as approximately constant compared to the timescale of molecules diffusion.

Hence, a gradient in concentration results in a diffusive flux through a spherical shell at radius r . This flux, denoted $j(r)$, is $j(r) = -D \frac{\partial}{\partial r} c(r)$, with D as the diffusion coefficient. As total molecule count remains constant, so does flux across the shell's surface at r . This constant total flux is given by:

$$J = -4\pi D r^2 \frac{\partial}{\partial r} c(r) = const.$$

This equation has solution $c(r) = k_1 + k_2/R$, with constants $k_{1,2}$ given by the boundary conditions at R and ∞ ($c(R) = c_{out}^{eq}$ and $c(\infty) = c_{\infty}$). From this it follows that

$$c(r) = c_{\infty} + (c_{out}^{eq} - c_{\infty}) \frac{R}{r} \quad r > R,$$

$$c(r) = c_{in}^{eq} \quad r < R.$$

The total protein outflow from the droplet is

$$J_R = -4\pi D R^2 \frac{\partial}{\partial r} c(r)|_{r=R} = 4\pi D R (c_{out}^{eq} - c_{\infty}). \quad (3.6)$$

The variation of the droplet volume is given by $\frac{dV_d}{dt} = -J_R/c_{in}^{eq}$, that is

$$\frac{d}{dt} \left(\frac{4\pi}{3} R^3 \right) = -\frac{1}{c_{in}^{eq}} 4\pi D R (c_{out}^{eq} - c_{\infty}),$$

which, in terms of $\frac{dR}{dt}$ and of $c_{in/out}^{(0)}$ yields

$$\frac{dR}{dt} = \frac{D c_{out}^{(0)}}{R c_{in}^{(0)}} \left(\frac{c_{\infty}}{c_{out}^{(0)}} - 1 - \frac{l_{\gamma}}{R} \right).$$

This expression can be readily extended to the scenario involving N droplets that are widely separated from each other, allowing us to neglect direct interactions between the droplets. In this case, the droplets solely compete for material exchange through the shared surrounding medium. This directly yields Equation (3.2) in the main text, where, for simplicity of notation, we have defined $c_{in/out}^{(0)}$ as $c_{in/out}$. Material conservation implies that material is shared between the droplets, (of volume V_i and inner concentration c_{in}), and the outer space, (of volume $V_n - \sum_i^N V_i$ and concentration c_{∞}). Thus, the mean concentration \bar{c} in the entire volume V_n will follow Equation (3.3) in the main text.

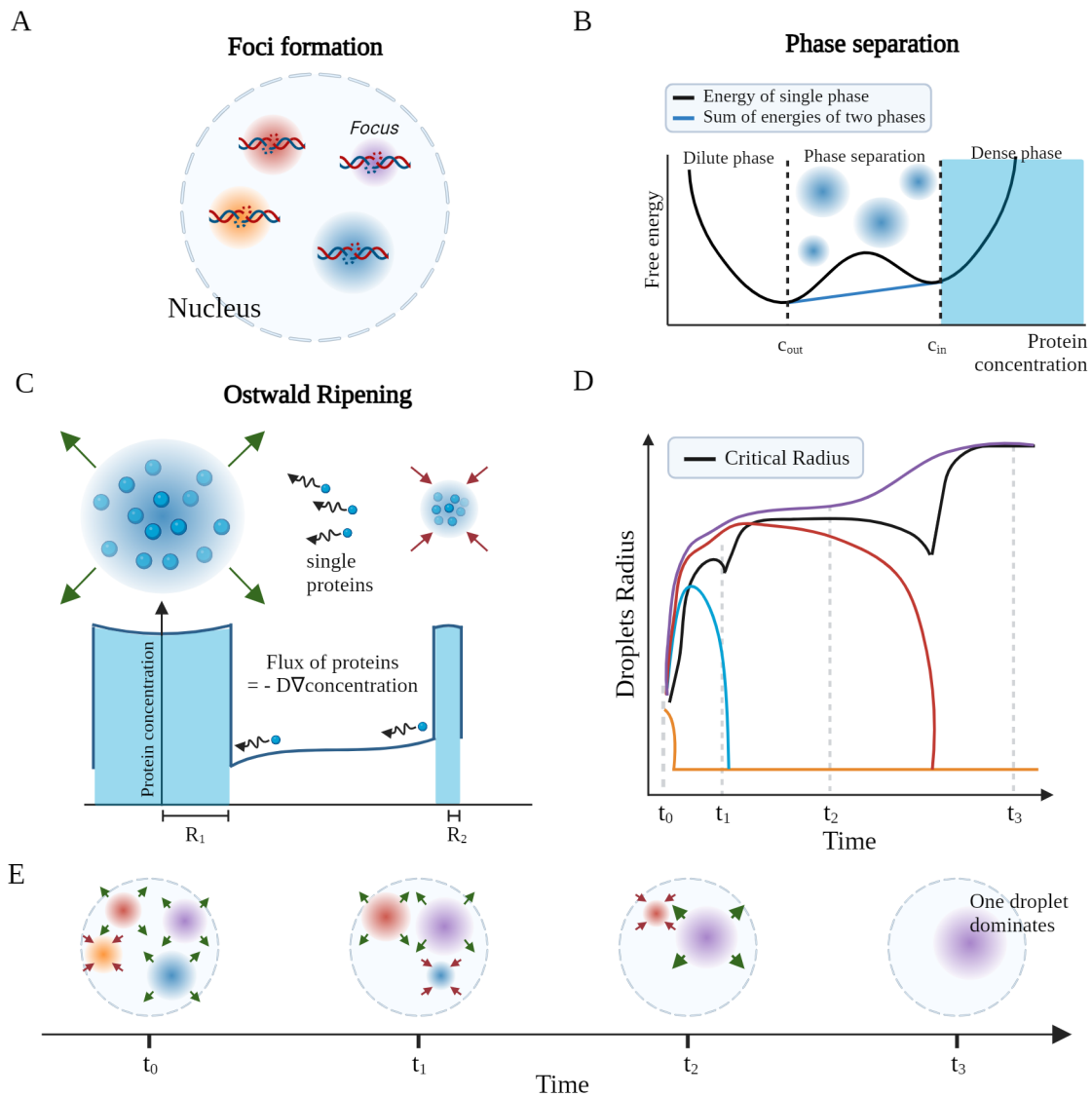


Figure 3.3: (A) Foci formation in correspondence to DNA damage sites. (B) Foci form as a result of liquid-liquid phase separation in supersaturated environments. (C) The competition of material leads to the phenomenon of Ostwald Ripening (OR) (D) Dynamics of several droplets: all those smaller than a critical radius shrink. (E) 2D schematics of the OR mechanism in which only one droplet dominates in the end and takes up all the material. (B-C) are adapted from Söding *et al.*, 2020.

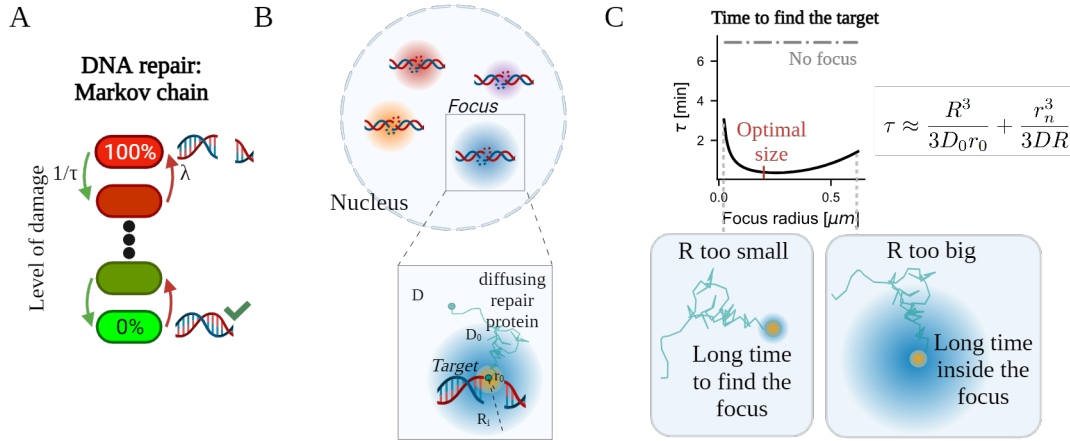


Figure 3.4: (A) Process of DNA repair in the presence of foci (B) Time to find the target is made of two contributions: the time necessary to find the focus edge from the boundary of the nucleus, plus the time necessary to reach the target from there (Heltberg, Miné-Hattab, *et al.*, 2021). Adapted from Heltberg *et al.* (2022).

3.2.3 Diffusion-limited repair processes

The process of DNA repair is a rather intricate and complicated phenomenon, involving a huge number of steps (Friedberg, 2003). A way to mathematically model it in the simplest way possible is to consider it as a Markov chain made of M steps, where each step corresponds to a small action in the chain of DNA repair that is performed at a certain rate $1/\tau$, and all steps need to be completed sequentially (Figure 3.4A). If we assume that the process is diffusion-limited, meaning that the time it takes to perform each step of repair τ essentially coincides with the time it takes for the repair proteins to reach the target (Figure 3.4B), we can use *first-passage times* argumentations to determine how long it takes for the molecules to reach the target in the presence of foci. Heltberg, Miné-Hattab, *et al.* (2021) have shown that, if the free energy is lowered inside the droplets, the foci basically act as "funnels", which accelerate the search time τ , following the equation (see Theory Box 3.2.2 for the full derivation)

$$\tau \approx \frac{R^3}{3D_0r_0} + \frac{r_n^3}{3DR}. \quad (3.7)$$

Here R is the radius of the droplet, D_0 the diffusion coefficient inside the droplet, r_0 the radius of the target, r_n the radius of the nucleus, and D the diffusion coefficient in the nucleus. Therefore, the rate consists of the sum of two terms: the time it takes to reach the boundary of the focus in the nucleus, plus the time it takes to reach the boundary of the target in the focus (Figure 3.4C). Given that within the focus the diffusion coefficient is lower than outside ($D_0 \ll D$), because the environment is denser, there exists a focus radius such that the rate to find the target is optimized. Intuitively, if the focus is too big, the particle will find it fast, but then it will take a long time to navigate inside it. If it is too small, it will take a long time to find it in the first place. In the absence of a focus, the expression simply reduces to the search-time of the target from the nucleus boundary,

$$\tau_{nofocus} = \frac{r_n^3}{3Dr_0}.$$

Theory Box 3.2.2: Derivation of first passage times

We first consider a Langevin equation of the form

$$d\mathbf{r} = dt \left[\nabla D(\mathbf{r}) - \frac{D(\mathbf{r})}{k_B T} \nabla U(\mathbf{r}) \right] + \sqrt{2D(\mathbf{r})} d\mathbf{W},$$

where \mathbf{W} is a 3D-Wiener process, $U(r)$ is the potential perceived by the particle and $D(r)$ is the diffusion coefficient.

The following derivation can be found in Heltberg, Miné-Hattab, *et al.* (2021). We assume that the focus is a spherical liquid droplet characterized by a sudden change in the energy landscape, thus having diffusion coefficient $D(r)$ and sigmoidal potential $U(r)$, both spherically symmetric around the center of the focus:

$$D(r) = D_0 + \frac{D_n - D_0}{1 + e^{-b(r-R)}}, \quad U(r) = \frac{A}{1 + e^{-b(r-R)}}.$$

Here D_0 is the diffusion coefficient inside the focus, D_n the diffusion coefficient inside the nucleus, R is the radius of the focus, b the steepness of the sigmoidals and A the surface potential.

With these assumptions, the Langevin equation can be written as

$$dr = dt \left[\frac{2D}{r} + \partial_r D - \frac{D}{k_B T} \partial_r U(r) \right] + \sqrt{2D(r)} dW,$$

where W is a 1-D Wiener process.

The goal is to find if the focus, with its enhanced concentration of proteins, can act as a "funnel" allowing diffusing proteins to find the target faster. We thus assume a simplified scenario, with a perfectly absorbing target of radius r_0 , in the center of a focus of radius R , which is in turn centered in the nucleus of radius r_n . This creates a probability flux $J = 1/\tau$, which represents the rate of finding the target for one molecule. If we denote by $p(\mathbf{r}) = p(r)$ the probability distribution of a molecule, then the corresponding probability density $q(r)$, of being at a certain distance r from the absorbing center, thus follows $q(r) = 4\pi r^2 p(r)$.

The Fokker-Planck equation for $q(r)$ is therefore defined as

$$\partial_t q = -\partial_r \left[\left(\frac{2D}{r} + \partial_r D - \frac{D}{k_B T} \partial_r U(r) \right) q \right] + \partial_r^2 (Dq) = -\partial_r J.$$

At steady state with a non-vanishing flux $J = \text{const}$,

$$\left(\frac{2D}{r} - \frac{D}{k_B T} \partial_r U \right) q = D \partial_r q - J.$$

Introducing the variable $\phi = -2 \ln(r) + U/k_B T$, we simplify this as:

$$q \partial_r \phi + \partial_r q = \frac{J}{D}.$$

Multiplying by e^ϕ , yields

$$\partial_r (e^\phi q) = \frac{J}{D} e^\phi,$$

whose general solution is

$$q(r) = C e^{-\phi(r)} + J e^{-\phi(r)} \int_{r_0}^r \frac{e^{\phi(r')}}{D(r')} dr'.$$

Because of the absorbing boundary condition $q(r_0) = 0$, C is null in this case. The constant J follows from the normalization $\int_{r_0}^{r_n} dr q(r) = 1$, yielding:

$$J^{-1} = \tau = \int_{r_0}^{r_n} dr e^{-\phi(r)} \int_{r_0}^r dr' \frac{e^{\phi(r')}}{D(r')}.$$

We then insert the definition of $\phi(r)$ and assume a strong surface potential of the droplet, so that we get

$$\tau = \int_{r_0}^{r_n} dr r^2 e^{-U(r)/k_B T} \int_{r_0}^r \frac{dr'}{D(r') r'^2} e^{U(r')/k_B T}.$$

Considering a sharp boundary $bR \gg 1$ so that U and D can be considered step-functions, the integral has the following exact solution

$$\tau = \frac{R^3 - r_0^3}{3D_0 r_0} + \frac{r_0^2 - R^2}{2D_0} + e^{-\frac{A}{k_B T}} \left(\frac{r_n^3 - R^3}{3D_0 r_0} + \frac{R^3 - r_n^3}{3D_0 R} \right) + \frac{r_n^3 - R^3}{3D_n R} + \frac{R^2 - r_n^2}{2D_n}.$$

In the limit $r_0 \ll R \ll r_n$ and of a strong potential $A \gg k_B T$, the previous equation simplifies to

$$\tau \approx \frac{R^3}{3D_0 r_0} + \frac{r_n^3}{3D_n R}.$$

It should be noted that in the main text, the diffusion coefficient in the nucleus is denoted as D instead of D_n .

3.2.4 How to simulate stochastic processes: the Gillespie algorithm

The Gillespie algorithm (Gillespie, 1976) is a powerful tool for modelling and simulating the dynamics of chemical reactions and other stochastic processes occurring in biological systems for which the reaction rates are known. It is an event-driven algorithm, meaning that the time proceeds by events and not by fixed time-steps.

Given a Poisson process, i.e. a process where events happen at a constant rate r , it can be easily shown that the probability density of the time between two events $P(\tau)$ follows an exponential distribution $P(\tau) = r e^{-r\tau}$. In this case, the algorithm consists of the following steps:

1. Draw a random number $\tau > 0$ from the distribution $P(\tau)$;
2. Proceed the time by τ and make an event happen (updating the corresponding state variable);
3. Repeat 1. and 2.

However, in most scenarios, multiple types of events can happen simultaneously: the algorithm can be generalized to take into account this possibility too. We thus consider m possible events, with r_i being the rate of the i -th kind event ($i = 1 \dots m$). We also assume that the rates can depend

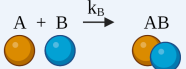
on the system status, but do not change between events. This implies that the inter-event interval distribution still follows an exponential distribution characterized by r_i . In this case, the algorithm is the following:

1. Calculate the probability that any of the possible events occur ($R_{TOT} = \sum_{i=1}^m r_i$);
2. Find the time it takes for the event to occur, by drawing a random number $\tau > 0$ from the distribution $P(\tau) = R_{TOT}e^{-R_{TOT}\tau}$;
3. Find which of the m events is the one taking place: draw a random number a from the uniform distribution in $[0, 1]$. If $\sum_{j=1}^{i-1} r_j/R_{TOT} < a < \sum_{j=1}^i r_j/R_{TOT}$, it means the event occurring is the i -th.
4. Repeat 1. to 3.

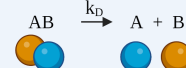
The Gillespie algorithm is therefore a valuable tool for accurate stochastic modelling of biological systems, as it captures molecular fluctuations and provides insights into the system behaviour that deterministic approaches cannot reveal. By simulating individual reactions in a system, it provides a dynamic view of how molecules interact, making it particularly well-suited for understanding complex biochemical processes. In the following example, we illustrate how we can apply the algorithm in a simple scenario with two possible chemical reactions, namely binding and dissociation between two species A and B .

Example 3.2.1: Reversible binding of A and B into AB dimers

The reactions

$A + B \xrightarrow{k_B} AB$


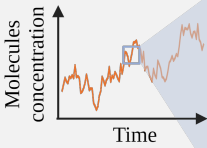
(binding)

$AB \xrightarrow{k_D} A + B$


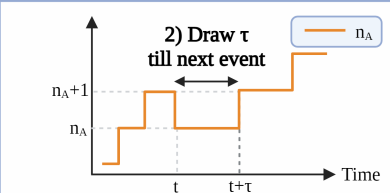
(dissociation)

1) Find rate of any event

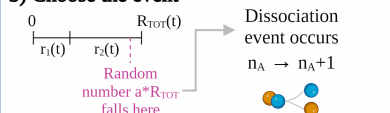
$$R_{TOT} = r_1 + r_2 = k_B n_A n_B + k_D n_{AB}$$



2) Draw τ till next event



3) Choose the event



Dissociation event occurs
 $n_A \rightarrow n_A + 1$

Given a system with two species (A, B) which can reversibly form a dimer (AB), the possible reactions are:

$$A + B \xrightarrow{k_B} AB$$

$$AB \xrightarrow{k_D} A + B,$$

with $k_{B,D}$ being the binding/dissociation constants. The rates of the two events are therefore

$$r_1 = k_B \cdot n_A \cdot n_B \text{ (binding),}$$

$$r_2 = k_D \cdot n_{AB} \text{ (dissociation),}$$

where n_A, n_B are the number of A and B molecules, and n_{AB} the number of dimers present in the system. For this system:

1. The total reaction rate is $R_{TOT} = r_1 + r_2$.
2. The probability that any of the two events (binding or dissociation) occurs after time τ follows the distribution $P(\tau) = R_{TOT}e^{-R_{TOT}\tau}$. We draw a random number from $P(\tau)$.
3. To determine whether the events occurring is binding or dissociation, we draw a random number a from a uniform distribution between $[0,1]$. If $a < r_1/R_{TOT}$, binding occurs (meaning that $n_{AB} \rightarrow n_{AB} + 1$ and $n_{A,B} \rightarrow n_{A,B} - 1$, otherwise, dissociation occurs ($n_{AB} \rightarrow n_{AB} - 1$ and $n_{A,B} \rightarrow n_{A,B} + 1$)).
4. We repeat 1.- 3.

3.3 Main results

In Figure 3.5 we sum up the mathematical model that we developed to describe the system. The three parts correspond to the three building blocks of the system described in Figure 3.1. First, the p53 signal is assumed to be simply sinusoidal, and to stimulate the production of repair proteins, whose concentration linearly follows p53 concentration (only subsequently we reintroduced the model of the p53-Mdm2 network as described in Mengel *et al.* (2010)). Secondly, we assume that N droplets emerge, which start competing for material, following Lifshitz and Slyozov (1961) theory, resulting in the phenomenon of Ostwald Ripening (OR). This is a mean-field model, so the spatial distribution of the droplets is not taken into account, as the droplets share material through the surrounding medium. Thirdly, the process of damage repair is modelled as a Markov chain, such that completing the whole repair consists of M steps. Each step has a certain probability to be accomplished and another constant rate to be reversed. Assuming that the repair process is diffusion-limited, we can consider that the repair rate coincides with the first passage time of proteins to reach the target, with radius r_0 , within the focus of radius R , as described in the previous section. The whole system is modelled through the Gillespie algorithm, where there are four possible events for each droplet, namely:

- Growth of droplet from addition of a protein;
- Shrinkage of the droplet from loss of a protein;
- One step of damage repair;
- One step of damage addition.

The presence of noise in the system is essential to generate a mixed initial state and to ensure the initial expansion of the droplets after nucleation. Afterwards, stochasticity only plays a minor role.

With this model, we first showed that an oscillatory p53 nuclear abundance results in suppression of OR (Figure 3.6A): as p53 increases, the droplets grow, and are subsequently forced to shrink as p53 decreases below saturation levels. This provides a window of time for the cell to distribute its resources to few cells at each oscillation, giving them the possibility to repair the damage before

The model

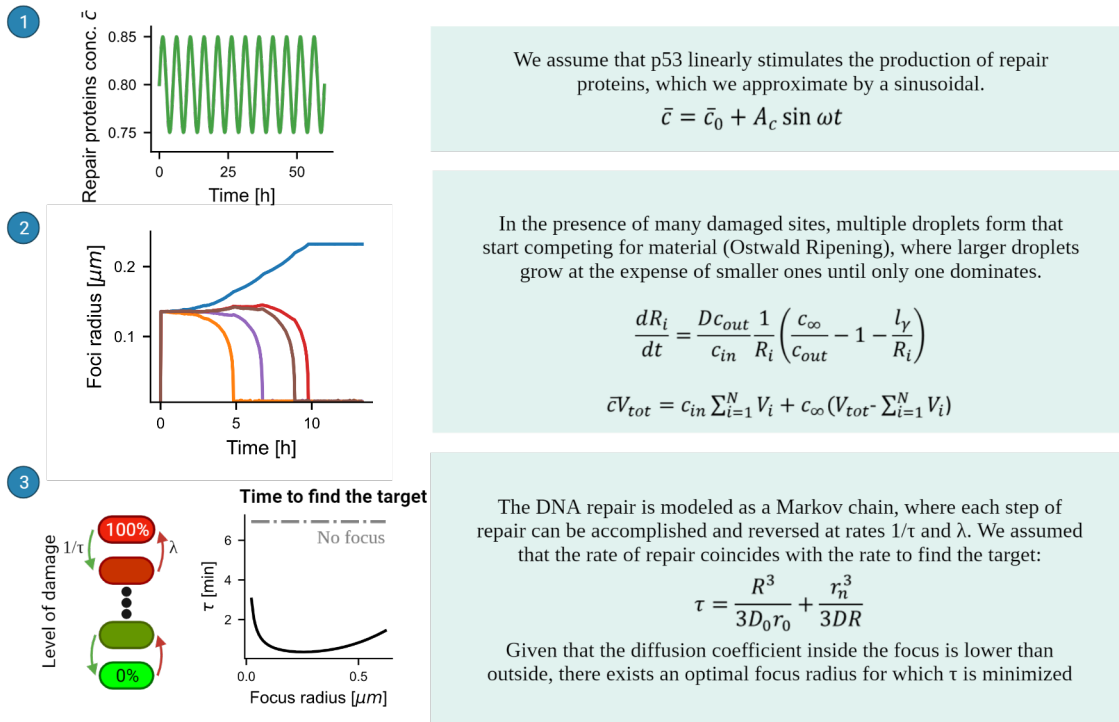


Figure 3.5: Description of the mathematical model used. Adapted from Heltberg *et al.* (2022).

redistributing the material to other sites at a subsequent oscillation. This essentially leads to a sequential damage removal (Figure 3.6B, central panel). We thus realized that there must be an optimal time-window for cells to repair the damage, which should neither be too long (or else OR would dominate, as shown in Figure 3.6B, left panel) nor too short, or else cells would not have enough time to repair the damage (Figure 3.6B, right panel). Simulating a wide range of frequencies for p53 oscillations, we thus found an optimum in the timescale of hours, which is where the experimental value of p53 lies (Figure 3.6C).

Moreover, we investigated the role of the amplitude of the oscillations: interestingly, we found an optimal region at low mean concentration and high amplitudes where the repair could occur much faster than at high constant levels of p53. Even if experimentally it is not possible to determine the absolute values of p53 concentration, given that the experiments only measure fluorescent levels through imaging techniques, it is still possible to measure relative quantities, such as the ratio amplitude/mean concentration. What we observed is that the region of optimal repair overlapped with the line that corresponds to the ratio of amplitude/mean concentration measured for p53.

We thus aimed to experimentally test these predictions, in particular, compare the repair efficiency between oscillatory levels of p53 and sustained levels. The experiments were fully performed by our experimental collaborators at Academia Sinica, Taiwan, led by professor Sheng-hong Chen. First, DNA damage was induced by adding neocarzinostatin (NCS), a γ -irradiation mimetic drug, as a result of which, p53 naturally starts to oscillate. In order to obtain constant high p53 levels, the non-genotoxic small molecule nutlin-3a was administered at 2.5 h and 5.5 h after DNA damage induction, in correspondence to p53 troughs. Indeed, nutlin has the effect to prevent Mdm2-inhibition by

binding to Mdm2 itself, thus rescuing p53 levels when they are low, resulting in constant high levels (Figure 3.6E). DNA damage was quantified after 1h and after 24h from induction, by immunofluorescent staining of the γ -H2AX foci. It should be noted that these damage-foci are distinct from the repair-foci that we have discussed up to this point, since they have *not* been shown to arise as a result of phase-separation, and merely represent the level of DNA damage. Our analysis shows that the number of γ -H2AX foci is lower for cells with oscillatory dynamics compared to those with sustained levels of p53 (Figure 3.6F). This is confirmed by plotting the distribution of the number of damaged sites in cells (Figure 3.6G). Finally, comparing different cell lines, we overall observed that the fraction of repaired cells is always lower for sustained levels than for oscillatory ones (Figure 3.6H).

To sum up, our model makes several predictions (Figure 3.7):

- Oscillatory p53 levels lead to better DNA repair compared to high constant levels;
- Oscillatory p53 levels suppress OR in the repair foci;
- The repair foci have an oscillatory dynamics which follows the p53 one;
- p53 experimental amplitude and frequency leads to optimal repair.

The first of these hypotheses has been experimentally tested and confirmed, while the others remain to be tested.

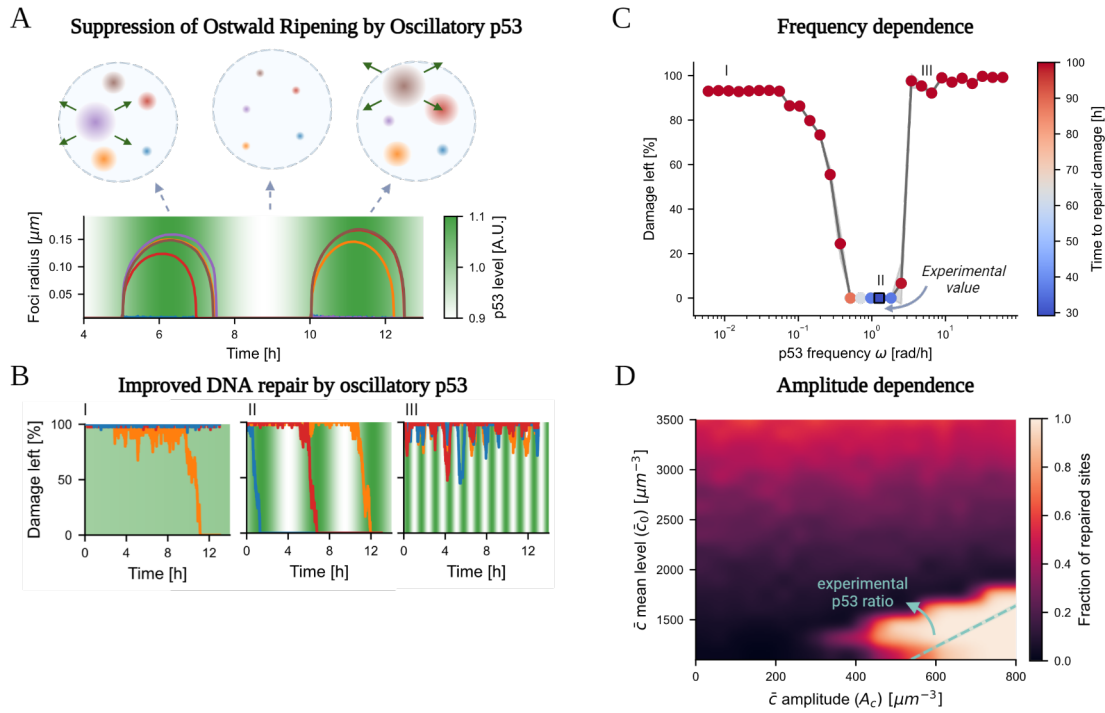
3.4 Discussion and Perspectives

The role of oscillations in TFs and their connection to DNA repair mechanisms are complex and unresolved questions. Recent findings on the formation of DNA repair foci through liquid-liquid phase separation motivated our investigation into how oscillations in TFs, specifically p53, interact with droplet formation. With this work, we thus establish a bridge between the dynamics of TFs and the formation of biomolecular condensates in cells, showing how the cell can exploit the physics of phase separation to perform an optimal distribution of resources in case of stress. This mechanism would be particularly beneficial in the case of low amount of resources compared to the amount of damage. Indeed, in our model, all the repair material is distributed sequentially in different sites. On the other hand, different ways of stabilizing the droplets against OR have been proposed, such as with trapped species (Webster and Cates, 2001) or by lowering the surface tension. These may not be necessarily beneficial for the cell, though: if material is equally shared between all the sites simultaneously, the foci may not reach the right size to efficiently repair the damage.

Our research focuses on the stimulation of downstream repair by p53 and assumes a linear relationship between p53 concentration and the proteins involved in phase transition. To support this assumption, it has been shown that p53 directly recruits key proteins involved in repair, such as 53BP1 (Wang *et al.*, 2022), and p53 itself can form liquid droplets (Petronilho *et al.*, 2021; Kamagata *et al.*, 2020). However, even in the case of a non-linear relationship between p53 and droplet proteins, we showed that the output would still be oscillatory.

Furthermore, we speculate that there might even be a mutual relation between foci and oscillations in p53. Tsabar *et al.* (2020) have recently shown that approximately 10% of irradiated cells transition from oscillatory p53 levels to a sustained high level after 24 h. Therefore, it would be intriguing to

Theoretical predictions



Experimental results

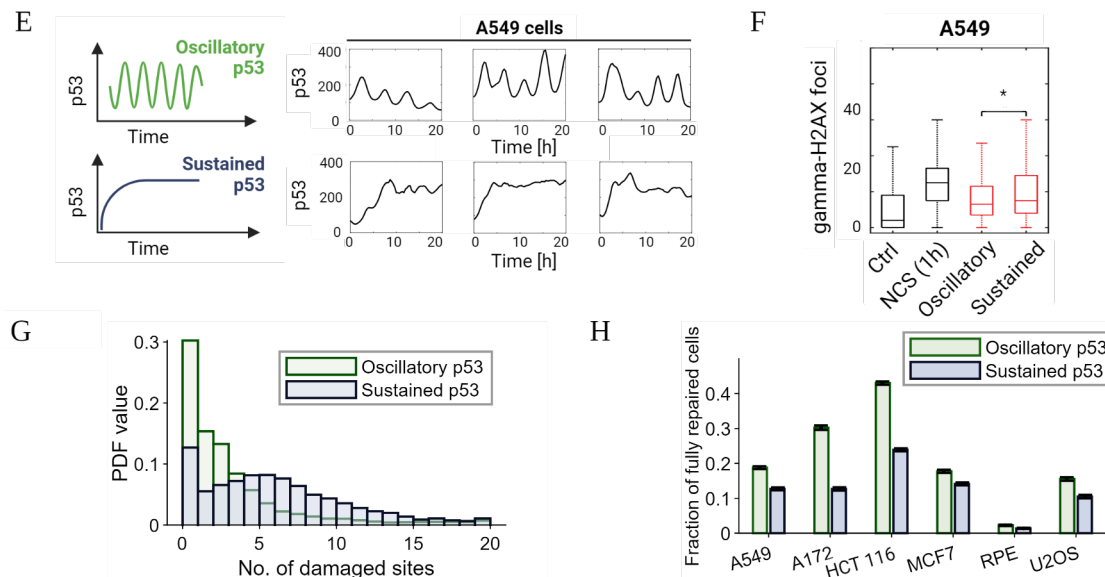


Figure 3.6: (A) Oscillatory p53 levels lead to a sequential growth and shrinkage of droplets, thus a specific spatio-temporal distribution of resources. (B) p53 oscillations (II) lead to optimal DNA repair compared to constant levels (I) or compared to much faster oscillations (III). (C) The experimental p53 frequency is optimal to repair multiple DNA damages. (D) Amplitude heatmap shows a region of optimal repair for high amplitude and low mean concentration. (E) p53 oscillatory and sustained dynamics in three example cells from A549 cell line. (F) Quantification of γ -H2AX DNA damage foci in A549 cell line. (G) Distribution of number of damaged sites in cells for A172 cell line. (H) Bar plot on fraction of fully repaired sites for different cell lines. Adapted from Heltberg *et al.* (2022).

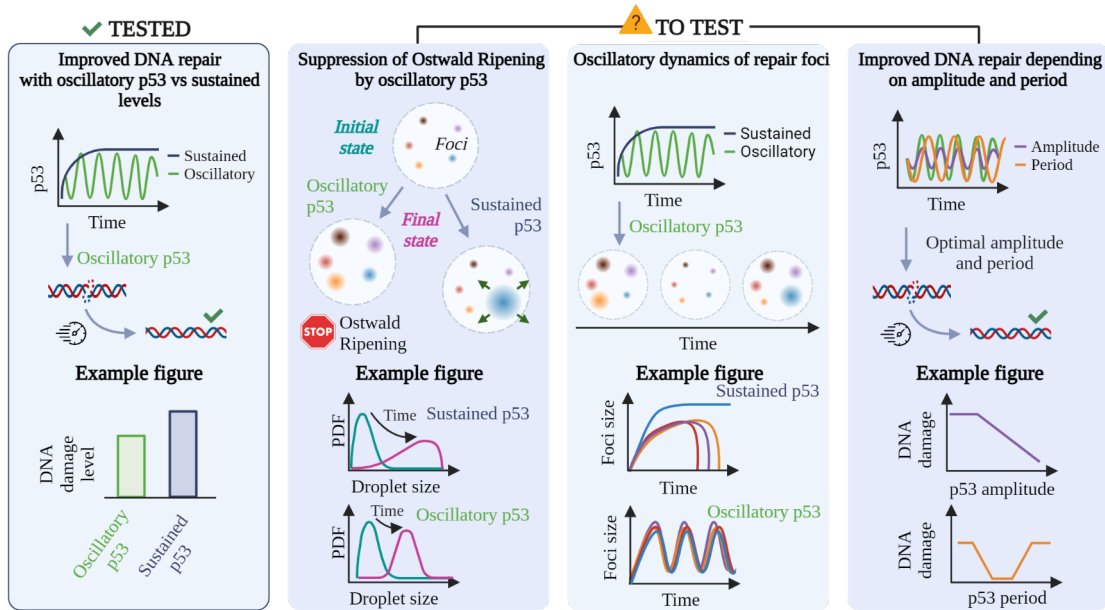


Figure 3.7: Theoretical predictions which have been experimentally tested and those that remain to be tested. Adapted from Heltberg *et al.* (2022).

determine whether it is possible to predict the switch from oscillatory p53 to constant high levels based on foci behaviour. Indeed, it is conceivable that the foci also serve as a protective barrier against Mdm2 inhibition, which could further contribute to elevate p53 concentration and cause the switch.

Other aspects worth investigating include, for instance, how the phenomenon of coalescence of different droplets impacts the repair efficacy: one can imagine that fusing several droplets and therefore combining different DNA breakpoints would come at risk of chromosomal translocation. Moreover, recent studies show that the p53 period tends to increase as time passes: it would be intriguing to model if this transition could also arise as a feedback mechanism from the foci.

Our study reveals the importance of oscillations in TFs, both in terms of amplitude and periodicity, for optimal DNA repair. It suggests that other types of dynamics, such as random fluctuations, stability, or chaos, would not perform as effectively. Experimental verification confirms the positive role of p53 oscillations in DNA repair. Oscillations may work in conjunction with other mechanisms to stabilize foci and optimize repair processes. Given the prevalence of liquid sub-compartments in cellular regulation (Brangwynne *et al.*, 2009; Larson *et al.*, 2017; Strom *et al.*, 2017), these findings may have broader implications for gene regulation. Understanding the role of oscillations in p53 would significantly advance our knowledge of damage repair and reveal the connection between fundamental physical processes and essential regulatory mechanisms in life.

3.5 Manuscript: Enhanced DNA repair through droplet formation and p53 oscillation

Authors: Mathias S. Heltberg, Alessandra Lucchetti, Feng-Shu Hsieh, Duy Pham Minh Nguyen, Sheng-hong Chen, Mogens H. Jensen

Journal: Cell

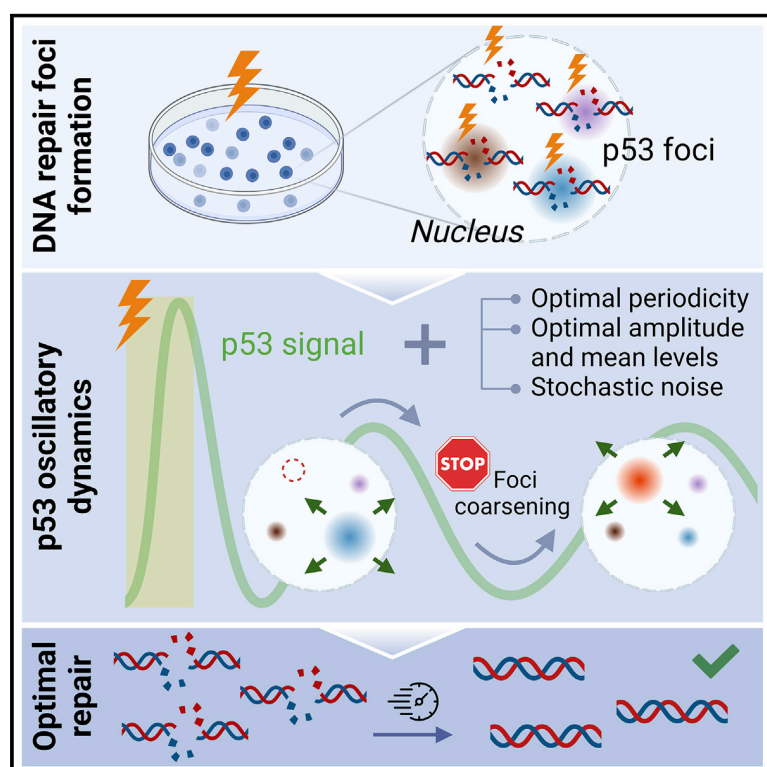
Vol./page: 185/4394–4408

DOI: <https://doi.org/10.1016/j.cell.2022.10.004>

My contributions: I performed all the numerical simulations of the theoretical model and analysed the results. I contributed to the production of all figures and to writing all sections, apart from the paragraph regarding the experimental results.

Enhanced DNA repair through droplet formation and p53 oscillations

Graphical abstract



Authors

Mathias S. Heltberg,
Alessandra Lucchetti, Feng-Shu Hsieh,
Duy Pham Minh Nguyen,
Sheng-hong Chen, Mogens H. Jensen

Correspondence

mathias.heltberg@nbi.ku.dk (M.S.H.),
mhjensen@nbi.dk (M.H.J.)

In brief

A theory explains how oscillations in p53 nuclear abundance optimize DNA damage repair.

Highlights

- p53 oscillations optimize DNA repair compared to cells with sustained levels
- Enhanced DNA repair efficiency may be achieved by suppression of Ostwald ripening
- Natural p53 periodicity and amplitude enable optimal distribution of repair material
- Oscillations enhance robustness of DNA damage response in stochastic environments



Theory

Enhanced DNA repair through droplet formation and p53 oscillations

Mathias S. Heltberg,^{1,4,*} Alessandra Lucchetti,^{1,4} Feng-Shu Hsieh,² Duy Pham Minh Nguyen,² Sheng-hong Chen,^{2,3} and Mogens H. Jensen^{1,5,*}

¹Niels Bohr Institute, University of Copenhagen, Copenhagen, 2100, Denmark

²Lab for Cell Dynamics, Institute of Molecular Biology, Academia Sinica, Taipei, 115, Taiwan

³National Center for Theoretical Sciences, Physics Division, Complex Systems, Taipei, 10617, Taiwan

⁴These authors contributed equally

⁵Lead contact

*Correspondence: mathias.heltberg@nbi.ku.dk (M.S.H.), mhjensen@nbi.dk (M.H.J.)

<https://doi.org/10.1016/j.cell.2022.10.004>

SUMMARY

Living organisms are constantly exposed to DNA damage, and optimal repair is therefore crucial. A characteristic hallmark of the response is the formation of sub-compartments around the site of damage, known as foci. Following multiple DNA breaks, the transcription factor p53 exhibits oscillations in its nuclear concentration, but how this dynamics can affect the repair remains unknown. Here, we formulate a theory for foci formation through droplet condensation and discover how oscillations in p53, with its specific periodicity and amplitude, optimize the repair process by preventing Ostwald ripening and distributing protein material in space and time. Based on the theory predictions, we reveal experimentally that the oscillatory dynamics of p53 does enhance the repair efficiency. These results connect the dynamical signaling of p53 with the microscopic repair process and create a new paradigm for the interplay of complex dynamics and phase transitions in biology.

INTRODUCTION

Living organisms need to have highly specialized and optimized responses to external stresses, as a result of which many transcription factors (TFs) portray a complex dynamics. Indeed, decades of research in the field have shown how proteins such as nuclear factor κ B (NF- κ B) (Hoffmann et al., 2002; Nelson et al., 2004), Hes1 (Kobayashi et al., 2009), and p53 (Lahav et al., 2004) show oscillations in their nuclear concentration with periods on the timescale of hours. A typical quantitative approach consists of studying the underlying biochemical network structure and formulating coupled differential equations in order to understand the occurrence of these oscillations (Tiana et al., 2002; Jensen et al., 2003; Geva-Zatorsky et al., 2006). However, as of today surprisingly little effort has been made to investigate what advantages the cell may gain by exhibiting this dynamics, and this fundamental question has been too often left for qualitative discussions (Heltberg et al., 2021a). It has previously been revealed how large amplitudes can stimulate groups of downstream genes (Heltberg et al., 2016, 2019b), but how the most fundamental trace of oscillations—the periodicity—may be beneficial has been largely overlooked. It would be evolutionary surprising if these oscillations, occurring in some of the most vital TFs, did not serve a distinct role, and it is therefore crucial that biological research applies the biophysical foundations to investigate why the cell has included such dynamical response in specific situations.

In this context, the tumor suppressor protein, p53, is a master regulator of DNA damage response, stimulating numerous genes related to DNA repair. When the cell is exposed to DNA damage, through for instance chemical components or radiation, p53 nuclear concentration is typically elevated. However, following multiple DNA double-strand breaks (DSBs), it exhibits sustained oscillations with a well-defined period of approximately 5.5 h (Lahav et al., 2004; Chen et al., 2016). These oscillations mainly originate as a result of the negative feedback loop with the downstream target Mdm2, even though several other proteins play a role in this loop (Batchelor et al., 2008; Heltberg et al., 2019a).

While the process of DNA repair is complicated, involving a large number of steps, one characteristic hallmark of the response to DSBs is the formation of small sub-compartments rich of repair proteins around the site of damage (Lisby et al., 2004). These have been named ionizing radiation-induced foci (IRIF) and will be referred to simply as foci in this paper. Recently it has been shown that repair foci have properties similar to liquid droplets, and their formation can therefore be described as a second-order phase transition (Oshidari et al., 2020; Miné-Hattab et al., 2021; Pessina et al., 2019; Kilic et al., 2019).

The main focus of this paper is to investigate how the features of liquid droplets can affect the reaction rates of repair proteins in the diffusion-limited regime, and consequently, how the formation of foci can enhance the DNA repair process. In the presence of



multiple liquid droplets, only the largest can grow due to the process of Ostwald ripening. Therefore, serious problems arise when the cell needs to repair multiple damaged sites. What we discovered is that this issue is resolved directly by the presence of oscillations in the TF p53. First, we investigated the case of fast droplet formation, in which case we revealed an optimal period similar to the one found in p53. Secondly, we investigated the regime of slowly forming droplets, where oscillations lead to stabilization of droplet sizes depending on the concentration of proteins to form liquid droplets. Then, we used these results in combination with the mathematical modeling of p53, outlining how single parameter perturbations might alter the underlying repair process. Finally, we tested experimentally the very fundamental hypothesis of the theory—i.e., that p53 oscillations enhance the efficiency of DNA repair—and discovered a significantly reduced level of DNA damage in cells with p53 oscillations. Hence, this work introduces a new role for p53 oscillations and establishes a bridge between the dynamical properties of a TF and the microscopic processes of droplet formation and DNA repair.

RESULTS

Repair of DNA damage through droplet formation

Following multiple DSBs, the cell needs to respond as quickly and efficiently as possible through the process of repairing the damaged sites, by distributing resources at the right position at the right time (Figure 1A). In this context, the three main players that characterize the building blocks of our model are:

- (1) the p53 oscillatory dynamics,
- (2) the formation of liquid foci, and
- (3) the actual process of damage repair.

The experimental oscillatory trace of p53 (Figure 1B), which arises following multiple DSBs, can be reproduced by modeling the negative feedback loop between p53 and Mdm2, as shown for instance by Mengel et al. (2010). In this model, the period and amplitude can be altered by small changes in the parameters, allowing fine-tuned oscillations (Figure 1C). p53 then stimulates the production of repair proteins, which may segregate into liquid droplets, the repair foci, giving rise to an uneven concentration c in the cell nucleus (of radius r_n and volume V_n). It has recently been observed that p53 rapidly accumulates at DSBs sites and directly recruits repair proteins to the foci, suggesting that p53 itself may have significant transcription-independent functions in the DNA damage response (Wang et al., 2022a). Due to the microscopic interactions, proteins will have energetically favorable states inside the droplet, resulting in a lower free energy in this region and therefore in a much higher concentration inside the droplet than right outside it (Figure 1D). In the presence of multiple foci, a fascinating interplay occurs known as Ostwald ripening (Lifshitz and Slyozov, 1961; Wagner, 1961; Hyman et al., 2014; Nishanov and Sobyenin, 1986), where all droplets larger than a critical radius grow, while all the others shrink. Since the critical radius changes accordingly, only one dominating droplet exists in the end. In the presence of N damaged sites and thereby N droplets—assumed to be spherical and far apart from each other—their surrounding can be considered to

be spherically symmetric with a common concentration $c_\infty(t)$ far away from each droplet, which depends on time and mediates the interactions between them. Therefore, the change of radius of the i -th droplet R_i is given by Lifshitz and Slyozov (1961)

$$\frac{dR_i}{dt} = \frac{Dc_{out}}{c_{in}} \frac{1}{R_i} \left(\frac{c_\infty(t)}{c_{out}} - 1 - \frac{l_\gamma}{R_i} \right), \quad (1)$$

where D is the diffusion coefficient outside the droplet, $c_{in,out}$ are the concentrations inside/outside the droplets in the limit $R \rightarrow \infty$ and l_γ is the capillary length. Material conservation dictates that material is shared between the droplets, of volume V_i and internal concentration c_{in} , and the dilute phase, which occupies the volume $V_n - \sum_i^N V_i$ and has a concentration given by c_∞ . Therefore, the average concentration \bar{c} in the total volume V_n is given by:

$$\bar{c}V_n = c_{in} \sum_i^N V_i + c_\infty(t) \left(V_n - \sum_i^N V_i \right). \quad (2)$$

Recently, it was discovered that the DNA repair foci do follow the predictions of the Lifshitz-Slyozov theory to a surprising level. After initial nucleation and growth of droplets, coarsening eventually took place, where small droplets dissolved while large droplets continued to grow, with a rate of the radius $R \propto t^{1/3}$. Furthermore, it was revealed that coarsening predominantly happened without physical contact among the droplets, thereby due to Ostwald ripening, with a timescale of a few hours (Pessina et al., 2019).

To link the formation of liquid foci to p53, we assumed that the concentration of proteins responsible for droplet formation (\bar{c}) linearly follows the p53 concentration.

Simulating the system (Equation 1 and 2) with constant p53 levels—therefore constant \bar{c} —results in a metastable system with one dominating droplet. This is shown in Figure 1E, where the radius of each droplet is portrayed in a different color, matching the schematic representation of Figure 1D. Here, we used the Gillespie algorithm to simulate the evolution of droplet sizes in a stochastic environment (see STAR Methods).

Lastly, we considered the process of DNA damage repair on a single site as a Markov chain consisting of M steps, which need to be sequentially made in order to retrieve the intact DNA (Hahnfeldt et al., 1992; Mohseni-Salehi et al., 2020). Each step is accomplished at a certain rate $1/\tau$, but it can also be reversed at another constant rate λ , until the site is fully repaired (Figure 1F). To calculate the repair rate $1/\tau$, we assumed that this was diffusion limited, allowing us to use first passage time calculations in the Smoluchowski limit (see STAR Methods). Here, we applied a previously derived theory (Heltberg et al., 2021b) of how the presence of a droplet can alter the first passage time of a molecule, leading to an optimal droplet size that reduces the search time maximally (Figure 1G). If the free energy is significantly lowered inside the droplet, this equation takes the form

$$\tau = \frac{R^3}{3D_0r_0} + \frac{r_n^3}{3DR}, \quad (3)$$

where R is the radius of the droplet, D is the diffusion coefficient in the nucleus, D_0 is the diffusion coefficient inside the droplet,

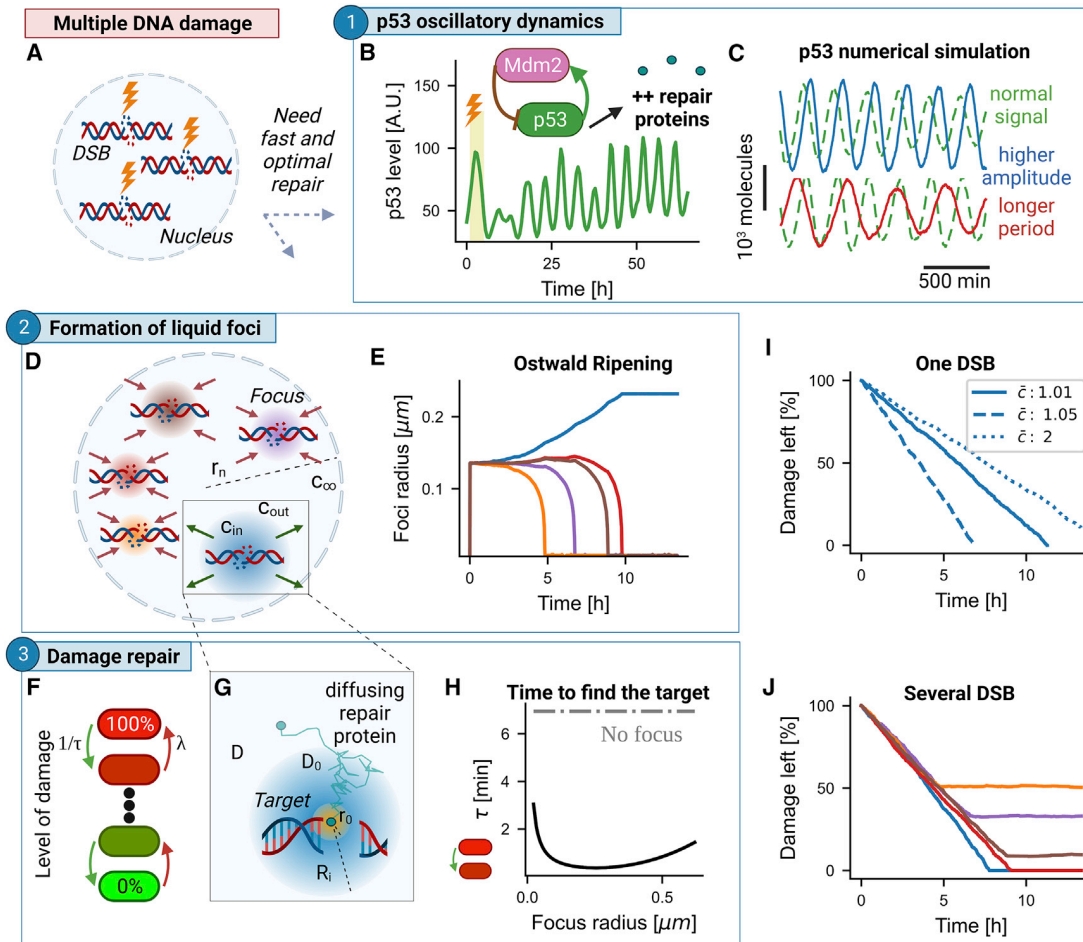


Figure 1. Multiple DNA damage induces p53 oscillatory dynamics and the formation of liquid foci

(A) Schematic figure showing multiple DNA double-strand breaks (DSBs) in the nucleus of a cell following irradiation.
 (B) Experimental trace of p53 following irradiation. The oscillatory dynamics is believed to stem mainly from the negative feedback loop between p53 and Mdm2. p53 then stimulates the production of repair proteins.
 (C) Simulations of the p53 network, where oscillations occur and periodicity and amplitude may be varied by modifying the parameters of the network.
 (D) Schematic figure showing the formation of foci around the sites of damage and the parameters related in the process. Each droplet is represented by a different color. Arrows indicate whether droplets are shrinking (red) or growing (green).
 (E) The process of Ostwald ripening with one final dominating droplet shown by plotting the individual radii as a function of time. Same color code as in (D).
 (F) Schematic figure showing the DNA repair at a specific site as a discrete Markov chain.
 (G) Schematic figure revealing the droplet around a site of damage and the parameters related in the process.
 (H) First passage time for repair molecules to find a target as a function of the size of the focus (Equation 3). The gray dotted line indicates the time to find a target in the absence of foci (Equation 4).
 (I) The damage as a function of time when only one site is damaged. The three lines indicate different constant average concentrations for the repair proteins. In the legend, \bar{c} is expressed in units of C_{out} .
 (J) The damage as a function of time when five sites are damaged. Same color code as in (D) and (E).
 See Table S1 for the specific parameters used in this figure.

and r_0 is the radius of the site of interest (Figure 1H, black line). In the absence of foci, it reduces to the time it takes to find the target from the edge of the nucleus, which corresponds to the constant value (Figure 1H, gray dashed-dotted line)

$$\tau_{no\ focus} = \frac{r_n^3}{3Dr_0}. \quad (4)$$

All the typical parameters used and the ranges investigated can be found in Table 1 (see Tables S1–S4 for the specific parameters used in each figure). It is worth noting that the three components of our model described above all build on previous experimental observations combined with biophysical results.

Based on this mathematical framework, we first considered the case with only one damaged site, no oscillations in the p53

Table 1. Parameters used in this study with their typical values and the ranges investigated

Parameter	Description	Value	Source	Range	Units
c_{in}	protein concentration inside droplets in the lim $R \rightarrow \infty$	10^6	(Söding et al., 2020)	10^5 – 10^{-7}	μm^{-3}
c_{out}	protein concentration outside droplets in the lim $R \rightarrow \infty$	10^3	(Söding et al., 2020)	$(0.8\text{--}1.5) \times 10^3$	μm^{-3}
\bar{c}_0	mean average concentration of proteins in the nucleus	10^3	(Söding et al., 2020)	$(0\text{--}3.5) \times 10^3$	μm^{-3}
A_c	amplitude of average concentration in the nucleus	10^2	(Chen et al., 2016)	$(0\text{--}8) \times 10^2$	μm^{-3}
ω	frequency of p53/of average proteins concentration	0.02	(Geva-Zatorsky et al., 2006)	10^{-3} – 10^1	min^{-1}
l_γ	capillary length	5×10^{-6}	(Söding et al., 2020)	10^{-6} – 10^{-4}	μm
D	diffusion coefficient outside droplets	10	(Matsuda et al., 2008)	1–100	$\mu\text{m}^2\text{s}^{-1}$
D_0	diffusion coefficient inside droplets	0.1	(Miné-Hattab et al., 2021)	0.01–1	$\mu\text{m}^2\text{s}^{-1}$
r_n	radius of the nucleus	5.0	(Sun et al., 2000)	fixed	μm
r_0	radius of the target to repair	0.01	(Heltberg et al., 2021b)	fixed	μm
N	no. of damaged sites	15	(Pessina et al., 2019)	5–50	dimensionless
M	no. of repair steps	40	(Mohseni-Salehi et al., 2020)	40–3,000	dimensionless
λ	rate of damage recreation	0.01	(Hahnfeldt et al., 1992)	0.01–1.5	min^{-1}

See STAR Methods for further explanation on the choices of parameters values and ranges. See Tables S1–S4 for the specific parameters used in each figure.

dynamics and the constant level of $\bar{c} = \bar{c}_0 \forall t$ always above the critical concentration c_{out} (Figure 1I, full line). In this setting, we observed a constant rate of damage repair that is optimized for intermediate values of \bar{c} ($\bar{c}_0 = 1.05c_{out}$) (Figure 1I, dashed line). Indeed, we found that increasing this value too much ($\bar{c}_0 = 2c_{out}$) leads to a reduced decay rate (Figure 1I, dotted line), since the focus grows too large, thus increasing the search time.

On the other hand, in the case of multiple DSBs subject to the Ostwald ripening mechanism, some of them will dissolve, resulting in a significantly inhibited repair rate and an overall repair process that is far from optimal (Figure 1J; note the same color code as the droplets shown in Figures 1D and 1E). This result highlights the problems that the cell encounters with several damaged sites. While the formation of liquid foci can lower the search time of proteins significantly, it has the inherent problem that when multiple sites are present, due to the metastability of the system, small droplets will dissolve before the site is repaired. The next section will discuss how the oscillations found in p53 might influence this situation.

Multiple sites repairment is enhanced by oscillations and suggests the existence of optimal frequencies

In order to investigate the behavior of the system in the presence of p53 oscillations, we first assumed that the p53 concentration can be approximated by a sinusoidal, which would lead to the same dynamics for the average repair proteins concentration:

$$\bar{c} = \bar{c}_0 + A_c \sin(\omega t). \quad (5)$$

Therefore, \bar{c} is calculated at each time step and is then inserted in Equation 2, as mass conservation naturally still holds, in order to determine the value of $c_\infty(t)$. This, in turn, affects the droplet growth through Equation 1. Thereby, the oscillations of the droplet material are mediated through the proteins' concentration far away (c_∞), thus indirectly affecting the foci.

In order to ensure robustness of the model, we tested other simple possible waveforms for p53 (Figure S1A), and non-linear dependencies between p53 and droplet proteins concentration (Figure S1B), still obtaining similar outputs.

By assuming $\bar{c}_0 \geq c_{out}$, one could logically analyze the expected behavior before turning to simulations. If either $A_c = 0$ or $\omega = 0$, the behavior is analogous to the one seen in Figures 1E–1J; on the other hand, as ω becomes similar to the timescale of droplet separation, one droplet would still grow and dominate, but only in the time allowed by the external period. This means that oscillations would effectively prevent Ostwald ripening, thereby allowing the cell to distribute resources among the sites.

To test these predictions, we simulated the typical p53 period of ~ 5 h (Lahav et al., 2004) and observed the formation and dissolution of droplets, with different droplets dominating in different periods (Figure 2A). By combining this dynamics with the damage removal mechanism, we observed that for slow oscillations only one site would be repaired within the simulation time (Figure 2B, left). For the p53 period, the dominating droplets grow to optimal sizes, giving enough time to repair the damaged site properly within each oscillation (Figure 2B, middle). For oscillations much faster than p53, droplets would still emerge, but they would in this regime dissolve well before the sites could be fully repaired (Figure 2B, right). Therefore, this result suggested that optimal frequencies for oscillations could exist. Simulating the system over a wide range of frequencies, we found that the only ones able to achieve a full DNA repair—within a maximum simulation time of 100 h—were those on the timescale of hours (Figure 2C). In those cases of full damage repair, we further recorded the time to reach this condition, which we indicated by a color gradient from blue to red (Figure 2C, see right color bar): *the experimental p53 frequency turned out to be among the most efficient values to repair the damage in the presence of multiple DNA breaks.*

To validate these results, we first simulated the system with several values of damaged sites N , studying whether a high

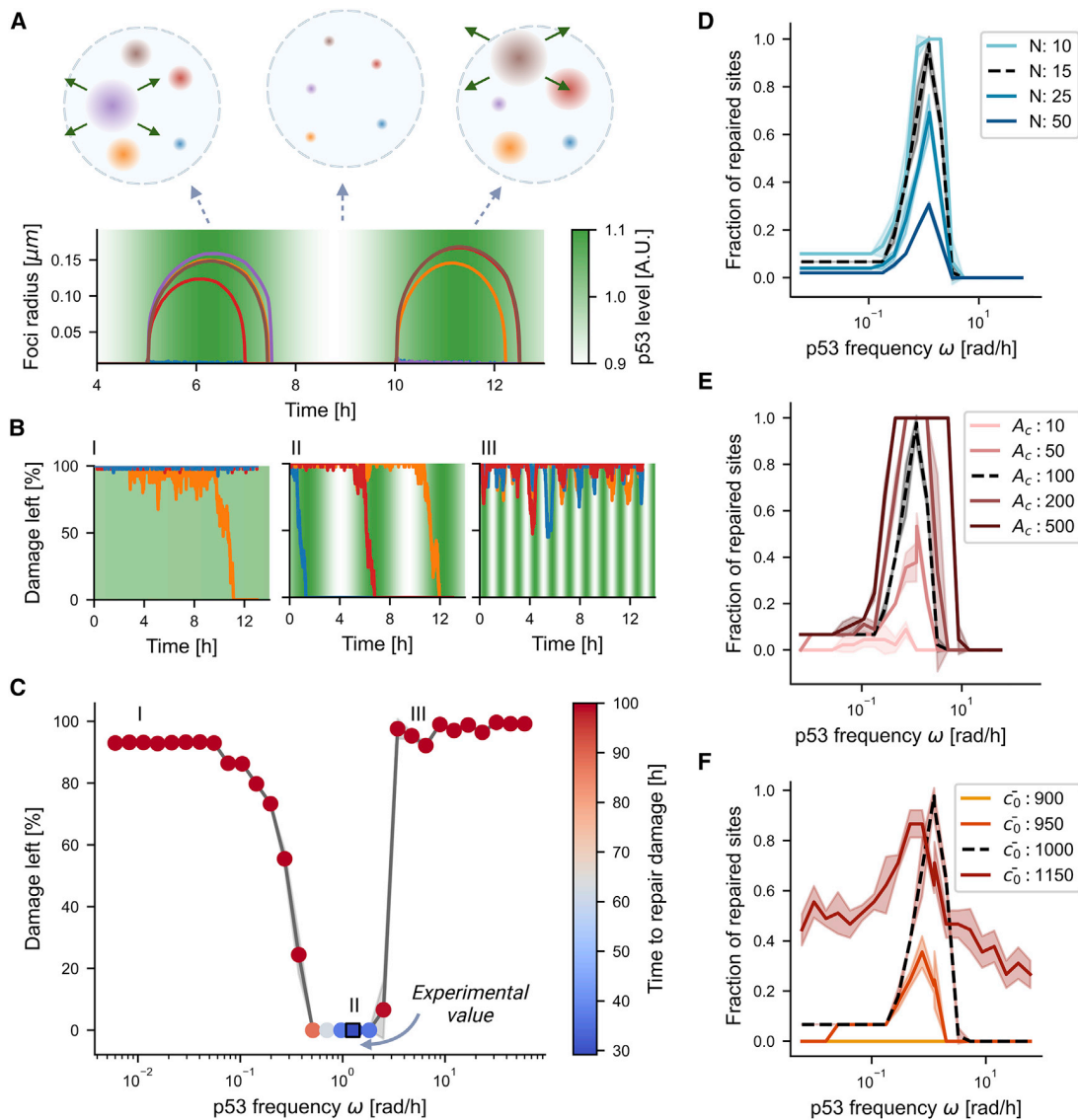


Figure 2. p53 periodicity optimizes the damage repair process in the fast droplets formation regime

(A) Droplet sizes at various points in time (above) and the radii of five damaged sites (below) in the presence of p53 oscillatory dynamics (green gradient). (B) Damage at each individual site as a function of time (note that, for simplicity, only three traces out of the $N = 15$ are shown here). Left: $\omega = 0.01 \text{ rad h}^{-1}$; middle: $\omega = 2\pi/5.5 \text{ rad h}^{-1}$ (experimental value); right: $\omega = 5 \text{ rad h}^{-1}$. (C) The total amount of damage left on the sites after 100 h as a function of applied frequency. For the sites that were fully repaired, the color bar indicates the time necessary to remove all the damage. (D) Fraction of repaired sites after 30 h as a function of frequency. The four curves represent different initial numbers of damaged sites N , while the shaded area corresponds to the SD. The black dashed curve corresponds to the parameters used in (C) (with the only difference of a shorter simulation time). (E) Same as (D) but shown for five different values of the oscillatory amplitude A_c . (F) Same as (D) but shown for four different values of the mean concentration level \bar{c}_0 . The shaded region in (C)–(F) corresponds to the SD calculated by simulating the system multiple times, and assuming Gaussian errors, dividing by the square root of the number of runs. See Table S2 for the specific parameters used in this figure.

competition among numerous sites would prevent the droplets from reaching an optimal radius within the considered periods. On the contrary, we found that the peak in the fraction of repaired sites was conserved over a wide range of N (Figure 2D). Next, we investigated how the result depended on the amplitude and

found that increasing amplitudes enhance the overall repair rate of the system (Figure 2E). Finally, we tested the dependency on \bar{c}_0 , since this had so far only been evaluated at the critical level. What we found is that for low values of \bar{c}_0 , the repair rate is significantly decreased, which is not surprising since the

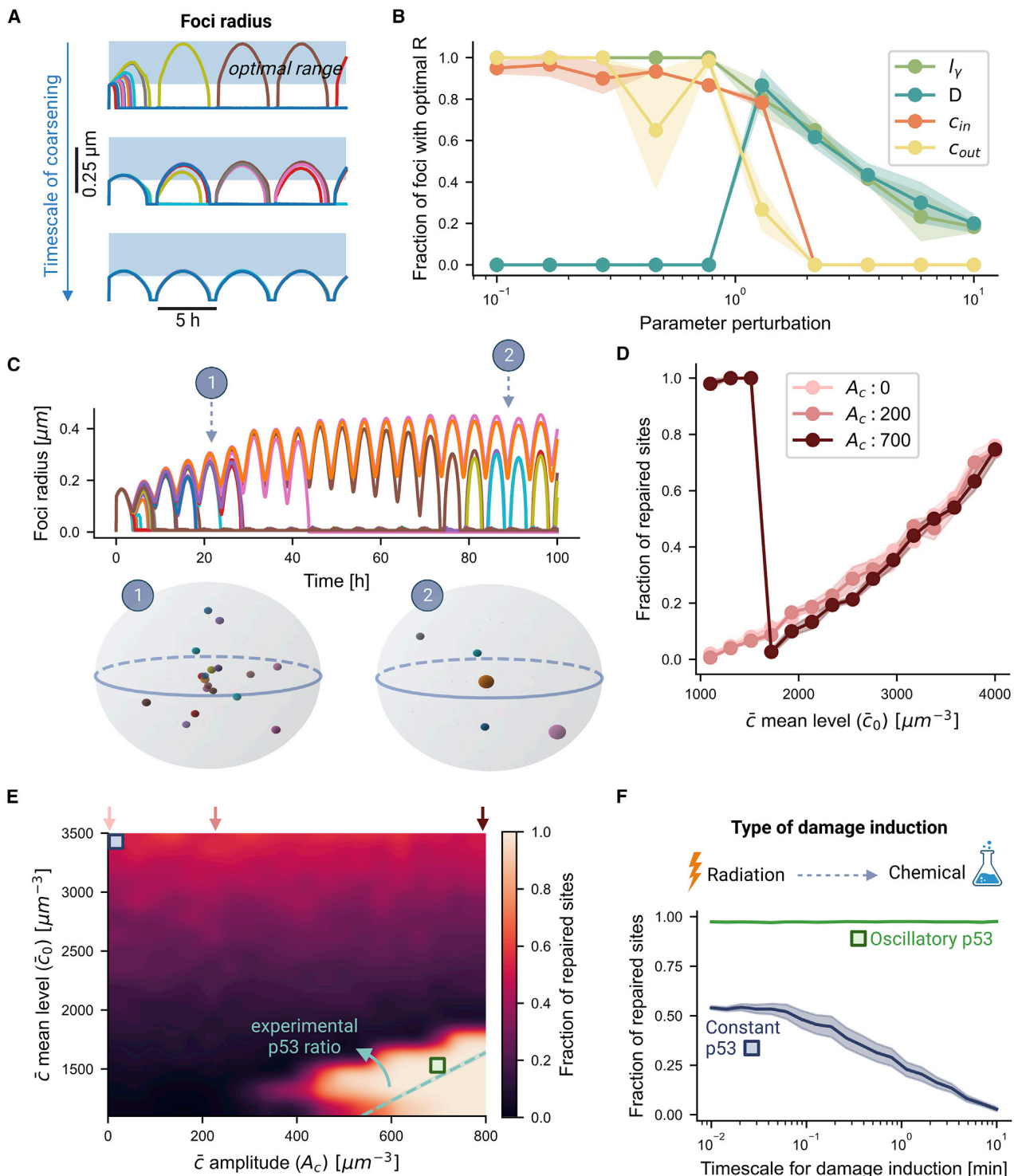


Figure 3. p53 oscillations stabilize droplets sizes in the slow droplets formation regime

(A) Foci radius as a function of time. Three graphs shown for increasing timescales of coarsening (obtained by varying I_γ). The light-blue shaded region indicates the optimal range of radii for which repair of one step of damage takes less than 0.5 min.

(B) Fraction of droplets around a specific site that spend time in the optimal range, for variations in the parameters I_γ , D, C_{in} , and C_{out} . See also Figure S2.

(C) Radii of individual foci as a function of time, when the average concentration is above the critical concentration. Different colors correspond to different foci. Points 1 and 2 (below) visualize the droplet environment at these specific points in time.

(legend continued on next page)

critical concentration spends less time above the critical state; therefore, droplets exist for shorter times. However, by increasing the level of \bar{c}_0 , the repair rate is less sensitive to the frequency, and the maximal repair rate is reduced compared to the critical concentration (Figure 2F). This suggested a fundamental relation between the amplitude of oscillations A_c and the average concentration level \bar{c}_0 .

We speculated that enhancing the average concentration might change the number of stable droplets as more material might be available, thereby enhancing the overall repair rate significantly.

Stabilization and optimization of multiple droplets by enhancing amplitudes

At this stage, our results had revealed how the oscillatory behavior of p53 could distribute the limited resources at the specific damaged sites over time. This naturally brought up the questions (1) what would happen with a wider availability of droplet material, and (2) how would the whole picture be altered in case of a faster/slower droplet coarsening?

To shed light on this, we first considered two factors: in particular, the point when competition for material starts and the point when Ostwald ripening is “complete”—i.e., when one droplet has become dominant. The first occurs when $c_\infty \approx c_{out}$, and following Equation 2, one can derive the formula for the volume of the i -th droplet V_i at which competition for material starts (see STAR Methods),

$$V_i \approx \frac{\bar{c} - c_{out}}{c_{in} - c_{out}} \cdot \frac{V_n}{N} \approx \frac{\bar{c} - c_{out}}{c_{in}} \cdot \frac{V_n}{N}, \quad (6)$$

the last holding since $c_{in} \gg c_{out}$. Consequently, we derived the timescale of Ostwald ripening (T_{OR}), that is the time necessary for one droplet to dominate on the others (Söding et al., 2020) (see STAR Methods), which takes the form

$$T_{OR}(R) = \frac{R_c}{D l_\gamma} \frac{c_{in}}{c_{out}} R^2, \quad (7)$$

where R_c is the critical radius for the system in steady state. If the timescale of coarsening is lower than the period of p53 oscillations, the dominating droplet quickly prevails within each period, preventing all the others from growing (Figure 3A, top). On the other hand, for longer T_{OR} , multiple droplets, with volume given by Equation 6, may co-exist within each oscillation (Figure 3A, bottom) as Ostwald ripening (and competition for material) would occur at a much later time. The latter would seem like the optimal scenario for the cell, which would be able to repair multiple sites simultaneously within each period. It should be noted, though,

that in this case the maximum radius reached by the droplets is lower than before, as material is distributed equally among all of them. Following this reasoning, we defined an “optimal range” of radii (light-blue shaded region of Figure 3A) around the minimum of τ (Equation 3), where damage repair would be the fastest and chose an interval such that one damage removal would take less than 0.5 min. At this point it was clear that a slower timescale of coarsening would benefit the cell only in the presence of enough material to distribute among the foci, in order to perform a parallel repair of multiple damaged sites.

Following Equation 7, we then investigated the role of the different parameters ($D, c_{in}, l_\gamma, c_{out}$) in altering the timescale of coarsening and consequently the number of droplets whose radius is within the optimal range (Figure 3B). We found that increasing l_γ leads to a shorter timescale of coarsening and therefore a lower number of droplets whose size is in the optimal range. Increasing the diffusion coefficient D both results in a fast timescale of coarsening but also in a wider range of optimal radii. On the other hand, greater c_{in} results in progressively smaller droplets that do not grow in the optimal range. Finally, we realized that varying c_{out} over two orders of magnitude, such that the system transitions from being constantly supersaturated ($c_{out} < \bar{c}$) to undersaturated ($c_{out} > \bar{c}$) leads to stabilization of droplets in the first case and impossibility to grow in the latter (see Figure S2 for explanatory panels).

Next, we further investigated what would happen if the mean concentration were significantly increased, such that oscillations of \bar{c} would always be above the critical concentration c_{out} . In this case the system revealed an interesting property: while Ostwald ripening still occurs in the sense that one droplet dominates in the end (Figure 3C, point 2), the meta-stable state can exist for a very long time (Figure 3C, point 1), and many of the otherwise dissolved sites still show droplets emerging. However, in this picture the Ostwald ripening also results in a vast amount of material centered around a few number of sites until only one dominates.

Therefore, we wondered how the number of repaired sites would scale as the mean concentration were elevated. We found that in the absence of oscillations, there is a linear relation between the number of repaired sites and the mean concentration (Figure 3D, pink curve). The reason is that increasing the amount of material leads to more states that can co-exist in the meta-stable state before they dissolve, resulting in more repaired sites. However, introducing oscillations and increasing the amplitude, we observed a new region emerging, where the damage is resolved at a much higher rate (Figure 3D, brown curve). In this regime the effect of the oscillations is large enough to prevent the Ostwald ripening, while there is still enough material available for droplets to grow to optimal sizes. This suggested a non-trivial relation between the average concentration and the values of the

(D) Fraction of fully repaired sites as a function of the mean concentration level. Curves are shown for three different values of the amplitude.

(E) Heatmap showing the fraction of repaired sites (indicated by colormap) as a function of the amplitude (x axis) and the mean concentration level (y axis). The three small arrows on the top correspond to the three values of A_c investigated in (D). The light-blue dashed line represents the experimental p53 ratio between the average p53 level and its amplitude. The green and blue squares show the parameters used in (F).

(F) Fraction of repaired sites assuming different timescales for damage induction, spanning from fast (radiation induced) to slow (chemically induced); oscillatory p53 (green line) is always advantageous against constant p53 level (blue line). The shaded region in (B), (D), and (F) corresponds to the SD calculated by simulating the system multiple times, and assuming Gaussian errors, dividing by the square root of the number of runs.

See Table S3 for the specific parameters used in this figure.

amplitude, and we realized that a region of optimal DNA repair emerged for large values of the amplitude and intermediate values of the mean concentration (Figure 3E). Moreover, we quantified the ratio r between mean level and amplitude in the experimental p53 signal (Figure 1B), obtaining $r = 2.050 \pm 0.023$. Very interestingly, by plotting the line with slope corresponding to r , we discovered that it spans precisely the region of optimal repair (light-blue dashed line, Figure 3E).

Up to now, we have considered an instantaneous initial nucleation (corresponding to irradiation), but in nature damage might often be chemically induced reflected by a longer timescale, and thereby higher variation, in the initial nucleation time. We observed that for a large time of damage induction, some initially larger droplets quickly take up all material, leading to non-optimal repair (Figure 3F, blue line). This does not affect the droplets in the presence of p53 oscillations (Figure 3F, green line), which ensure the distribution of material to different sites over time.

This aspect highlights the overall advantageous effect of p53 oscillations compared to constant levels.

Enhancing the repair by parameter stimulation and noise induction in the p53 network

Finally, we combined the theory of droplets with the p53-Mdm2 protein network, in order to make predictions on how altering this network, with stochastic noise, affects the DNA repair. The network of p53 takes the form (Mengel et al., 2010):

$$\begin{aligned} \frac{dp}{dt} &= k_1 - k_2 M \frac{p}{k_3 + p} \\ \frac{dm}{dt} &= k_4 p^2 - k_5 m \\ \frac{dM}{dt} &= k_6 m - k_7 M \end{aligned} \quad (8)$$

where p , m , and M are the concentration of p53, of Mdm2-mRNA, and Mdm2 itself, respectively. In this model, the material forming droplets still follow p53 concentration linearly, and p53 is produced at a fixed rate (k_1) and degraded following binding to Mdm2 by a saturated degradation process (k_2, k_3). The Mdm2-mRNA is produced proportionally to the p53 level squared—since p53 acts as a dimer—scaling with a production parameter (k_4) and degraded through a first-order decay process (k_5). Finally, the protein Mdm2 is produced proportionally to the Mdm2-mRNA with constant k_6 and again degraded through a first-order decay process (k_7). Inspired by previous analyses, we used simulations to make the network agree with the biological findings, where p53 levels are constant until stimulated externally, at which point oscillations arise with a frequency of ~ 5.5 h (Figure 4A).

In order to include stochasticity, we simulated the model using the Gillespie algorithm (see STAR Methods), which let us combine the dynamics of p53 with the dynamics of droplet formation and damage removal. We first analyzed the behavior of the limit cycle by varying the parameters with particular interest in the role of enhanced degradation (k_2), since we have previously revealed that this is a main component in the induction of

p53 oscillations (Heltberg et al., 2019a). We found that high values of k_2 result in low, non-oscillatory, steady-state levels of both p53 and Mdm2. On the other hand, decreasing k_2 gives rise to a Hopf-bifurcation and a stable limit cycle, but very low levels of this parameter again lead to a non-oscillatory state, regardless of the p53 and Mdm2 levels. We visualized this by plotting the levels of p53 versus the level of Mdm2 after the transient phase, where the dynamics had reached the steady state. In the phase spanned by their concentrations, we observed how the limit cycle can emerge for intermediate values of k_2 (Figure 4B, top). The same behavior can be obtained by increasing the Mdm2 production rate k_4 , whereas increasing the p53 production by enhancement of k_1 mainly results in a continuous increase in the amplitude of p53 (Figure 4B, bottom). See Figure S3 for the correspondent time series. Based on these considerations, we investigated the repair rate by perturbing the three parameters, k_1 , k_2 , and k_4 (Figure 4C). The regions of optimal repair were those corresponding to high amplitudes and optimal mean levels for the p53 signals, obtained for intermediate values of k_2 and k_4 (red and purple curves) and high values of k_1 (yellow curve).

Finally, we investigated the role of noise in the p53 oscillations on the droplet formation and repair rate (Figure 4D). Visualizing the p53-Mdm2 trajectories in polar coordinates (see STAR Methods) reveals that higher noise levels amplify the SD, pushing the radial coordinate outward and therefore leading to effectively enhanced amplitudes (Figure 4E).

Based on these observations, we hypothesized that stochasticity in the oscillator could be a method to further enhance the repair rate, and we found that this is particularly effective for situations with many damaged sites (Figure 4F). Thereby, we concluded that the protein network could be tweaked to optimize the repair rate both through adjusting the parameters and enhancing the stochasticity.

This theoretical work overall reveals how the dynamics of oscillations can be used in saturated environments, to distribute resources over nucleation points in time and space. This in turn not only prevents the Ostwald ripening from introducing a monopoly on resources for one large droplet but also enables a few droplets of optimal size to exist instead, thereby optimizing the use of material. In Figure 4G, we have schematically summarized these conclusions into a working model that might stimulate future research in the combination of dynamics and phase transitions. Based on this, we wanted to experimentally test the most striking feature of our conclusions: that the oscillatory dynamics in p53 would enhance the efficiency of DNA repair.

Model's predictions and their validation

Our theoretical model directly leads to predictions that can be experimentally tested (Figure 5A). Since the mechanism proposed is quite delicate, depending on the quantitative nature of the biological oscillators (e.g., period, amplitude), we believe it should be tested in multiple cell lines, possibly including non-cancerous ones. Indeed, the fine balance of phase transitions and the ability to form and dissolve repair foci could easily be disturbed or suppressed in a cell-line- and context-dependent manner.

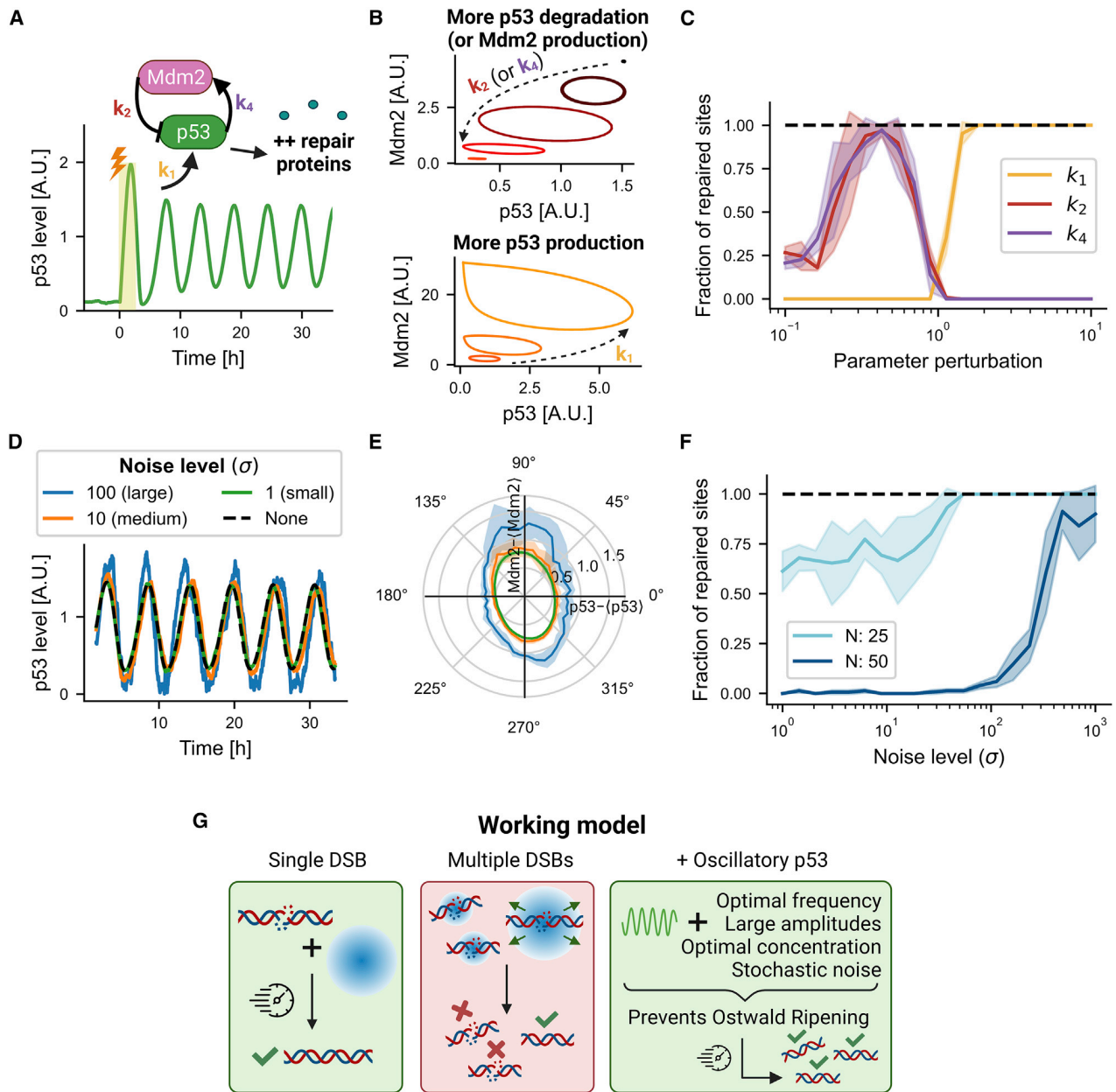


Figure 4. Tweaking p53 network parameters and enhancing the stochasticity may optimize the repair rate

(A) Simulated trace of p53 according to the model of Equation 8, following induction of damaged sites.

(B) Visualization of the steady-state phase space, spanned by p53 and Mdm2, for different parameter choices. Top: increased p53 degradation, thus higher k_2 . Note that increased Mdm2 production (i.e., higher k_4) leads to the same behavior (not shown). Bottom: increased p53 production, thus higher k_1 . See also Figure S3.

(C) Fraction of repaired sites, as a function of parameter perturbations in the parameters k_1 , k_2 , and k_4 . Shaded areas correspond to the SD on these numbers.

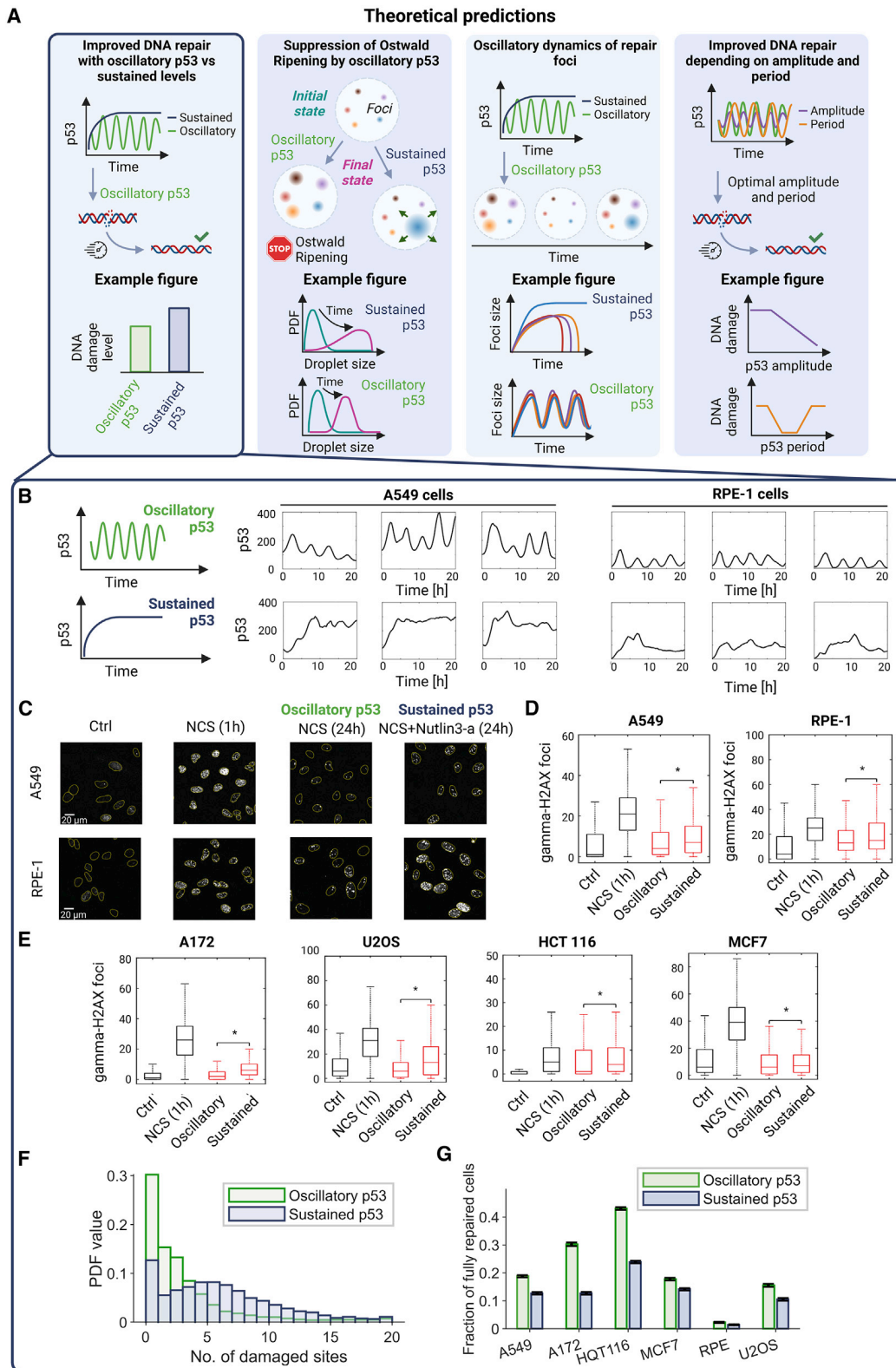
(D) Nuclear concentration of p53 as a function of time, shown for three different levels of noise and the related deterministic simulation.

(E) The p53-Mdm2 phase space transformed into polar coordinates, shown for the three levels of noise. In both (D) and (E), noise was introduced by applying the Gillespie algorithm.

(F) Fraction of fully repaired sites as a function of the applied noise level in the external concentration oscillations. Two curves shown for different numbers of initially induced damaged sites. Shaded areas correspond to the SD on these numbers.

(G) Schematic figure, revealing the working model of how a single damaged site can be repaired fast and efficiently through the formation of a droplet and how multiple damaged sites need external dynamics to prevent Ostwald ripening and maintain this functioning role.

See Table S4 for the specific parameters used in this figure.



(legend on next page)

The first of our predictions is that the p53 oscillations should be more efficient in repairing DNA damage compared to sustained levels, leading to a higher number of fully repaired sites. This can be experimentally tested by controlling the p53 dynamics—oscillatory vs. sustained—and by measuring in each case the DNA damage level, as shown in an “example figure” in [Figure 5A](#), left.

Second, we predict that the oscillations in p53 can prevent the coarsening of DNA repair foci and thereby prevent some droplets from growing to extreme sizes. This could be tested by measuring the size distribution of DNA repair foci at different time points, similar to [Pessina et al. \(2019\)](#)—the authors there used U2OS cells, whose p53 dynamics is highly sensitive to the level of genotoxic stress and is dose dependent ([Stewart-Ornstein and Lahav, 2017](#); [Yang et al., 2018](#)); therefore, it is likely not oscillatory under their conditions (2 Gy). Due to Ostwald ripening, the foci would grow to larger sizes in case of sustained p53 levels ([Figure 5A](#), bottom mid-left). To monitor the coarsening of the DNA damage foci, there are two candidate markers, 53BP1 ([Pessina et al., 2019](#)) and MRNIP ([Wang et al., 2022b](#)). Distinct in their function, 53BP1 and MRNIP represent the DNA damage repair foci via the mechanisms of non-homologous end-joining (NHEJ) and homologous recombination (HR), respectively. These markers can be introduced to a p53 reporter cell line for simultaneous quantification of p53 and DNA damage foci dynamics.

Third, our prediction is that the DNA repair foci, in the presence of p53 oscillations, should show some kind of oscillatory dynamics too. This also means that those repair foci that would disappear under sustained p53 levels, due to Ostwald ripening, should instead be maintained under p53 oscillations. We suggest that this hypothesis could be tested by measuring the dynamics of DNA repair foci in their number and intensity over time ([Figure 5A](#), bottom mid-right).

Finally, our model predicts that p53 may have some optimal amplitude and frequency to perform DNA repair. We suggest to test this aspect by altering the properties of p53 oscillations while quantifying the DNA repair efficiency ([Figure 5A](#), bottom right). Since our predicted valley in [Figure 2C](#) is relatively broad, we suspect that one would need to change the frequency of p53 oscillations by an order of magnitude in order to observe significantly altered results. In contrast, the amplification of the amplitude should lead to an obvious improvement of the DNA repair efficiency.

We therefore sought to experimentally test the most fundamental hypothesis: the oscillatory p53 dynamics promotes DNA repair efficiency. Therefore, we introduced DNA damage by adding neocarzinostatin (NCS), a γ -irradiation mimetic drug that causes DSBs and oscillatory p53 dynamics ([Figure 5B](#), top). In order to achieve sustained p53 dynamics, we added a non-genotoxic small molecule, nutlin-3a, that stabilizes p53 by suppressing its Mdm2-mediated ubiquitination and degradation. Nutlin-3a was added 2.5 and 5.5 h after NCS treatment to obtain sustained p53 dynamics in A549 and RPE-1 cells ([Figure 5B](#), bottom). We then quantified the DNA damage levels by immunofluorescent staining of the γ -H2AX foci before and 1 h after DNA damage, as well as 24 h after DNA damage introduction under the oscillatory or sustained p53 dynamics ([Figure 5C](#)). Note that these DNA damage foci are different from the DNA repair foci (e.g., ones measured in [Pessina et al. \[2019\]](#)) as they have not been shown to exhibit liquid-droplet properties and are merely representing the levels of DNA damage. Based on the immunofluorescent images, we quantified the number of γ -H2AX DNA damage foci in individual cells. [Figure 5D](#) shows that cells with oscillatory p53 dynamics have a lower number of γ -H2AX foci 24 h after NCS treatment, thus exhibiting higher DNA damage repair efficiency, compared to those with sustained p53.

To further strengthen these observations, we carried out the same experiments in four more cell lines: A172, U2OS, HCT116, and MCF7. Interestingly, in all of them, cells with oscillatory p53 dynamics show less γ -H2AX DNA damage foci 24 h after DNA damage compared to those with sustained p53 ([Figure 5E](#)), supporting the prediction of oscillatory p53 in promoting DNA damage repair. To further validate that the distributions of damage differed between cells with oscillatory p53 and sustained levels, we performed a two-sided KS test and obtained p values smaller than 10^{-7} . Finally, we also investigated the fraction of cells that were completely repaired, which is often the most significant value in biology. Here, we found that all cell lines with oscillatory p53 had a larger fraction of fully repaired cells, and calculating the probability that the oscillatory cell lines would have more fully repaired cells, we obtained p values smaller than 10^{-6} for all cell lines (see [Figures 5F](#) and [5G](#)).

Taken together, our experimental results are in strong agreement with the first theoretical prediction and reveal that the oscillations in p53 can enhance the efficiency of DNA repair.

Figure 5. Model-inspired hypotheses and experimental validation

- (A) Schematics showing four theoretical predictions and suggested example figures for validation through experimental measurements.
- (B–E) Experimental results testing the leftmost (encircled) hypothesis.
- (B) p53 oscillatory (top) and sustained (bottom) dynamics in three representative A549 (left) and RPE-1 cells (right).
- (C) Immunofluorescent images of γ -H2AX DNA damage foci under oscillatory and sustained p53 dynamics. DNA damage was introduced by treating cells with NCS (400 ng/ml). Upper: A549 cells; lower: RPE-1 cells. First column: control before introducing DNA damage; second column: 1 h after DNA damage introduction by addition of NCS; third column: 24 h after DNA damage introduction under oscillatory p53 dynamics (NCS treatment alone); fourth column: 24 h after DNA damage introduction in the presence of sustained p53 levels (NCS + nutlin-3a, see [STAR Methods](#) for details).
- (D) Quantification of γ -H2AX DNA damage foci in A549 (left) and RPE-1 cells (right). γ -H2AX foci under oscillatory and sustained p53 dynamics were labeled in red ($n > 1,000$, Wilcoxon rank-sum tests, $*p < 10^{-19}$).
- (E) Quantification of γ -H2AX DNA damage foci in four additional cell lines. From left to right: A172, U2OS, HCT116, and MCF7 ($n > 1,000$, Wilcoxon rank-sum tests, $*p < 10^{-9}$).
- (F) Distribution of the number of damaged sites in cells. Data shown for A172 cell line.
- (G) Barplot showing the fraction of fully repaired sites and the uncertainty on this number.

DISCUSSION

How oscillations in TFs can be used to optimize specific processes and why evolution has created these complex responses remain open and deep questions. The emerging evidence that DNA repair foci might form as a result of liquid-liquid phase separation, inspired us to investigate the interplay between oscillations in TFs, such as p53, and the formation of multiple droplets. We thus revealed that the properties of oscillations can stabilize these structures in an ordered and efficient way, leading to an optimal repair mechanism.

These two aspects had not been combined in areas of biophysics before. Hereby, we do not only show an interesting result based on coupled differential equations but apply a direct biophysical mechanism that mediates the connection and creates the optimal repair strategy, offering clear experimentally testable predictions. The vast majority of parameters applied in this work are well defined from numerous experiments, and even though some values can differ (the number of damaged sites and the concentration inside droplets), our results are robust to variations in these parameters and overall suggest why oscillations can be of fundamental importance.

Droplet formation is a popular topic in science, and many experiments have currently reported the observation of liquid sub-compartments in the cell (Brangwynne et al., 2009; Larson et al., 2017; Strom et al., 2017). Preventing the Ostwald ripening has been the topic of many papers, who sought to create a stationary state in the equation for droplet growth and thereby to chemically stabilize droplet sizes. The mechanism that liquid droplets can oscillate in size, thereby preventing Ostwald ripening, has been shown to occur for nanoparticles (Xin and Zheng, 2012), but other ways to stabilize the droplets have also been suggested. One mechanism, for instance, consists in the inclusion of trapped species in the dense phase (Webster and Cates, 2001), where droplets will grow to a specific (relatively small) size, unless they cross a critical threshold where the large droplets will again grow. Another possibility is to considerably slow down Ostwald ripening—which for normal timescales might be enough to stabilize the emulsions—by lowering the surface tension so that it becomes effectively zero. Moreover, the chemical turnover of droplet material inside the droplet has been recently indicated as another way to obtain a stationary state (Söding et al., 2020; Weber et al., 2019; Zwicker et al., 2015; Kirschbaum and Zwicker, 2021). However, if the droplet material is finite and many damaged sites emerge, preventing Ostwald ripening altogether might not be optimal, since the remaining droplets will then share the material and all be small. With oscillations, in the presence of Ostwald ripening, material can be clustered at some specific sites, only to be redistributed at later times at other sites. We speculate that this might further optimize processes in biology, where material needs to be shared among a variable number of locations.

In this work we focused on how downstream repair is stimulated by p53. We assume for simplicity that the proteins causing the phase transition are stimulated as a linear function of the p53 concentration. Present literature has revealed that p53 not only works as a TF for the proteins related to DNA repair but also directly recruits important proteins such as 53BP1 and DDP1,

whose concentrations seem to scale linearly with the p53 level (Wang et al., 2022a). Moreover, it has been shown that p53 is one of the fastest proteins to relocate to the site of DNA damage, which occurs on timescales of seconds (Wang et al., 2022a), whereas studies *in vitro* have found that p53 itself can form a liquid droplet state (Kamagata et al., 2020; Petronilho et al., 2021). These results may suggest that p53 plays a crucial role on shorter timescales and on a more direct level than what is typically considered as a downstream effect, being a potential main candidate to induce the droplet formation observed in DNA repair. On the other hand, we have shown (Figure S1B) that a non-linear relation between p53 and downstream droplet proteins anyway results in the majority of cases in an oscillatory signal for the droplet proteins concentration.

At the same time, the oscillations in p53 could very well be stimulated themselves by the damaged sites and thereby possibly by the intensity of foci. This could potentially be a sensing mechanism that signals back to the p53 loop and stops it from oscillating when all sites have been successfully repaired. Furthermore, it is well known that cells showing oscillations in the p53 concentration can become senescent after some time, which could again be an interesting signal from the foci structures. We thus hypothesize that the present results are one link in the network that couples p53 dynamics, DNA repair, and ultimately cell-fate decisions.

In this regard, it is also interesting to consider that p53 has been revealed to show circadian oscillations, through the interaction with circadian protein Per2 (Gotoh et al., 2015, 2016). However, these oscillations occur in the absence of multiple damaged sites, which is the main problem investigated in this paper. Nevertheless, if the oscillations of p53 due to DNA damage interfered with the circadian oscillations, there could be an intriguing interplay. Indeed, this would theoretically constitute a set of coupled oscillators, where one could imagine that the periodicity of the damage-related oscillations could entrain to the external, circadian oscillator.

The reparation of damaged sites is a complicated process involving a large number of steps and specific proteins that we mathematically modeled and approximated as a discrete Markov chain. It is important to note that the actual structure of such a chain is not crucial to the results. Indeed, it merely represents the feature of the repair process of having a characteristic time to finish and potentially also the situation where fractionally repaired damaged sites might lose their state if not repaired fully within a characteristic time.

In this work we revealed how oscillations can play an important role both through the amplitude and the periodicity, suggesting that no other type of dynamics (random fluctuations, stability, or chaos) would perform as well, and we validated these theoretical predictions with an experimental verification of the positive role of p53 oscillations on DNA repair. Of course, it is very plausible that the proposed mechanism may work together with other mechanisms in the stabilization of foci and optimization of repair, meaning that the oscillations are only one part of the entire puzzle. Furthermore, there are many other systems with oscillations, for instance in the TF NF- κ B. With the growing evidence that liquid sub-compartments exist in many aspects of cell regulation (Brangwynne et al., 2009; Larson et al., 2017;

Strom et al., 2017), we speculate that these findings might also be fundamental to other aspects of gene regulation in the presence of complex dynamics. If these results really revealed one key role for the oscillations in p53, it would be a major step forward in our understanding of damage repair. It is at least tempting that two fundamental processes in physics might guard one of life's most fundamental regulatory processes.

Limitations of the study

This study presents a theoretical description of droplet formation in an oscillatory field and relates it to the process of DNA repair. Here, we describe the simplified scenario of a binary phase separation along with identical repair proteins. Future research should investigate the properties of this in more complex phase separations and in the presence of active emulsions that might further stabilize the droplets. Furthermore, while the liquid nature of the repair foci has been well established, it is of fundamental importance to reveal which proteins are responsible for creating this phase transition *in vivo*. While we have successfully obtained one experimental validation of the hypotheses of the model, our work is fundamentally of theoretical character, and it needs to be thoroughly tested *in vivo* under many different conditions. The main foundations of the work are (1) DNA repair happens in the presence of droplet formation and (2) p53 stimulates numerous DNA repair processes and shows sustained oscillations following severe degree of DNA damage. These are both well established from experiments, but future experimental work should test whether p53 mediates the phase transitions (either directly by causing the phase separation of indirectly by upregulating proteins responsible for the phase separation) and whether the repair foci can show signs of oscillatory dynamics. We also acknowledge that the experimental results presented in this paper might not produce complete evidence of the specific theoretical mechanisms proposed, and further validation is still needed to reveal the important roles of p53 oscillations.

STAR★METHODS

Detailed methods are provided in the online version of this paper and include the following:

- **KEY RESOURCES TABLE**
- **RESOURCE AVAILABILITY**
 - Lead contact
 - Materials availability
 - Data and code availability
- **EXPERIMENTAL MODEL AND SUBJECT DETAILS**
 - Cell culture
- **METHOD DETAILS**
 - Live cell imaging
 - Single cell tracking and p53 level quantification
 - Immunofluorescence
 - γ -H2AX foci quantification
 - Parameter estimates
 - First passage time in the Smoluchowski limit
 - Derivation of droplet growth
 - Simulation of droplet growth and damage repair with the Gillespie algorithm

- Transition from diffusion to Ostwald ripening
- Ostwald Ripening timescale of coarsening
- Visualizing p53 dynamics in polar coordinates
- On non-linear p53 stimulation and the dependency of waveforms

● QUANTIFICATION AND STATISTICAL ANALYSIS

SUPPLEMENTAL INFORMATION

Supplemental information can be found online at <https://doi.org/10.1016/j.cell.2022.10.004>.

ACKNOWLEDGMENTS

We are grateful to Galit Lahav, Michael Tsabar, Yonatan Chemla, Judith Miné-Hattab, Angela Taddei, Aleksandra Walczak, and Thierry Mora for inspiration in the work on DNA repair, p53 dynamics, focus formation, and first passage times. We thank Chia-Chou Wu in the Lab for Cell Dynamics for his help with image analysis. This project has received funding from the European Research Council (ERC) under the European Union's Horizon 2020 research and innovation program under grant agreement no. 740704. S.H.C. acknowledges the funding supports from the Taiwan National Science and Technology Council (grant: 111-2311-B-001-012) and from Academia Sinica (grant: AS-CDA-108-L01). M.S.H. acknowledges the Carlsberg Foundation (grant: CF20-0621) and the Lundbeck Foundation (grant: R347-2020-2250). M.H.J. acknowledges support from the Independent Research Fund Denmark (grant: 9040-00116B) and from the Novo Nordisk Foundation (grant: NNF20OC0064978). [Figures 1–5](#) were created with [BioRender.com](#).

AUTHOR CONTRIBUTIONS

Planning and conceptualization, M.S.H. and M.H.J.; Simulations and mathematical analysis, M.S.H. and A.L.; Experimental design, F.-S.H. and S.-h.C.; Carrying out the experiments, F.-S.H.; Analysis of the experimental results, D.P.M.N. and S.-h.C.; Writing the manuscript, M.S.H., A.L., S.-h.C., and M.H.J.; Editing the manuscript, M.S.H., A.L., S.-h.C., and M.H.J.

DECLARATION OF INTERESTS

The authors declare no conflict of interests.

INCLUSION AND DIVERSITY

We support inclusive, diverse, and equitable conduct of research.

Received: April 13, 2022

Revised: August 23, 2022

Accepted: October 5, 2022

Published: November 10, 2022

REFERENCES

- Batchelor, E., Mock, C.S., Bhan, I., Loewer, A., and Lahav, G. (2008). Recurrent initiation: a mechanism for triggering p53 pulses in response to DNA damage. *Mol. Cell* 30, 277–289. <https://doi.org/10.1016/j.molcel.2008.03.016>.
- Brangwynne, C.P., Eckmann, C.R., Courson, D.S., Rybarska, A., Hoesge, C., Gharakhani, J., Jülicher, F., and Hyman, A.A. (2009). Germline P Granules Are Liquid Droplets That Localize by Controlled Dissolution/Condensation. *Science* 324, 1729–1732. <https://doi.org/10.1126/science.1172046>.
- Chen, S.-h., Forrester, W., and Lahav, G. (2016). Schedule-dependent interaction between anticancer treatments. *Science* 351, 1204–1208. <https://doi.org/10.1126/science.aac5610>.
- Gaglia, G., Guan, Y., Shah, J.V., and Lahav, G. (2013). Activation and control of p53 tetramerization in individual living cells. *Proc. Natl. Acad. Sci. USA* 110, 15497–15501. <https://doi.org/10.1073/pnas.1311126110>.

- Geva-Zatorsky, N., Rosenfeld, N., Itzkovitz, S., Milo, R., Sigal, A., Dekel, E., Yarnitzky, T., Liron, Y., Polak, P., Lahav, G., and Alon, U. (2006). Oscillations and variability in the p53 system. *Mol. Syst. Biol.* 2, 2006.0033. <https://doi.org/10.1038/msb4100068>.
- Gotoh, T., Kim, J.K., Liu, J., Vila-Caballer, M., Stauffer, P.E., Tyson, J.J., and Finkielstein, C.V. (2016). Model-driven experimental approach reveals the complex regulatory distribution of p53 by the circadian factor Period 2. *Proc. Natl. Acad. Sci. USA* 113, 13516–13521. <https://doi.org/10.1073/pnas.1607984113>.
- Gotoh, T., Vila-Caballer, M., Liu, J., Schiffhauer, S., and Finkielstein, C.V. (2015). Association of the circadian factor Period 2 to p53 influences p53's function in DNA-damage signaling. *Mol. Biol. Cell* 26, 359–372. <https://doi.org/10.1091/mbc.e14-05-0994>.
- Hahnfeldt, P., Sachse, R.K., and Hlatky, L.R. (1992). Evolution of DNA damage in irradiated cells. *J. Math. Biol.* 30, 493–511. <https://doi.org/10.1007/bf00160533>.
- Heltberg, M., Kellogg, R.A., Krishna, S., Tay, S., and Jensen, M.H. (2016). Noise Induces Hopping between NF- κ B Entrainment Modes. *Cell Syst.* 3, 532–539.e3. <https://doi.org/10.1016/j.cels.2016.11.014>.
- Heltberg, M.L., Chen, S.-H., Jiménez, A., Jambhekar, A., Jensen, M.H., and Lahav, G. (2019a). Inferring Leading Interactions in the p53/Mdm2/Mdmx Circuit through Live-Cell Imaging and Modeling. *Cell Syst.* 9, 548–558.e5. <https://doi.org/10.1016/j.cels.2019.10.010>.
- Heltberg, M.L., Krishna, S., and Jensen, M.H. (2019b). On chaotic dynamics in transcription factors and the associated effects in differential gene regulation. *Nat. Commun.* 10, 71. <https://doi.org/10.1038/s41467-018-07932-1>.
- Heltberg, M.L., Krishna, S., Kadanoff, L.P., and Jensen, M.H. (2021a). A tale of two rhythms: Locked clocks and chaos in biology. *Cell Syst.* 12, 291–303. <https://doi.org/10.1016/j.cels.2021.03.003>.
- Heltberg, M.L., Miné-Hattab, J., Taddei, A., Walczak, A.M., and Mora, T. (2021b). Physical observables to determine the nature of membrane-less cellular sub-compartments. *Elife* 10, e69181. <https://doi.org/10.7554/elife.69181>.
- Hoffmann, A., Levchenko, A., Scott, M.L., and Baltimore, D. (2002). The I κ B-NF- κ B signaling module: temporal control and selective gene activation. *Science* 298, 1241–1245. <https://doi.org/10.1126/science.1071914>.
- Hyman, A.A., Weber, C.A., and Jülicher, F. (2014). Liquid-liquid phase separation in biology. *Annu. Rev. Cell Dev. Biol.* 30, 39–58. <https://doi.org/10.1146/annurev-cellbio-100913-013325>.
- Jensen, M.H., Sneppen, K., and Tiana, G. (2003). Sustained oscillations and time delays in gene expression of protein Hes1. *FEBS Lett.* 541, 176–177. [https://doi.org/10.1016/s0014-5793\(03\)00279-5](https://doi.org/10.1016/s0014-5793(03)00279-5).
- Kamagata, K., Kanbayashi, S., Honda, M., Itoh, Y., Takahashi, H., Kameda, T., Nagatsugi, F., and Takahashi, S. (2020). Liquid-like droplet formation by tumor suppressor p53 induced by multivalent electrostatic interactions between two disordered domains. *Sci. Rep.* 10, 580. <https://doi.org/10.1038/s41598-020-57521-w>.
- Kilic, S., Lezaja, A., Gatti, M., Bianco, E., Michelena, J., Imhof, R., and Altmeier, M. (2019). Phase separation of 53BP1 determines liquid-like behavior of DNA repair compartments. *EMBO J.* 38, e101379. <https://doi.org/10.15252/emboj.2018101379>.
- Kim, J.K., Josić, K., and Bennett, M.R. (2015). The relationship between stochastic and deterministic quasi-steady state approximations. *BMC Syst. Biol.* 9, 87–13. <https://doi.org/10.1186/s12918-015-0218-3>.
- Kirschbaum, J., and Zwicker, D. (2021). Controlling biomolecular condensates via chemical reactions. *J. R. Soc. Interface* 18, 20210255. <https://doi.org/10.1098/rsif.2021.0255>.
- Kobayashi, T., Mizuno, H., Imayoshi, I., Furusawa, C., Shirahige, K., and Kagayama, R. (2009). The cyclic gene Hes1 contributes to diverse differentiation responses of embryonic stem cells. *Genes Dev.* 23, 1870–1875. <https://doi.org/10.1101/gad.1823109>.
- Lahav, G., Rosenfeld, N., Sigal, A., Geva-Zatorsky, N., Levine, A.J., Elowitz, M.B., and Alon, U. (2004). Dynamics of the p53-Mdm2 feedback loop in individual cells. *Nat. Genet.* 36, 147–150. <https://doi.org/10.1038/ng1293>.
- Larson, A.G., Elnatan, D., Keenen, M.M., Trnka, M.J., Johnston, J.B., Burlingame, A.L., Agard, D.A., Redding, S., and Narlikar, G.J. (2017). Liquid droplet formation by HP1 α suggests a role for phase separation in heterochromatin. *Nature* 547, 236–240. <https://doi.org/10.1038/nature22822>.
- Lifshitz, I., and Slyozov, V. (1961). The kinetics of precipitation from supersaturated solid solutions. *J. Phys. Chem. Solid.* 19, 35–50. [https://doi.org/10.1016/0022-3697\(61\)90054-3](https://doi.org/10.1016/0022-3697(61)90054-3).
- Lisby, M., Barlow, J.H., Burgess, R.C., and Rothstein, R. (2004). Choreography of the DNA damage response: spatiotemporal relationships among checkpoint and repair proteins. *Cell* 118, 699–713. <https://doi.org/10.1016/j.cell.2004.08.015>.
- Matsuda, T., Miyawaki, A., and Nagai, T. (2008). Direct measurement of protein dynamics inside cells using a rationally designed photoconvertible protein. *Nat. Methods* 5, 339–345. <https://doi.org/10.1038/nmeth.1193>.
- Mengel, B., Hunziker, A., Pedersen, L., Trusina, A., Jensen, M.H., and Krishna, S. (2010). Modeling oscillatory control in NF- κ B, p53 and Wnt signaling. *Curr. Opin. Genet. Dev.* 20, 656–664. <https://doi.org/10.1016/j.gde.2010.08.008>.
- Miné-Hattab, J., Heltberg, M., Villemeur, M., Guedj, C., Mora, T., Walczak, A.M., Dahan, M., and Taddei, A. (2021). Single molecule microscopy reveals key physical features of repair foci in living cells. *Elife* 10, e60577. <https://doi.org/10.7554/elife.60577>.
- Mohseni-Salehi, F.S., Zare-Mirakabad, F., Sadeghi, M., and Ghafouri-Fard, S. (2020). A Stochastic Model of DNA Double-Strand Breaks Repair Throughout the Cell Cycle. *Bull. Math. Biol.* 82, 11. <https://doi.org/10.1007/s11538-019-00692-z>.
- Nelson, D.E., Ihekwaba, A.E.C., Elliott, M., Johnson, J.R., Gibney, C.A., Foreman, B.E., Nelson, G., See, V., Horton, C.A., Spiller, D.G., et al. (2004). Oscillations in NF- κ B Signaling Control the Dynamics of Gene Expression. *Science* 306, 704–708. <https://doi.org/10.1126/science.1099962>.
- Nishanov, V.N., and Sobyani, A.A. (1986). Diffusive decay of the metastable state in periodic field. *Phys. Status Solidi* 95, 41–50. <https://doi.org/10.1002/pssa.2210950103>.
- Oshidari, R., Huang, R., Medghalchi, M., Tse, E.Y.W., Ashgriz, N., Lee, H.O., Wyatt, H., and Mekhail, K. (2020). DNA repair by Rad52 liquid droplets. *Nat. Commun.* 11, 695. <https://doi.org/10.1038/s41467-020-14546-z>.
- Pessina, F., Giavazzi, F., Yin, Y., Gioia, U., Vitelli, V., Galbiati, A., Barozzi, S., Garre, M., Oldani, A., Flaus, A., et al. (2019). Functional transcription promoters at DNA double-strand breaks mediate RNA-driven phase separation of damage-response factors. *Nat. Cell Biol.* 21, 1286–1299. <https://doi.org/10.1038/s41556-019-0392-4>.
- Petronilho, E.C., Pedrote, M.M., Marques, M.A., Passos, Y.M., Mota, M.F., Jakobus, B., Sousa, G.d.S.d., Pereira da Costa, F., Felix, A.L., Ferretti, G.D.S., et al. (2021). Phase separation of p53 precedes aggregation and is affected by oncogenic mutations and ligands. *Chem. Sci.* 12, 7334–7349. <https://doi.org/10.1039/d1sc01739j>.
- Reyes, J., Chen, J.-Y., Stewart-Ornstein, J., Karhohs, K.W., Mock, C.S., and Lahav, G. (2018). Fluctuations in p53 signaling allow escape from cell-cycle arrest. *Mol. Cell* 71, 581–591.e5. <https://doi.org/10.1016/j.molcel.2018.06.031>.
- Schindelin, J., Arganda-Carreras, I., Frise, E., Kaynig, V., Longair, M., Pietzsch, T., Preibisch, S., Rueden, C., Saalfeld, S., Schmid, B., et al. (2012). Fiji: an open-source platform for biological-image analysis. *Nat. Methods* 9, 676–682. <https://doi.org/10.1038/nmeth.2019>.
- Schmidt, U., Weigert, M., Broadus, C., and Myers, G. (2018). Cell detection with star-convex polygons. *International Conference on Medical Image Computing and Computer-Assisted Intervention* (Springer), pp. 265–273. https://doi.org/10.1007/978-3-030-00934-2_30.
- Stewart-Ornstein, J., and Lahav, G. (2017). p53 dynamics in response to DNA damage vary across cell lines and are shaped by efficiency of DNA repair and activity of the kinase ATM. *Sci. Signal.* 10, eaah6671. <https://doi.org/10.1126/scisignal.aah6671>.

- Strom, A.R., Emelyanov, A.V., Mir, M., Fyodorov, D.V., Darzacq, X., and Karpen, G.H. (2017). Phase separation drives heterochromatin domain formation. *Nature* 547, 241–245. <https://doi.org/10.1038/nature22989>.
- Sun, H.B., Shen, J., and Yokota, H. (2000). Size-Dependent Positioning of Human Chromosomes in Interphase Nuclei. *Biophys. J.* 79, 184–190. [https://doi.org/10.1016/s0006-3495\(00\)76282-5](https://doi.org/10.1016/s0006-3495(00)76282-5).
- Söding, J., Zwicker, D., Sohrabi-Jahromi, S., Boehning, M., and Kirschbaum, J. (2020). Mechanisms for Active Regulation of Biomolecular Condensates. *Trends Cell Biol.* 30, 4–14. <https://doi.org/10.1016/j.tcb.2019.10.006>.
- Tiana, G., Jensen, M.H., and Sneppen, K. (2002). Time delay as a key to apoptosis induction in the p53 network. *Eur. Phys. J. B* 29, 135–140. <https://doi.org/10.1140/epjb/e2002-00271-1>.
- Wagner, C. (1961). Theorie der Alterung von Niederschlägen durch Umlösen (Ostwald-Reifung). *Ber. Bunsen Ges. Phys. Chem.* 65, 581–591. <https://doi.org/10.1002/bbpc.19610650704>.
- Wang, Y.-H., Ho, T.L.F., Hariharan, A., Goh, H.C., Wong, Y.L., Verkaik, N.S., Lee, M.Y., Tam, W.L., van Gent, D.C., Venkitaraman, A.R., et al. (2022a). Rapid recruitment of p53 to DNA damage sites directs DNA repair choice and integrity. *Proc. Natl. Acad. Sci. USA* 119. e2113233119. <https://doi.org/10.1073/pnas.2113233119>.
- Wang, Y.L., Zhao, W.W., Bai, S.M., Feng, L.L., Bie, S.Y., Gong, L., Wang, F., Wei, M.B., Feng, W.X., Pang, X.L., et al. (2022b). MRNIP condensates promote DNA double-strand break sensing and end resection. *Nat. Commun.* 13, 2638. <https://doi.org/10.1038/s41467-022-30303-w>.
- Weber, C.A., Zwicker, D., Jülicher, F., and Lee, C.F. (2019). Physics of active emulsions. *Rep. Prog. Phys.* 82, 064601. <https://doi.org/10.1088/1361-6633/ab052b>.
- Webster, A.J., and Cates, M.E. (2001). Osmotic stabilization of concentrated emulsions and foams. *Langmuir* 17, 595–608. <https://doi.org/10.1021/la000699m>.
- Xin, H.L., and Zheng, H. (2012). In situ observation of oscillatory growth of bismuth nanoparticles. *Nano Lett.* 12, 1470–1474. <https://doi.org/10.1021/nl2041854>.
- Yang, R., Huang, B., Zhu, Y., Li, Y., Liu, F., and Shi, J. (2018). Cell type-dependent bimodal p53 activation engenders a dynamic mechanism of chemoresistance. *Sci. Adv.* 4, eaat5077. <https://doi.org/10.1126/sciadv.aat5077>.
- Zwicker, D., Hyman, A.A., and Jülicher, F. (2015). Suppression of Ostwald ripening in active emulsions. *Phys. Rev. E Stat. Nonlin. Soft Matter Phys.* 92, 012317. <https://doi.org/10.1103/PhysRevE.92.012317>.

STAR★METHODS

KEY RESOURCES TABLE

REAGENT or RESOURCE	SOURCE	IDENTIFIER
Antibodies		
Anti-phospho-Histone H2A.X (Ser139) Antibody, clone JBW301	Millipore	Cat#05-636; RRID: AB_309864
Goat anti-Mouse IgG (H + L) Highly Cross-Adsorbed Secondary Antibody, Alexa Fluor Plus 647	Invitrogen	Cat#A32728; RRID: AB_2633277
Chemicals, peptides, and recombinant proteins		
Neocarzinostatin from Streptomyces carzinostaticus	Sigma-Aldrich	Cat#N9162
Nutlin-3a	Sigma-Aldrich	Cat#SML0580
DAPI [4,6-Diamidino-2-phenylindole, dihydrochloride]	AAT Bioquest	Cat#17510
Paraformaldehyde 16% (w/v) in aqueous solution methanol-free	Thermo Scientific Chemicals	Cat#43368
DPBS (10X), no calcium, no magnesium	Gibco	Cat#14200075
RPMI 1640 Media	Gibco	Cat#11875093
Antibiotic-Antimycotic (100X)	Gibco	Cat#15240062
Characterized FBS, Canadian Origin	HyClone	Cat#SH30396.03
Albumin, Bovine Serum, Fraction V, low Heavy Metals (BSA)	MerckMillipore	Cat#12659
Triton X-100 Reagent Grade	BioShop	Cat#TRX506
SiR700-DNA Kit	Spirochrome	Cat#SC015
Experimental models: Cell lines		
A172	ATCC	Cat#CRL-1620; RRID: CVCL_0131
A549	ATCC	Cat#CCL-185; RRID: CVCL_0023
HCT116	ATCC	Cat#CCL-247; RRID: CVCL_0291
hTERT RPE-1	ATCC	Cat#CRL-4000; RRID: CVCL-4388
U2OS	ATCC	Cat#HTB-96; RRID: CVCL_0042
MCF7+p53shRNA + p53-mCerulean	Gaglia et al. (2013)	N/A
A549+UbCp-p53-mVenus	Stewart-Ornstein and Lahav (2017)	N/A
RPE-1+UbCp-p53-mNeonGreen	Reyes et al. (2018)	N/A
Software and algorithms		
MATLAB (2020b)	The Mathworks	https://MATLAB.mathworks.com/
Single cell tracking algorithm	Reyes et al. (2018)	https://github.com/balvahal/p53CinemaManual
Fiji	Schindelin et al. (2012)	https://fiji.sc/
StarDist	Schmidt et al. (2018)	https://github.com/stardist/stardist
γ H2AX foci quantification algorithm	This paper	N/A

RESOURCE AVAILABILITY

Lead contact

Further information and requests for resources should be directed to and will be fulfilled by the lead contact, Mogens H. Jensen (mhjensen@nbi.dk).

Materials availability

All materials are commercially available.

Data and code availability

- All data reported in this paper will be shared by the [lead contact](#) upon request.
- All software and code used in this study are available through a Github repository at <https://github.com/MathiasHeltberg/EnhancedDNARepairThroughDropletFormationAndp53Oscillations>.
- Any additional information required to reproduce the simulations and reanalyze the data reported in this paper are available from the [lead contact](#) upon request.

EXPERIMENTAL MODEL AND SUBJECT DETAILS

Cell culture

All cell lines were adopted and maintained in RPMI 1640 media supplemented with 5% FBS and antibiotics (Streptomycin, Amphotericin B, Penicillin). Cells were grown in the humidified incubator at 37°C with 5% CO₂.

METHOD DETAILS

Live cell imaging

A549 and RPE-1 p53 reporter cells were seeded at 2x10³ cells/well in a μ -Plate 96 Well Black plate (ibidi Cat#89626) 1 day before imaging with Nikon Eclipse Ti inverted microscope. Cells were switched to transparent RPMI (RPMI without riboflavin and phenol red, customized by US Biological) 1 h before imaging and SiR700 DNA probe (1:40,000) was added to label nuclei for single-cell tracking purposes. During imaging, cells were maintained in a chamber controlling CO₂ (5%), temperature (37°C), and humidity. Images were acquired every 30 min with appropriate filter sets: SiR700 (ex:640/30; em:700/75) and p53 (ex:510/25; em:544/24). NCS was added to induce oscillatory p53 dynamics. To achieve sustained p53 levels, 0.75 and 0.55 μ M Nutlin-3a were added 2.5 and 5.5h after NCS treatment, respectively.

Single cell tracking and p53 level quantification

Individual cells were tracked using a semi-automated MATLAB program described previously ([Reyes et al., 2018](#)). p53 level was quantified by averaging the p53 signals within the cell nucleus. Individual p53 traces were smoothed using a 1h sliding window.

Immunofluorescence

Cells were seeded at 2x10³ cells/well in 96-Well Micro-Well Plates (Nunc Catt#167008) 2 days before NCS treatment. After treatment, cells were fixed at indicated time in 4% paraformaldehyde for 10 min, washed three times with PBS, and then permeabilized with PBS containing 1% Triton X-100 for 5 min at room temperature. After permeabilization, cells were blocked in antibody dilution buffer (2% BSA and 0.1% Triton X-100 in PBS) for 1 h, followed by primary antibody (Anti-phospho-Histone H2A.X Ser139, 1:1000) incubation overnight at 4°C. Cells were then washed three times in PBS, incubated in antibody dilution buffer containing secondary antibodies (Goat anti-Mouse Alexa FluorPlus 647, 1:1000) for 1 h, followed by DAPI staining (5 μ g/ml in PBS) for 5 min at room temperature. Cells were washed three times with PBS and imaged with ImageXpress Micro XL High-Content Screening System (Molecular Device). The filter settings: Cy5 (ex:628/40; em:692/40) and DAPI (ex:377/50; em:447/60).

γ -H2AX foci quantification

Cell nuclei were segmented according to DAPI signals using StarDist ([Schmidt et al., 2018](#)), a plugin for Fiji ([Schindelin et al., 2012](#)). Images of the γ -H2AX (Cy5 channel) were background subtracted (rolling ball radius: 50 pixels) prior to quantification. γ -H2AX foci were quantified using custom MATLAB scripts. Generally, within each nucleus, Cy5 intensities below an absolute intensity threshold were filtered out. For nuclei with strong Cy5 background, the intensities were normalized to range between 0 and 1 and pixels below a normalized intensity threshold were filtered out. Peaks of Cy5 intensities with prominences above a threshold were detected using the findpeaks function in MATLAB. The coefficient of variation (CV) in intensity between each detected peak and its adjacent pixels were taken. Peaks with CV above a threshold stood out well from its surrounding and therefore were considered as γ -H2AX foci centroids. The number of such centroids in each nucleus represented the number of presenting γ -H2AX foci. All thresholds were determined manually for each cell line to best match visual inspection of γ -H2AX foci.

Parameter estimates

- D : The diffusion coefficient in the nucleus. This has been thoroughly investigated in the past, and even though it differs for different types of proteins, it can be roughly approximated as $D \approx 10 \mu\text{m}^2 \text{s}^{-1}$.
- D_0 : The diffusion coefficient inside the focus. This has been estimated in the work of [Miné-Hattab et al. \(2021\)](#), where it is shown to be 1/100 D . Even though it might vary for different types of proteins, this should reflect the right order of magnitude.
- c_{in} : The protein concentration inside droplets. [Söding et al. \(2020\)](#) estimate the internal concentration of biomolecular condensates, assuming a 1:1 protein to water ratio, a protein density similar to water and a protein molecular weight of 30kDa, obtaining $c_{in} \approx 17 \text{mM}$. This corresponds to $\approx 10^7$ molecules μm^{-3} . In order to confine the search, we have fixed $c_{in} \approx 10^6 \mu\text{m}^{-3}$.

- l_γ : The capillary length of the droplets. This is typically estimated to follow the relation: $l_\gamma \approx (2\gamma / c_{in}k_B T)$, with γ being the surface tension of the droplets. From the work of [Pessina et al. \(2019\)](#) γ is roughly $0.1 \mu Nm^{-1}$, which together with the previous estimate of c_{in} , define a physiological value for l_γ .
- c_{out} : The protein concentration outside droplets. We know that in a supersaturated environment proteins are enriched in the condensates. [Söding et al. \(2020\)](#) estimate the ratio of $c_{in}/c_{out} \approx 100$. In our paper, again to confine the search, we fixed this ratio to 1000.
- N : The number of foci arising as a result of DNA damage has been measured by [Pessina et al. \(2019\)](#) to be approximately 30, and anyway in the range 10–100, therefore we also considered values in this range.
- ω : The p53 periodicity has extensively been measured in the past ([Lahav et al., 2004](#)).
- \bar{c} : We have fixed the average concentration of repair proteins to be close to c , so that the oscillations of p53 of the right amplitude would make the environment oscillate between being supersaturated and undersaturated.
- A : We have varied the amplitude of the oscillations in a range such that the ratio \bar{c}_0/A_c would be consistent with the ratio of p53 mean level and amplitude.
- M : The number of steps necessary to repair the DNA damages. [Hahnfeldt et al. \(1992\)](#) modeled the evolution of DNA damage in irradiated cells as a Markov chain, in which several steps had to be accomplished to achieve full repair. In a recent biophysical work ([Mohseni-Salehi et al., 2020](#)), the DNA repair process is modeled as a Markov chain and the number of possible steps is estimated to be around 20.
- λ : The rate of damage recreation. We assumed that, along with the correct repair mechanisms, “misrepair events” may also occur, such as mistakes by the repair enzymes or a gradual loss of a lesion’s ability to undergo any reaction ([Hahnfeldt et al., 1992](#)). This parameter is not strictly relevant for the conclusions of our work, therefore is assumed to be small for the majority of the simulations. It only serves the purpose to define a timescale for repair processes to be completed.

First passage time in the Smoluchowski limit

In the following we describe the rate of capture for a diffusing molecule, that can get absorbed by (i.e. react with) another molecule. We write up the Smoluchowski equation in spatial coordinates assuming angular symmetry. In the stationary state this takes the form

$$0 = \nabla \cdot D(r)(\nabla - \beta F(r))p(r),$$

with the two boundary conditions:

$$p(r \rightarrow \infty) = c_1 c_2$$

$$D(R_0)(\nabla - \beta F(R_0))p(R_0, t) = \kappa p(R_0)$$

The first guarantees a constant concentration of molecules away from the sphere of interest and the second is the radiation Boundary Condition. The parameter κ defines the absorbance of the binding site. Integrating with respect to the volume and applying Gauss theorem yields

$$\int_V \nabla \cdot D(r)(\nabla - \beta F(r))p(r, t) dV = 4\pi r^2 D(r)(\nabla - \beta F(r))p(r, t)$$

Next, inserting the Boundary Condition 2) and rewriting the first term gives

$$\partial_r (e^{\beta U(r)} p(r)) = \frac{R_0^2 \kappa}{r^2 D(r)} e^{\beta U(r)} p(R_0).$$

Integrating on both sides, from R_0 to ∞ results in

$$\frac{c_1 c_2}{\left(e^{-\beta U(R_0)} R_0^2 \kappa \int_{R_0}^{\infty} \frac{1}{r^2 D(r)} e^{\beta U(r)} dr + 1 \right)} e^{-\beta U(R_0)} = p(R_0).$$

The total radial current into the partially absorbing sphere is equivalent to the rate of absorption:

$$I_{rad} = k^* = 4\pi R_0^2 \kappa p(R_0) = 4\pi R_0^2 \kappa \frac{c_1 c_2}{\left(e^{-\beta U(R_0)} R_0^2 \kappa \int_{R_0}^{\infty} \frac{1}{r^2 D(r)} e^{\beta U(r)} dr + 1 \right)} e^{-\beta U(R_0)}.$$

We define the actual on-rate as a constant multiplied by the concentrations of the two interacting molecules: $k^* = k^+ c_1 c_2$. Therefore removing the dependencies on c_1 and c_2 yields

$$k^+ = \frac{4\pi}{\left(\int_{R_0}^{\infty} \frac{1}{r^2 D(r)} e^{\beta U(r)} dr + \frac{e^{\beta U(R_0)}}{R_0^2 \kappa} \right)}.$$

If we assume that $\kappa \approx 0$ we note that we recover the Arrhenius equation. Assuming diffusion limited reactions (i.e. $U(r) \approx 0$) we get:

$$k^+ = \frac{4\pi}{\int_{R_0}^{\infty} \frac{1}{r^2 D_0} dr + \frac{1}{R_0^2 \kappa}} = \frac{4\pi D_0 R_0}{1 + \frac{D_0}{R_0 \kappa}}$$

We see that we here arrive at the diffusion limited reaction rate ($k^+ = 4\pi D_0 R_0$) if we also assume that $\kappa \rightarrow \infty$. We note here that the classical result derived by Berg and Purcell, where one assumes a surface of small absorbing disks, leads to an on-rate of

$$k_{BP}^+ = 4\pi D R_0 \frac{Na}{\pi R_0 + Na}$$

where a is the radius of the small disks covering the absorbing spheres. These two expressions are therefore equivalent if $\kappa = (NaD / \pi R_0^2)$. We now assume that the absorbing center is in the middle of a liquid droplet, which we model by a spherically symmetric potential $U(r)$. The probability distribution of a molecule is denoted by $p(\mathbf{r}) = p(r)$. The probability density of being at distance r from the absorbing site is given by $q(r) = 4\pi r^2 p(r)$. At steady state with a non-vanishing flux $J = \text{const}$, we have:

$$\left(\frac{2D}{r} - \frac{D}{k_B T} \partial_r U \right) q = D \partial_r q - J.$$

Introducing the variable $\varphi = -2\ln(r) + U/k_B T$, we simplify this as:

$$q \partial_r \varphi + \partial_r q = \frac{J}{D}.$$

By multiplication with e^φ , we obtain:

$$\partial_r (e^\varphi q) = \frac{J}{D} e^\varphi.$$

The general solution to that equation is:

$$q(r) = C e^{-\varphi(r)} + J e^{-\varphi(r)} \int_{r_0}^r \frac{e^{\varphi(r')}}{D(r')} dr'.$$

Here $C = 0$ due to the absorbing boundary condition $q(r_0) = 0$. The constant J is determined by the normalization $\int_{r_0}^{r_n} dr q(r) = 1$ yielding:

$$J^{-1} = \tau_a = \int_{r_0}^{r_n} dr e^{-\varphi(r)} \int_{r_0}^{r_0} dr' \frac{e^{\varphi(r')}}{D(r')},$$

By replacing $\varphi(r)$ by its definition and assuming a strong surface potential of the liquid droplet we directly retrieve [Equation 3](#).

Derivation of droplet growth

We first describe an infinite system with two inhomogeneous phases, whose free energy F is therefore given by

$$F = V_1 f(c_1) + V_2 f(c_2),$$

where f is the free energy density, $V_{1,2}$ are the volumes of the two phases and $c_{1,2}$ are the respective equilibrium concentrations. Assuming that the total volume is constant and that the number of molecules is fixed leads to $V_T = V_1 + V_2$ and $c_T V_T = V_1 c_1 + V_2 c_2$, with V_T being the total volume and c_T the average concentration. Thus F can be written in terms of c_1, V_1, c_T, V_T as

$$F = V_1 f(c_1) + (V_T - V_1) f\left(\frac{c_T V_T - V_1 c_1}{V_T - V_1}\right).$$

The stability of the inhomogeneous state corresponds to a minimum of the free energy in terms of the concentration and the volume of the first phase. Therefore we differentiate the free energy with respect to c_1 and V_1 and equate these to zero, which yields

$$\partial_{c_1} F = 0 \Rightarrow f'(c_1) - f'(c_2) = 0, \tag{S1}$$

$$\partial_{V_1} F = 0 \Rightarrow f(c_1) - f(c_2) + f'(c_2) \cdot [c_2 - c_1] = 0. \tag{S2}$$

Being in the thermodynamic limit, we have been entitled up to now to ignore surface effects. On the contrary, these play a major role in the regime of droplets, where the free energy portrays an additional term ($+A\gamma$, with A being the area of the interface and γ the surface tension). Therefore, in the case of a spherical droplet, the free energy takes the form:

$$F = V_d f(c_{in}) + (V - V_d) f(c_{out}) + 4\pi R^2 \gamma,$$

where $V_d = (4\pi/3)R^3$ is the volume of a spherical droplet of radius R , $c_{in/out}$ are the internal/external concentrations and V is the total volume of the system. With similar reasoning as before, we differentiate with respect to c_{in} and V_d , which results in

$$0 = f'(c_{in}^{eq}) - f'(c_{out}^{eq}),$$

$$0 = f(c_{in}^{eq}) - f(c_{out}^{eq}) + (c_{out}^{eq} - c_{in}^{eq}) f'(c_{out}^{eq}) + \frac{2\gamma}{R},$$

where $c_{in/out}^{eq}$ are the internal/external equilibrium concentrations. We see that the last term (known as the Laplace pressure) is negligible in the thermodynamic limit, in which case we retrieve [Equations S1](#) and [S2](#). At this point we could write the equilibrium concentrations as a first order correction of the correspondent concentration in the thermodynamic limit ($c_{in/out}^{(0)}$), such that $c_{in/out}^{eq} = c_{in/out}^{(0)} + \delta c_{in/out}$. In this way we derive the following expressions:

$$c_{out}^{eq} = c_{out}^{(0)} \cdot \left(1 + \frac{l_\gamma}{R}\right), \quad (S3)$$

$$c_{in}^{eq} \approx c_{in}^{(0)}, \quad (S4)$$

with l_γ defined as the capillary length and the latter expression holding since we consider the case $c_{in}^{(0)} \gg c_{out}^{(0)}$.

We now seek to find an expression for the concentration c of molecules at some distance r from a single droplet of radius R embedded in an infinite medium, knowing that the concentration far away from the droplet is fixed to c_∞ . Given the symmetry of the system, c will only be a function of r . We further assume that the droplet radius varies slowly such that it can be considered constant on the timescale of the diffusing molecules. The concentration gradient then causes a net diffusive flux density through a spherical shell of radius r given by $j(r) = -D \frac{\partial}{\partial r} c(r)$ with D being the diffusion coefficient. Given that the number of molecules is fixed, the total flux across shell surfaces of radius r must be constant, and given by

$$J = -4\pi D r^2 \frac{\partial}{\partial r} c(r) = \text{const.}$$

This equation has solution $c(r) = k_1 + k_2/R$, with constants k_1, k_2 given by the boundary conditions at R and ∞ ($c(R) = c_{out}^{eq}$ as defined in [Equation S3](#) and $c(\infty) = c_\infty$). Therefore the solution reads

$$c(r) = c_\infty + (c_{out}^{eq} - c_\infty) \frac{R}{r} \quad r > R,$$

$$c(r) = c_{in}^{eq} \quad r < R.$$

The total flux of molecules leaving the droplet is

$$J_R = 4\pi D R^2 \frac{\partial}{\partial r} c(r)_{r=R} = -4\pi D R (c_{out}^{eq} - c_\infty). \quad (S5)$$

The variation of the droplet volume is given by $(dV_d/dt) = J_R/c_{in}^{eq}$, that is

$$\frac{d}{dt} \left(\frac{4\pi}{3} R^3 \right) = -\frac{1}{c_{in}^{eq}} 4\pi D R (c_{out}^{eq} - c_\infty),$$

which, rearranged in terms of dR/dt and written in terms of $c_{in/out}^{(0)}$ yields

$$\frac{dR}{dt} = \frac{D c_{out}^{(0)}}{R c_{in}^{(0)}} \left(\frac{c_\infty}{c_{out}^{(0)}} - 1 - \frac{l_\gamma}{R} \right)$$

This expression can be easily generalized in case of N droplets far apart from each other, so that direct interactions can be neglected, while droplets only compete for material exchanging it through the common media. This directly yields [Equation 1](#) and [Equation 2](#) in the main text, where, for simplicity of notation, we have defined $c_{in/out}^{(0)}$ as $c_{in/out}$.

Simulation of droplet growth and damage repair with the Gillespie algorithm

Let us first consider an initial distribution of proteins $n_i \forall i = 1, \dots, N$, and then, given the assumptions of a constant internal concentration c_{in} (such that $V_i = n_i/c_{in}$), and spherical droplets, each radius R_i is computed accordingly as

$$R_i = \left(\frac{3n_i}{4\pi c_{in}} \right)^{1/3}.$$

The concentration far away from each droplet c_∞ is adjusted in order to ensure the mass conservation as

$$c_\infty = \frac{\bar{c}V_n - \sum_i n_i}{V_n - \frac{1}{c_{in}} \sum_i n_i}.$$

The flux of proteins in and out of the droplets is given by Equation S5, while at the same time damage can be repaired or re-created. This gives rise to four possible processes for the i -th droplet, whose rates are

1. Growth of droplet by addition of one protein: $r_{1,i} = 4\pi D(c_\infty - c_{out})R_i$
2. Shrinkage of droplet by removal of one protein: $r_{2,i} = 4\pi Dc_{out}l_\gamma$
3. One step of damage repair: $r_{3,i} = 1/\tau$
4. One step of damage recreation: $r_{4,i} = \lambda$

Therefore we can include the rates (here denoted $\mu_i \in [r_{1,i}, r_{2,i}, r_{3,i}, r_{4,i}]$) of all the possible events and calculate the time until the next event as

$$T_{event} = \frac{-\ln(\mathcal{R})}{\sum \mu_i}, \quad (S6)$$

where \mathcal{R} is a random number, uniformly distributed between 0 and 1. Then, in order to find which of the possible events take place, we assign a number to each reaction rate and choose the reaction, m , that satisfies:

$$\frac{\sum_{i=1}^{m-1} \mu_i}{\sum_{i=1}^N \mu_i} \leq \mathcal{R} \leq \frac{\sum_{i=1}^m \mu_i}{\sum_{i=1}^N \mu_i} \quad (S7)$$

After each event we update all the rates, and then repeat the steps. With this algorithm one can therefore simulate the system, based on single proteins dynamics, in the presence of intrinsic noise. We note that since our equations have been derived in the quasi-steady state approximation, the direct application of the Gillespie algorithm can lead to inaccurate estimation of the noise level, in general to an underestimation of stochasticity compared to the full system (Kim et al., 2015). However, this potential imprecision does not affect the main results, since the stochasticity is mainly responsible for generating a mixed initial state and the very early growth of the droplets. As soon as the droplets get past this initial phase, the forces are so strong that the stochasticity only plays a minor role. Having higher noise would result in an earlier dominance of Ostwald ripening, since the fluctuations could in principle drive the system out of the metastable state in which some droplets temporarily co-exist. This would further enhance the need for an oscillatory mechanism to prevent the effect of Ostwald ripening.

Transition from diffusion to Ostwald ripening

Material flux from far away toward the droplets surface ceases when the gradient of concentration is null, that is when $c_\infty \approx c_{out}$. Considering the same initial radius $R_i \approx 0 \forall i$ one can assume that all droplets roughly reach the same size at that point, so that

$\sum_{i=1}^N V_i = N \cdot V_i$. In this case Equation 2 takes the form

$$\bar{c}V = c_{in}N \cdot V_i + c_{out}V - c_{out}N \cdot V_i.$$

Isolating for V_i and considering that $c_{in} \gg c_{out}$ directly yields Equation 6.

Ostwald Ripening timescale of coarsening

By considering the definition of the critical radius

$$R_c = \frac{c_{out}}{c_\infty - c_{out}} l_\gamma,$$

it is possible to express Equation 1 as

$$(dR / dt) = (Dl_{\gamma} / R^2 R_c)(c_{out} / c_{in})(R - R_c).$$

Moreover, considering that R_c changes much more slowly than R

$$\frac{dR}{dt} \approx \frac{d(R - R_c)}{dt} = \frac{1}{T_{OR}}(R - R_c),$$

with T_{OR} being the timescale of coarsening as defined in Equation 7.

Visualizing p53 dynamics in polar coordinates

The p53 and Mdm2 levels are first centered around their mean values such that $x = p53 - \langle p53 \rangle$ and $y = Mdm2 - \langle Mdm2 \rangle$, which are then transformed in polar coordinates (r, θ) as $r = \sqrt{x^2 + y^2}$ and $\theta = \arctan(y/x)$. The angular space is then divided in 50 sections, within each of whom the mean and SD of the trajectories are calculated.

On non-linear p53 stimulation and the dependency of waveforms

In the paper we have investigated how the oscillations in p53 concentration affected the repair foci, generally assuming, for simplicity, a sinusoidal p53 signal and a linear relation with the droplet material concentration. In the following, we would first like to compare different types of waveforms on the resulting repair of damage. Secondly, we investigate the effect of non-linear relations between p53 and downstream droplet proteins, which would be a fair assumption if the main role of p53 were in the transcriptional-dependent processes.

To test the dependency of other waveforms on the Ostwald ripening, we considered three very distinct waveforms: sinusoidal, square and triangular waves. Keeping the frequency and amplitude fixed, we measured the repair efficiency for each of the waveforms (Figure S1A). Here we find that they all have a frequency dependency that enhances the repair efficiency and that this is very similar for the triangular and sinusoidal waveform, but covers a larger range of frequencies for the square wave. This is explained by the fact that the square wave will spend longer time at the maximal concentration level, that allows more droplets to co-exist and thereby enhancing the overall efficiency of repair.

Secondly, from a mathematical point of view, the dynamics of downstream proteins (denoted by L) leading to the liquid-liquid phase separation, would be given by

$$\dot{L} = f(p) - \delta L,$$

where we have assumed that L is spontaneously degraded at a rate δ , and that it is produced as a function of p53 (denoted by p). In the regime of biochemical functions, where we assume that p53 is not a repressor but an activator, we would demand that: 1) p is positive (since it is a concentration) 2) $f(p)$ is monotonically increasing (since it is an activator by definition). These two constraints allow us to distinguish four different cases for $f(p)$:

$$f''(p) = 0 \Rightarrow f(p) = cp$$

$$f''(p) > 0 \Rightarrow f(p) = cp^2$$

$$f''(p) < 0 \Rightarrow f(p) = \frac{p}{c+p}$$

$$f''(p) \begin{cases} > 0 \text{ for } p < c \\ < 0 \text{ for } p > c \end{cases} \Rightarrow f(p) = \frac{p^h}{c^h + p^h}$$

Here c is a positive parameter and h is the integer of a Hill function. For oscillatory levels of p53, we simulated the concentration of the protein L , which turned out to be itself oscillatory in each case, even though the shape of the waveforms may vary (Figure S1B). The only case where oscillations are completely absent is when $f(p) = \frac{p}{\epsilon + p}$, where $\epsilon \ll 1$. However, this is a very special case, and we would argue that it is more likely that downstream targets generally possess an oscillatory output. This means that for the majority of cases, oscillations in p53 would also lead to oscillations in the downstream targets.

QUANTIFICATION AND STATISTICAL ANALYSIS

To compare the experimentally found distributions we applied the Mann–Whitney–Wilcoxon two-sided test in Figures 5B–5E. To compare the similarities of the distributions we applied the two sided KS test (Figure 5F). To compare the fully repaired cells, we used the Student's t test to compare the two numbers, assuming Poisson counting statistics in the single bin (Figure 5G).

Supplemental figures

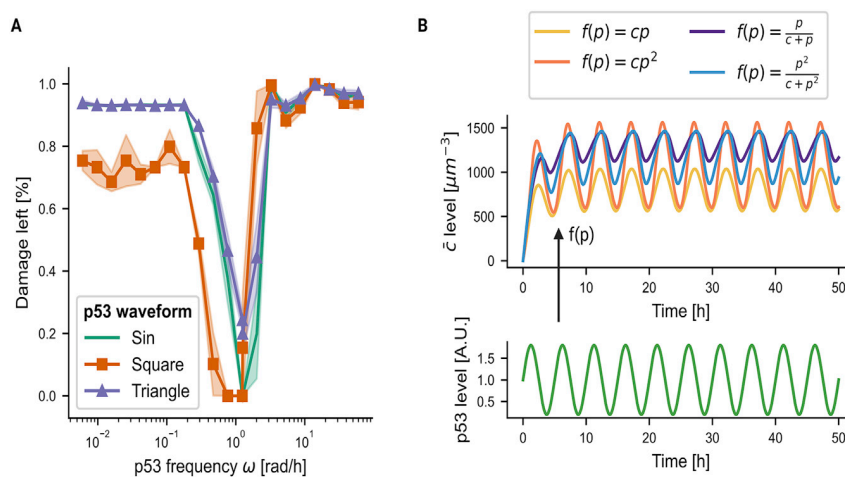


Figure S1. Effect of different p53 waveforms and non-linear relationship between p53 and droplet proteins concentration, related to STAR Methods

(A) Amount of damage left as a function of p53 frequency for three different p53 waveforms (sinusoidal, squared, triangular). (B) Oscillatory dynamics of p53 (below) and resulting average concentration of proteins, following 4 different types of stimulation.

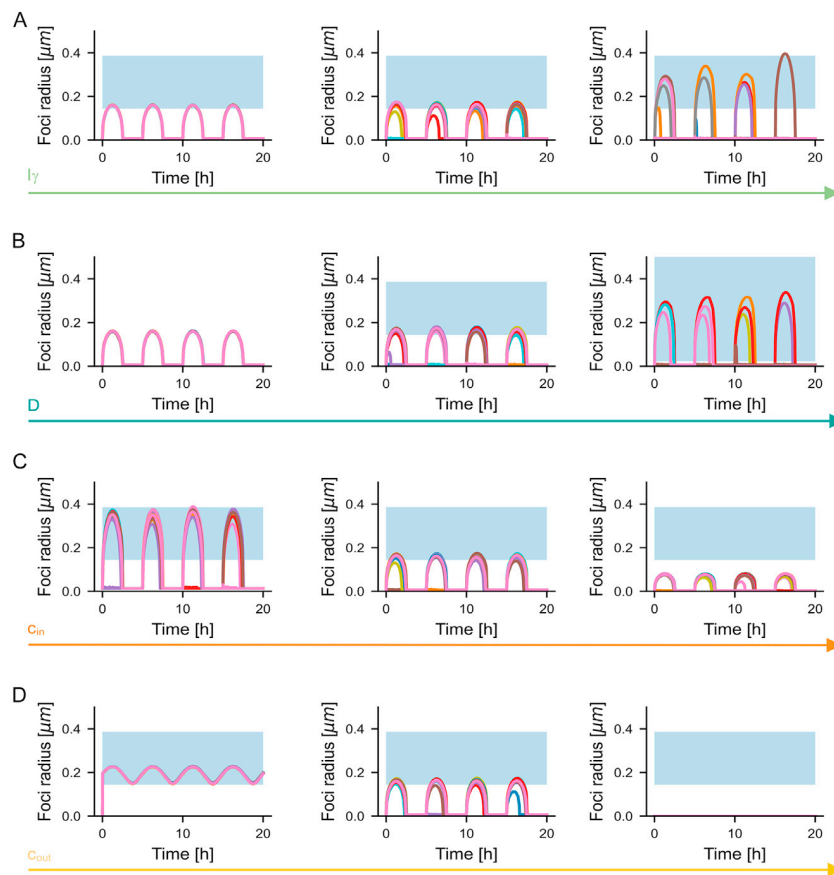


Figure S2. Effect of varying the parameters l_γ , D , c_{in} , and c_{out} on the timescale of coarsening, related to Figure 3

(A) Foci radius traces for increasing values of l_γ . The main effect is a shortening of the timescale of coarsening. (B) Same as (A), but for increasing values of D . The main effects are that the timescale of coarsening gets shorter and the optimal range gets wider. (C) Same as (A), but for increasing values of c_{in} . The main effect is that the resulting droplets are smaller, since the internal concentration is higher with the same average material. (D) Same as (A), but for increasing values of c_{out} . For $c_{out} < \bar{c}$ (left) the droplets are stabilized for long timescales, whereas for $c_{out} > \bar{c}$ (right) droplets cannot grow as the environment is undersaturated.

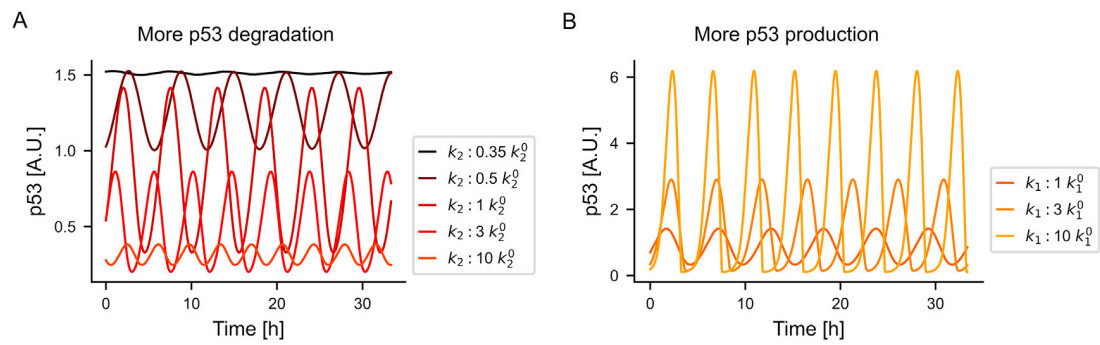


Figure S3. Different time series for p53 levels obtained by variation of the parameters k_2 and k_1 , related to Figure 4

(A) p53 level traces for increasing values of the degradation rate k_2 (with respect to a reference value k_2^0); low k_2 results in constant high levels for p53, while for higher k_2 a limit cycle with high amplitude oscillations emerges. (B) p53 level traces for increasing values of the production rate k_1 (with respect to a reference value k_1^0) show an increase in the amplitude of the oscillations.

Entrainment as control mechanism for the p53 oscillator

4.1 Introduction and Objectives

All of us who have travelled to a remote destination by plane, possibly crossing multiple time-zones, will be familiar with the typical symptoms of *jet-lag*, such as fatigue, insomnia, and difficulties with concentration. So what is the underlying reason? The problem is that the person's internal body clock, also known as the circadian rhythm, has not had enough time, during the travel, to adjust to the new environmental cues it receives from the outside. As a result, it inevitably falls out of sync. Indeed, the circadian clock is robustly locked (or *entrained*) to the light-dark cycle of the starting place, and will need some time before it can adjust to the new rhythm (Czeisler *et al.*, 1999).

The phenomenon of *entrainment*, characterized by the synchronization of an oscillator's frequency with an external pulsing rhythm (Pikovsky *et al.*, 2001), extends beyond the organismic level. Entrainment is crucial not only for the synchronization of internal processes, such as the alignment of the circadian clock with the cell cycle (Gérard and Goldbeter, 2012; Pfeuty *et al.*, 2011), or with metabolic cycles (Woller *et al.*, 2016), but also for enabling tissues to function cohesively. For instance, cardiac cells synchronize their oscillations with the rhythm of the sinoatrial node, ensuring coordinated heart contractions (Jalife, 1984).

As we thoroughly covered in the previous chapter, oscillations have been increasingly appreciated as important mechanisms in transcriptional regulation, as they guide gene expression outputs (Heltberg, Krishna, *et al.*, 2021; Hoffmann *et al.*, 2002; Lahav *et al.*, 2004; Nelson *et al.*, 2004; Gonze *et al.*, 2002; Zhang *et al.*, 2017; Levine *et al.*, 2013; Krishna *et al.*, 2006). In this context, one natural question to ask is whether these oscillations could also be artificially controlled and manipulated via entrainment to an external rhythm. In some cases, researchers have already found that this is indeed possible: Nuclear Factor kappa B (Nf- κ B) has been shown to entrain its frequency to externally applied periodic stimulations of Tumour Necrosis Factor (TNF) (Heltberg *et al.*, 2016; Kellogg and Tay, 2015), leading to a more robust transcriptional response. However, the possibility of modulating Transcription Factors (TFs)' natural frequency via entrainment remains unexplored for many systems, even well-studied ones such as the p53 network (Jiménez, Lu, Jambhekar, *et al.*, 2022).

In the previous chapter we have shown how p53 is activated by various cellular stresses (Purvis *et al.*, 2012; Hafner *et al.*, 2017; Reyes *et al.*, 2018; Kracikova *et al.*, 2013), and oscillates specifically in response to Double-Strand Breaks (DSBs) with a robust periodicity of approximately 5 h (Lahav *et al.*, 2004; Batchelor *et al.*, 2011; Chen, 2016). We have seen that the oscillations arise from p53's transcription of MDM2, a protein that induces p53 degradation (Wu *et al.*, 1993; Fuchs *et al.*, 1998; Haupt *et al.*, 1997; Honda *et al.*, 1997; Kubbutat *et al.*, 1997) (see Section 3.2.1). We have also briefly mentioned, describing the experiments in Section 3.3, that certain small molecule inhibitors of

MDM2, such as nutlin-3a, can alter p53 dynamics. This, in turn, affects the resulting gene expression programs, such as the transcription and protein levels of one of the most crucial target genes for cell-cycle regulation, p21 (Purvis *et al.*, 2012). The role of p21 is essential for maintaining proper cell-cycle control during DNA damage, preventing cell division until DNA has been repaired, or, in case of severe damage, stopping the cell from reproducing indefinitely (senescence) (Hsu *et al.*, 2019). Molecules such as nutlin-3a are therefore good candidates to be administered in pulses, in order to test the possibility of controlling p53 frequency and the effect on the downstream targets such as p21.

Our objective in this study is therefore to investigate whether p53 oscillations can be entrained by an external pulsing signal, specifically small molecule nutlin-3a. To achieve this, we aim to:

- Develop a theoretical model to describe the impact of single pulses of nutlin on the negative feedback loop between p53 and MDM2;
- Use the theory of Phase Transition Curves (PTCs) and Arnold Tongues, to predict the response of the system to a periodic pulse and the presence of entrainment modes;
- Compare our theoretical predictions with the experimental data;
- Investigate the effect on the downstream target p21 to understand the potential evolutionary advantage of p53's intrinsic frequency in regulating cellular processes related to cell fate determination (proliferation vs cell cycle arrest or senescence).

This project has been initially formulated by Alba Jimenez, Mathias S. Heltberg, Mogens H. Jensen, and Galit Lahav. All the experiments have been performed by Alba Jimenez, with the supervision of Ashwini Jambhekar and Galit Lahav at Harvard Medical School. The theoretical model and the data analysis have been carried out by Mathias S. Heltberg and me.

In the next section, we will review the main mathematical concepts necessary for the derivation of the model and the analysis of the results, focusing in particular on the Arnold Tongues theory and on Poincaré maps.

4.2 Background theory

4.2.1 Arnold tongues theory

When two oscillators interact, we define them as *coupled oscillators*. The phenomenon of entrainment usually manifests in case of unidirectional coupling (Stavans *et al.*, 1985), meaning that there is one oscillator, denoted the *internal* one (with period T_{int}) which is affected by another oscillator, the *external* one (with period T_{ext} and amplitude A_{ext}), that is not affected back (Figure 4.1A). Depending on the period mismatch ($\Delta T = T_{ext} - T_{int}$) and on the strength of the interaction, generally correlated to the amplitude of the forcing oscillator (A_{ext}), the internal oscillator modulates its intrinsic frequency in different possible ways.

To analyse its behaviour, the two oscillators can be described in terms of their phases $\theta_{INT,EXT}$ which, as we have seen in Chapter 2, grow linearly in the range $[0, 2\pi]$ within each oscillation and are reset to 0 every period T . Thus, at a given time t , the phase can be calculated from the trace as $\theta(t) = (t - t_0)/T \cdot 2\pi$, where t_0 is the time of the last peak. This allows us to visualize the

phase as an angle progressing with time on the unit circle (Figure 4.1B). Given that both phases of the internal and external oscillator are defined in the circle \mathbb{S} , the resulting state space is the 2-torus $\mathbb{T}^2 = \mathbb{S}^1 \times \mathbb{S}^1$ (Figure 4.1C, left), where θ_{EXT} and θ_{INT} are the longitude and the latitude respectively. The oscillators are frequency-locked, or *entrained*, when there is a periodic trajectory on the 2-torus, i.e. a *torus knot* (Figure 4.1C, right). The simplest type of entrainment occurs when ΔT is small and is progressively reduced to zero during a transient phase (Figure 4.1D). This is defined as 1:1 entrainment, since the internal oscillator goes through 1 cycle for each cycle of the external one. In general, if θ_{INT} makes p rotations in the time it takes for θ_{EXT} to make q rotations, the system is said to be $p:q$ entrained. This state is therefore characterized by the *rotation number* ω , which is simply defined as the ratio $\omega = p/q$ (Pikovsky *et al.*, 2001). In Figure 4.1E we show examples of entrainment modes such as 1:1, 1:2, 2:1.

The motion on the torus can be mapped into a 1D difference equation using a Poincaré section (Glass and Mackey, 1988; Heltberg, Krishna, *et al.*, 2021): the phase of the internal oscillator is recorded every time the phase of the external one passes through the section, that is, every time the external oscillator makes one full rotation (Figure 4.1F). Thus, we have a stroboscopic mapping of a circle to itself $\theta_{n+1} = P(\theta_n)$, where we have dropped the subscript INT for simplicity of notation. The sequence θ_n with $n = 1, 2, \dots$ is called the orbit of the map. Historically, the first to analyse coupled oscillators in these terms were Kolmogorov and Arnold (Arnold and Avez, 1968; Arnold, 1965) who studied the so-called *sine circle map*

$$\theta_{n+1} = \theta_n - A_{ext} \sin \theta_n + 2\pi \cdot \Omega,$$

where the coupling is sinusoidal with amplitude A_{ext} , which represents the coupling strength, while Ω corresponds to the ratio of external over internal period ($\Omega = T_{ext}/T_{int}$).

One can readily observe that if $A_{ext} = 0$, the two oscillators are uncoupled, and their independent motions proceed unperturbed. Only in the case Ω is a rational number, the two oscillators are intrinsically frequency-locked, since their natural frequencies are a multiple of each other. However, given that there are infinitely more irrational than rational numbers, the $A_{ext} = 0$ line will be dominated by *quasi-periodic motion*, where no stable entrainment is found for any initial condition (Feigenbaum *et al.*, 1982; Strogatz, 2018). When $A_{ext} > 0$, the internal oscillator frequency will be pulled by the external one, leading to a small region of entrainment around each rational number for Ω . These regions expand for increasing values of A_{ext} , leading to the characteristic Arnold Tongues, depicted in Figure 4.1G for the specific case of sine circle maps. The figure shows the regions of frequency-locking in gray, with highlighted in yellow, pink and blue the three tongues for 1:2, 1:1 and 2:1 entrainment respectively.

For $A_{ext} < 1$, the Poincaré maps are invertible circle maps, i.e. with a 1-1 correspondence between values of θ_n and θ_{n+1} on the unit circle. It can be shown that in this case, the system has a unique solution for each value of (A_{ext}, Ω) , meaning that the internal oscillator displays regular oscillations which may entrain (inside the tongue) or not (outside the tongue) to the external oscillator. In other words, the Arnold tongues in this region are distinct and do not overlap (Glass and Mackey, 1988). For increasing values of A_{ext} the tongues widen, the space left outside the tongues (for non-entrained solution) gets smaller and smaller until at $A_{ext} = 1$, the irrational numbers occupy a fractal set of the whole line, with universal dimension 0.870 (Jensen *et al.*, 1984): therefore, the rational numbers fill up the critical line $A_{ext} = 1$ (opposite to what happens at $A_{ext} = 0$).

Further increasing the strength of the external perturbation ($A_{ext} > 1$), results in the map becoming non-invertible: the tongues start to overlap, thus possibly giving rise to multiple stable solutions, which depend on the initial conditions. In the presence of noise, the oscillator may then jump between different stable states, a phenomenon called “mode-hopping” (Heltberg *et al.*, 2016), as shown in the first panel of Figure 4.1H.

This level of interaction strength may also lead to a type of bifurcation known as *period-doubling* (Figure 4.1H, middle panel), which is generally found at the center of each Arnold tongue. This phenomenon occurs when a new trajectory emerges from an existing periodic trajectory – with the emerging one having double the period of the original, which is manifested in the data as a pattern of alternating amplitudes in the oscillations. By definition, period-doubling means that it takes double the time for a trajectory to repeat itself. Thus, a period-doubling cascade (i.e. an infinite sequence of period-doubling bifurcations), in which the trajectory takes longer and longer to repeat itself, is a common route by which dynamical systems develop *chaotic dynamics* (Strogatz, 2018) (Figure 4.1H, right panel), indeed characterized by infinite-period trajectories. In chaotic dynamics, two trajectories with initial conditions separated by an infinitesimal distance will exponentially diverge as time progresses. Given that it is impossible to know initial conditions with perfect precision, the long-term behaviour of the system is totally unpredictable.

In the next section, we show how to derive a Poincaré map for a system of coupled oscillators in order to predict the Arnold tongues, and therefore uncover the ability of the external pulsing signal to entrain the internal system.

4.2.2 Poincaré maps to predict entrainment from single perturbations

In this section, we consider an internal oscillator of the form

$$\dot{x} = f(x) + A\delta(t - t_s)$$

with an exponentially stable limit cycle, which receives a stimulation by an external pulsing signal at times t_s (Izhikevich, 2018) (δ here represents the Dirac delta function). This results in an immediate update of the state variable x to a new value $x + A$. The goal of this section is to determine the response of the system to a single perturbation and extrapolate it to the case of repeated pulses, in order to compute the Poincaré map and predict the ability of the system to become entrained by an external periodic signal. The initial assumption ensures that the effect of a pulse is over before the next pulse is received, so that subsequent pulses can be regarded as independent. This may not be valid for any external oscillatory rhythm, such as in case of strong external pulses, short time between pulses or weak attraction to the limit cycle (Izhikevich, 2018).

When an external perturbation is introduced at time t , it can induce a phase shift $\Delta\theta$ in the ongoing oscillation. This shift causes the system to transition from an initial phase $\theta_i(t)$ to a new phase $\theta_f(t)$, where $\Delta\theta = \theta_f - \theta_i$, as shown in Figure 4.2A. While $\theta_i(t)$ is computed based on the unperturbed trace (blue curve), the final phase $\theta_f(t)$ is obtained from the perturbed trace (red curve) by extrapolating back to the time of the last peak (black dotted curve). The system typically undergoes a short transient phase (gray curve) before returning to the stable cycle at its new phase. Therefore, while amplitude changes decay over time, phase changes persist.

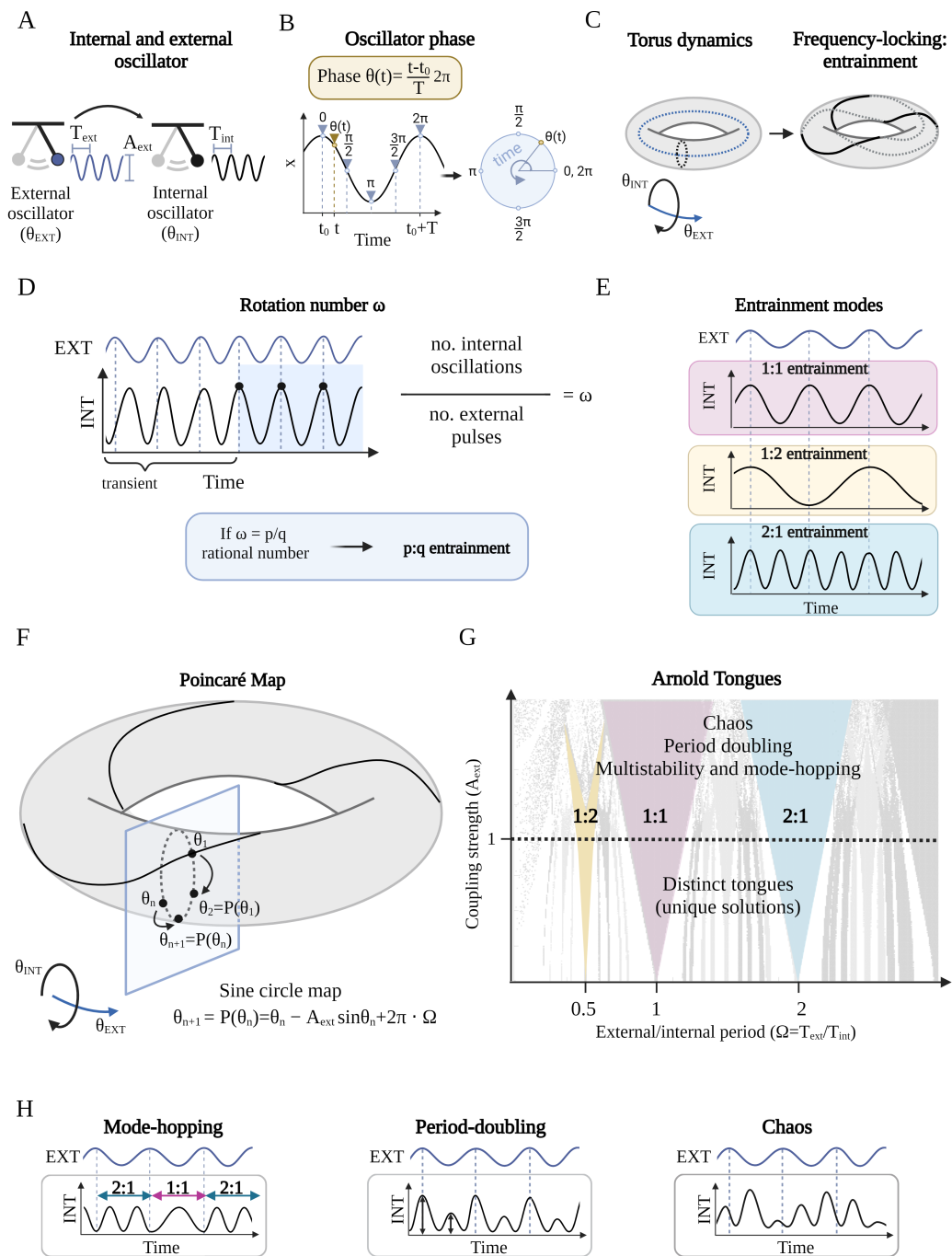


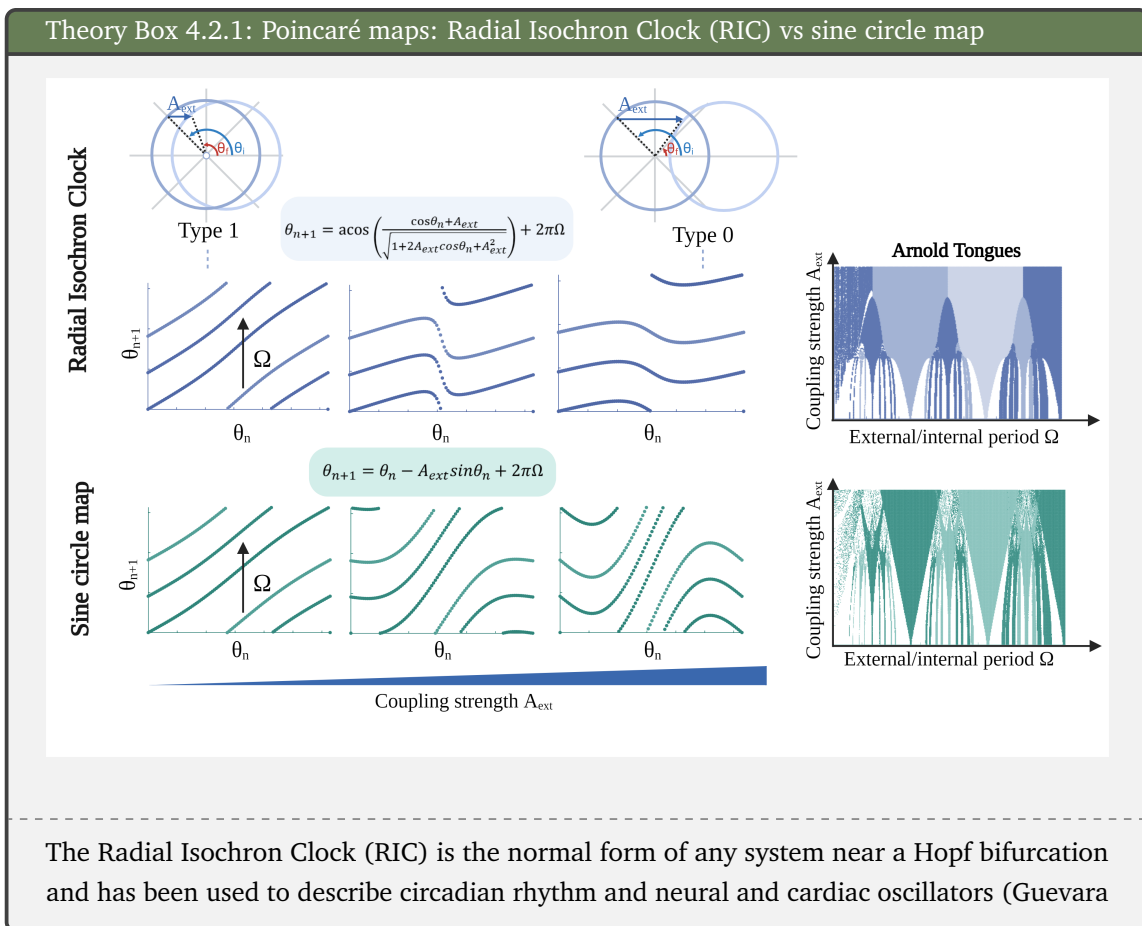
Figure 4.1: (A) Entrainment occurs when an external oscillator affects unidirectionally an internal oscillator. (B) Definition of the phase. (C) The dynamics of an internal and external oscillator can be mapped to a torus: frequency-locking (or entrainment) corresponds to a torus-knot, i.e. a periodic trajectory on the torus. (D) Definition of the rotation number as ratio between no. of internal oscillations over external ones, computed after an initial transient time. (E) Examples of 1:1, 1:2 and 2:1 entrainment modes. (F) Poincaré map and definition of sine circle map. (G) Arnold Tongues for the sine circle map. (H) Examples of mode-hopping, period-doubling and chaos which can be found in regions of overlapping tongues, where there is multi-stability.

The phase can also be defined outside the limit cycle (Izhikevich, 2018) using the notion of *isochrons*: intuitively, an isochron is a set of initial conditions that result in oscillations with the same phase (Josic *et al.*, 2006). To illustrate this concept, we make a 2D example in the (x_1, x_2) coordinates (Figure 4.2B). We consider a trajectory $x'(t)$ outside the limit cycle (thus non-periodic), that is attracted to the limit cycle, and therefore approaches it as $t \rightarrow \infty$. Thus, there must be a point $x(t)$ on the limit cycle such that

$$x'(t) \rightarrow x(t) \text{ as } t \rightarrow \infty. \tag{4.1}$$

The phase of x' at time t_0 is therefore defined as the phase of its periodic proxy x at time t_0 . The set of all initial conditions in the phase space having the same phase as $x(t_0)$ is defined as the isochron of $x(t_0)$. The phase space is filled with isochrons, that all converge in the unstable fixed point inside the limit cycle.

So when an external pulse results in a phase shift for the ongoing oscillation, the system is, in other words, transitioning from one isochron to another. This is illustrated in Figure 4.2C for the case of a circular limit cycle with radial isochrons with an horizontal pulse (along the variable x_1) (this model is defined as Radial Isochron Clock (RIC), and is explained in more details in the Theory Box 4.2.1). The system receives the horizontal pulse of length A_{ext} at initial phase θ_i , and ends up in the vertical isochron, in which all points have phase θ_f . If the relaxation time to the limit cycle was really short, the trajectory would follow the black arrow and approach the limit cycle almost instantaneously. Otherwise, the system may follow a longer transient trajectory (gray curve) outside the limit cycle, before approaching it.



and Glass, 1982; Granada *et al.*, 2009), as well as the embryonic segmentation clock (Sanchez *et al.*, 2022). The corresponding equations in polar coordinates are

$$\frac{dr}{dt} = r(\mu - r^2), \quad \frac{d\theta}{dt} = 1. \quad (\mu = \text{const}) \quad (4.2)$$

Indeed, when $\mu < 0$, the only fixed point is at $r = 0$, which is a stable spiral. When $\mu > 0$ the fixed point at the origin becomes unstable and a stable limit cycle appears at $r = \sqrt{\mu}$ (Hopf-bifurcation). If we assume that an external pulse causes an horizontal shift to the right of length A_{ext} , the system transitions from an initial point A with coordinates $(r \cos \theta_i, r \sin \theta_i)$ to a point B with coordinates $(r \cos \theta_f, r \sin \theta_f)$. It is straightforward from the geometry of the system to determine the coordinates of B in terms of θ_i , $(r \cos \theta_i + A_{ext}, r \sin \theta_i)$. It follows that $\tan \theta_f = \frac{\sin \theta_f}{\cos \theta_f} = \frac{\sin \theta_i}{\cos \theta_i + A_{ext}}$, which relates the phase of the system before and after the pulse. Isolating θ_f yields

$$\theta_f = PTC(\theta_i) = \begin{cases} \arccos \left(\frac{\cos \theta_i + A_{ext}}{\sqrt{1 + 2A_{ext} \cos \theta_i + A_{ext}^2}} \right) & \text{if } \theta_i < \pi, \\ 2\pi - \arccos \left(\frac{\cos \theta_i + A_{ext}}{\sqrt{1 + 2A_{ext} \cos \theta_i + A_{ext}^2}} \right) & \text{if } \theta_i > \pi. \end{cases} \quad (4.3)$$

The corresponding Poincaré map thus follows directly as $PTC + 2\pi\Omega$, with $\Omega = T_{ext}/T_{int}$ as defined in the main text. For small A_{ext} , the map can be approximated as a sine circle map. For increasing values of the external stimulus one can see that the behaviour of the two maps is intrinsically different: while the sine circle map maps the whole circle, the RIC map becomes an interval map, as it maps the circle to an interval in $[0, 2\pi]$. The corresponding Arnold tongues are therefore similar for small A_{ext} and become substantially different for high pulses: while the Arnold tongues for sine circle maps show tongues that keep broadening and therefore have multi-stability and chaotic dynamics, some of the tongues for the RIC have a characteristic mushroom shapes, while others have vertical boundaries at high A_{ext} , thus none of them overlap.

In general, the observed phase shift can depend on the initial phase θ_i at which the perturbation is received. This dependence can be visualized through the PTC, which plots the final phase θ_f as a function of the initial phase θ_i , or through the Phase Response Curve (PRC), which plots the phase shift in terms of the initial phase. Both are represented in Figure 4.2D. The two approaches are equivalent: using PRCs is more convenient in case of small phase shifts, which can be magnified, whereas PTCs are generally used for large phase shift of the order of the period of oscillation (Izhikevich, 2018). In the case of weak external pulses (Figure 4.2D, top), the PTC slightly deviates from the diagonal line ($\theta_i = \theta_f$), which has mean slope 1, resulting in the so-called *type 1 resetting*. In this case, the PRC slightly deviates from $\Delta\theta = 0$, indicating that the external perturbation has minimal effect on the oscillator. Conversely, in the case of strong pulses (Figure 4.2D, bottom), the final phases of the oscillators are reset within a narrow range with mean slope 0 (hence defined *type 0 resetting*), and the phase shifts are large.

Through the PTC we therefore know the response of the system to a single external pulse. How can we find the response to a periodic pulse? If we give the system enough time to relax to the limit cycle before the next stimulus arrives, we can assume that we can use the same PTC for subsequent pulses, too. The first stimulus occurs at an initial phase $\theta_{1,i}$, causing a phase shift $\Delta\theta_1$

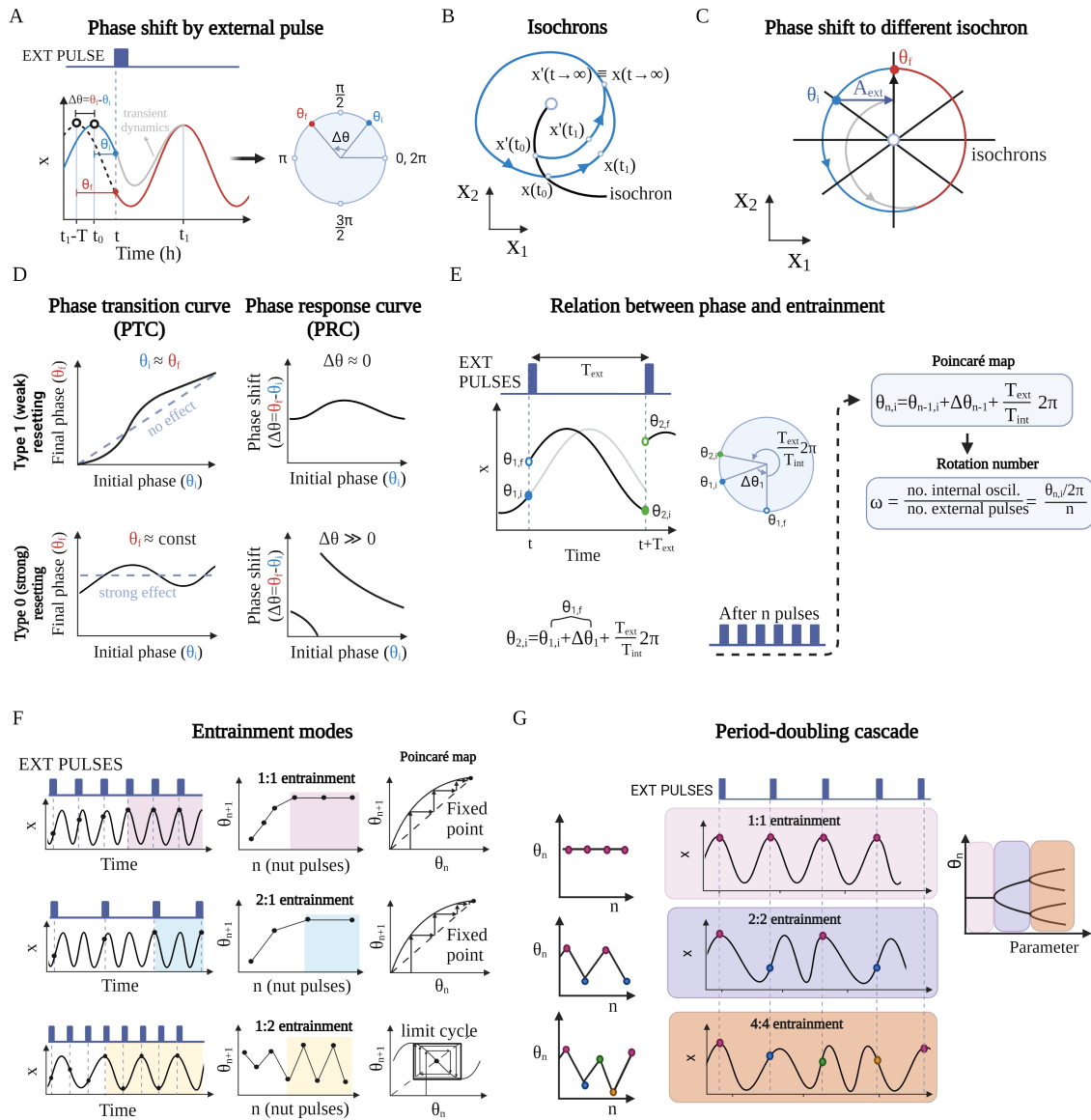


Figure 4.2: (A) An external pulse causes a phase shift $\Delta\theta$ on the ongoing oscillation. (B) Definition of isochrons. (C) A phase shift causes the system to hop to a new isochron. (D) Examples of Phase Transition Curves (PTCs) and Phase Response Curves (PRCs) for weak and strong resetting stimuli. (E) From the PTC it is possible to derive the Poincaré map, which gives information about the Arnold tongues. (F) The fixed points of the Poincaré map correspond to $p:1$ locked states (such as 1:1 or 2:1), while limit cycle correspond to $p:q$ locked states (such as 1:2 shown). (G) Period-doubling cascade in the Poincaré maps.

such that the final phase at the end of the stimulus is $\theta_{1,f} = \theta_{1,i} + \Delta\theta_1$. The phase will then proceed unperturbed until the time of the second perturbation, and will reach a new "initial phase" $\theta_{2,i}$ equal to $\theta_{2,i} = \theta_{1,i} + \Delta\theta_1 + \frac{T_{ext}}{T_{int}}2\pi$. At this point, the second pulse causes a new phase shift etc. By iterating this procedure for n pulses, as shown in Figure 4.2E, one can derive the Poincaré map $\theta_{n,i} = \theta_{n-1,i} + \Delta\theta_{n-1} + \frac{T_{ext}}{T_{int}}2\pi$. Numerically iterating the map n times and registering the final phase of the internal oscillator after n external pulses directly leads to compute the rotation number ω , and therefore plot the Arnold tongues for the system.

However, even before turning to simulation, it is possible to predict the presence of phase-locked solution, directly looking at the different possible orbits for the maps, in particular, the presence of fixed points or limit cycles. In general, for a discrete map $\theta_{n+1} = f(\theta_n)$, a fixed point θ^* is defined as (Strogatz, 2018)

$$\theta^* = f(\theta^*),$$

which is the analogue of an equilibrium point for a continuous dynamical system. Indeed, applying the map to a fixed point returns the fixed point itself, indicating that it is an equilibrium point. Geometrically, if we plot θ_{n+1} as a function of θ_n , the fixed point lies at the intersection between the map f and the diagonal line (where $\theta_n = \theta_{n+1}$).

The stability of the fixed point is determined by the slope

$$m = f'(\theta^*),$$

so that the fixed point is stable if $|m| < 1$, unstable otherwise. A fixed point therefore corresponds to either a 1:1 or a p:1 locked state, since the phase is the same at every iteration (Figure 4.2F, first and second row). Given that the map ignores everything that occurs between two subsequent pulses, in order to determine which p:1 locked state it is, the map has to be numerically simulated. What about a p:q solution? That would correspond to a stable periodic orbit of the Poincaré map with period q (Figure 4.2F, third row), such that

$$\theta_n = \theta_{n+q} \quad \forall n.$$

Stable fixed points and limit cycles can coexist in maps, resulting in multistability of the corresponding phase-locked solutions for the oscillator.

Up to this point, we only considered boundaries in the Arnold tongues between different phase-locking zones due to changes in rotation number. However, there is another possible type of boundary, which is given by a *period-doubling bifurcations* of the associated Poincaré map. This occurs when

$$m = f'(\theta^*) = -1.$$

For instance, this bifurcation occurs at the boundary between the 1:1 and 2:2 or 2:2 and 4:4 zones, where there is no change in rotation number, but the number of iterations it takes for the map to get back to the same point is doubled (Figure 4.2G).

4.3 Results

4.3.1 Derivation of the Phase Transition Curves (PTCs)

Our collaborators at Harvard Medical School, led by Galit Lahav, devised an experimental set-up in which the natural oscillations of p53, which constitute the "internal oscillator", with an endogenous period $T_{int} = 5.5$ h, can systematically be perturbed by an "external oscillator", given by pulses of the small molecule nutlin-3a (Figure 4.3A). As mentioned in the Introduction, p53 oscillatory dynamics mainly arises as a result of the negative feedback loop with inhibitor MDM2 (see Section 3.2.1 for more details), and nutlin-3a effect is to prevent the MDM2-mediated degradation of p53, thus elevating p53 levels.

Experimentally, cells are subjected to γ -radiation, in order to start p53 oscillations (Figure 4.3B). A macrofluidic device then quickly and efficiently flows media containing or lacking Nutlin-3a in and out of the cell culture while cells are being imaged. Changes in p53 dynamics are monitored by fluorescence time-lapse imaging of a p53-YFP reporter integrated in the MCF7 cell line.

First, the natural oscillations of p53 are perturbed with a single 40-minutes pulse of Nutlin-3a, at concentrations of $A_{ext} = 0.125 \mu\text{M}$ and $A_{ext} = 1 \mu\text{M}$, about 30 hours post-irradiation. As we have seen in Section 4.2.2, the response to a single pulse can provide crucial information about the dynamical properties of an oscillator and predict its entrainability to an external periodic input. Indeed, if subsequent perturbations are regarded as independent, the knowledge acquired from single-pulse experiments can be applied iteratively to make predictions on the effect of a series of perturbations. In Figure 4.3C we show an example of two single cell traces (first row) and the population average (second row, standard deviation in gray). Because of noise, by the time the perturbation is delivered, single cells' endogenous oscillations are desynchronized, as can be observed from the single cell traces. This effect is evident at the population level through damped oscillations in the average p53 signal. While there seem to be very little effect after the $0.125 \mu\text{M}$ nutlin pulse, immediately after the $1 \mu\text{M}$ nutlin pulse, the cells re-synchronize, which is seen as a pulse in the average p53 signal. This suggests that the phases of all the cells have been reset within a narrow range, and that repeated pulses may lead to entrainment at sufficient nutlin concentration.

We therefore used the following set of ordinary differential equations (ODEs) as a model of the p53-MDM2 loop (Mengel *et al.*, 2010) to simulate the effect of nutlin concentration on p53 re-setting (Figure 4.3D):

$$\begin{cases} \frac{dp}{dt} = k_1 - k_2 \frac{M_{free}p}{k_3+p} \\ \frac{dm}{dt} = k_4p^2 - k_5m, \\ \frac{dM_{free}}{dt} = k_6m - k_7M_{free} - k_8nM_{free}, \\ \frac{dM_{bound}}{dt} = k_7M_{bound} + k_8nM_{free}, \\ \frac{dn}{dt} = -k_8nM_{free}, \quad n(t = T_{on}) = A_{ext}, \quad n(t < T_{on} \text{ or } t > T_{off}) = 0, \end{cases}$$

where p , m , M_{free} and M_{bound} are the concentration of p53, of MDM2-mRNA, MDM2 free from and bound to nutlin, respectively; n is the concentration of available nutlin, administered with a pulse at time T_{on} and washed at time T_{off} . p53 production is constant (k_1) while its saturated degradation occurs via binding to MDM2 (k_2, k_3). MDM2-mRNA production is directly proportional to the square

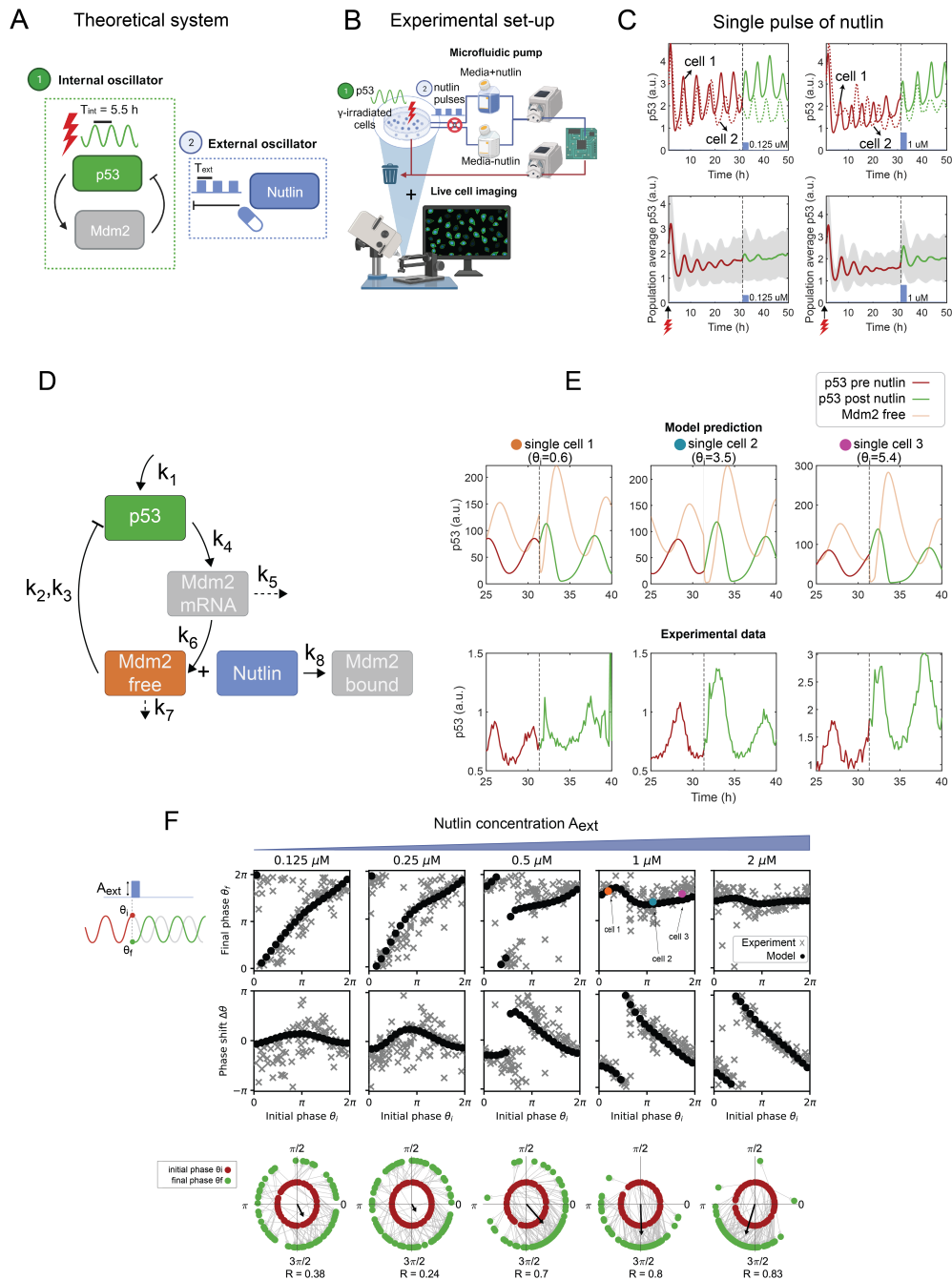


Figure 4.3: (A) Theoretical system with an internal (p53) and an external (nutlin) oscillator. (B) Experimental set-up with microfluidic device coupled with live cell imaging. (C) Single cell traces (first row) and population average \pm Standard Deviation (second row) of endogenous p53 oscillations with a 5.5 h period after 10Gy radiation. At about 30 h post radiation, a 40 min pulse of nutlin of 0.125 μ M (left) and 1 μ M (right) is administered. (D) Theoretical model for the negative feedback loop between p53 and MDM2. The binding between MDM2 and nutlin prevents p53 inhibition by MDM2. (E) Comparison between experimental data and the model prediction for three cells that received the nutlin pulse at three different phases. (F) Top: Phase Transition Curves (PTCs) and Phase Response Curves (PRCs) calculated from the experimental traces (gray crosses) and from the model (black dots) for increasing values of the nutlin concentration (A_{ext}). Bottom: Initial phases (red) and final ones (green) portrayed in the unit circle. The length of the black arrows (R) represent the order parameter, which shows increasing levels of synchrony for increasing nutlin concentrations.

of the p53 level - as p53 forms a tetramer of pre-existing dimers – and is scaled by a production parameter (k_4). It is degraded through a first-order decay process (k_5). MDM2 protein production is directly proportional to MDM2-mRNA (k_6) and exponentially decays (k_7). Finally, nutlin binds to MDM2 at a certain rate (k_8), preventing it from inhibiting p53.

One can easily show that introducing the pulse of nutlin to the model affects the binding affinity between p53 and MDM2, turning k_2 into a time dependent constant. Indeed, if we define the total MDM2 concentration at time t as $M(t) = M_{free}(t) + M_{bound}(t)$, it follows that

$$\frac{dM}{dt} = \frac{dM_{free}}{dt} + \frac{dM_{bound}}{dt} = k_6m - k_7(M_{free} + M_{bound}) = k_6m - k_7M,$$

whereas the equation for p53 reads

$$\frac{dp}{dt} = k_1 - \frac{k_2(M - M_{bound})p}{k_3 + p} = k_1 - k_2 \left(1 - \frac{M_{bound}}{M}\right) \frac{Mp}{k_3 + p} = k_1 - k_2(t) \frac{Mp}{k_3 + p},$$

with $k_2(t) = k_2(1 - M_{bound}(t)/M(t))$. The corresponding equations are therefore

$$\begin{cases} \frac{dp}{dt} &= k_1 - k_2(t) \cdot \frac{Mp}{k_3+p} \\ \frac{dm}{dt} &= k_4p^2 - k_5m \\ \frac{dM}{dt} &= k_6m - k_7M. \end{cases}$$

The model predicts that if the concentration of nutlin is saturating so that all MDM2 is bound, the concentration of free MDM2 drops, leading to an increase in p53 concentration after the pulse. Shortly afterwards, the system goes back to the unperturbed oscillatory state. A saturating concentration of nutlin is the only prerequisite for causing an immediate p53 peak after perturbation. This effect is confirmed by comparing our model predictions to experimental data from three single cells. Regardless of the phase θ_i of their ongoing oscillation at the time of receiving the nutlin pulse, all three cells show an immediate peak in p53 concentration (Figure 4.3E).

We then repeated the experiment for five increasing concentrations of nutlin to derive the PTCs, which represent the resulting final phase θ_f as a function of initial phase θ_i (Figure 4.2). Experimental (grey crosses, Figure 4.3F, top) and ODE-model derived (black dots, Figure 4.3F, top) PTCs correspond well. The same can be visualized through the PRCs, which are shown on the second row of Figure 4.3F. For increasing values of A_{ext} , the system transitions from a regime of weak phase resetting (type 1), in which the final phase resembles the initial one, to a regime of strong resetting (type 0), in which the final phases of all cells are reset in a narrow range, therefore the cells are synchronized. Transition into synchrony is visualized using concentric unit circles (Figure 4.3F, bottom) that show the distribution of initial (inner) and final (outer) phases. In order to quantify the level of synchronization after the pulse, we use the Kuramoto order parameter, defined as the complex sum of the phases of all the cells:

$$Re^{i\psi} = \left| \frac{1}{N} \sum_{i=1}^N e^{i\theta_f(i)} \right|,$$

where N is the number of cells. The order parameter is therefore represented in Figure 4.3F as the black vector that points in the direction of the average phase (ψ) and whose length (R) quantifies the level of synchronization. As expected, R increases for increasing values of the nutlin concentration.

This behaviour is typical of limit cycle models that show a transition from type 1 to type 0 PTCs when going from low- to high-stimulus strengths (Glass and Mackey, 1988).

4.3.2 Prediction of the Arnold Tongues from the Poincaré maps

PTCs can be applied iteratively, to compute the phase shift caused by subsequent repeated pulses, giving rise to Poincaré maps, which enables the computation of the rotation number. The main assumption of this approach is that subsequent pulses are treated as independent, which means that they give rise to the same PTC. To test this assumption, we computed the PTC after a first pulse and after a second pulse, both of amplitude A_{ext} , both of 40 min in duration, delivered at a distance of T_{ext} . If the transient dynamics of the p53 limit cycle is fast enough, we should see that the two curves overlap. We plot the results in Figure 4.4A in a range of A_{ext} and T_{ext} . We observe that the curves do overlap in the majority of the parameter region investigated, but, as expected, they do not if the strength of the perturbation is too strong or the period between subsequent pulses too little (top-left region). Therefore, one has to be careful and avoid drawing strong conclusions from the Arnold tongues predicted in that region, where this method is unreliable.

We could already make some predictions even before turning to numerical simulations, by looking at the PTCs of Figure 4.3F: at low nutlin concentration ($< 0.5 \mu\text{M}$), the maps are invertible circle maps, indicating that Arnold tongues do exist, and thus p53 has the capacity to display regular oscillations which may entrain (inside the tongue) or not (outside the tongue) to nutlin (Jensen *et al.*, 1984). Above a critical value of nutlin concentrations ($> 0.5 \mu\text{M}$), Poincaré maps become non-invertible, indicating that complex dynamics might occur (Guevara and Glass, 1982; Glass and Mackey, 1988).

We next performed numerical simulations to draw the Arnold tongues of the system. To do so, we first needed an analytical function to iterate. Given that the shape of the PTCs computed from the theoretical model highly resembled the RIC model (Glass and Winfree, 1984; Glass and Mackey, 1988), we used an analytical function inspired by it, to which we added 2 extra parameters (B, C)

$$PTC(\phi) = \begin{cases} \phi - \psi - B & \text{if } 0 \leq \phi - C \leq \pi, \\ \phi + \psi - B & \text{if } \pi \leq \phi - C \leq 2\pi, \end{cases}$$

$$\psi = \arccos \left(\frac{1 + A \cos(\phi - C)}{\sqrt{1 + 2A \cos(\phi - C) + A^2}} \right).$$

The original parameter A quantifies the strength of the pulse. The addition of the two extra parameters make the PTCs shift horizontally and vertically by a constant amount, and can be justified by the fact that the p53 model has more dimensions than the RIC model (which is only 2D), and therefore cannot fully capture the complexity of the p53 dynamics. However, as shown in Figure 4.4B, adding these parameters leads to a good correspondence between theoretical model (black dots) and analytical fits (red squares), where we report three example PTCs and PRCs for increasing nutlin concentrations. Repeating the fit over a range of nutlin strengths $[0 - 1] \mu\text{M}$ showed that A grows approximately linearly in the range investigated, (as expected, since in the original RIC model it represents the strength of the perturbation), while B and C could be approximated with piecewise

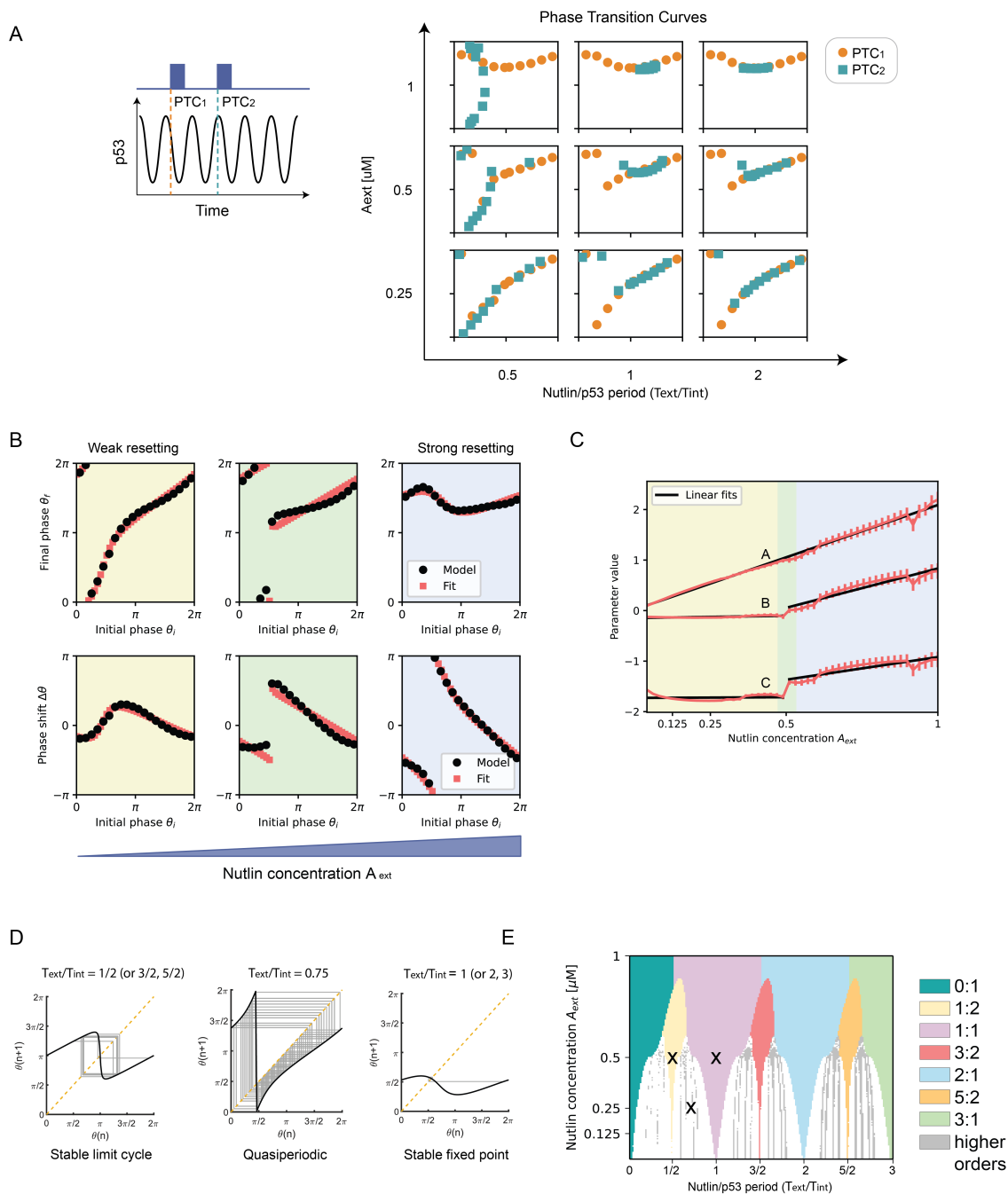


Figure 4.4: (A) Test of transient dynamics by computing two Phase Transition Curves (PTCs) after a first pulse and a second pulse. If the transient dynamics is fast enough, the two curves should overlap. (B) Analytical fit of the PTCs obtained from the ODE-model with curves inspired from the Radial Isochron Clock (RIC) model at weak and strong resetting regimes shows good accordance. (C) The parameters A,B,C of the analytical curves vary as a function of nutlin concentration and are fit with piecewise linear functions. (D) Cobwebs show the presence of stable limit cycles, quasiperiodic motion and stable fixed points, indicating the presence of $p:q$ entrainment, non-entrained solutions and $p:1$ entrainment. (E) Arnold tongues predicted from the Poincaré maps. The three crosses (x) are the parameters used in (D).

linear functions (black lines), constant in the “weak resetting” regime (yellow shadow) and linearly growing in the “strong resetting” regime (blue shadow) (Figure 4.4C).

In this way, having an analytic expression for the PTC, and knowing how the parameters change as a function of the external perturbation, we could first draw the cobwebs for different values of T_{ext}/T_{int} , showing the presence of limit cycles for 1/2 (or equivalently, 3/2 or 5/2, meaning p:q entrainment (Figure 4.4D, left), quasiperiodic motion for irrational values of T_{ext}/T_{int} (Figure 4.4D, middle) and fixed point for $T_{ext}/T_{int} = 1$ (or equivalently, 2 or 3) (Figure 4.4D, right).

Iterating the simulations in a variety of nutlin periods and concentrations, we could obtain the Arnold Tongues depicted in Figure 4.4E. As expected, the predicted Arnold tongues of p53 closely resemble those of the RIC model: some tongues (e.g., 1:2, 3:2, 5:2) have a convex shape, thus certain entrainment modes are absent at high coupling strengths, whereas others (e.g. 1:1, 2:1, 3:1) have vertical boundaries, thus do not overlap at high nutlin concentrations.

4.3.3 The pace of the p53 oscillator can be locked to a wide range of entrainment periods

At this point, we wanted to experimentally test the theoretical predictions, by perturbing the natural radiation-induced oscillations of p53 with periodic pulses of Nutlin-3a. In the experiment, periodic pulses consist of a square wave signal of amplitude A_{ext} (nutlin3 concentration) that alternates between nutlin “on” and “off” states at a period (T_{ext}), with the on/off states within a single cycle being equal in duration. In the absence of γ -radiation, periodic pulses alone can drive synthetic p53 oscillations whose frequency could thus be controlled by tuning the interval between media changes ($T = T_{ext}$). For example, synthetic pulses can match the endogenous period ($T_{int} = 5.5$ h) (Figure 4.5A, bottom left) or double it ($T_{int} = 11$ h) (Figure 4.5A, bottom right). A single other study (Harton *et al.*, 2019) has attempted to control p53 period using a similar microfluidic design.

Having established both an internal oscillator and an external oscillator with a tunable periodic input, we next analysed whether p53 oscillations could entrain to an external nutlin input (Figure 4.5B, top), as predicted by single pulse experiments. To address this question, p53 oscillations are first triggered by irradiation (IR) (zone1), subjected to oscillating nutlin concentrations (zone2), then released from nutlin treatment (zone 3) (Figure 4.5B, bottom). First, we tested the effect of varying nutlin concentration (A_{ext}) at a fixed external input ($T_{ext} = 11$ h) on entrainment dynamics (Figure 4.5C). Our results show that the p53 oscillator can be entrained to double its endogenous period (11 h) at all nutlin concentrations tested (A_{ext} tested: $0.25 \mu\text{M}$, $0.5 \mu\text{M}$, $1 \mu\text{M}$ and $2 \mu\text{M}$ of nutlin). As expected, higher A_{ext} resulted in more robust entrainment, indicated by the progressive decrease in cell-to-cell variability (the gray shadow in Figure 4.5C represents the interquartile range). To observe the most diverse set of single cell responses, we fixed A_{ext} to $0.5 \mu\text{M}$. Next, we tested entrainment at periods from half (2.5 h) to double (11 h) the endogenous period, while keeping nutlin concentration constant ($A_{ext} = 0.5 \mu\text{M}$) (Figure 4.5C). Our results show that p53 oscillations closely entrained to the external period over the full tested range. Hence, we were able to speed up and slow down the pace of p53 oscillations using entrainment, as shown by the single cell responses in Figure 4.5D.

While entrainment is observed across all external periods tested, certain periods lead to higher cell-to-cell variability (Figure 4.5E-F), as shown for example by the wider interquartile range of single cell traces at 9 h compared to 4 h. Indeed, examples of single traces show homogeneity at 4 h

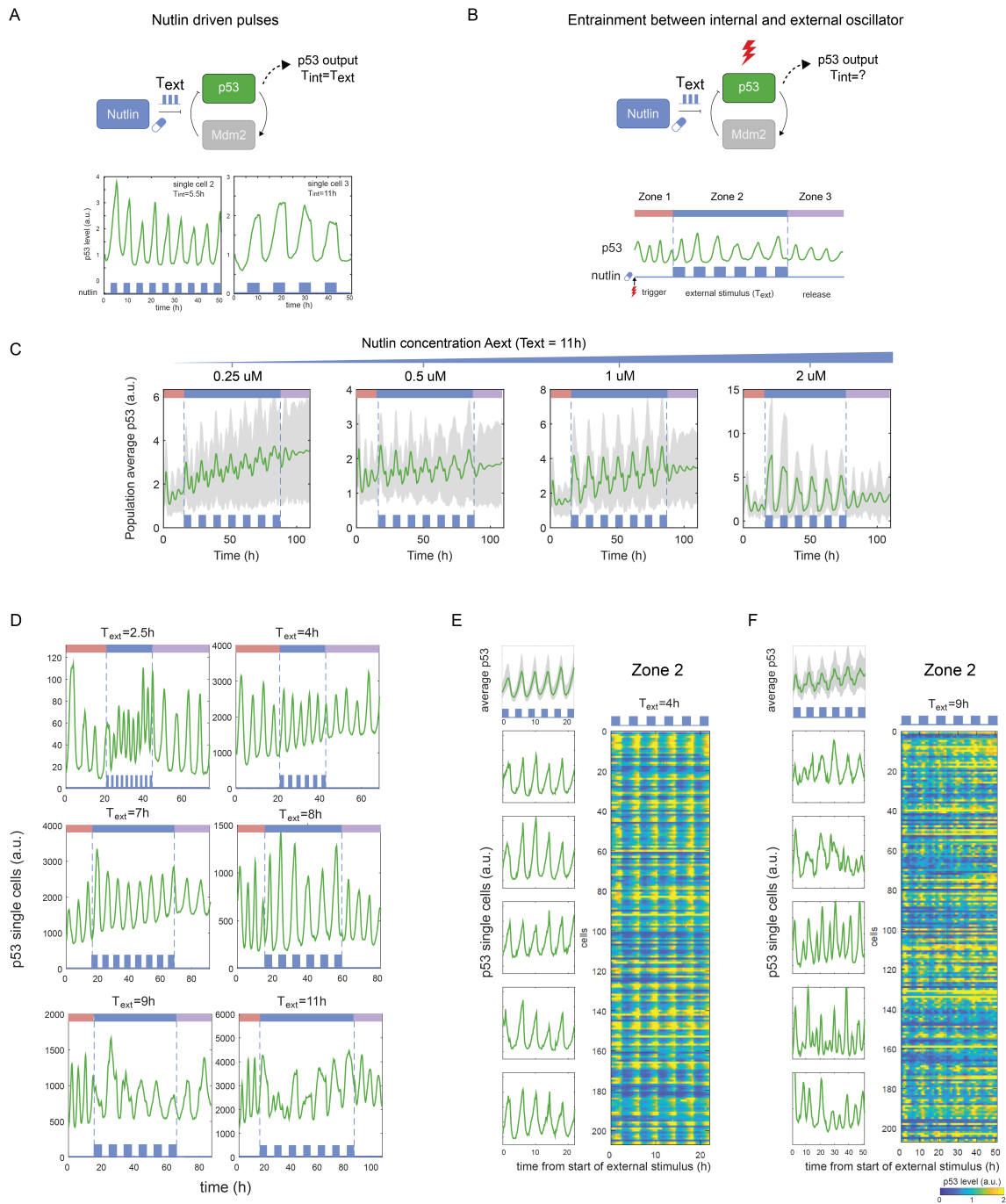


Figure 4.5: (A) Single-cell traces of unirradiated cells subjected to oscillating nutlin concentrations with $T_{ext} = 5.5h$ or $11h$. (B) Entrainment set up: the endogenous p53 oscillator is triggered by irradiation (IR) (zone 1), subjected to an external period input of nutlin (zone 2) and released (zone 3). (C) Average p53 dynamics across a range of nutlin concentrations at $T_{ext} = 11h$, where bold and shaded areas correspond to median and interquartile range, respectively. (D) Examples of locking (1:1 entrainment) across a range of external periods T_{ext} . Each trace represents a single cell. (E-F) Zone 2 dynamics at $T_{ext} = 4h$ and $T_{ext} = 9h$. Average p53 dynamics, where bold and shaded areas correspond to median and interquartile range, respectively. Single cell trace examples. Heatmaps showing p53 levels over time in single cells.

and heterogeneity at 9 h (Figure 4.5E-F). Interestingly, at 9 h cells entrain on average less robustly, with single cells displaying frequencies faster than the entraining frequencies. We next investigated whether the existence of multiple entrainment modes within a population (multistability) could explain the cell-to-cell variability at periods far from the endogenous value.

4.3.4 Higher-order entrainment of the p53 oscillator

The higher variance between single cell traces at a particular external input could be due to the co-existence of several modes of entrainment (multi-stability). Strikingly, we observed multiple forms of higher-order entrainment under a fixed external signal (Figure 4.6). While the distributions of intervals between peaks in zone 2 at T_{ext} equal to 4 h, 7 h or 8 h is unimodal, suggesting a single 1:1 mode, distributions at external periods further from endogenous are bimodal ($T_{ext} = 2.5$ h and 9 h) and trimodal ($T_{ext} = 11$ h) (Figure 4.6A). The average Fourier spectrum across external forces also indicates the dominant periods within each cell population (Figure 4.6B). Indeed, we found cases of cells showing either 1:1 or 2:1 entrainment under the same nutlin regimen, suggesting the existence of multi-stability, as exemplified by single cells A and B oscillating either once or twice per each nutlin pulse (Figure 4.6C). Figure 4.6D further shows how the number of peaks in the autocorrelation function corresponds to a cell's entrainment mode.

We further developed an algorithm that considers peak-to-peak distance to extract a cell's entrainment mode and plotted the distribution of entrainment modes across T_{ext} values (Figure 4.6E). For each cell, we first detrended the data by subtracting a polynomial fit and then applied a Gaussian filter to smooth the traces. We thus found the peaks in the traces which had a certain prominence and computed the peak-to-peak distance to find how the period (and thus the rotation number) evolved in time. The algorithm checks for possible "complex dynamics" (such as mode-hopping and period-doubling, that are investigated in details in the next section). In the absence of those, if the mean rotation number is close to one of the rational numbers within a certain threshold (1:2, 1:1, 3:2, 2:1, 3:1), it classifies it as entrained to it. If it is not, the trace is considered "Unclassified".

Our results show that external periods closest to the natural 5.5 h p53 period (T_{ext} 4 h and 7 h) lead to predominantly single entrainment modes, in which the cell population behaves homogeneously. Thus, a particular range of external periods leads to homogenous behaviour in a cell population, whereas other periods generate greater heterogeneity, as summarized in the schematic of Figure 4.6F.

Although the observation of multistability seems in contrast to single pulse experiments predictions, it should be noted that the Poincaré maps give an approximation of the Arnold Tongues, for which the main assumption is that the system has recovered from one stimulus before the next one is delivered, so that subsequent pulses give rise to the same PTC. This may be true for repeated short pulses (like 40-min single pulse delivered in Figure 4.3) but not for longer pulses, which may explain the discrepancies between predictions and experiments.

Taken together, our observations reveal that entrainment through an external oscillator allows control of p53 oscillations in time and under a range of periods close to the natural period. Control over the period of p53 oscillations was diminished at periods further from the natural period (2.5 h, 9 h and 11 h), when individual cells became phase-locked to different periods, leading to heterogeneity in single cell responses.

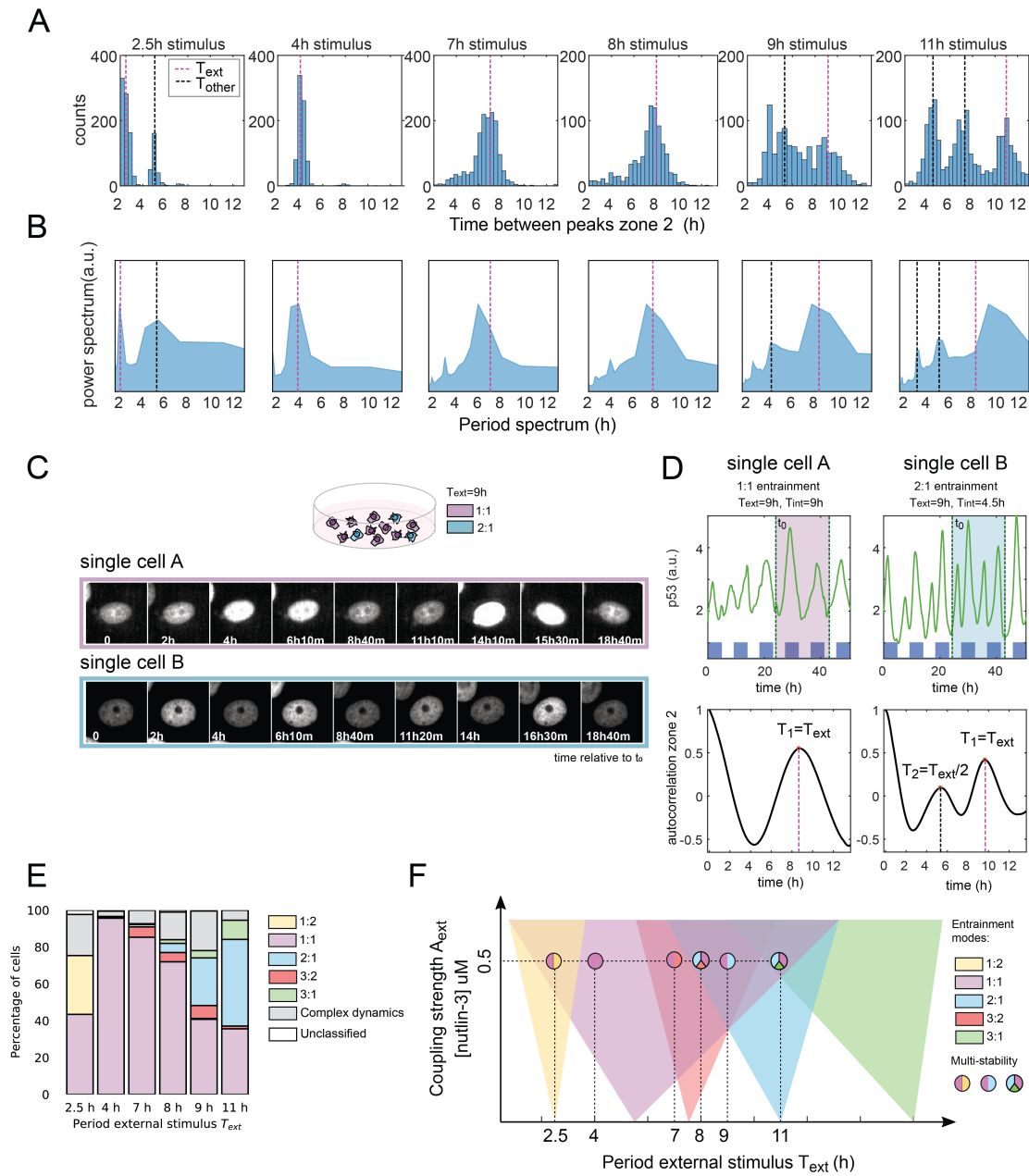


Figure 4.6: (A) Distributions of interpeak distance and (B) corresponding power spectrum in zone 2 shows unimodal, bimodal and trimodal distributions for different values of T_{ext} . Each interpeak measurement corresponds to a single peak-to-peak distance in a single cell trajectory. (C) Two examples of cells showing 1:1 or 2:1 entrainment (cell A and B, respectively) under the same 9 h nutlin stimulus suggest the existence of multi-stability. (D) Single cell traces for cell A and B in (C) and their autocorrelation function. (E) Distribution of entrainment modes across T_{ext} values. (F) Qualitative Arnold Tongues picture with regions of multi-stability at $0.5 \mu M$ suggested by experimental measurements.

4.3.5 Complex dynamics: mode-hopping, period doubling and hunt for chaos

As shown in Figure 4.6, in regions of overlapping Arnold Tongues, entrained oscillators can adopt (and maintain in time) various entrainment modes depending on their initial condition, for example single cell A adopting 1:1 and neighbouring single cell B adopting 1:2 (Figure 4.6C). This phenomenon (multi-stability) leads to the co-existence of cells oscillating at different fixed entraining modes in a population. Besides multi-stability, other types of complex dynamics might occur in regions in which the coupling strength is above critical level, such as mode-hopping and chaos (see Section 4.2.1). Mode-hopping occurs when oscillators dynamically hop between modes due to noise. Chaos, on the other hand, is characterized by a very high sensitivity to initial conditions, which leads to unpredictable and non-repeating behaviours over time, seemingly random despite being governed by deterministic rules, which make long-term predictions impossible. One of the features which suggests the emergence of chaotic dynamics is a cascade of period-doubling bifurcations in which peaks show patterns of alternating amplitudes.

The algorithm that we described in the previous section is able to distinguish between the aforementioned dynamics, namely, whether cells maintain different modes (entrainment), fluctuate between them (mode-hopping) or show patterns of oscillating amplitudes (period-2 traces), with the aim of exploring the possibility of chaotic dynamics. If the inter-peak distance and therefore the period between p53 pulses jumped between two stable states, the algorithm would classify it as mode-hopping. If the difference in amplitude of alternating peaks is higher than some threshold, the algorithm would classify the trace as period-2.

We observed mode-hopping and period-2 trajectories across conditions (Figure 4.7A). Single cell examples show cells can hop between two states, as shown by the period actively changing over time (Figure 4.7B-C). We also observe single cell trajectories with a clear tendency for amplitude of peaks to alternate between two amplitudes (Figure 4.7D).

As mentioned above, period-2 traces may be an indication of an imminent cascade of period-doubling bifurcations, which is a route to chaos (Figure 4.7E). At every bifurcation the period (meaning the time after which the trajectory repeats itself) doubles, and these bifurcations occur faster and faster, meaning that at a finite concentration of nutlin it would take infinite time for the trajectory to repeat itself, which corresponds to chaotic dynamics. One of the characteristics of chaotic dynamics is also a very high dependency on initial conditions, such that two trajectories that start very closely would exponentially diverge. Moreover, within regions of chaos, the presence of period-3 windows has been observed, such that the trajectory repeats periodically after three external pulses (Li and Yorke, 2004). If we further increase the nutlin concentration we finally expect an overall transition to a 1:1 entrainment regime, as the 1:1 tongue dominates among all the others.

To test these theoretical predictions, we considered one external frequency ($T_{ext} = 11$ h) and gradually increased the nutlin concentration from $0.5 \mu\text{M}$ to $1 \mu\text{M}$ and $2 \mu\text{M}$. As mentioned before, at $0.5 \mu\text{M}$ we observed period-2 traces (Figure 4.7F, first panel), but also traces that, despite starting from very similar initial conditions, gradually diverged in their frequency, without being entrained to the external one, which might be an indication of chaos (Figure 4.7F, second panel). At $1 \mu\text{M}$, period-3 traces could also be observed (Figure 4.7F, third panel). Finally, as predicted, further increasing the nutlin concentration led to a strong synchronization to the external signal (Figure 4.7F,

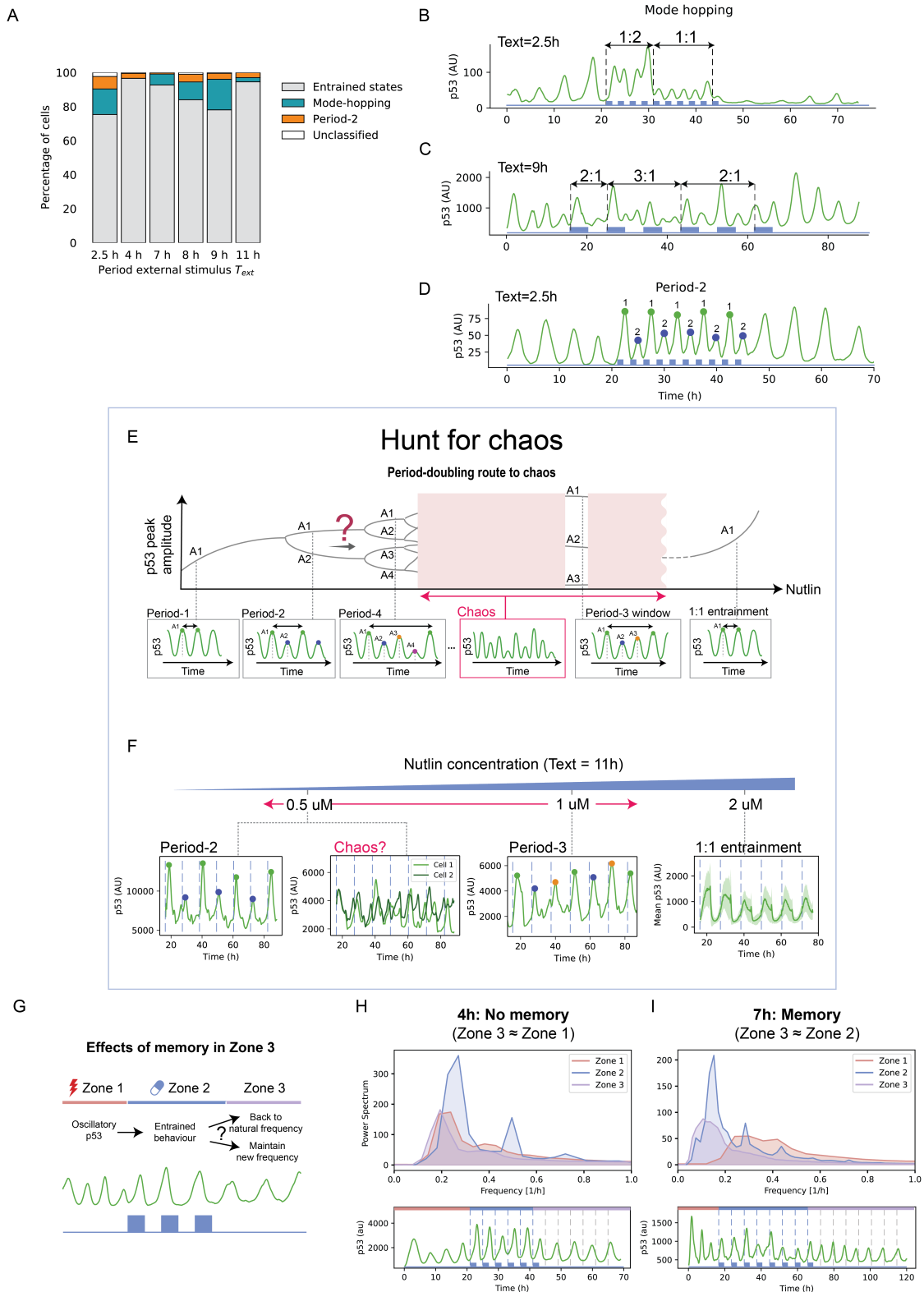


Figure 4.7: (A) Barplot showing the percentage of complex dynamics (Mode-hopping, Period-2). (B-C) Single-cell example of mode-hopping traces at 2.5 h and 9 h. (D) Single-cell example of a period-2 trace at 2.5 h. (E) Schematic showing the period-doubling route to chaos, the emergence of period-3 windows within the chaotic regime (red double-headed arrow) and the dominance of the 1:1 entrainment regime for high nutlin. (F) Increasing the nutlin concentration (from 0.5 μ M to 2 μ M at $T_{ext} = 11$ h) shows period-2 traces and possibly chaotic dynamics at 0.5 μ M, period-3 windows at 1 μ M, and the transition to 1:1 entrainment at 2 μ M. (G) Schematic showing the effect of memory in Zone 3 (H) Top: The 4 h nutlin stimulation shows no memory, as the power spectrum in Zone 3 is similar to that in Zone 1. Bottom: Corresponding single cell trace (I) Top: The 7 h nutlin stimulation shows a memory effect, as the power spectrum in Zone 3 is similar to that in Zone 2. Bottom: Corresponding single cell trace.

fourth panel). Although these observations may not be sufficient per se to establish the presence of chaotic dynamics, they might indicate that the p53 network is constructed so that, if present, the chaotic window would be anyway quite narrow, since the complex dynamics is quickly replaced by robust entrainment, which might play the role of stabilising the p53 oscillations in externally stressful conditions.

We next extended our analysis to the dynamical behaviour following nutlin removal in Zone 3 to determine whether the system returns to its natural oscillatory state (zone 1), or whether entrainment affects its behaviour (Figure 4.7G). We tested the condition with the highest, most robust single mode entrainment (4 h). By comparing the Fourier spectrum in all three zones, we observed a clear overlap between the curves in zone 3 and zone 1, indicating that the system returned to its natural oscillatory period ($T_{int} = 5.5$ h) when released (Figure 4.7H, above). This is clear by looking at single cell traces (Figure 4.7H, below), where the p53 peaks, which are entrained to nutlin in zone 2, gradually drift away from the nutlin pulses timings in zone 3 (where there is no external stimulation) (gray dashed lines). This reveals that the p53 oscillation is memoryless when stimulated with a 4 h external stimulation and the oscillation can return to the original state. However, at 7 hours, Fourier spectrum of zone 3 mostly overlaps with that of zone 2, and is markedly different from that of zone 1 (Figure 4.7I, above), meaning that zone 3 retains the entrainment period of zone 2, which can again be visualized in single cell traces (Figure 4.7I below). Our findings show that the period of the external stimulus determines whether p53 will resume oscillating at its natural period or retain the entrained period after removal of the stimulus.

4.3.6 P21 accumulation rate is lowest at the natural frequency of p53

We next investigated how entrainment of p53 to a signal with a period close to the natural period affects the accumulation rate of one of its major downstream targets, p21 (Figure 4.8A). As mentioned in the Introduction, p21 is key to cell fate decision, and is necessary to establish cell-cycle arrest after damage (Brugarolas *et al.*, 1995; El-Deiry *et al.*, 1993; Hsu *et al.*, 2019). The p21 concentration was monitored across zones 1, 2, and 3 for 4 h and 7 h external signals (applied in zone 2) (Figure 4.8B-C). Because single cell traces showed a great deal of heterogeneity in p21 responses, we used k-means clustering to group cells according to their p21 dynamics. We found that a cluster comprising 75% and 48% of cells for the 4 h and 7 h case respectively, showed a graded response in Zone 2, for which the accumulation rate could be computed by a linear fit (Figure 4.8D). We restricted the analysis to these clusters and computed the slope of the linear fits in each zone, namely $\Delta_{1,2,3}$ (Figure 4.8E-F). We observe that for both 4 h and 7 h nutlin stimulation, the slope in Zone 2 was greater than the slope in Zone 1, meaning that the p21 accumulation rate was at a minimum for the natural p53 periodicity of 5.5 h (Figure 4.8G, left). This may suggest that the 5.5 h natural frequency of p53 has evolved to dampen the rise in p21, presumably to protect cells from committing to senescence too quickly.

We further confirmed this finding using a different method, namely computing the weighted average of all the traces, using as weights the error of the linear fits (Figure 4.8G, right). This gives a higher weight to those traces that can be better approximated by a linear fit, i.e., where there is some graded response. In this case too, the growth in Zone 2 is greater than that in Zone 1 for both 4 h and 7 h of nutlin stimulation. Subsequently, we investigated how the system responds to the nutlin stimulation

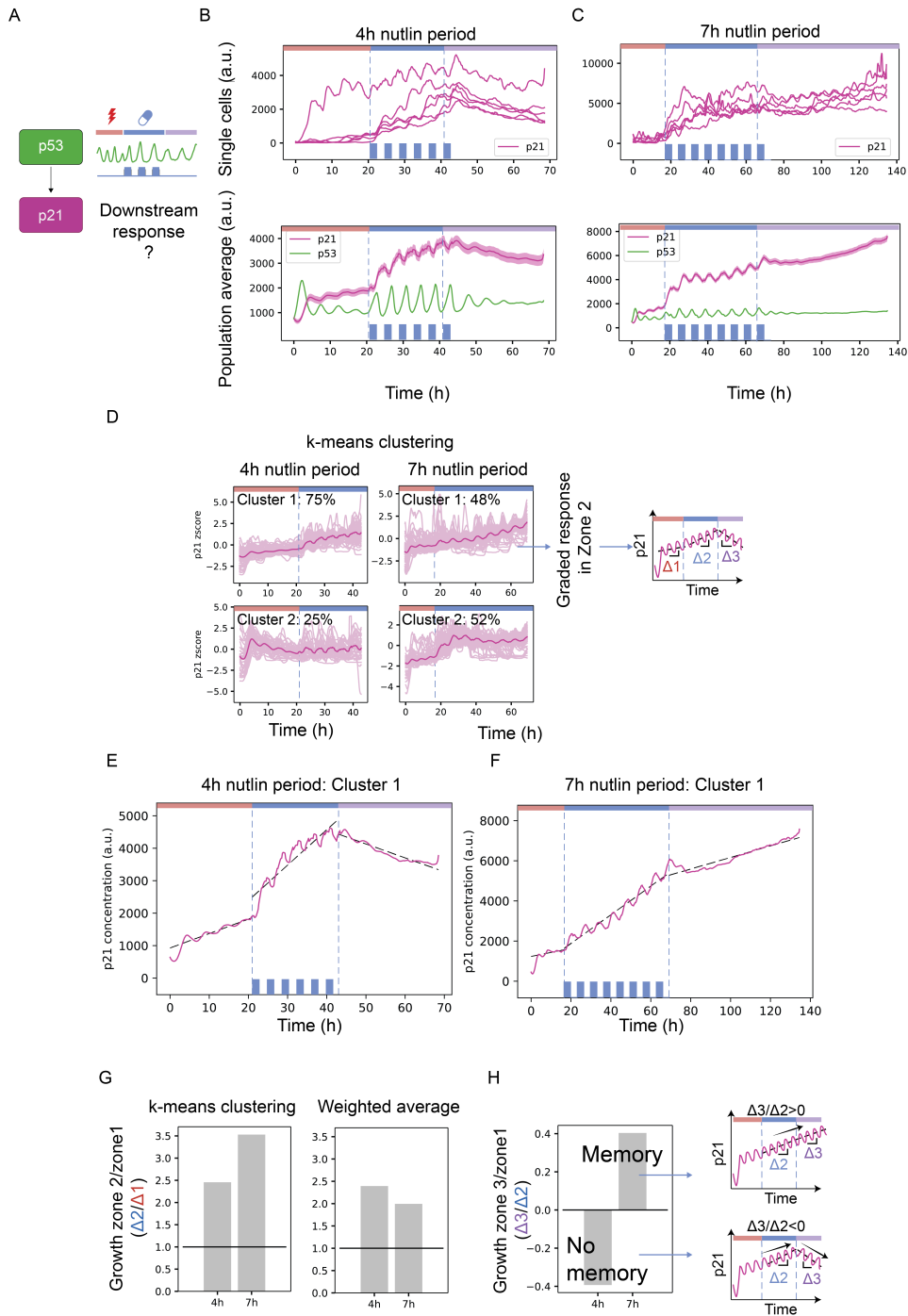


Figure 4.8: (A) Schematic figure showing the downstream response of p21 when p53 is entrained to an external frequency given by an oscillatory nutlin concentration. (B) Single cell traces (top panel) and population averages (bottom panel) for the p21 concentration dynamics, shown in pink, for nutlin stimulation period of 4 h. The correspondent p53 signal is shown in green. (C) Same as (B), but for nutlin stimulation period of 7 h. (D) Performing k-means clustering on the p21 z-scores shows the existence of different clusters of p21 response, with one cluster having a graded response in Zone 2 for both 4 h and 7 h of nutlin stimulation. For this cluster, the growth is computed in Zone 1, 2 and 3 as $\Delta_{1,2,3}$. (E) Average p21 concentration in the two clusters for 4 h nutlin pulses. (F) Same as (E), for 7 h nutlin pulses. (G) The growth rate in Zone2/Zone1 > 1 for both 4 h and 7 h nutlin pulses, both with the k-means clustering method (left panel) and the weighted average of traces (right panel). (H) The growth rate in Zone3/Zone1 shows that the system has memory for the 7 h nutlin pulses, while it has no memory for the 4 h case.

in Zone 3, when the stimulus has ceased (Figure 4.8H). What we observed is that for entrainment at 4 h, where cells do not display memory (Figure 4.7G), thus return to their natural p53 frequency in zone 3, the p21 concentration relaxes to the value of Zone 1 ($\Delta_3/\Delta_2 < 0$). On the other hand, for 7 h entrainment, where cells do display memory (Figure 4.7H), the p21 concentration increases despite the ceasing of nutlin pulses ($\Delta_3/\Delta_2 > 0$).

4.4 Discussion and Perspectives

Oscillations and complex dynamics control many processes in living organisms: for instance, the oscillations observed in the nuclear concentration of transcription factors such as p53 or Nf- κ B in response to stress. However, the downstream effects on gene expression resulting from these dynamics are still debated (Zambrano *et al.*, 2016; Nelson *et al.*, 2004; Jiménez, Lu, Kalocsay, *et al.*, 2022). A challenge in this research lays in precisely manipulating aspects of these oscillations, like their intrinsic frequency, especially *in vivo* (Heltberg, Krishna, *et al.*, 2021). A way to address this issue is by entraining the signal with an external oscillator controlled by the experimenter. This has been achieved with Nf- κ B, entrained to external pulses of TNFa (Kellogg and Tay, 2015; Heltberg *et al.*, 2016), but, as of today, not with p53. This approach enables us to systematically explore how downstream effects change as the oscillations are perturbed and their frequency varied, as well as to quantify the robustness and tunability of the oscillations in response to perturbations. Indeed, a deeper understanding of the mechanisms and principles behind how these oscillations are naturally regulated and controlled within the complexity of their environment, would be a major step forward in the field.

In this work, we show how to control the dynamics in the nuclear concentration of the tumor-suppressive transcription factor p53 by perturbing it with an external, oscillatory signal. We present the first evidence of entrainment of the p53 clock to an external pulsing signal, to provide insights into p53's essential dynamical properties. By combining experimental measurements, using a novel microfluidic device and live-cell microscopy, with theoretical tools from nonlinear dynamics, we produce for the first time a compelling coarse-grained model of entrainment in the p53 network. Here, we highlight the potential of mathematical modelling as a means to simplify the great biological complexity of the p53 network: by defining simple ODEs which capture the dynamics of p53 oscillations, we study the response to single external perturbations and predict the possibility of achieving entrainment with repeated pulses. We then experimentally demonstrate the existence of period locking of the p53 network across a wide range of entrainment parameters, including higher-order coupling, multi-stability, and memory effects. Entrainment to external signals and the emerging of complex dynamics has been observed in other biological systems, such as the embryonic segmentation clock (Sanchez *et al.*, 2022), and cardiac rhythm (Glass *et al.*, 1987). Finally, we show how the p53 natural frequency minimizes the accumulation rate of the downstream target p21, and we suggest that this may be a mechanism to prevent cells from committing to senescence too quickly.

It should be noted, that some of the experimental findings were rather unexpected, and seemingly in contrast with the theoretical predictions: in particular, the presence of multi-stability of different entrained states. As we mention in the main text, this may be due to the fact that the assumptions of the model are not completely satisfied in the experiments with periodic-pulses, as these may be too

strong and too close in time for the system to have time to return to its natural oscillations before the next pulse arrives.

One of the main limitations of this work, which is common to many biological systems, is the presence of high levels of stochasticity and noise in the data, and the limited length of recorded traces, which make the computation of the entrainment mode challenging. This also highly complicates the detection of chaos: in general, the canonical way to determine the presence of chaotic dynamics would be to compute the Lyapunov exponent, to determine whether two points that are initially very close in phase space diverge exponentially with time. However, the presence of high levels of noise generally make traces diverge even in the absence of chaos, only due to phase drift (Heltberg, Krishna, *et al.*, 2021). Finally, the results regarding p21 accumulation rate would highly benefit from further experimental verifications with 5.5 h stimulation of nutlin in zone 2, to make sure that the accumulation of p21 in the system is really an effect of p53 frequency and not of the addition of nutlin per sé.

To conclude, in this work, we show that it is possible to control p53 frequency by entraining it to an external pulsing signal, elucidating a possible role for its intrinsic natural frequency in the downstream effects on target p21. It should be noted that this is an artificial setting where an external drug (nutlin) is delivered in periodic pulses: p53 is not naturally entrained to it *in vivo*. In general, this approach could also be exploited to build synthetic oscillators that are heavily intertwined in nature in order to elucidate the mechanisms behind their coupling (Jiménez, Lu, Jambhekar, *et al.*, 2022).

In the future, it would be interesting to test, as a possible therapeutic application, whether synchronizing p53 levels in a population of cancer cells to a specific phase, prior to delivering radiotherapy/chemotherapy, could make the population more prone to death depending on the phase at which the drug is received. Indeed, if cells were more "protected" at some specific phase of the ongoing p53 oscillations (for instance, when p53 is high), one could imagine that having a heterogeneous population could maximize the chances of cells to survive, while having all cells in the same state could result in either survival or death for all of them depending on the timing of the therapy.

Conclusion

In this thesis, we have delved into the world of biological oscillators, learning how oscillations are ubiquitous in nature and serve a myriad of different purposes, from neuronal signalling to gene regulation, from the circadian clock to the rhythmic beating of the heart. We have observed the phenomenon of collective synchronization, a fascinating outcome of coupled oscillators working in harmony, and we have witnessed how this harmony can spontaneously break and create exotic patterns of coherence and incoherence. We have discovered how oscillating concentration fields of transcription factors in the cellular nucleus can save cells in danger by distributing vital resources to specific locations. In this case, the ingenious mechanism cells employ for survival makes wise use of the physics of phase separation. Finally, we have shown how we can manipulate the transcription factors' oscillating dynamics by locking them to external rhythms controlled from the outside. By artificially perturbing the oscillators from their preferred natural frequency, we have also gained insights into the evolutionary benefits of portraying that specific dynamics.

Understanding the diverse dynamics that arise as a result of a system's surrounding network, along with their respective roles, functionalities, and the emergent properties resulting from collective behaviour, holds tremendous potential for advancing our comprehension of life's fundamental mechanisms. It also has the power to revolutionize applications in medicine and biotechnology. For instance, a longstanding aspiration among researchers is to pinpoint the precise external stimulus that, when administered to the brains of Parkinson's patients, could decisively disrupt their neuronal pathological synchronization. Moreover, the ability to control and influence the dynamics of specific systems in a predictable manner lies at the heart of synthetic biology. Here, researchers strive to design and program engineered biological circuits that exhibit desired dynamics.

Still so many open questions remain to be addressed, which demand an interdisciplinary approach, weaving together physics, applied mathematics, systems biology and neuroscience. The past half-century has witnessed an extraordinary surge in these fields, driven by groundbreaking advances in experimental techniques such as time-lapse microscopy and live-cell imaging. These innovations empower researchers with an unprecedented level of precision in monitoring the dynamic behaviours of individual cells, or in recording the activity of single neurons. Simultaneously, we now have increasingly sophisticated computers available for data analysis and simulations. However, the anticipated exponential growth in data volume in the years ahead raises concerns about a potential data overload. Navigating through this abundance and extracting relevant information to understand the complexities of biological systems may prove to be a significant challenge.

This is where mathematical theories and models will become absolutely indispensable, as a means to identify the critical components of the systems, provide intuition, guide further experiments and make predictions. Indeed, the beauty of mathematics is that it uncovers unifying principles and coherence, revealing similarities between seemingly disparate systems. The ultimate dream is that

one day we will be able to understand life itself as a prodigious collective phenomenon, stemming from the interplay of the intricate dynamics of all elements in the natural world.

Bibliography

- Abrams, Daniel M and Steven H Strogatz (2006). “Chimera states in a ring of nonlocally coupled oscillators”. In: *International Journal of Bifurcation and Chaos* 16.01, pp. 21–37.
- Abrams, Daniel M., Rennie Mirollo, Steven H. Strogatz, and Daniel A. Wiley (Aug. 2008). “Solvable Model for Chimera States of Coupled Oscillators”. In: *Phys. Rev. Lett.* 101 (8), p. 084103.
- Abrams, Daniel M. and Steven H. Strogatz (2004). “Chimera states for coupled oscillators”. In: *Physical Review Letters* 93.17, pp. 2–5.
- Alberts, Bruce (2017). *Molecular biology of the cell*. Garland science.
- Arnold, Vladimir I (1965). “Small denominators, I: mappings of the circumference into itself”. In: *AMS Trans. Series 2* 46, p. 213.
- Arnold, Vladimir Igorevich and André Avez (1968). “Ergodic problems of classical mechanics”. In: (*Addison-Wesley*).
- Aylon, Yael and Moshe Oren (2007). “Living with p53, dying of p53”. In: *Cell* 130.4, pp. 597–600.
- Batchelor, Eric, Alexander Loewer, Caroline Mock, and Galit Lahav (2011). “Stimulus-dependent dynamics of p53 in single cells”. In: *Molecular systems biology* 7.1, p. 488.
- Behar, Marcelo and Alexander Hoffmann (2010). “Understanding the temporal codes of intra-cellular signals”. In: *Current opinion in genetics & development* 20.6, pp. 684–693.
- Bianchi, Arianna, Thomas Hillen, Mark A Lewis, and Yingfei Yi (2019). *The dynamics of biological systems*. Vol. 4. Springer.
- Brangwynne, Clifford P, Christian R Eckmann, David S Courson, Agata Rybarska, Carsten Hoege, Jöbin Gharakhani, Frank Jülicher, and Anthony A Hyman (2009). “Germline P granules are liquid droplets that localize by controlled dissolution/condensation”. In: *Science* 324.5935, pp. 1729–1732.
- Brugarolas, James, Chitra Chandrasekaran, Jeffrey I Gordon, David Beach, Tyler Jacks, and Gregory J Hannon (1995). “Radiation-induced cell cycle arrest compromised by p21 deficiency”. In: *Nature* 377.6549, pp. 552–557.
- Byrne, Helen M (2010). “Dissecting cancer through mathematics: from the cell to the animal model”. In: *Nature Reviews Cancer* 10.3, pp. 221–230.
- Chen, Jiandong (2016). “The cell-cycle arrest and apoptotic functions of p53 in tumor initiation and progression”. In: *Cold Spring Harbor perspectives in medicine* 6.3, a026104.
- Crick, Francis H (1958). “On protein synthesis”. In: *Symp Soc Exp Biol*. Vol. 12. 138-63, p. 8.
- Czeisler, Charles A., Jeanne F. Duffy, Theresa L. Shanahan, *et al.* (1999). “Stability, Precision, and Near-24-Hour Period of the Human Circadian Pacemaker”. In: *Science* 284.5423, pp. 2177–2181. eprint: <https://www.science.org/doi/pdf/10.1126/science.284.5423.2177>.

- El-Deiry, Wafik S, Takashi Tokino, Victor E Velculescu, Daniel B Levy, Ramon Parsons, Jeffrey M Trent, David Lin, W Edward Mercer, Kenneth W Kinzler, and Bert Vogelstein (1993). “WAF1, a potential mediator of p53 tumor suppression”. In: *Cell* 75.4, pp. 817–825.
- Douglass, John K, Lon Wilkens, Eleni Pantazelou, and Frank Moss (1993). “Noise enhancement of information transfer in crayfish mechanoreceptors by stochastic resonance”. In: *Nature* 365.6444, pp. 337–340.
- Elowitz, Michael B, Arnold J Levine, Eric D Siggia, and Peter S Swain (2002). “Stochastic gene expression in a single cell”. In: *Science* 297.5584, pp. 1183–1186.
- Ermentrout, Bard (1986). “Losing amplitude and saving phase”. In: *Nonlinear Oscillations in Biology and Chemistry: Proceedings of a meeting held at the University of Utah, May 9–11, 1985*. Springer, pp. 98–114.
- Ermentrout, Bard (1996). “Type I membranes, phase resetting curves, and synchrony”. In: *Neural computation* 8.5, pp. 979–1001.
- Ermentrout, G Bard and Nancy Kopell (1986). “Parabolic bursting in an excitable system coupled with a slow oscillation”. In: *SIAM journal on applied mathematics* 46.2, pp. 233–253.
- Feigenbaum, Mitchell J, Leo P Kadanoff, and Scott J Shenker (1982). “Quasiperiodicity in dissipative systems: a renormalization group analysis”. In: *Physica D: Nonlinear Phenomena* 5.2-3, pp. 370–386.
- Fell, Juergen and Nikolai Axmacher (2011). “The role of phase synchronization in memory processes”. In: *Nature reviews neuroscience* 12.2, pp. 105–118.
- Ferrell, James E, Tony Yu-Chen Tsai, and Qiong Yang (2011). “Modeling the cell cycle: why do certain circuits oscillate?” In: *Cell* 144.6, pp. 874–885.
- Friedberg, Errol C (2003). “DNA damage and repair”. In: *Nature* 421.6921, pp. 436–440.
- Fuchs, Serge Y, Victor Adler, Thomas Buschmann, Xiangwei Wu, and Ze’ev Ronai (1998). “Mdm2 association with p53 targets its ubiquitination”. In: *Oncogene* 17.19, pp. 2543–2547.
- Galán, Roberto F, G. Bard Ermentrout, and Nathaniel N. Urban (2007). “Reliability and stochastic synchronization in type I vs. type II neural oscillators”. In: *Neurocomputing* 70.10. Computational Neuroscience: Trends in Research 2007, pp. 2102–2106.
- Gérard, Claude and Albert Goldbeter (2012). “Entrainment of the mammalian cell cycle by the circadian clock: modeling two coupled cellular rhythms”. In: *PLoS computational biology* 8.5, e1002516.
- Gerstner, Wulfram, Werner M Kistler, Richard Naud, and Liam Paninski (2014). *Neuronal dynamics: From single neurons to networks and models of cognition*. Cambridge University Press.
- Gillespie, Daniel T (1976). “A general method for numerically simulating the stochastic time evolution of coupled chemical reactions”. In: *Journal of computational physics* 22.4, pp. 403–434.
- Glass, L, AL Goldberger, M Courtemanche, and A Shrier (1987). “Nonlinear dynamics, chaos and complex cardiac arrhythmias”. In: *Proceedings of the Royal Society of London. A. Mathematical and Physical Sciences* 413.1844, pp. 9–26.
- Glass, Leon and Michael C Mackey (1988). *From clocks to chaos: The rhythms of life*. Princeton University Press.
- Glass, Leon and Arthur T Winfree (1984). “Discontinuities in phase-resetting experiments”. In: *American Journal of Physiology-Regulatory, Integrative and Comparative Physiology* 246.2, R251–R258.
- Goldbeter, Albert (1995). “A model for circadian oscillations in the *Drosophila* period protein (PER)”. In: *Proceedings of the Royal Society of London. Series B: Biological Sciences* 261.1362, pp. 319–324.

- Gonze, Didier, José Halloy, and Albert Goldbeter (2002). “Robustness of circadian rhythms with respect to molecular noise”. In: *Proceedings of the National Academy of Sciences* 99.2, pp. 673–678.
- Granada, A, RM Hennig, B Ronacher, A Kramer, and H Herzel (2009). “Phase response curves: elucidating the dynamics of coupled oscillators”. In: *Methods in enzymology* 454, pp. 1–27.
- Guevara, Michael R and Leon Glass (1982). “Phase locking, period doubling bifurcations and chaos in a mathematical model of a periodically driven oscillator: A theory for the entrainment of biological oscillators and the generation of cardiac dysrhythmias”. In: *Journal of mathematical biology* 14, pp. 1–23.
- Hafner, Antonina, Jacob Stewart-Ornstein, Jeremy E Purvis, William C Forrester, Martha L Bulyk, and Galit Lahav (2017). “p53 pulses lead to distinct patterns of gene expression albeit similar DNA-binding dynamics”. In: *Nature structural & molecular biology* 24.10, pp. 840–847.
- Hagerstrom, Aaron M, Thomas E Murphy, Rajarshi Roy, Philipp Hövel, Iryna Omelchenko, and Eckehard Schöll (2012). “Experimental observation of chimeras in coupled-map lattices”. In: *Nature Physics* 8.9, pp. 658–661.
- Hansel, David, Germán Mato, and Claude Meunier (1995). “Synchrony in excitatory neural networks”. In: *Neural computation* 7.2, pp. 307–337.
- Harton, Marie D, Woo Seuk Koh, Amie D Bunker, Abhyudai Singh, and Eric Batchelor (2019). “p53 pulse modulation differentially regulates target gene promoters to regulate cell fate decisions”. In: *Molecular Systems Biology* 15.9, e8685.
- Hastings, J Woodland and Beatrice M Sweeney (1958). “A persistent diurnal rhythm of luminescence in *Gonyaulax polyedra*”. In: *The Biological Bulletin* 115.3, pp. 440–458.
- Hastings, Stuart, John Tyson, and Dallas Webster (1977). “Existence of periodic solutions for negative feedback cellular control systems”. In: *Journal of Differential Equations* 25.1, pp. 39–64.
- Haugland, Sindre W (June 2021). “The changing notion of chimera states, a critical review”. In: *Journal of Physics: Complexity* 2.3, p. 032001.
- Haupt, Ygal, Ruth Maya, Anat Kazaz, and Moshe Oren (1997). “Mdm2 promotes the rapid degradation of p53”. In: *Nature* 387.6630, pp. 296–299.
- Heltberg, Mathias, Ryan A Kellogg, Sandeep Krishna, Savaş Tay, and Mogens H Jensen (2016). “Noise induces hopping between NF- κ B entrainment modes”. In: *Cell systems* 3.6, pp. 532–539.
- Heltberg, Mathias L, Sandeep Krishna, and Mogens H Jensen (2019). “On chaotic dynamics in transcription factors and the associated effects in differential gene regulation”. In: *Nature communications* 10.1, p. 71.
- Heltberg, Mathias L, Sandeep Krishna, Leo P Kadanoff, and Mogens H Jensen (2021). “A tale of two rhythms: Locked clocks and chaos in biology”. In: *Cell Systems* 12.4, pp. 291–303.
- Heltberg, Mathias L, Judith Miné-Hattab, Angela Taddei, Aleksandra M Walczak, and Thierry Mora (2021). “Physical observables to determine the nature of membrane-less cellular sub-compartments”. In: *Elife* 10, e69181.
- Heltberg, Mathias S, Alessandra Lucchetti, Feng-Shu Hsieh, Duy Pham Minh Nguyen, Sheng-hong Chen, and Mogens H Jensen (2022). “Enhanced DNA repair through droplet formation and p53 oscillations”. In: *Cell* 185.23, pp. 4394–4408.
- Hodgkin, Alan L (1948). “The local electric changes associated with repetitive action in a non-medullated axon”. In: *The Journal of physiology* 107.2, p. 165.
- Hodgkin, Alan L and Andrew F Huxley (1952). “A quantitative description of membrane current and its application to conduction and excitation in nerve”. In: *The Journal of physiology* 117.4, p. 500.

- Hoffmann, Alexander, Andre Levchenko, Martin L Scott, and David Baltimore (2002). “The I κ B-NF- κ B signaling module: temporal control and selective gene activation”. In: *science* 298.5596, pp. 1241–1245.
- Holehouse, James, Zhixing Cao, and Ramon Grima (2020). “Stochastic modeling of autoregulatory genetic feedback loops: a review and comparative study”. In: *Biophysical Journal* 118.7, pp. 1517–1525.
- Holt, Abbey B, Eszter Kormann, Alessandro Gulberti, Monika Pötter-Nerger, Colin G McNamara, Hayriye Cagnan, Magdalena K Baaske, Simon Little, Johannes A Köppen, Carsten Buhmann, *et al.* (2019). “Phase-dependent suppression of beta oscillations in Parkinson’s disease patients”. In: *Journal of Neuroscience* 39.6, pp. 1119–1134.
- Honda, Reiko, Hirofumi Tanaka, and Hideyo Yasuda (1997). “Oncoprotein MDM2 is a ubiquitin ligase E3 for tumor suppressor p53”. In: *FEBS letters* 420.1, pp. 25–27.
- Hoppensteadt, Frank C. and Eugene M. Izhikevich (1997). “Weakly connected neural networks”. In: Hsu, Chien-Hsiang, Steven J Altschuler, and Lani F Wu (2019). “Patterns of early p21 dynamics determine proliferation-senescence cell fate after chemotherapy”. In: *Cell* 178.2, pp. 361–373.
- Izhikevich, Eugene M (2000). “Phase equations for relaxation oscillators”. In: *SIAM Journal on Applied Mathematics* 60.5, pp. 1789–1804.
- Izhikevich, Eugene M (2004). “Which model to use for cortical spiking neurons?” In: *IEEE transactions on neural networks* 15.5, pp. 1063–1070.
- Izhikevich, Eugene M. (2018). *Dynamical Systems in Neuroscience*.
- Jalife, John (1984). “Mutual entrainment and electrical coupling as mechanisms for synchronous firing of rabbit sino-atrial pace-maker cells.” In: *The Journal of physiology* 356.1, pp. 221–243.
- Jensen, MH, Kim Sneppen, and G Tiana (2003). “Sustained oscillations and time delays in gene expression of protein Hes1”. In: *Febs Letters* 541.1-3, pp. 176–177.
- Jensen, Mogens Høgh, Per Bak, and Tomas Bohr (1984). “Transition to chaos by interaction of resonances in dissipative systems. I. Circle maps”. In: *Physical review A* 30.4, p. 1960.
- Jiménez, Alba, Dan Lu, Marian Kalocsay, Matthew J Berberich, Petra Balbi, Ashwini Jambhekar, and Galit Lahav (2022). “Time-series transcriptomics and proteomics reveal alternative modes to decode p53 oscillations”. In: *Molecular Systems Biology* 18.3, e10588. eprint: <https://www.embopress.org/doi/pdf/10.15252/msb.202110588>.
- Jiménez, Alba, Ying Lu, Ashwini Jambhekar, and Galit Lahav (2022). “Principles, mechanisms and functions of entrainment in biological oscillators”. In: *Interface Focus* 12.3, p. 20210088.
- Josic, K., E. T. Shea-Brown, and J. Moehlis (2006). “Isochron”. In: *Scholarpedia* 1.8. revision #182469, p. 1361.
- Kamagata, Kiyoto, Saori Kanbayashi, Masaya Honda, Yuji Itoh, Hiroto Takahashi, Tomoshi Kameda, Fumi Nagatsugi, and Satoshi Takahashi (2020). “Liquid-like droplet formation by tumor suppressor p53 induced by multivalent electrostatic interactions between two disordered domains”. In: *Scientific reports* 10.1, p. 580.
- Kay, Sophie K, Heather A Harrington, Sarah Shepherd, Keith Brennan, Trevor Dale, James M Osborne, David J Gavaghan, and Helen M Byrne (2017). “The role of the Hes1 crosstalk hub in Notch-Wnt interactions of the intestinal crypt”. In: *PLoS computational biology* 13.2, e1005400.
- Kellogg, Ryan A and Savaş Tay (2015). “Noise facilitates transcriptional control under dynamic inputs”. In: *Cell* 160.3, pp. 381–392.

- Kobayashi, Taeko, Hiroaki Mizuno, Itaru Imayoshi, Chikara Furusawa, Katsuhiko Shirahige, and Ryoichiro Kageyama (2009). “The cyclic gene Hes1 contributes to diverse differentiation responses of embryonic stem cells”. In: *Genes & development* 23.16, pp. 1870–1875.
- Kondo, Takao, Tetsuya Mori, Nadya V Lebedeva, Setsuyuki Aoki, Masahiro Ishiura, and Susan S Golden (1997). “Circadian rhythms in rapidly dividing cyanobacteria”. In: *Science* 275.5297, pp. 224–227.
- Kracikova, M, G Akiri, A George, R Sachidanandam, and SA Aaronson (2013). “A threshold mechanism mediates p53 cell fate decision between growth arrest and apoptosis”. In: *Cell Death & Differentiation* 20.4, pp. 576–588.
- Krishna, Sandeep, Mogens H Jensen, and Kim Sneppen (2006). “Minimal model of spiky oscillations in NF- κ B signaling”. In: *Proceedings of the National Academy of Sciences* 103.29, pp. 10840–10845.
- Kruse, Karsten and Frank Jülicher (2005). “Oscillations in cell biology”. In: *Current opinion in cell biology* 17.1, pp. 20–26.
- Kubbutat, Michael HG, Stephen N Jones, and Karen H Vousden (1997). “Regulation of p53 stability by Mdm2”. In: *Nature* 387.6630, pp. 299–303.
- Kuramoto, Yoshiki (1975). “International symposium on mathematical problems in theoretical physics”. In: *Lecture notes in Physics* 30, p. 420.
- Kuramoto, Yoshiki and Dorjsuren Battogtokh (2002). “Coexistence of Coherence and Incoherence in Nonlocally Coupled Phase Oscillators”. In: July.
- Lahav, Galit, Nitzan Rosenfeld, Alex Sigal, Naama Geva-Zatorsky, Arnold J Levine, Michael B Elowitz, and Uri Alon (2004). “Dynamics of the p53-Mdm2 feedback loop in individual cells”. In: *Nature genetics* 36.2, pp. 147–150.
- Laing, Carlo R (2015). “Chimeras in networks with purely local coupling”. In: *Physical Review E* 92.5, p. 050904.
- Lambert, Samuel A, Arttu Jolma, Laura F Campitelli, Pratyush K Das, Yimeng Yin, Mihai Albu, Xiaoting Chen, Jussi Taipale, Timothy R Hughes, and Matthew T Weirauch (2018). “The human transcription factors”. In: *Cell* 172.4, pp. 650–665.
- Lane, David and Arnold Levine (2010). “p53 Research: the past thirty years and the next thirty years”. In: *Cold Spring Harbor perspectives in biology* 2.12, a000893.
- Lane, David P (1992). “p53, guardian of the genome”. In: *Nature* 358.6381, pp. 15–16.
- Larger, Laurent, Bogdan Penkovsky, and Yuri Maistrenko (2013). “Virtual chimera states for delayed-feedback systems”. In: *Physical review letters* 111.5, p. 054103.
- Larson, Adam G, Daniel Elnatan, Madeline M Keenen, Michael J Trnka, Jonathan B Johnston, Alma L Burlingame, David A Agard, Sy Redding, and Geeta J Narlikar (2017). “Liquid droplet formation by HP1 α suggests a role for phase separation in heterochromatin”. In: *Nature* 547.7662, pp. 236–240.
- Latchman, David S (1997). “Transcription factors: an overview”. In: *The international journal of biochemistry & cell biology* 29.12, pp. 1305–1312.
- Levine, Joe H, Yihan Lin, and Michael B Elowitz (2013). “Functional roles of pulsing in genetic circuits”. In: *Science* 342.6163, pp. 1193–1200.
- Li, Tien-Yien and James A Yorke (2004). “Period three implies chaos”. In: *The theory of chaotic attractors*, pp. 77–84.
- Lifshitz, Ilya M and Vitaly V Slyozov (1961). “The kinetics of precipitation from supersaturated solid solutions”. In: *Journal of physics and chemistry of solids* 19.1-2, pp. 35–50.

- Lisby, Michael, Jacqueline H Barlow, Rebecca C Burgess, and Rodney Rothstein (2004). “Choreography of the DNA damage response: spatiotemporal relationships among checkpoint and repair proteins”. In: *Cell* 118.6, pp. 699–713.
- Lisby, Michael, Rodney Rothstein, and Uffe H. Mortensen (2001). “Rad52 forms DNA repair and recombination centers during S phase”. In: *Proceedings of the National Academy of Sciences* 98.15, pp. 8276–8282. eprint: <https://www.pnas.org/doi/pdf/10.1073/pnas.121006298>.
- Lotka, Alfred J. (1910). “Contribution to the Theory of Periodic Reactions”. In: *The Journal of Physical Chemistry* 14.3, pp. 271–274. eprint: <https://doi.org/10.1021/j150111a004>.
- Lucchetti, Alessandra, Mogens H Jensen, and Mathias L Heltberg (2021). “Emergence of chimera states in a neuronal model of delayed oscillators”. In: *Physical Review Research* 3.3, p. 033041.
- Ma, Lan, John Wagner, John Jeremy Rice, Wenwei Hu, Arnold J Levine, and Gustavo A Stolovitzky (2005). “A plausible model for the digital response of p53 to DNA damage”. In: *Proceedings of the National Academy of Sciences* 102.40, pp. 14266–14271.
- Majhi, Soumen, Bidesh K Bera, Dibakar Ghosh, and Matjaž Perc (2019). “Chimera states in neuronal networks: A review”. In: *Physics of life reviews* 28, pp. 100–121.
- Martens, Erik Andreas, Shashi Thutupalli, Antoine Fourriere, and Oskar Hallatschek (2013). “Chimera states in mechanical oscillator networks”. In: *Proceedings of the National Academy of Sciences* 110.26, pp. 10563–10567.
- Meek, David W (2004). “The p53 response to DNA damage”. In: *DNA repair* 3.8-9, pp. 1049–1056.
- Mengel, Benedicte, Alexander Hunziker, Lykke Pedersen, Ala Trusina, Mogens H Jensen, and Sandeep Krishna (2010). “Modeling oscillatory control in NF- κ B, p53 and Wnt signaling”. In: *Current opinion in genetics & development* 20.6, pp. 656–664.
- Mofakham, Sima, Christian G Fink, Victoria Booth, and Michal R Zochowski (2016). “Interplay between excitability type and distributions of neuronal connectivity determines neuronal network synchronization”. In: *Physical Review E* 94.4, p. 042427.
- Murray, James D (2002). “Mathematical biology: I. An introduction. Interdisciplinary applied mathematics”. In: *Mathematical Biology, Springer* 17.
- Murray-Zmijewski, Fiona, Elizabeth A Slee, and Xin Lu (2008). “A complex barcode underlies the heterogeneous response of p53 to stress”. In: *Nature reviews Molecular cell biology* 9.9, pp. 702–712.
- Nag, Subhasree, Jiangjiang Qin, Kalkunte S Srivenugopal, Minghai Wang, and Ruiwen Zhang (2013). “The MDM2-p53 pathway revisited”. In: *Journal of biomedical research* 27.4, p. 254.
- Nelson, DE, AEC Ihekwaba, M Elliott, JR Johnson, CA Gibney, BE Foreman, G Nelson, V See, CA Horton, DG Spiller, *et al.* (2004). “Oscillations in NF- κ B signaling control the dynamics of gene expression”. In: *Science* 306.5696, pp. 704–708.
- Novák, Béla and John J Tyson (2008). “Design principles of biochemical oscillators”. In: *Nature reviews Molecular cell biology* 9.12, pp. 981–991.
- Omel’chenko, Oleh E (2018). “The mathematics behind chimera states”. In: *Nonlinearity* 31.5, R121.
- Ott, Edward and Thomas M. Antonsen (2008). “Low dimensional behavior of large systems of globally coupled oscillators”. In: *Chaos* 18.3.
- Panaggio, Mark J. and Daniel M. Abrams (2015). “Chimera states: Coexistence of coherence and incoherence in networks of coupled oscillators”. In: *Nonlinearity* 28.3, R67–R87.
- Pessina, Fabio, Fabio Giavazzi, Yandong Yin, Ubaldo Gioia, Valerio Vitelli, Alessandro Galbiati, Sara Barozzi, Massimiliano Garre, Amanda Oldani, Andrew Flaus, *et al.* (2019). “Functional transcription promoters at DNA double-strand breaks mediate RNA-driven phase separation of damage-response factors”. In: *Nature cell biology* 21.10, pp. 1286–1299.

- Petronilho, Elaine C, Murilo M Pedrote, Mayra A Marques, Yulli M Passos, Michelle F Mota, Benjamin Jakobus, Gileno dos Santos de Sousa, Filipe Pereira da Costa, Adriani L Felix, Giulia DS Ferretti, *et al.* (2021). “Phase separation of p53 precedes aggregation and is affected by oncogenic mutations and ligands”. In: *Chemical science* 12.21, pp. 7334–7349.
- Pfeuty, Benjamin, Quentin Thommen, and Marc Lefranc (2011). “Robust entrainment of circadian oscillators requires specific phase response curves”. In: *Biophysical journal* 100.11, pp. 2557–2565.
- Pikovsky, Arkady, Michael Rosenblum, and Jürgen Kurths (2001). *Synchronization: A Universal Concept in Nonlinear Sciences*. Cambridge Nonlinear Science Series. Cambridge University Press.
- Purvis, Jeremy E, Kyle W Karhohs, Caroline Mock, Eric Batchelor, Alexander Loewer, and Galit Lahav (2012). “p53 dynamics control cell fate”. In: *Science* 336.6087, pp. 1440–1444.
- Purvis, Jeremy E and Galit Lahav (2013). “Encoding and decoding cellular information through signaling dynamics”. In: *Cell* 152.5, pp. 945–956.
- Rattenborg, N.C, C.J Amlaner, and S.L Lima (2000). “Behavioral, neurophysiological and evolutionary perspectives on unihemispheric sleep”. In: *Neuroscience & Biobehavioral Reviews* 24.8, pp. 817–842.
- Reyes, José, Jia-Yun Chen, Jacob Stewart-Ornstein, Kyle W Karhohs, Caroline S Mock, and Galit Lahav (2018). “Fluctuations in p53 signaling allow escape from cell-cycle arrest”. In: *Molecular cell* 71.4, pp. 581–591.
- Riley, Todd, Eduardo Sontag, Patricia Chen, and Arnold Levine (2008). “Transcriptional control of human p53-regulated genes”. In: *Nature reviews Molecular cell biology* 9.5, pp. 402–412.
- Rinzel, J and GB Ermentrout (1989). *Analysis of neural excitability and oscillations* In Koch, C. and Segev, I., eds., *Methods in Neuronal Modeling*.
- Rodriguez, Eugenio, Nathalie George, Jean-Philippe Lachaux, Jacques Martinerie, Bernard Renault, and Francisco J Varela (1999). “Perception’s shadow: long-distance synchronization of human brain activity”. In: *Nature* 397.6718, pp. 430–433.
- Sanchez, Paul Gerald Layague, Victoria Mochulska, Christian Mauffette Denis, Gregor Mönke, Takehito Tomita, Nobuko Tsuchida-Straeten, Yvonne Petersen, Katharina Sonnen, Paul François, and Alexander Aulehla (2022). “Arnold tongue entrainment reveals dynamical principles of the embryonic segmentation clock”. In: *Elife* 11, e79575.
- Schmidt, Lennart, Konrad Schonleber, Katharina Krischer, and Vladimir Garcia-Morales (2014). “Coexistence of synchrony and incoherence in oscillatory media under nonlinear global coupling”. In: *Chaos: An Interdisciplinary Journal of Nonlinear Science* 24.1.
- Schöll, Eur (2016). “Synchronization patterns and chimera states in complex networks: Interplay of topology and dynamics”. In: *The European Physical Journal Special Topics* 225, pp. 891–919.
- Smeal, Roy M., G. Bard Ermentrout, and John A. White (2010). “Phase-response curves and synchronized neural networks”. In: *Philosophical Transactions of the Royal Society B: Biological Sciences* 365.1551, pp. 2407–2422. eprint: <https://royalsocietypublishing.org/doi/pdf/10.1098/rstb.2009.0292>.
- Söding, Johannes, David Zwicker, Salma Sohrabi-Jahromi, Marc Boehning, and Jan Kirschbaum (2020). “Mechanisms for active regulation of biomolecular condensates”. In: *Trends in Cell Biology* 30.1, pp. 4–14.
- Stavans, J, F Heslot, and A Libchaber (1985). “Fixed winding number and the quasiperiodic route to chaos in a convective fluid”. In: *Physical Review Letters* 55.6, p. 596.
- Strogatz, Steven H (2018). *Nonlinear dynamics and chaos with student solutions manual: With applications to physics, biology, chemistry, and engineering*. CRC press.

- Strogatz, Steven H and Ian Stewart (1993). “Coupled oscillators and biological synchronization”. In: *Scientific american* 269.6, pp. 102–109.
- Strom, Amy R, Alexander V Emelyanov, Mustafa Mir, Dmitry V Fyodorov, Xavier Darzacq, and Gary H Karpen (2017). “Phase separation drives heterochromatin domain formation”. In: *Nature* 547.7662, pp. 241–245.
- Tinsley, Mark R, Simbarashe Nkomo, and Kenneth Showalter (2012). “Chimera and phase-cluster states in populations of coupled chemical oscillators”. In: *Nature Physics* 8.9, pp. 662–665.
- Tsabar, Michael, Caroline S Mock, Veena Venkatachalam, Jose Reyes, Kyle W Karhohs, Trudy G Oliver, Aviv Regev, Ashwini Jambhekar, and Galit Lahav (2020). “A switch in p53 dynamics marks cells that escape from DSB-induced cell cycle arrest”. In: *Cell reports* 32.5.
- Tsimring, Lev S (2014). “Noise in biology”. In: *Reports on Progress in Physics* 77.2, p. 026601.
- Turing, Alan Mathison (1952). “The chemical basis of morphogenesis”. In: *Philosophical Transactions of the Royal Society of London. Series B, Biological Sciences* 237.641, pp. 37–72. eprint: <https://royalsocietypublishing.org/doi/pdf/10.1098/rstb.1952.0012>.
- Uhlhaas, Peter J and Wolf Singer (2006). “Neural synchrony in brain disorders: relevance for cognitive dysfunctions and pathophysiology”. In: *neuron* 52.1, pp. 155–168.
- Venkatachalam, Veena, Ashwini Jambhekar, and Galit Lahav (2022). “Reading oscillatory instructions: How cells achieve time-dependent responses to oscillating transcription factors”. In: *Current Opinion in Cell Biology* 77, p. 102099.
- Vogelstein, Bert, David Lane, and Arnold J Levine (2000). “Surfing the p53 network”. In: *Nature* 408.6810, pp. 307–310.
- Volterra, Vito (1927). *Variazioni e fluttuazioni del numero d'individui in specie animali conviventi*. Vol. 2. Società anonima tipografica "Leonardo da Vinci".
- Wang, Yu-Hsiu, Teresa LF Ho, Anushya Hariharan, Hui Chin Goh, Yao Liang Wong, Nicole S Verkaik, May Yin Lee, Wai Leong Tam, Dik C van Gent, Ashok R Venkitaraman, *et al.* (2022). “Rapid recruitment of p53 to DNA damage sites directs DNA repair choice and integrity”. In: *Proceedings of the National Academy of Sciences* 119.10, e2113233119.
- Webster, AJ and ME Cates (2001). “Osmotic stabilization of concentrated emulsions and foams”. In: *Langmuir* 17.3, pp. 595–608.
- Woller, Aurore, Hélène Duez, Bart Staels, and Marc Lefranc (2016). “A mathematical model of the liver circadian clock linking feeding and fasting cycles to clock function”. In: *Cell reports* 17.4, pp. 1087–1097.
- Wu, Hui and Mukesh Dhamala (2018). “Dynamics of Kuramoto oscillators with time-delayed positive and negative couplings”. In: *Physical Review E* 98.3, p. 032221.
- Wu, Xiangwei, J Henri Bayle, David Olson, and Arnold J Levine (1993). “The p53-mdm-2 autoregulatory feedback loop.” In: *Genes & development* 7.7a, pp. 1126–1132.
- Yeargin, Jo and Martin Haas (1995). “Elevated levels of wild-type p53 induced by radiolabeling of cells leads to apoptosis or sustained growth arrest”. In: *Current Biology* 5.4, pp. 423–431.
- Yeung, MK Stephen and Steven H Strogatz (1999). “Time delay in the Kuramoto model of coupled oscillators”. In: *Physical review letters* 82.3, p. 648.
- Zambrano, Samuel, Ilario De Toma, Arianna Piffer, Marco E Bianchi, and Alessandra Agresti (Jan. 2016). “NF- κ B oscillations translate into functionally related patterns of gene expression”. In: *eLife* 5. Ed. by Suzanne Gaudet, e09100.
- Zhang, Yuan, Haihong Liu, Fang Yan, and Jin Zhou (2017). “Oscillatory dynamics of p38 activity with transcriptional and translational time delays”. In: *Scientific reports* 7.1, p. 11495.

Ziaemehr, Abolfazl, Mina Zarei, and Aida Sheshbolouki (2020). "Emergence of global synchronization in directed excitatory networks of type I neurons". In: *Scientific reports* 10.1, p. 3306.